Raman spectroscopy: Techniques and applications in the life sciences

DUSTIN W. SHIPP[1,*]**, FARIS SINJAB**[1,*]**, AND IOAN NOTINGHER**[1,**]

[1] *School of Physics and Astronomy, University of Nottingham, Nottingham NG7 2RD, United Kingdom*
[*] *Both authors contributed equally to this work.*
[**] *Corresponding author: Ioan.Notingher@nottingham.ac.uk*

Raman spectroscopy is an increasingly popular technique in many areas including biology and medicine. It is based on Raman scattering, a phenomenon in which incident photons lose or gain energy via interactions with vibrating molecules in a sample. These energy shifts can be used to obtain information regarding molecular composition of the sample with very high accuracy. Applications of Raman spectroscopy in the life sciences have included quantification of biomolecules, hyperspectral molecular imaging of cells and tissue, medical diagnosis, and others. This review briefly presents the physical origin of Raman scattering explaining the key classical and quantum mechanical concepts. Variations of the Raman effect will also be considered, including resonance, coherent, and enhanced Raman scattering. We discuss the molecular origins of prominent bands often found in the Raman spectra of biological samples. Finally, we examine several variations of Raman spectroscopy techniques in practice, looking at their applications, strengths, and challenges. This review is intended to be a starting resource for scientists new to Raman spectroscopy, providing theoretical background and practical examples as the foundation for further study and exploration. © 2017 Optical Society of America

OCIS codes: (300.6450) Spectroscopy, Raman; (180.5655) Raman microscopy; (300.6230) Spectroscopy, coherent anti-Stokes Raman scattering; (170.3880) Medical and biological imaging; (170.6510) Spectroscopy, tissue diagnostics.

CONTENTS

1. INTRODUCTION

Raman scattering is a phenomenon in which photons incident on a sample are inelastically scattered after interacting with vibrating molecules within the sample. The effect was first discovered by Chandrasekhara Venkata Raman in 1928[1], for which discovery Prof. Raman received the 1930 Nobel Prize in Physics. While Raman spectroscopy is now used in biology and medicine, Raman spectroscopy found its first applications in physics and chemistry[2] and was mainly used to study vibrations and structure of molecules[3, 4]. One early factor limiting the implementation of Raman spectroscopy was the weak scattering signal. Large intensities of monochromatic light are required to excite a detectable signal. This requirement became much easier to realize following the invention of the laser in 1960. Soon thereafter, lasers were used to drive Raman scattering[5, 6] and the number of applications increased rapidly, particularly in the analysis of biomolecules. Other important developments accelerating the progress of Raman spectroscopy include the digitization of spectra using charge-coupled devices (CCDs)[7, 8], the confocal Raman microscope[9], and improved filters to remove light at the laser wavelength[10]. These inventions allowed a rapid increase in the popularity of using Raman to study biological samples in the early 1990s[11–13].

    Raman spectroscopy is a popular technique in the biological sciences partially because it is non-destructive and in principle requires no sample preparation. It is therefore well-suited for applications requiring the sample to be unaltered, including *in vivo* measurements. Additionally, Raman systems operate at visible or near-infrared wavelengths can be easily integrated into standard microscopes and conventional optical fibers. Although usually a point-measurement technique, Raman spectroscopy based on laser or sample scanning can be used to create hyperspectral images.

    For biological samples, Raman spectroscopy is typically sensitive to concentrations of bio-molecules such as lipids, proteins, carbohydrates, and nucleic acids. Raman spectroscopy can very accurately measure relative concentrations of these molecular classes, but is poorly suited to identify specific molecules (*i.e.* specific proteins or DNA sequences). The high accuracy of Raman spectroscopy comes from detecting small changes in the relative concentrations of bio-molecules, *e.g.*, the ratio of protein to lipid within a cell or higher nucleic acid concentrations in tumour tissue. The high accuracy of Raman spectroscopy has received a great deal of attention as a potential diagnostic tool. Raman spectroscopy has been used to classify bacteria [14–16] and diagnose a broad range of diseases[17–19].

    One significant shortcoming of Raman spectroscopy is the weak scattering signals from most samples (see Section 2.3). This results in long acquisition times, which can be particularly disadvantageous when creating hyperspectral images. This disadvantage can be overcome through the use of coherent Raman techniques including coherent anti-Stokes Raman scattering (CARS) and stimulated Raman scattering (SRS), which have much stronger signals than spontaneous (or incoherent) Raman scattering. This increase in signal and imaging speed comes at the expense of diverse spectral information, often acquiring signal at only one or a few wavenumbers.[20–23]. The low Raman scattering signal also limits the technique's ability to detect small concentrations of molecules. Surface enhanced Raman scattering (SERS) uses a metal substrate to enhance the Raman signal, making even trace amounts of molecules detectable[24, 25].

Overview   This review is meant as an introduction to the theory and techniques of Raman spectroscopy, as used in biological and medical applications. The theory of Raman scattering phenomena will be treated with sufficient depth to understand the technical requirements, strengths, and weaknesses of common Raman spectroscopy techniques.

Section 2 will outline the mechanism behind spontaneous, coherent, and enhanced Raman scattering. This will begin with a description of molecular vibrations. We will then describe various interactions of light with these molecular vibrations using both classical and quantum mechanical treatments.

Section 3 will address the molecular origins of some of the most common and most dominant Raman bands encountered when measuring biological samples. This section will focus on Raman spectral contributions from proteins, nucleic acids, lipids, and other common biological molecules.

Section 4 will discuss many of the common techniques currently used in Raman spectroscopy, including the biological applications and shortcomings of each technique. Some of these techniques include spontaneous Raman scattering, coherent anti-Stokes Raman scattering (CARS), stimulated Raman scattering (SRS), surface-enhanced Raman scattering (SERS), fiber optic probes, selective scanning Raman spectroscopy (SSRS), spatially offset Raman spectroscopy (SORS), and Raman-based labeling techniques.

Section 5 will outline some general techniques for classification and modeling studies using Raman spectroscopy. This discussion will address the segregation of data into training, validation, and test sets as well as basic principles of some of the classification models most popularly used with Raman spectroscopy.

Finally, Section 6 will present a brief outlook on the future of Raman spectroscopy in the life sciences.

2. RAMAN SCATTERING: INELASTIC SCATTERING OF LIGHT BY MOLECULES

2.1. Molecular vibrations

Molecular vibrational modes describe the relative motion of atoms within a molecule. For a molecule with N atoms, there are $3N$ degrees of freedom associated with the x, y, and z positions of each atom. Three of these degrees of freedom include translating the whole molecule without changing any of the intra-molecular distances. Three additional degrees of freedom are accounted for by rotating the whole molecule (two for linear molecules). All other changes in the positions of atoms result in stretching, contracting, or otherwise deforming chemical bonds between atoms. These represent the vibrational modes. There are therefore $3N - 6$ vibrational modes for a molecule with N atoms ($3N - 5$ if molecule is linear).[26]

The analysis below will show that the energies of these molecular vibrations are quantized. The allowed vibrational energies are set by the properties of the atoms in the molecule and the bonds between them. These vibrational energies are fundamental to the phenomenon of Raman scattering.

2.1.1. Mass on a Spring

A molecular bond can be approximated as a spring connecting two masses. The potential energy U of the "spring" is given by

$$U = \frac{1}{2}kx^2, \tag{1}$$

where k is the "spring constant," and x is the displacement of the nuclei from their equilibrium bond position. Applying Schrödinger's equation to this potential gives

$$\frac{-\hbar^2}{2m}\frac{d^2\psi}{dx^2} + \frac{1}{2}kx^2\psi = E\psi, \tag{2}$$

where E is the vibration energy and ψ is the wavefunction of the system. In this equation, m is the reduced mass of the atoms involved in the vibration, given by $m = \frac{m_1 m_2}{m_1 + m_2}$.

Solving Equation 2 reveals that these vibrations are quantized. The vibrational energies are given by

$$E_v = (v + \frac{1}{2})\hbar\sqrt{\frac{k}{m}}, \tag{3}$$

where v is the quantum number of the vibrational mode. This result can be applied to vibrational modes of molecules and shows that the energies are quantized. Indeed, for larger and more complex molecules, the dependence of k and m on the force constants and masses of the atoms is more complicated.

2.1.2. Energies of Molecular Vibrations

Wavenumbers   Traditionally, energies of molecular vibrational modes are expressed with units of wavenumbers, or cm^{-1}. This convention is a result of the origins of Raman spectroscopy in chemistry and the similarity of the technique to IR absorption spectroscopy, which also probes molecular vibrations.

The method of using wavenumbers as a unit of energy can be seen in the following example. Suppose a sample is illuminated with laser light at 785 nm. This wavelength can also be expressed as a photon energy in terms of wavenumbers. To do this,

$$\tilde{\nu} = \frac{1}{\lambda[\text{cm}]}. \tag{4}$$

For $\lambda_i = 785$ nm $= 7.85 \times 10^{-5}$ cm,

$$\tilde{\nu}_i = \frac{1}{7.85 \times 10^{-5} \text{ cm}} = 1.27 \times 10^4 \text{ cm}^{-1}. \tag{5}$$

Although these units are not equivalent to energy (*e.g.*, Joules), this value is often referred to as an energy

Rules of Thumb for Vibration Energies   A precise value for the spring constant, k, is difficult to calculate from theory for most molecules. Density-functional theory is sometimes used to estimate vibrational energies, but more often, the energy of a vibration is taken from measurements. However, several rules of thumb can provide useful information to estimate a vibrational mode's energy or identify the vibration associated with a measured signal.

An increase in the reduced mass m in Equation 3 will lead to lower energies. Thus, bonds involving larger atoms will vibrate with lower energies. This is very apparent when comparing carbon-hydrogen (C-H) vibrations (2800-3100 cm^{-1}) to carbon-carbon (C-C) vibrations (800-1100 cm^{-1}).

Stronger bonds such as double- or triple-bonds increase the spring constant in Equation 3. This leads to higher energies. For example, carbon double-bond vibrations (C=C) are found at 1550-1660 cm^{-1}. The bond strength (*i.e.* spring constant) also depends on the type of vibration. Different types of vibrations include stretching, deformation (*i.e.* scissors, wagging), and others. The relationships between these vibrations can be complex, but some general rules apply. For example, stretching modes have a higher k than deformations and thus occur at higher energies[26].

If multiple bonds are involved in a vibrational mode, Raman scattering is usually more intense if the stretches happen in phase with each other (*i.e.* bonds get longer/shorter at the same time). In-phase vibrations allow the dipoles to constructively interfere with each other. Multiple similar bonds vibrating in phase often produce the most intense Raman scattering. Some examples of this include the breathing of a ring shaped molecule such as benzene or a nucleic acid base[26].

2.1.3. Vibrational Modes and Group Theory

Not all vibrations are active in absorption or Raman scattering. Multiple methods exist to determine if a particular vibration will be absorption-active, Raman-active, both, or neither. This behavior depends on the symmetry properties of the vibrational mode (treated in detail in Sections 2.2 and 2.3).

In this analysis, it can be useful to categorize vibrational modes using group theory. Group theory classifies complicated molecular vibrations into groups that share symmetry properties. We will introduce this using the linear molecule CO_2 as an example. As a linear, invertible molecule, CO_2 is in symmetry group (or point group) $D_{\infty h}$. This symmetry group has six symmetry operations (named by Mulliken[27]): the identity operation (E), rotation of any angle about the dominant axis ($2C_\infty$), reflection about any plane intersecting the dominant axis ($\infty\sigma_v$), inversion (i), improper rotation (rotation followed by reflection) of any angle about the dominant axis ($2S_\infty$), and rotation of $180°$ perpendicular to the dominant axis (∞C_2).

The various vibrational modes of molecules belonging to symmetry group $D_{\infty h}$ (including CO_2) can be analyzed using the character table in Table 1. Each vibrational mode can be expressed as one of the irreducible representations found in the rows of Table 1. The table describes how each irreducible representation behaves under each of the symmetry operations (columns). This behavior determines whether the mode will be absorption-active, Raman-active, both, or neither (see Section 2.3). Similar tables for other symmetry groups (applying to other molecules) can be found in numerous sources, including Long[28] and Diem[29].

$D_{\infty h}$	E	$2C_\infty$	$\infty\sigma_v$	i	$2S_\infty$	∞C_2
A_{1g}	1	1	1	1	1	1
A_{2g}	1	1	-1	1	1	-1
E_{1g}	2	$2\cos(\phi)$	0	2	$-2\cos(\phi)$	0
E_{2g}	2	$2\cos(2\phi)$	0	2	$2\cos(2\phi)$	0
E_{3g}	2	$2\cos(3\phi)$	0	2	$-2\cos(3\phi)$	0
A_{1u}	1	1	1	-1	-1	-1
A_{2u}	1	1	-1	-1	-1	1
E_{1u}	2	$2\cos(\phi)$	0	-2	$2\cos(\phi)$	0
E_{2u}	2	$2\cos(2\phi)$	0	-2	$-2\cos(2\phi)$	0
E_{3u}	2	$2\cos(3\phi)$	0	-2	$2\cos(3\phi)$	0

Table 1. Character table for Point Group $D_{\infty h}$ showing behavior of irreducible representations under symmetry operations. CO_2 is a member of this point group, so the irreducible representations describe vibrational modes of this linear molecule.

For example, the symmetric stretching mode of CO_2 (see Figure 1(a)) is unchanged by each of the symmetry operations for $D_{\infty h}$. This matches the behavior of the irreducible representation A_{1g}.

On the other hand, the asymmetric stretching mode (see Figure 1(b)) reverses orientation under the inversion (i), improper rotation (S_∞), and perpendicular axis-rotation (C_2) operations. This behavior is described by the irreducible representation A_{1u}. The other vibrational modes of CO_2 will not be treated here. It should be noted, however, that while every vibrational mode can be expressed as one of the irreducible representations for the molecule's point group, every irreducible representation will not necessarily be found as a vibrational mode for a given molecule. Irreducible representations simplify the description of Raman and absorption selection rules. Section 2.3 will describe how group theory can be used to determine if a vibrational mode will be Raman-active, absorption-active, both, or neither.
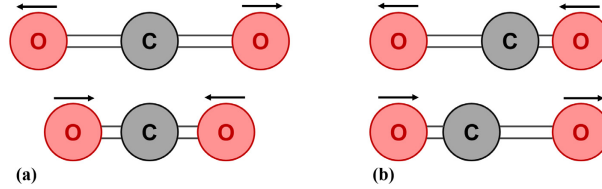
Fig. 1. (a) CO_2 symmetric stretching vibrational mode. This mode can be expressed as the irreducible representation A_{1g} (b) CO_2 asymmetric stretching vibrational mode. This mode can be expressed as the irreducible representation A_{1u}

2.2. Classical Description of Raman Scattering

2.2.1. Electromagnetically Induced Changes to the Molecular Polarizibility

Many of the properties of Raman scattering can be understood by examining the process of an oscillating electric field interacting with a polarizible molecule. The most complete early derivation of the Raman effect was presented by Placzek in 1934[30]. An electric field with amplitude E_0 oscillating with frequency ω_{rad} induces an electric dipole proportional to the polarizibility (α) of the molecule that can be expressed as

$$\mu = \alpha E_0 \sin(\omega_{rad} t), \tag{6}$$

where t is time. While this oscillating dipole can be responsible for absorption or elastic scattering of light, the polarizibility α of the molecule changes during molecular vibrations. If the vibration has frequncy ω_{vib}, the vibration changes the displacement x between atoms by

$$x = x_0 \sin(\omega_{vib} t + \phi), \tag{7}$$

where ϕ is the phase of the vibration. Without knowing the exact dependence of α on x, we can analyze α generally. Assuming the displacement is small, we can expand α in a Taylor series to get

$$\alpha = \alpha_0 + \frac{\partial \alpha}{\partial x}\bigg|_{x=0} x + \dots. \tag{8}$$

Knowing the dependence of x on the molecular vibrations, the polarizibility can be written

$$\alpha = \alpha_0 + \frac{\partial \alpha}{\partial x}\bigg|_{x=0} x_0 \sin(\omega_{vib} t + \phi). \tag{9}$$

Applying this form of the polarizibility to Equation 6, the electric dipole becomes

$$\mu = [\alpha_0 + \frac{\partial \alpha}{\partial x}\bigg|_{x=0} x_0 \sin(\omega_{vib} t + \phi)] E_0 \sin(\omega_{rad} t), \tag{10}$$

which can be rewritten as

$$\mu = \alpha_0 E_0 \sin(\omega_{rad} t) + \frac{E_0}{2} \frac{\partial \alpha}{\partial x}\bigg|_{x=0} x_0 \big(\cos[(\omega_{rad} - \omega_{vib})t - \phi] - \cos[(\omega_{rad} + \omega_{vib})t + \phi] \big). \tag{11}$$

An induced dipole oscillating with a frequency ω emits radiation along an angle θ with intensity

$$I = \frac{\omega^4 \mu_0^2 \sin\theta^2}{32\pi^2 \varepsilon_0 c^3}, \tag{12}$$

where μ_0 is the amplitude of the induced electric dipole and ε_0 and c are the permittivity and speed of light in a vacuum, respectively[28, 31]. The dipole derived in Equation 11 then radiates electromagnetic waves at the frequencies ω_{rad}, $(\omega_{rad} - \omega_{vib})$, and $(\omega_{rad} + \omega_{vib})$. In practice, it is usually the case that $\omega_{rad} \gg \omega_{vib}$. Thus, as with other types of scattering, the intensity of Raman scattered light decreases with the fourth power of the incident wavelength. The amplitude of the induced dipole, p_0, scales linearly with the incident electric field. Therefore the intensity of Raman scattered light will scale linearly with the excitation intensity.

Rayleigh Scattering   Analyzing each of the radiative frequencies in Equation 11 reveals different light scattering phenomena. The $\sin(\omega_{rad} t)$ term corresponds to scattered radiation with a frequency equal to the incident light, which is called Rayleigh scattering. As there is no change in energy, this event is also called elastic scattering.

Stokes Raman Scattering   The radiation represented by the $\cos[(\omega_{rad} - \omega_{vib})t] - \phi$ term has been shifted down in frequency by ω_{vib}. This means that the scattered radiation has lost energy equal to the energy of the molecular vibrations. This difference in energy is called a Stokes shift. This energy has been absorbed by molecule to excite the vibrational mode corresponding to ω_{vib}. This energy is generally dissipated non-radiatively following the scattering event. Because the phase ϕ is different for every molecule, Stokes Raman scattered light (generally refered to as simply "Raman scattering," or "spontaneous Raman scattering") is incoherent.

Anti-Stokes Raman Scattering   The $\cos[(\omega_{rad} + \omega_{vib})t]$ term describes an increase in frequency of scattered radiation. In this process, the scattered radiation has gained energy equal to the energy of the molecular vibration. In order for this to be possible, the molecule must begin the process in an excited vibrational state and finish in the ground state (or a lower vibrational state). This phenomenon is called anti-Stokes Raman scattering. Similarly to Stokes Raman scattering, anti-Stokes Raman scattering is also incoherent.

2.2.2. Energy Shift in Wavenumbers

Scattered radiation loses energy in the process of Stokes Raman scattering. Expressing this energy in terms of wavenumbers, the energy becomes

$$\tilde{\nu}_f = \tilde{\nu}_i - \tilde{\nu}_{shift}. \tag{13}$$

For example, if the 785 nm radiation discussed in 5 excites the CH_2 scissors vibration vibrating at 1450 cm^{-1},

$$\tilde{\nu}_f \;=\; 1.27 \times 10^4 \text{ cm}^{-1} \;-\; 1450 \text{ cm}^{-1} \;=\; 1.13 \times 10^4 \text{ cm}^{-1}. \tag{14}$$

This value is again expressed as energy in terms of wavenumbers. We can convert this into the familiar wavelength by inverting Equation 4. This gives us $\lambda_f = 8.86 \times 10^{-5}$ cm $= 886$ nm. This method of calculation can be very useful when designing the filters and detectors for a Raman system.

2.2.3. Selection Rules

From Equation 11, for Stokes or anti-Stokes Raman scattering to occur, the derivative of the molecule's polarizibility must be non-zero. In more physical terms, the vibration must change the molecule such that it is more polarizible in one direction and less polarizible in the other. This provides a selection rule for vibrations that will be Raman-active.

This criterion is different from the selection rule for absorption-active vibrations used in infrared spectroscopy. Absorption-active vibrations must have a non-zero derivative of the electric dipole, rather than the polarizability. These criteria are non-exclusive; some vibrations are absorption-active, some are Raman-active, some are both, and some are neither.

Carbon dioxide (CO_2) provides examples of vibrational modes to illustrate these selection rules. Figure 1(a) shows the symmetric stretching mode of CO_2. In both directions of the vibration, the centers of positive and negative charge remain unchanged. Thus, the derivative of the electric dipole is zero and this vibration is absorption-inactive. On the other hand, when the atoms are extended in this vibration, the electron clouds are stretched and less tightly bound, making the molecule more polarizible. The opposite is true in the other direction of vibration. This means that the derivative of the polarizibility is non-zero and the vibration is Raman-active.

Another case is illustrated by the asymmetric stretching mode in Figure 1(b). In the extremes of this vibration, the center of positive charge shifts back and forth, changing the dipole. This vibration is absorption-active because the electric dipole changes. However, the molecule's polarizibility is the same in these extremes. Thus, the derivative of the polarizibility is zero and the vibration is Raman-inactive.

2.3. Quantum Mechanical Description of Raman Scattering

Additional insight may be gained by considering Raman scattering through the lens of quantum mechanics. In short, this quantum mechanical treatment reveals Raman scattering as a transition between energy levels via a "virtual state." This virtual state is crucial to the phenomenon of resonance Raman scattering, which will be discussed in Section 2.4. Quantum mechanics will also allow us to estimate the intensities of Raman bands. Additionally, quantum mechanics allows us to understand the relative dominance of Stokes Raman scattering over anti-Stokes and derive selection rules using group theory for different molecular vibrations.

2.3.1. Raman Scattering as a Transition Between States

Figure 2 shows various depctions of relevent scattering processes. The Jablonski energy level diagram of spontaneous Raman scattering in Figure 2(c) describes the process in two steps. First, the incident light drives the molecule into an excited "virtual state." This virtual state has arbitrary energy and does not have to correspond to an actual allowed state of the molecule.

Second, the molecule decays from the virtual state, releasing a photon. Most of the time $\big($depending on the temperature and distribution of states in the molecule (see Equation 20)$\big)$, the molecule will decay back into the ground state. The scattered photon will be equal in energy (and wavelength) to the incident photon. This event is called Rayleigh scattering.

Alternatively, the molecule may decay into an excited vibrational state. The scattered photon can lose energy equal to that of the vibrational state and increases in wavelength – this is Stokes Raman scattering. In anti-Stokes Raman scattering, the photon can be scattered by a molecule initially in an excited vibrational state. The scattered photon gains energy and decreases in wavelength as the molecule returns to the ground state.

The quantum paths for these processes are depicted in the Feynman diagrams in Figure 2(d). The involvement of the virtual state is again apparent in this representation. Furthermore, the Feynman diagrams reveal the dependence of spontaneous Raman scattering on an interaction with the vacuum field[32]. This interaction has an arbitrary phase, making the resulting scattered radiation incoherent[33].

2.3.2. Transition Rate of Raman Scattering

Fermi's Golden Rule uses quantum mechanics to provide a mathematical description of the transition rate between two states mediated by a transition dipole. Fermi's Golden Rule is written as

$$R_{|i\rangle \to |f\rangle} \approx \left| \langle f | \mu_{if} | i \rangle \right|^2 |E_0|^2 \delta(\epsilon_f), \tag{15}$$

where $R_{|i\rangle \to |f\rangle}$ is the rate of transition from initial state $|i\rangle$ to final state $|f\rangle$, μ_{if} is the perturbation of the Hamiltonian coupling $|i\rangle$ to $|f\rangle$, E_0 is the electric field amplitude of the incident light, and $\delta(\epsilon_f)$ is the density of final states[34]. Here, $d_{|i\rangle \to |f\rangle} = \mu_{if} E_0$ is the transition dipole facilitating the transition from $|i\rangle$ to $|f\rangle$. The coupling between the initial and final states of a given transition can
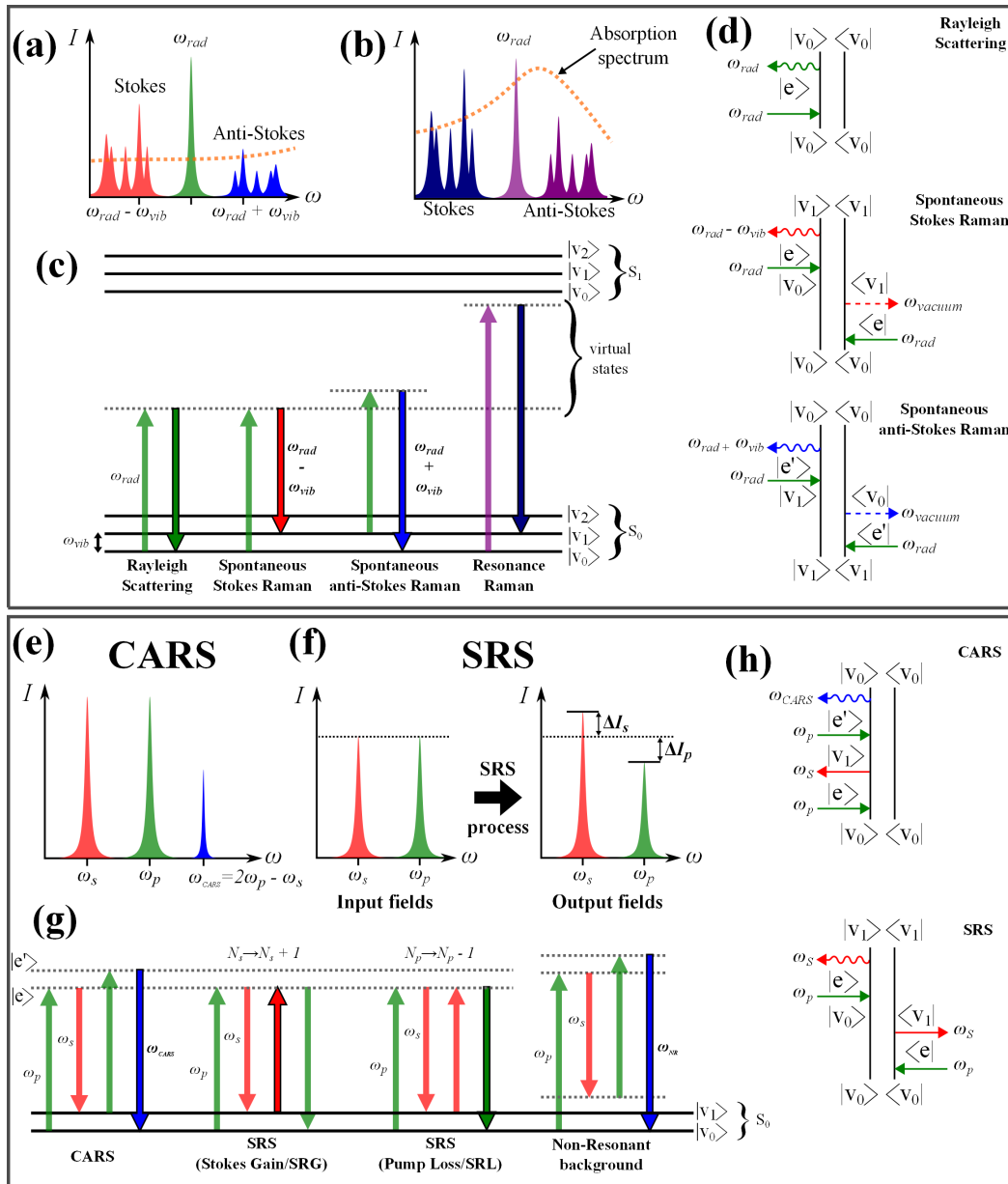
Fig. 2. Energy level, spectral, and Feynman diagrams for spontaneous and coherent Raman processes. Transition arrows with black outlines and bold labels indicate the experimentally measured feature. Spectral intensities are not to scale.

(a) Using a single excitation beam (away from absorption band) will generate weak Raman scattering at many different vibrational Stokes and anti-Stokes frequencies.

(b) Excitation near electronic resonance (absorption band) greatly increases the scattering signal (see resonance Raman, Section 2.4)

(c) Energy level diagrams for spontaneous scattering processes including Rayleigh, Stokes Raman, anti-Stokes Raman, and resonance Raman scattering.

(d) Feynman diagrams for Rayleigh, Stokes Raman, and anti-Stokes Raman scattering. In the spontaneous Raman scattering processes, the *bra* state interacts with the vacuum field[32].

(e) CARS utilizes pump and Stokes beams tuned to ω_{vib} to populate the excited vibrational state, from which anti-Stokes Raman scattering is measured. Non-resonant contributions are also possible in this scheme, whereby all intermediate transitions are mediated via virtual states.

(f) SRS also uses two input beams, but no additional frequencies are generated by the SRS process. Instead, the intensity change in the pump or Stokes beam is measured.

(g) Energy level diagrams for coherent scattering processes including CARS, SRS, and non-resonant background (see Section 2.5).

(h) Feynman diagrams for CARS and SRS. These processes are driven by coherent interactions with pump and Stokes (or probe) beams[32]. These coherent interactions greatly increase the measurable signal.

be written in terms of the transition dipole, a complex vector quantifying the interaction between the states. The transition dipole for Raman scattering is

$$d_{|i\rangle \to |f\rangle} = \frac{E_0}{\hbar} \sum_e \left[\frac{\mu_{ef}^{(1)} |e\rangle \langle e| \mu_{ie}^{(1)}}{\omega_{rad} - \omega_{ei} - i\Gamma_e} + \frac{\mu_{ef}^{(2)} |e\rangle \langle e| \mu_{ie}^{(2)}}{\omega_{rad} + \omega_{ei} + i\Gamma_e} \right],$$ (16)

where $|e\rangle$ is an arbitrary excited electronic state, ω_{rad} is the frequency of incident light, ω_{ei} is the separation of the ground state $|i\rangle$ and the excited state $|e\rangle$ expressed as a frequency, and Γ_e is $\hbar/(2\tau_e)$, where τ_e is the lifetime of $|e\rangle$ before decaying to $|i\rangle$[28]. Each term within the sum can be considered independently and transition through different virtual states, so two transition dipoles are seen in Equation 16. The total transition consists of contributions from the transitions involving all possible virtual states $|e\rangle$. By applying Fermi's Golden Rule to this transition and restricting our analysis to the most significant terms, we find the rate of Raman scattering to be

$$R_{|i\rangle \to |f\rangle} \approx \left| \langle f| d_{|i\rangle \to |f\rangle} |i\rangle \right|^2 \approx \sum_e \left| \frac{\langle f| \mu_{ef} |e\rangle \langle e| \mu_{ie} |i\rangle}{\omega_{rad} - \omega_{ei} + i\Gamma_e} \right|^2 |E_0|^2 \delta(\epsilon_f).$$ (17)

The two step process of Raman scattering can be seen in the numerator of Equation 17. The term $\langle e| \mu_{ie} |i\rangle$ describes the transition from the ground state to the virtual state while the term $\langle f| \mu_{ef} |e\rangle$ describes the transition from the virtual state to the final state – an excited vibrational state.

Equation 17 can be assumed provided that

$$\omega_{rad} > \omega_{fi},$$ (18)

where ω_{fi} is the frequency corresponding to the energy difference between the final and initial states $|f\rangle$ and $|i\rangle$, respectively[28]. In other words, the photon initiating the Raman process must have more energy than the vibrational transition it is exciting. Most vibrational modes are quite low in energy, corresponding to mid-infrared radiation. Therefore, satisfying this condition is rarely a problem in practice.

2.3.3. Raman Scattering Rate

A number of properties of Raman scattering can be seen from these results. First, Equation 17 shows that the rate of the transition is proportional to $|E_0|^2$, meaning that Raman scattering scales linearly with the incident intensity. This is consistent with the classical model discussed in Section 2.2.

Second, Raman scattering relies on a transition through a virtual state $|e\rangle$. The molecule is not stable in this virtual state, meaning that the Raman scattering process happens very fast. In practice, the time for a scattering event is on the order of femtoseconds. The difference in timing between Raman scattering and other phenomena is useful to discriminate against these slower effects (*e.g.*, fluorescence (see Section 4.1)).

Scattering Cross-section   Long shows that typical values for the transition dipole can be calculated or measured to be on the order of $5 \times 10^{-42} \frac{Cm^2}{V}$ [28]. This value can be used to estimate the Raman scattering cross-section, σ'. The scattering cross section is used to express the intensity of scattered light as a function of the incident irradiance and density of scatterers being irradiated. Following the calculations by Long, σ' takes values on the order of $5 \times 10^{-35} \frac{m^2}{sr\ molecule}$ [28].

The scattering cross-section can be used to find the scattered intensity by

$$I = \sigma' J N,$$ (19)

where I is the scattered intensity in Watts per steradiant, J is the excitation irradiance in Watts per meter^2, and N is the number of molecules irradiated.

Because typical values for σ' are very small, this results in very weak levels of Raman scattering compared to Rayleigh scattering. In most samples, one photon is Raman scattered for every $10^6 - 10^{10}$ excitation photons incident on the sample. This weak signal is one of the main disadvantages of Raman spectroscopy. This will be discussed further in Section 4.1.

Stokes and Anti-Stokes Raman Scattering Intensities   From Equation 17, the transition can also happen in the reverse direction, starting from the excited vibrational state and ending in the ground state. This event results in a blue-shifted photon and is called anti-Stokes Raman scattering. However, anti-Stokes Raman scattering can only occur if there are molecules already in an excited vibrational state when the incident photon arrives. The number of molecules in this state (N_v) relative to the ground state (N_g) is given by

$$\frac{N_v}{N_g} = e^{-\frac{\hbar \omega_v}{k_B T}},$$ (20)

where ω_v is the frequency corresponding the the energy of the vibration, k_B is the Boltzman constant, and T is the temperature of the sample. The occurence of anti-Stokes Raman scattering will be proportional to the number of molecules in an excited vibrational state. Therefore, the ratio of anti-Stokes Raman intensity I_{AS} to Stokes Raman intensity I_S can be estimated by

$$\frac{I_{AS}}{I_S} = e^{-\frac{\hbar \omega_v}{k_B T}}.$$ (21)

This relationship has been used to remotely estimate the temperature of samples at very low temperatures[35–37].

2.3.4. Selection Rules

The quantum mechanically-derived selection rules for Raman-active vibrational modes are based on the transition dipole μ_{if}. These rules match the classical selection rules, but can be derived in different ways. This can simplify the selection rules for some molecules.

The quantum mechanically-derived selection rules can be generalized using group theory. The character table in Table 2 again shows the irreducible representations in point group $D_{\infty h}$, corresponding to the vibrational modes of CO_2. Here, however, the table shows which irreducible representations describe the transformations of linear, rotational, and quadratic coordinates. Similar tables for common symmetry groups have been published elsewhere, including by Long[28] and Diem[29].

$D_{\infty h}$	linear	rotation	quadratic
A_{1g}			$x^2 + y^2, z^2$
A_{2g}		R_z	
E_{1g}		R_x, R_y	x^2, y^2
E_{2g}			$x^2 - y^2, xy$
E_{3g}			
A_{1u}	z		
A_{2u}			
E_{1u}	x, y		
E_{2u}			
E_{3u}			

Table 2. Character table for Point Group $D_{\infty h}$ showing linear, rotational, and quadratic transformations of irreducible representations.

The numerator of Equation 17 contains transitions through two dipole terms, μ_{ie} and μ_{ef}. Each transition must be coupled through a dipole (expressed as linear components). Thus, the polarizibility components are expressed as products of two linear components. These products are shown in Table 2 as quadratic components (*e.g.* x^2, xy, yz, etc.)[29].

More formally, the product of the final state, polarizibility, and initial state must belong to a totally symmetric repesentation[28]. In most cases, the initial state will be the ground state and will not contribute to the triple product. Therefore, a vibrational mode will be Raman-active if its representation contains one or more quadratic components[29]. A vibrational mode is absorption-active if its representation contains one or more linear components.

As noted in Section 2.1, the symmetric stretch of CO_2 can be expressed as A_{1g}. From Table 2, we see this vibrational mode transforms as $x^2 + y^2$, and z^2. Because this representation describes quadratic transitions, this vibrational mode is Raman-active. There are no linear transitions associated with this representation, so the vibrational mode is absorption-inactive.

The asymmetric stretch corresponds to A_{1u}. This irreducible representation transforms as z, so the vibrational mode is absorption-active, but Raman-inactive.

Because the selection rules depend on the transition dipoles, they are also based on the incident and detected polarization. However, these effects tend to be less important in biological samples as the molecules are randomly oriented. In crystaline structures, on the other hand, these polarization effects are very pronounced.

Polarization effects can also be used to selectively detect some vibrations. For example, a symmetric vibration scatters with the same polarization as the incident light. An asymmetric vibration will partially scramble the polarization[29]. By detecting only the same polarization as the incident radiation, one can reduce the contribution of anti-symmetric vibrations. This can be helpful to characterize which vibrations are contributing to a complicated Raman spectrum.

2.4. Resonance Raman scattering

Looking at the denominator of Equation 17, one can see that the rate of Raman scattering will be greatly enhanced when $\omega_{rad} \approx \omega_{ei}$. This occurs when the incident light is tuned near resonance with an electronic transition of the molecule (see Figure 2(c)). This enhancement is called resonance Raman scattering.

Unlike other enhancement effects, resonance Raman only amplifies Raman scattering from a specific vibrational mode of the molecule in resonance with the excitation illumination. Other modes and molecules in the sample are not affected. A suitable target molecule for resonance Raman spectroscopy must have strong Raman-active bands as well as absorption bands at practical wavelengths. It is also desirable that this absorption occurs without high levels of accompanying fluorescence.

The selection rules for resonance Raman differ slightly from traditional Raman scattering. Instead of an arbitrary virtual state, resonance Raman must be coupled through a strong absorption band. Each of the transitions (*i.e.* $|i\rangle$ to $|e\rangle$ and $|e\rangle$ to $|f\rangle$) must be allowed[26]. Additionally, one must consider the effects of the excited electronic state on molecular symmetry and selection rules[28]. The molecule may belong to a different symmetry group when electronically excited, which changes how the transitions are considered in group theory.

2.5. Coherent Raman Scattering

With the development of the laser, it became possible to generate light at much higher irradiances than previously achievable. This revealed a plethora of new optical effects in materials, involving multiple photon transitions. This family of transitions were not observable previously, as the time-scale of many optical interactions is short enough that only a single incident photon is involved in any particular transition, as with spontaneous Raman scattering.

If there are sufficient numbers of photons incident upon a molecule within a sufficiently short space of time, the probability of a multiple-photon transition pathway increases. Another way of visualizing this is that the light is of sufficient intensity to modify the optical properties of the material, which allows new processes to occur[38]. This is the premise of the field of nonlinear optics, which considers effects such as second (and higher order) harmonic generation, sum- and difference-frequency generation, saturable and multi-photon absorption, and coherent Raman processes, among many others. These techniques all rely on the ability of pulsed lasers (with pulse durations ranging from femtoseconds to picoseconds) to generate high peak powers, which allow nonlinear optical processes to occur, whilst maintaining a sufficiently low average power to avoid photo-damage.

The focus of this part of the review will be on coherent Raman effects, which are nonlinear optical processes that are mediated by vibrational states. In particular we will discuss coherent anti-Stokes Raman scattering (CARS) and stimulated Raman scattering (SRS), as they are pertinent to studies in the life sciences. Other coherent Raman processes such as the Raman-induced Kerr effect, coherent Stokes Raman scattering and higher order processes are addressed in references [38, 39].

To understand CARS and SRS, it is convenient to discuss the material response in terms of the macroscopic electromagnetic parameters. In linear optics, the relationship between the polarization density P and incident electric field E in one direction is written

$$P = \epsilon_0 \chi(\omega) E \tag{22}$$

where ϵ_0 is the permittivity of free space and $\chi(\omega)$ is the dielectric susceptibility, which is generally frequency dependent (note: this equation can be viewed as the macroscopic representation of Equation 6). For nonlinear optics however, this polarization response is not necessarily linear, and Equation 22 may be expanded more generally as

$$P_i = \epsilon_0 \chi_{ij}^{(1)} E_j + \epsilon_0 \chi_{ijk}^{(2)} E_j E_k + \epsilon_0 \chi_{ijkl}^{(3)} E_j E_k E_l + \ldots = P^{(1)} + P^{(2)} + P^{(3)} + \ldots \tag{23}$$

where the superscript denotes the order of the nonlinear effect, and the subscripts i, j, k, l each indicate a Cartesian component $1, 2, 3$ linked to the outgoing (P_i) and incident (E_j, E_k, E_l) fields (the subscripts will be omitted for clarity). For linear effects described by Equation 22 (corresponding to $P^{(1)}$), vector components can often be reduced to a scalar form. However in nonlinear optics, the efficiency of a process occurring generally requires consideration of the relative orientations of the incident and output field vectors, known as phase-matching conditions.

CARS and SRS processes in particular are mediated by the third-order nonlinear susceptibility ($\chi^{(3)}$) in Equation 23. The three electric field terms associated with $\chi^{(3)}$ in Equation 23 originate from two incident laser beams, usually labeled the pump frequency (ω_p) and the Stokes frequency (ω_s), such that the total third order polarization is $P^{(3)} = \chi^{(3)} E_p E_s E_p$. It should be noted that these naming conventions vary, with the second ω_p in the CARS process or ω_s in SRS sometimes being labeled the "probe" beam. Both CARS and SRS processes involve coherently driving the vibrational modes of molecules within a sample volume using these two input beams.

CARS is a parametric process, which means the initial and final real vibrational states of the material in the process are identical, and energy is only exchanged between the input/output fields, not the medium. Conversely, SRS is non-parametric meaning the fields exchange energy with the medium in a dissipative process. Another way of thinking about this is that CARS is analogous to other scattering processes such as Rayleigh and spontaneous Raman, whereas SRS is more of a nonlinear version of absorption/emission (loss/gain) involving Raman transitions. Introductory CARS and SRS theory focusing on the physical processes will be introduced in this section (more rigorous mathematical descriptions can be found in [38–40]). Specific information on CARS and SRS for microscopy will be introduced later in the corresponding application Sections 4.3 and 4.4.

2.5.1. CARS

CARS is a special case of the more general four-wave mixing nonlinear process, and was first reported in 1965 by Maker and Tehrune (where it was then termed "Raman laser action"). There it was described as the change in the refractive index of the medium (*i.e.* the introduction of a nonlinear contribution to the dielectric susceptibility) at one frequency, due to waves at a different frequency[41]. The authors were able to demonstrate CARS in liquid benzene, as seen in Figure 3(a) which highlights the angular-dependent scattering geometry for a collinear or weakly focused excitation source (this condition can be relaxed in a microscope using high NA objectives).

The left half of the resonant CARS Jablonski diagram in Figure 2(g) is similar to a spontaneous Stokes-Raman process, except that the second transition now predominantly results from a second input (Stokes) beam. This can be viewed as a driving force at the beat-frequency generated by the two input beams $\omega_p - \omega_s$, which when tuned to be resonant with ω_{vib}, will coherently drive molecular vibrations - resulting in the modified refractive index at this frequency mentioned above. The molecules collectively in this vibrational state undergo anti-Stokes Raman scattering excited by the beam at ω_p, producing light at the anti-Stokes frequency $\omega_{CARS} = 2\omega_p - \omega_s$, which can be detected by standard spectroscopic methods.

As the radiation at ω_{CARS} is generated coherently, contributions from the molecules vibrating in phase will constructively interfere, resulting in orders of magnitude stronger signals compared with spontaneous Raman processes. A related process called coherent Stokes-Raman scattering (CSRS) is possible, producing a frequency $\omega_{CSRS} = 2\omega_s - \omega_p$. However this process is not often studied as the process begins in the less populated excited vibrational states, similar to spontaneous anti-Stokes Raman scattering.
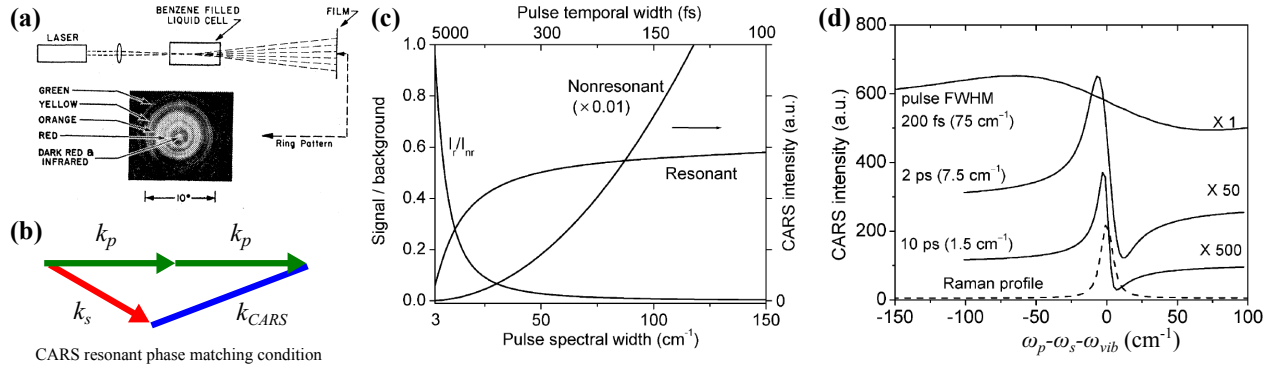
Fig. 3. CARS process.
(a) First observation of CARS (modified from [41]) in benzene (in our notation $\omega_p = \omega_L$, $\omega_{vib} = \Delta_b$ which is the 992 cm^{-1} benzene Raman mode).
(b) Phase-matching condition for CARS with two ω_p and one ω_s photon, demonstrating angular dependence of input and output field directions (see angular distribution in (a)).
(c) Theoretical dependence of the resonant and non-resonant intensities (and their ratio) on laser pulse-width used, and (d) the corresponding effect on CARS lineshape distortion (theoretical model using data from polystyrene 1601 cm^{-1} band[42]). Reprinted (adapted) with permission. Copyright 2004 American Chemical Society.

As fields of different frequencies are involved in the resonant CARS process, the matching of the corresponding wave-vectors ($|\mathbf{k_i}| = n(\omega_i)\omega_i/c$, where $n(\omega_i)$ is the refractive index and $i = p, s, CARS$) must be considered. As the CARS process requires

$$2\omega_p - \omega_s - \omega_{CARS} = 0 \tag{24}$$

for energy conservation, the momentum must also be conserved resulting in the phase–matching condition for the field k-vectors. This is shown schematically in Figure 3(b), and can be expressed as

$$\Delta k = |2\mathbf{k_p} - \mathbf{k_s} - \mathbf{k_{CARS}}| = 0 \tag{25}$$

where the k-vector subscripts correspond to the frequencies of each field involved. Figure 3(b) shows non-collinear excitation for $\mathbf{k_p}$ and $\mathbf{k_s}$, which is in fact necessary because of dispersion (the fact that n varies with ω)[39]. Explicitly, we need both equation 24 and 25 to be satisfied, which is not possible as collinear excitation implies the latter becomes $2n_p\omega_p - n_s\omega_s - n_{CARS}\omega_{CARS} = 0$, which is only compatible if the refractive indices are the same at different frequencies (this will not generally be true even for an isotropic medium). This suggests the need for angle-dependent excitation and/or detection to be used in general. This was observed for the first CARS measurements shown in Figure 3(a) (reproduced from Maker and Terhune[41]), where a single input pump beam was used, which generated an amplified Stokes field within the sample, leading to CARS scattering at various angles. However, this condition can be relaxed such that $\Delta k \neq 0$ for microscopic measurements by considering the shorter length scale of the vibrational coherence ($\Delta k < \pi/l$, where l is the typical sample length), and using collinear beams which are tightly focused (e.g. by a high-NA microscope objective) resulting in a distribution of incident directions for k_p and k_s[42].

One of the major drawbacks to CARS is the contributions generated by unwanted processes which are also possible with the incident light fields that are used. These can be seen when writing the third order susceptibility as

$$\chi^{(3)}(\omega_{vib}) = \chi_{RR}^{(3)}(\omega_{vib}) + \chi_{NR}^{(3)} + \chi_{TP}^{(3)} \tag{26}$$

where $\chi_{RR}^{(3)}$ represents the Raman-resonant susceptibility when $\omega_p - \omega_s = \omega_{vib}$ (which, by itself, would produce a normal lineshape), $\chi_{NR}^{(3)}$ represents non-resonant four-wave mixing contributions which are possible due to the electronic background allowing processes mediated by a virtual state at $\omega_p - \omega_s$ instead of a vibrational resonance, and $\chi_{TP}^{(3)}$ is a two-photon enhanced non-resonant contribution which occurs when $2\omega_p$ is close to an electronic energy level. From the form of Equation 23 it can be seen that the CARS signal intensity will follow

$$I_{CARS}(\omega_{vib}) \propto |\chi^{(3)}(\omega_{vib})|^2 \cdot I_p^2 \cdot I_s \tag{27}$$

where I_p and I_s denote the pump and Stokes beam intensities respectively. Due to the dependence of $I_{CARS}(\omega_{vib})$ on $|\chi^{(3)}(\omega_{vib})|^2$, there will be interference between the different contributions of $\chi^{(3)}(\omega_{vib})$ which create distorted lineshapes such as those seen in Figure 3(d). The two-photon term can be avoided using lower frequency near-infrared excitation, and the other non-resonant background contributions can be minimized by appropriate choice of pulse-width for the input lasers (see Figure 3)[42]. Additionally, as the CARS signal is coherent and will add constructively, the observed intensity will scale as N^2 (where N is the number of molecules generating CARS photons).

2.5.2. SRS

SRS was first observed during the development of the ruby laser in 1962 by Woodbury and Ng[43]. Their instrument, shown schematically in Figure 4(a), produced an additional emission line at the Stokes-shifted Raman frequencies of the nitrobenzene cell in the cavity (in the absence of the sample cell)[44]. This emission was too intense to be due to incoherent (*i.e.* spontaneous) Raman scattering, and was attributed to stimulated Raman gain (SRG) in the ruby laser cavity via the 1344 cm^{-1} nitrobenzene mode[45, 46]. This original experiment differs in that only one incident laser field (ω_p) is applied, and the second (ω_s) was generated due to SRG in the laser cavity, whereas modern SRS utilizes two applied fields with $\omega_p - \omega_s$ tuned to match a particular vibrational mode.

The use of two incident fields at ω_p and ω_s is the key difference between spontaneous and stimulated Raman processes. In terms of the photon population numbers, in spontaneous Raman the single incident excitation field has many photons, while the Stokes field has zero photons before the Raman transition, and one after. In SRS, both the ω_p and ω_s fields initially contain large photon populations, which will induce vibrational coherence in the material if it has a level at $\omega_p - \omega_s$. This leads to an increased rate of Raman transitions involving ω_p and ω_s, which can be detected by changes in their respective photon numbers, i.e. the measured beam intensities (loss in ω_p, gain in ω_s). Furthermore, as the SRS process does not generate any photons at frequencies different from ω_p and ω_s, the phase-matching condition is automatically satisfied as shown in Figure 4(b).

Expressions for the magnitude of gain or loss are dependent only on the $\chi_{RR}^{(3)}(\omega_{vib})$ component from Equation 26. The non-resonant contribution is not present as SRS detection is based on measuring intensity changes at pump and Stokes frequencies, not spectroscopic detection at the CARS frequency. As the CARS nonresonant background originates from a parametric generation process (no energy exchanged with the medium), this would not be observed in such intensity-based detection schemes. However other nonlinear optical processes such as cross-phase modulation, transient absorption and photothermal lensing can interfere with the phase-sensitive SRS detection, though are not typically as detrimental as the non-resonant background in CARS microscopy[47]. Several approaches have been demonstrated to reduce these contributions, such as spectral modulation of the lasers to switch on and off the Raman resonance in single-wavenumber SRS [48] and using polarization modulation combined with standard amplitude modulation for hyperspectral SRS[49]. Thus the interaction of the induced pump/Stokes nonlinear polarizations with the incident pump/Stokes fields leads to intensity gain (ΔI_s) and loss (ΔI_p) given by

$$\Delta I_s \propto \text{Im}[\chi_{RR}^{(3)}(\omega_{vib})] \cdot I_p \cdot I_s \tag{28}$$

for SRG of the Stokes field, and

$$\Delta I_p \propto -\text{Im}[\chi_{RR}^{(3)}(\omega_{vib})] \cdot I_p \cdot I_s \tag{29}$$

for stimulated Raman loss (SRL) in the pump field[22, 23]. These intensity differences are typically small compared with I_p and I_s. It should be noted that the SRG/SRL signals will also scale linearly with N. The phase-matching condition is also automatically satisfied as opposing $\mathbf{k_p}$ vectors experience the same $n(\omega_p)$ (similarly for the opposing $\mathbf{k_s}$ vectors at $n(\omega_s)$).

The cumulative effect of the SRG/SRL can be observed over large distances in simple crystals and liquids[43], but would be too small to directly measure from microscopic samples due to laser intensity noise. To circumvent this, Owyoung and Jones demonstrated SRS spectroscopy using intensity modulation techniques for detection by lock-in amplification[50]. They were able to measure the 992 cm^{-1} SRG band of liquid benzene with high spectral resolution, free of the artifacts seen in CARS due to non-resonant background (see Figure 4(c)). Extension of this idea to high-frequency modulation of pulsed laser beams was shown in the past decade by Xie and colleagues, who have demonstrated sufficient SRG/SRL detection sensitivity to measure microscopic biological samples (either SRL/SRG of the pump/Stokes fields can be used for generating image contrast by SRS, and provide similar sensitivity to one another[22]). This will be discussed further in Section 4.4.

2.6. Enhanced Raman Scattering

Spontaneous Raman scattering is very weak relative to the excitation radiation and other scattering processes, with roughly one in 1×10^8 excitation photons undergoing Raman scattering, depending on the particular vibrational mode (see Section 2.3). This typically limits the sensitivity of Raman spectroscopy of biological materials to roughly $\approx 0.1 - 1 \mu M$ concentrations or greater.

In order to attain measurements with improved sensitivity, the Raman scattering process must be aided by an enhancement mechanism. Resonance Raman can provide some enhancement, but depends on the absorption profile of the particular material being studied. By chance, Fleischmann et al. discovered a huge enhancement of Raman scattering from pyridine when molecules were adsorbed on a rough silver electrode in 1974[51], the dominant mechanism for which was attributed to a surface–plasmon–mediated electric field enhancement[52]. This came to be known as surface-enhanced Raman scattering (SERS). SERS experiments utilize the localized electric-field enhancement from many nanoparticles within the sampling volume. The instrumentation for the actual Raman spectra acquisition is then much the same as standard Raman spectrometer; it is the sample itself which is modified to include the enhancement particles. Tip-enhanced Raman spectroscopy (TERS) is an extreme variant of SERS in which only a single nanoparticle is used at the apex of a scanning tip. This particle can then be accurately manipulated in 3D, allowing enhanced Raman measurements with diffraction-limit-breaking nanoscale resolution.

The basic theory for the enhancement mechanism in SERS and TERS relies on the optical properties of metallic nanoparticles, primarily gold (Au) and silver (Ag) nanoparticles. In metals, the negative 'sea' of free electrons will oscillate about the lattice of positive nuclei in response to an external field $\vec{E}$ (see Figure 5(a)), following the Drude-Sommerfeld model equation

$$m_e \frac{\partial \vec{x}}{\partial t^2} + m_e \Gamma \frac{\partial \vec{x}}{\partial t} = e\vec{E} = e \cdot \frac{ne}{\epsilon_0 (1 - \epsilon)} \vec{x} \tag{30}$$

(a)

(b)


SRS automatic phase matching

(c)
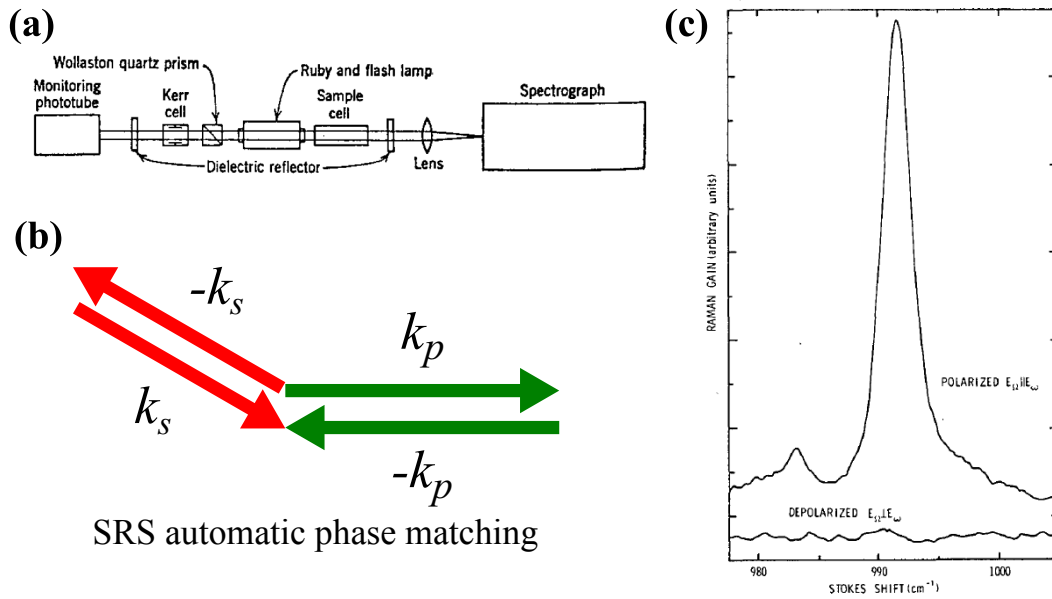
Fig. 4. SRS process.
(a) Schematic of the ruby laser in which SRS was first observed by Woodbury and Ng (reproduced from "The Stimulated Raman Effect" by N. Bloembergen, American Journal of Physics 35(11), 989 (1967) with the permission of the American Association of Physics Teachers[44]). The nitrobenzene Kerr cell produced stimulated emission at the Stokes-shifted frequency.
(b) Automatic phase matching inherent in SRS.
(c) SRG spectrum of liquid benzene (modified from Owyoung and Jones[50])

.

where we have used the macroscopic polarization $\vec{P} = ne\vec{x} = \epsilon_0(1 - \epsilon)\vec{E}$ to link the applied field $\vec{E}$ to the displacement of the free electrons $\vec{x}$. Here, e refers to electron charge, m_e is the electron effective mass, Γ is a damping term equal to the Fermi velocity over the electron mean-free path (*i.e.* $\Gamma = v_f/l_e$), ϵ_0 is the permittivity of free space, and ϵ is the relative permittivity of the metal. For an oscillating solution of the displacement $\vec{x}$, the solution to this equation (upon re-arranging for ϵ which we now write as a function of frequency, ω) is

$$\epsilon(\omega) = 1 - \frac{\omega_p^2}{\omega^2 + \Gamma^2} + i\frac{\Gamma\omega_p^2}{\omega(\omega^2 + \Gamma^2)} \tag{31}$$

where $\omega_p^2 = ne^2/\epsilon_0 m_e$ is called the plasma frequency - the natural frequency of the free electrons for a particular metal, known as a bulk plasmon. Empirical values for the permittivity (or equivalently the complex refractive index) can be found tabulated in various references[53–56]. For an $\vec{E}$ in the visible region of the spectrum, the real part of $\epsilon(\omega)$ will be negative, seen in Figure 6(a), resulting in rapid attenuation of the field through the material (as $n = \sqrt{\epsilon(\omega)}$ will have a significant imaginary component) at some characteristic length usually known as the skin-depth. However, if dimensions of the material are much smaller than this skin depth, $\vec{E}$ can be considered uniform (typically below 100 nm, depending on the metal). For small spherical particles of metal, the plasmon oscillation of the electron sea will now be highly localized, resulting in changes from bulk behavior. It can be shown[57–59] that for such a particle of diameter a surrounded by external medium of relative permittivity ϵ_2, the particle has an induced dipole $\vec{p} = \epsilon_2\alpha(\omega)\vec{E}$ where the polarizability is

$$\alpha(\omega) = 4\pi\epsilon_0 a^3 \frac{\epsilon(\omega) - \epsilon_2}{\epsilon(\omega) + 2\epsilon_2} \tag{32}$$

which will become large whenever near resonance ($\epsilon(\omega) \approx -2\epsilon_2$). The green line in Figure 6(a) shows this value for water ($n = \sqrt{\epsilon(\omega)} = 1.33$), with the points where it crosses $\epsilon(\omega)$ for gold and silver showing their expected resonant wavelengths conveniently placed in the visible spectrum. The scattering and absorption cross-sections can then be written in terms of the polarizability as

$$\sigma_{scatt} = \frac{k^4}{6\pi\epsilon_0^2}|\alpha(\omega)|^2 \tag{33}$$

and

$$\sigma_{abs} = \frac{k}{\epsilon_0}\text{Im}(\alpha(\omega)) \tag{34}$$

by considering the ratio of the total radiated power with incident power, and internal losses in the medium respectively[57]. Figure 6(c) and (d) shows the expected behavior for σ_{scatt} and σ_{abs} using experimental and theoretical data for $\epsilon(\omega)$, showing the localized plasmon resonance peaks. The extinction (absorption plus scattering) can be measured experimentally, as seen in figure
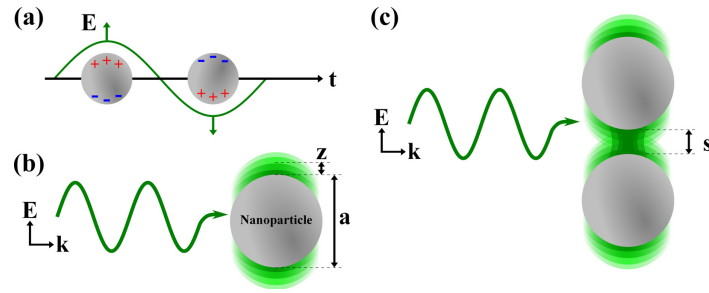
Fig. 5. Illustration of plasmonic near-field enhancement of noble metal nanoparticles.
(a) An incident E field close to the plasma frequency of the metal will cause the free electrons to oscillate about the positive fixed nuclei. This causes an oscillating dipole at the plasma frequency in the nanoparticle.
(b) The time-averaged electric near-field due to the free electrons will decay away from the surface of the metal, with hot-spots locations determined by the polarization of the incident field (here the simplest case of a dipolar mode for a sphere is shown).
(c) When two plasmonic nanoparticles as within the near-field distance, but sufficiently separated to avoid charge transfer or tunneling, an increased "gap-mode" enhancement is observed.

6(e), and match the results in Figure 6(c) and (d) remarkably well. The inset photographs also visually highlight the drastic change in appearance of the metals when they are reduced in size (first discussed scientifically by Michael Faraday in 1857[60]). It should be noted that the absorption component is most important for near-field enhancement, and will typically dominate for smaller particle size.
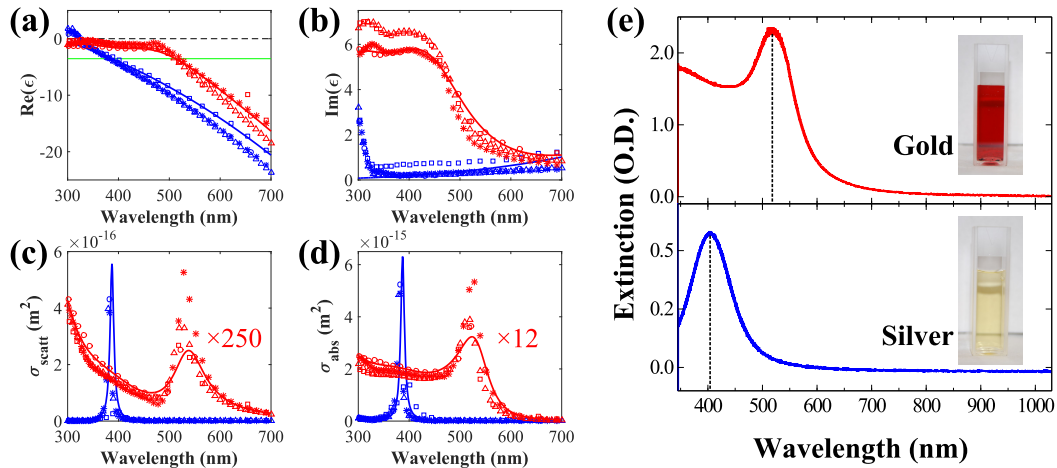

Fig. 6. Optical properties of gold (red lines and markers) and silver (blue lines and markers). Data in (a)-(d) corresponds to experimentally measured values for the dielectric constant ($\circ$[53], $\square$[54], $\ast$[55], $\triangle$[56]) and a theoretical model from the appendix of Le and Etchegoin[59] (solid line).
(a) Real part of the gold and silver dielectric constants. The green line shows the value of -$2\epsilon_2$ for water ($n = 1.33$), which (for a negligible imaginary part of the dielectric constant) will indicate the position of the polarizability resonance when it crosses the Re(ϵ) line.
(b) Imaginary part of the gold and silver dielectric constants.
The scattering (c) and absorption (d) cross sections calculated from the dielectric constant in (a) and (b) for 10 nm diameter particles surrounded by water.
(e) Experimental extinction (absorption + scattering) spectra measured using a UV-NIR spectrometer for gold and silver nanoparticles approximately 10 nm in diameter immersed in water. The inset shows photographs of the measured samples (Note: value of optical density (O.D.) is dependent on the particle solution concentration).

These plots also highlight the performance of silver and gold, with Im($\epsilon(\omega)$) in Figure 6(b), which relates to the internal losses in the material, being closer to zero for silver than in gold. This is particularly noticeable in gold, where intra-band excitation of bound electrons occurs at smaller wavelengths in addition to the driving of the free electrons (which is also the reason for the different colors of gold and silver at a macroscopic level). While it can be seen that silver is more ideal in terms of these parameters, gold is more popular due to other properties such as stability in ambient conditions and ease in synthesis procedures. Other metals also exhibit plasmons, but tend to have much weaker absorption, with frequencies in difficult spectral regions for laser excitation.

It should also be noted that in the current theory, changing the diameter of the particle will only change the magnitude of σ_{scatt} and σ_{abs} (absorption dominating scattering for smaller particles), not the position of the plasmon resonance. This is not true in reality, and the plasmon resonance will gradually redshift with increasing particle size. This is due to boundary effects relating to the electron

mean-free path which for these metals will be larger than the particle dimensions, which can be thought of as the particle having a size dependent dielectric constant ($\epsilon(\omega) \to \epsilon(\omega, a)$)[61]. Additionally, larger and anisotropic particles will produce additional extinction bands due to higher-order multipole and directional/polarized plasmons respectively. These features can actually be used for engineering nanoparticles with tailored excitation profiles[62–65].

At this stage, the properties of these plasmonic nanoparticles can be exploited in a variety of ways for a multitude of sensing applications. Their specific use in Raman spectroscopy comes as a result of the greatly enhanced electric field very close to the particle surface when it is being driven close to resonance by an applied EM wave (this location is often called the SERS 'hot-spot'). This enhanced field is evanescent, i.e. exponentially decaying intensity away from the surface as shown in Figure 5(b), where the decay length z is typically the order of tens of nanometers. Thus the analyte must be sufficiently close to experience noticeable Raman enhancement.

As the spontaneous Raman scattering process involves two dipole transitions (see Figure 2), the amplified field associated with each one results in approximately $|E|^4$ enhancement factor dependence, which is the major advantage of SERS. For a modest increase in the local field at a nanoparticle surface, the Raman scattering can be enhanced by as much as $\times 10^8$ for single silver particles. This can be increased further towards pico-molar sensitivity ($\approx \times 10^{14} - 10^{15}$[66]) by considering coupling between nanoparticles, allowing single-molecule sensitive measurements[66–68].

It should be understood that the $|E|^4$ dependence is an approximation, and enhancement can vary depending on several other parameters, which complicates interpretation for particular SERS configurations. This includes effects from excitation polarization relative to analyte which can modify Raman selection rules (often producing SERS spectra different to spontaneous Raman spectra for the same material), variation of the plasmon absorption (and by association the enhancement) profile in the Raman spectral window, and chemical-enhancement effects (involving charge transfer between nanoparticle and analyte).

To summarize, a good Raman–enhancing nanoparticle must fulfill several criteria. The laser wavelength being used on the Raman instrument should be close to a particle absorption resonance to maximize the near-field amplitude for enhancement. The analyte/label must be within the hot–spot set by the particle shape/size and excitation geometry. As SERS measurements usually measure many enhancing nanoparticles in a single acquisition, it is also preferable to have a nanoparticle population with as uniform a size/shape distribution as possible.

3. RAMAN SPECTRA OF BIOLOGICAL MOLECULES

Many biological molecules contribute to the Raman spectra of cells and tissues. Most common spectral features are caused by vibrational modes in lipid, protein, and nucleic acid molecules.

Raman spectra of biological samples are divided into three spectral regions. The fingerprint region covers the range between 600 and 1800 cm^{-1}. This region gets its name from the diversity of sharp, localized spectral features that give molecules unique "fingerprints." These molecular fingerprints can allow sample classification and chemometric analysis. Vibrations contributing bands to this region usually involve somewhat larger atoms (*e.g.*, carbon, nitrogen, oxygen) or complexes of several hydrogen atoms.

The fingerprint region of the Raman spectra of common bio-molecules is shown in Figure 7. The majority of this section will describe the most dominant components of these spectra in detail.

Most bonds involving independently vibrating hydrogen atoms vibrate with much higher energies than other bonds. The small mass of hydrogen causes a smaller reduced mass for the whole bond (see Equation 3). These higher energy vibrations occupy the region from 2500 to 3400 cm^{-1}, which is known as the "high wavenumber region" of a Raman spectrum. Vibrational modes contributing bands to the spectral region will be discussed in Section 3.5.

Between the fingerprint and high wavenumber regions lies the "silent region." This spectral region from 1800 to 2500 cm^{-1} is mostly empty of contributions from biological molecules, although there are some exceptions including alkynes (see Section 4.10).

Very large, usually non-biological atoms can contribute Raman bands in the "low wavenumber region" below 600 cm^{-1}. Any intersection of these bands with studies of biological samples will be very application dependent, so we will not provide a general treatment here.

3.1. Nucleic Acids

3.1.1. Molecular Structure

Nucleic acids, including DNA and RNA, are present in every organism. In eukaryotes, nucleic acid is the dominant material in the cell nucleus. The structure of a nuclic acid can be considered in two parts, the backbone and the nucleotide bases. The molecular structure of a nucleic acid backbone is shown in Figure 8(a). The difference between RNA and DNA is in the OH group shown in parentheses. This OH in RNA is replaced by an H in DNA. This structure is repeated in a chain with a nucleotide as each link. The bases attach at the location marked as B. RNA usually exists as one such chain while DNA is almost always double-stranded.

Figure 8(b) shows the structure of individual nucleotide bases. Thymine is shown bonding to its pair adenine while cytosine is shown with its pair guanine. In RNA, thymine is replaced by uracil, which differs in structure from thymine by replacing the CH_3 in parenthesis with a single hydrogen atom. These bases attach to their respective nucleic acid backbone at the locations marked as B.

3.1.2. Major Raman Bands

The most prominent Raman bands originating from the backbone of nucleic acids are located near 1095 and 785 cm^{-1} (see Figure 7(a)). The 1095 cm^{-1} band is associated with the symmetric stretching of the PO_2^- in the backbone, as shown in Figure 9(a). The band at 785 cm^{-1} is assigned to either symmetric stretching along the O-P-O backbone (see Figure 9(b)) or ring breathing in the cytosine, thymine, and uracil bases.
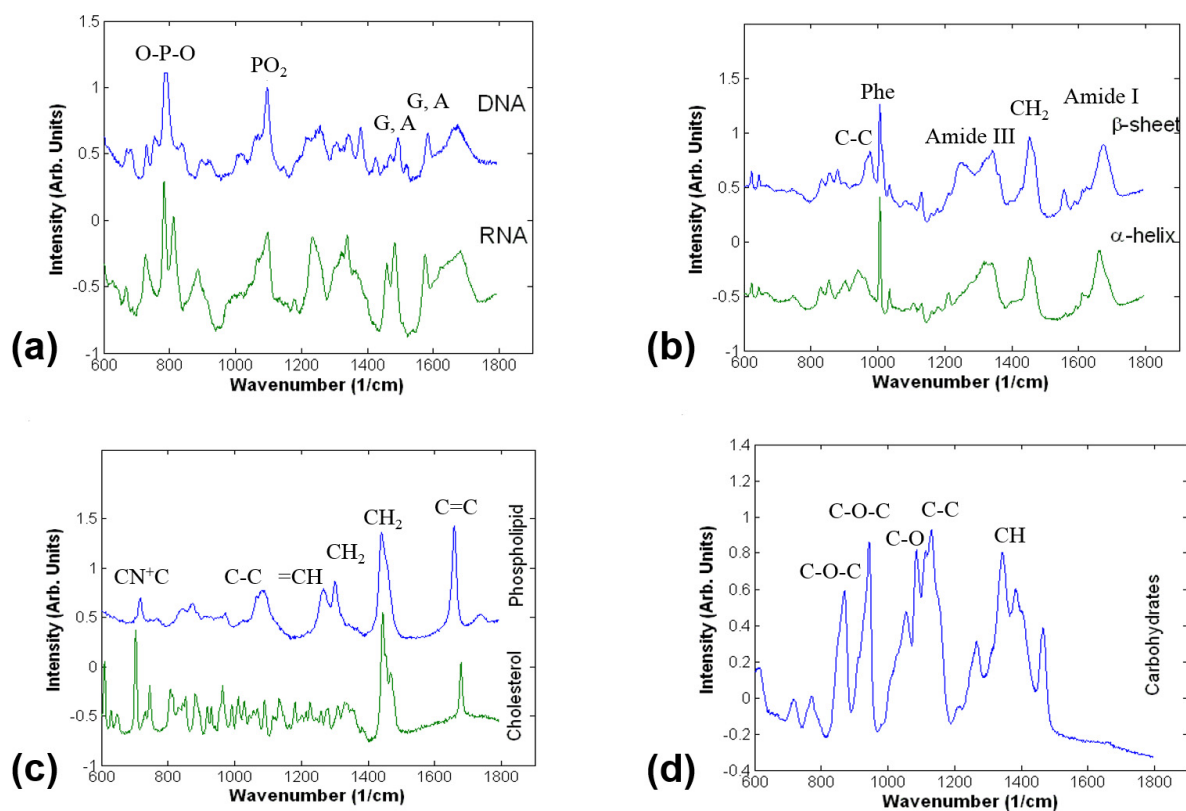
Fig. 7. Raman spectra of biological materials in the fingerprint region between 600 and 1800 cm^{-1}. Spectra are shifted vertically for clarity.
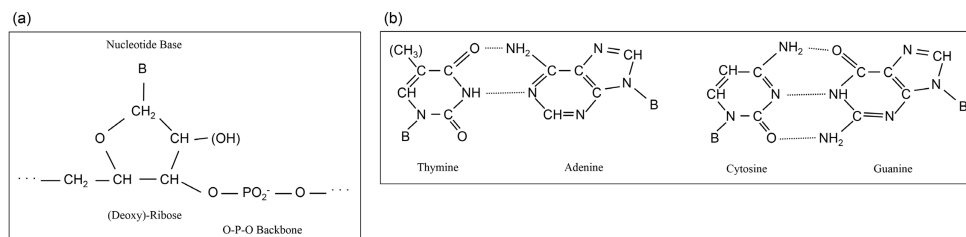

Fig. 8. (a) Structure of a nucleic acid molecule. The OH in parenthesis is only present in RNA. It is replaced by an H in DNA. The B represents the base: adenine, thymine, guanine, cytosine, or uracil. The dots connect the CH$_2$ of one nulceotide to the O-P-O backbone of the next.
(b) Structure of nucleotide bases. The CH$_3$ in parenthesis is replaced by an H in uracil. The B represents where the base group connects to the nucleic acid backbone
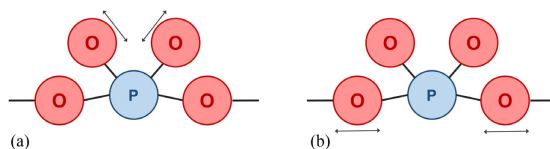

Fig. 9. Vibrational modes associated with most prominent Raman bands corresponding to the backbone in nucleic acids.
(a) PO$_2^-$ symmetric stretching associated with the band near 1095 cm^{-1}.
(b) O-P-O symmetric stretching often associated with the band near 785 cm^{-1}.

Band location (cm^{-1})	Assignment	References
669	Thymine, Guanine	[69]
723-728	C-N head group in Adenine	[69–74]
763	Pyrimidines (Cytosine, Thymine, Uracil)	[74–76]
782-792	Uracil, Cytosine, Thymine ring breathing; O-P-O symmetric stretch	[69, 70, 72, 73, 76–79]
813	RNA, A-type DNA	[77, 80, 81]
828	O-P-O	[69, 72, 73]
898	Adenine, nucleotide backbone	[69, 70, 72]
1084-1095	PO_2 stretch	[69, 71, 77, 82, 83]
1173-1180	Cytosine, Guanine, Adenine	[79, 84, 85]
1252-1254	Cytosine, Guanine, Adenine	[69, 70, 72, 84, 86]
1304-1342	Adenine, Guanine	[69, 70, 72, 73, 78, 84, 87–91]
1369	Thymine, Adenine, Guanine	[70, 72]
1487	Guanine, Adenine	[72]
1510	Adenine	[72]
1578	Guanine, Adenine	[69, 72]
1659-1671	Thymine, Guanine, Cytosine	[70, 71, 74, 75, 77, 79, 91–97]

Table 3. Assignments for major Raman bands associated with nucleic acids.

Table 3 lists other Raman bands originating from nucleic acids. Most of these bands are associated with vibrations of the individual nucleotide bases. Of these bands, the most visible are often the bands near 1330 and 1575 cm^{-1}, both of which are assigned to adenine and guanine.

3.2. Proteins

3.2.1. Molecular structure

Proteins are responsible for a myriad of structural and functional roles in living systems. Every protein is assembled from chains of amino acid building blocks, of which there are 21 main types. All amino acids consist of a backbone unit of $C_\alpha - C(= O) = N$ which repeats along the polypeptide, and a side-chain group attached to the alpha-Carbon (C_α), which distinguishes the amino acids from one another (usually denoted R).

For a chain of amino acids, the interaction between side-chain groups and the backbone determines the secondary structure, *i.e.* how the 1D backbone chain will be arranged and oriented. There are a several mechanisms for these interactions, as different side-chains can either be charged, polar, hydrophobic or contain certain atoms such as sulfur (for the amino acid cysteine) which can form disulfide bonds. These interactions also usually sensitive to the solvent and pH environment which surrounds the protein.

The two most common types of secondary structures in proteins are $\alpha-$helices and $\beta-$sheets (see Figure 10(c) and (d)), which usually occur within a single protein multiple times, leading to unique higher-order "tertiary", or globular, structure.

3.2.2. Major Raman bands

Since all proteins share the same amino-acid backbone molecular structure, they all contain a class of vibrations called the Amide modes. These modes are composed of complex combinations of motions from different parts of the backbone, and thus are not usually referred to by a specific chemical bond, but by their spectroscopic label of Amide vibrations (this terminology is shared with IR and NMR spectroscopies). Within this class of vibrations, the Amide I and Amide III modes (see Figure 11) are the most readily observed in Raman spectroscopy (Amide II, and IV-VII are observed in IR more strongly than Raman spectroscopy, Amide A and B overlap with water bands)[98]. The relatively large range of frequencies of the Amide I and III vibrations (see Table 4) is due to the varied local molecular environment in which each backbone unit will be in due to the secondary structure. For living systems such as cells or tissues, typically many different proteins with a mix of secondary structure will be measured in one sampling volume, resulting in broad amide bands, thus it is usually impossible to identify the presence of specific proteins directly.

Many side-chain groups have similar composition to many other biomolecules, for example the aliphatic side chains such as alanine, valine, leucine etc. The vibrations from these side-chains will typically overlap with common CH_2 and CH_3 bands in Raman spectra, making them difficult to distinguish. However, some side-chains contain molecular structures which are strongly Raman active and produce distinct bands in spectra. One of the most commonly seen is the strong sharp band due to the symmetric ring breathing mode of phenylalanine, which can usually be clearly seen in cell and tissue spectra at 1000-1006 cm^{-1}. Other aromatic side-
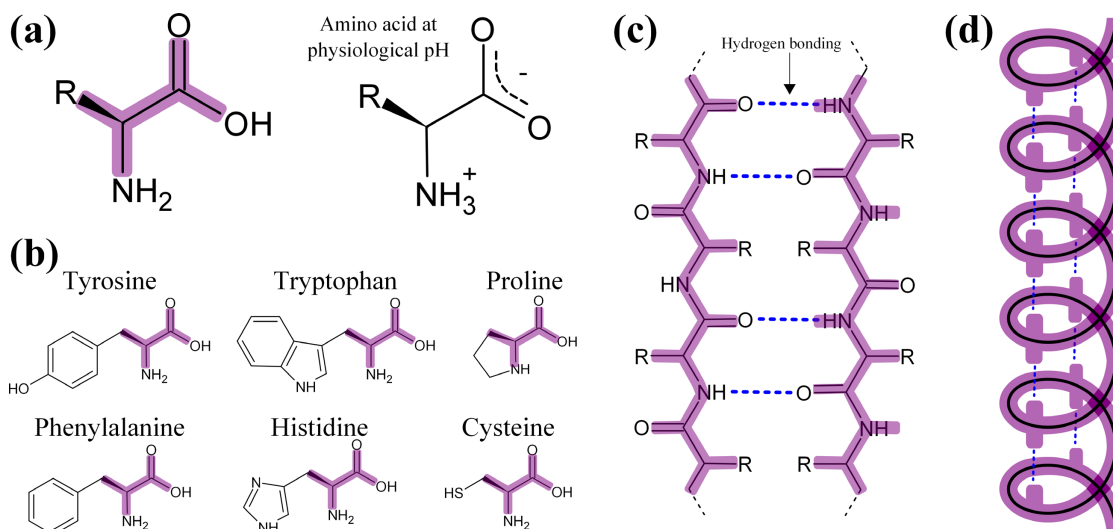
Fig. 10. (a) Generic amino acid unit, as well as its form in physiological solutions. R represents a side chain, which distinguishes a particular amino acid. The purple outline is a guide to highlight the backbone units in (b-d), which shows examples of amino acids with side-groups that contain distinguishing Raman features.

Examples of protein secondary structure: (c) β-sheet (anti-parallel) and (d) α-helix (chemical structure not shown for clarity), with hydrogen bonding between backbone chains.
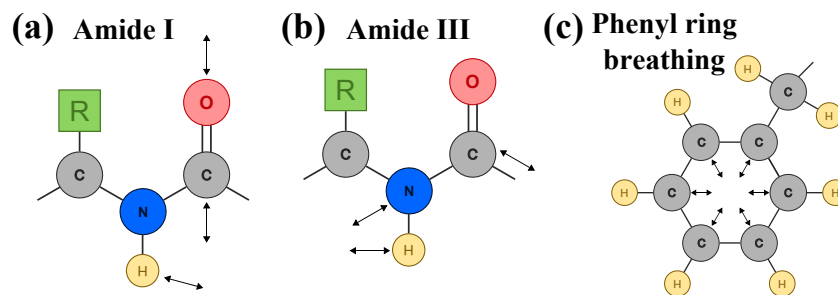
Fig. 11. Vibrational modes associated with most prominent Raman bands in proteins.

(a) The Amide I mode at 1650-1690 cm^{-1} mostly consists of carbonyl (C=O) stretching, with a small contribution from N-H in-plane bending.

(b) Amide III mode at 1250-1270 cm^{-1} has the largest contribution from the N-H mode.

(c) The sharp phenyl ring breathing mode is the most commonly observed side-chain vibration at 1000-1005 cm^{-1}.

chain groups that are visible include tryptophan and tyrosine, which has similar, but shifted, ring breathing modes to phenylalanine. Histidine and other charged side-chains are often difficult to observe in biological spectra as their conformation are sensitive to their environment, leading to variable spectra[99].

Methionine and cysteine are amino acids that contain sulfur atoms in their side-groups, and can thus form disulfide bridges (covalent S-S bonds) within a protein[98, 100]. The corresponding S-S and C-S vibrations are seen at the lower end of the fingerprint region, as seen in Table 4.

While we have stated that it is usually difficult to identify particular proteins using Raman spectroscopy, collagen, which is abundant in mammals as an extracellular structural component of tissue, can be an exception. This is due to the strong bands at 850 cm^{-1} and 950 cm^{-1}, which are attributed to the proline side-group C-C stretch, which is especially abundant in collagen[73].

Band location (cm^{-1})	Assignment	References
500-550	Disulfide S-S stretch (conformation dependent)	[78, 98, 100]
755-760	Trp ring br.	[69, 78, 98, 100–102]
828-830	Tyr out of plane ring br.	[69, 78, 98, 100–103]
850-855	Pro C-C stretch (Collagen); Tyrosine ring br.	[73, 101, 104];[98, 100–102]
935-937	Pro C-C stretch (Collagen); C-C backbone stretch (α-helix)	[73, 104]; [69, 78, 101]
1000-1006	Phe symmetric ring br.	[69, 78, 98, 100, 101, 101–103]
1014	Trp symmetric ring br.	[98, 100, 102]
1030-1033	Phe C-H in plane bend	[98, 100]
1066; 1080-1083; 1125-1128	C-N stretch	[69, 78, 101]
1155-1158	C-C/C-N stretch	[69, 101]
1170-1177	Tyr C-H in plane bend	[69, 78, 101]
1206-1214	Phe, Trp C-C$_6$H$_5$ stretch	[69, 78, 100, 101, 103]
1225-1280	Amide III (random coil 1225-1240; β-pleated sheet 1240-1260; α-helix 1260-1280)	[69, 78, 98, 100, 101]
1338-1340	C$_\alpha$-H deformation; Trp	[69, 78, 101, 103];[100, 101]
1446-1449	C-H$_2$ bending	[69, 78, 101, 103]
1600-1610	Phe, Tyr C=C in plane bending	[69, 78, 100, 101, 103]
1614-1617	Tyr, Trp C=C stretch	[69, 78, 100, 101, 103]
1645-1680	Amide I (α-helix 1645-1660; β-pleated sheet 1660-1670; random coil 1665-1680)	[98, 100, 101]

Table 4. Assignments for major Raman bands associated with proteins.

3.3. Lipids

3.3.1. Molecular Structure

Another common class of molecules encountered in biological specimen are lipids. Phospholipids (lipids containing phosphate groups at their heads) are the primary molecules in membranes, including the cellular, nuclear, and mitochondrial membranes. As these membranes are present in most cells, lipids are common in every cell type. Additionally, lipids are the dominant molecules in fatty tissue.

The basic structure of a phospholipid molecule is shown in Figure 12. The majority of the molecule consists of two long hydrocarbon chains. These chains are typically 14-24 carbons long[29]. If all the carbon-carbon bonds in the chain are single bonds, then the lipid tail contains the maximum possible number of hydrogen atoms. Lipids that are "full" of hydrogen atoms are called saturated. Unsaturated lipids contain one or more double bonds in the carbon chains.

The alcohol group at the head of the phospholipid varies in different types of molecules. The alcohol group also gives the molecule its name. The example in Figure 12 contains a choline group and is called phosphatidylcholine.

3.3.2. Major Raman Bands

The Raman spectrum of a lipid molecule is dominated by the large number of bonds in the hydrocarbon chain (see Figure 7(c)). The most prominent bands are located near 1440 and 1650 cm^{-1} and associated with CH$_2$ scissors bending and the stretching of C=C
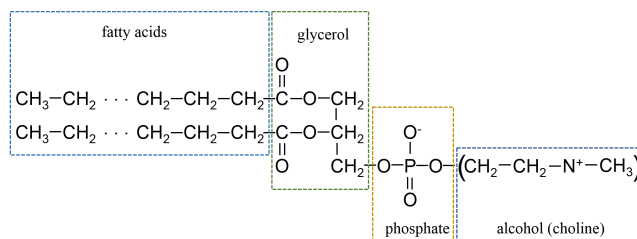
Fig. 12. Structure of a phospholipid molecule (phosphatidylcholine). The alcohol group (in parenthesis) varies. This example shows choline as the alcohol.

double bonds, respectively (see Figure 13). While the band at 1650 cm^{-1} overlaps with the Amide I protein peak, the lipid peak is generally much narrower due to the relative lack of diversity in molecular structures surrounding the C=C double bonds in the hydrocarbon chain.
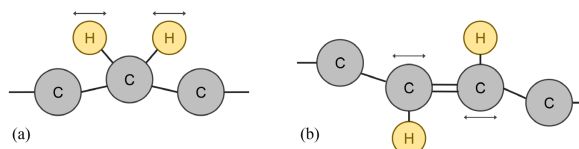

Fig. 13. Vibrational modes associated with most prominent Raman bands in lipids.
(a) CH_2 scissors bending associated with the band near 1440 cm^{-1}.
(b) C=C double bond stretching associated with the band near 1650 cm^{-1}.

Other highly visible lipid bands are listed in Table 5. Some of these can be seen in Figure 7. Besides the CH_2 scissors and C=C bands described above, other consistently detectable bands include the CH_2 deformation band near 1300 cm^{-1}, the CH deformation band near 1265 cm^{-1}, and the C-C backbone stretches between 1030-1130 cm^{-1}. Various structures in the glycerol and alcohol head groups create a broad collection of bands between 840-890 cm^{-1}.

Band location (cm^{-1})	Assignment	References
719	CN^+C (choline)	[105]
887	CH_2 deformations	[90]
955-975	CH_3 deformations	[73, 90, 91]
985	C-C head groups	[69]
1030-1130	skeletal C-C stretches (*cis* 1030-1040; chain *trans* 1055-1066; chain *random* 1080-1085; chain 1092-1098; *trans* 1127)	[69, 70, 73, 77, 90, 91, 93, 106]
1254-1284	=CH deformations	[69–72, 77]
1295-1305	CH_2	[69, 70, 72, 73, 90, 91]
1310-1315	CH_3CH_2 twisting	[70, 77, 78, 85, 107]
1336-1341	CH deformations	[70, 71, 73]
1365-1380	CH_3 symmetric stretch	[69, 70, 85, 91, 108]
1440-1460	CH_2 scissors	[69, 70, 70, 71, 73, 90, 91]
1645-1660	C=C cis stretch	[69–71, 73–75, 77, 79, 91–97]
1720-1750	C=O esters	[69, 77, 91, 94, 109, 110]

Table 5. Assignments for major Raman bands associated with lipids.

3.4. Other Biomolecules

Here we will give a brief overview of other biomolecules which either are not classed as proteins, lipids or nucleic acids, or are sufficiently unusual in structure to present noticeable changes in cell or tissue spectra. A vast number of other biomolecules have been studied in the past using vibrational spectroscopy, though often they are not studied in cells or tissues either due to their

low native concentrations, bands which are indistinct or overlap with stronger contributions, or variability in a dynamic biological environment. Though somewhat hard to find and out of print, the book by A. Tu [98] gives an excellent overview of many of these other biological Raman spectra.

3.4.1. Hydroxyapatite

Hydroxyapatite (HA) is the key mineral component of many hard biological tissues such as bone, dental enamel, and calcifications. The crystal unit cell consists of $Ca_{10}(PO_4)_6(OH)_2$, which has a Raman spectrum with a very strong band between 957-963 cm^{-1} due to the symmetric strething mode of PO_4^{3-} seen in Figure 14[111]. Other weaker modes include the anti-symmetric stretching modes of PO_4^{3-} at 578-617 cm^{-1} and at 1006-1055 cm^{-1}[111].
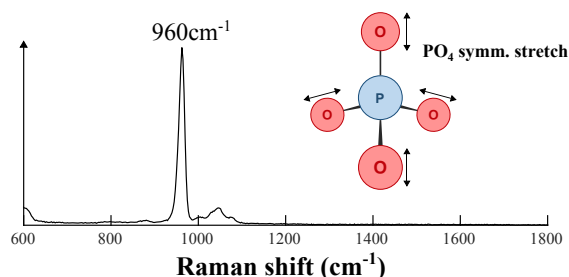

Fig. 14. Raman spectrum of pure hydroxyapatite powder, with inset diagram of the PO_4 symmetric stretching mode responsible for the strong band at 960 cm^{-1}.

Bone is formed of an organic matrix (mostly collagen) which supports the HA minerals. Thus comparisons of the 960 cm^{-1} band to other protein/collagen bands from the organic matrix can be used to infer biomedically relevant information such as age and structural integrity [111, 112]. The strength of the 960 cm^{-1} HA phosphate band also makes it useful for distinguishing it from tissue using transmission/spatially-offset Raman techniques, which will be discussed in section 4.7.

3.4.2. Heme and other natural porphyrins

Porphyrins are a class of cyclic aromatic molecules containing four pyrrole groups (see Figure 15), which can form complexes with metal atoms, and occur in many naturally occuring biological systems, often serving roles as sensors. The most notable of these is heme, an iron-conjugated porphyrin which is found in hemoglobin in blood cells, and the metalloprotein cytochrome c. Heme also has an absorption band between 500-550 nm[98], which has allowed numerous studies by resonance Raman using 532 nm excitation, which produces spectra with strong bands, particularly the ring breathing mode of the pyrrole groups.
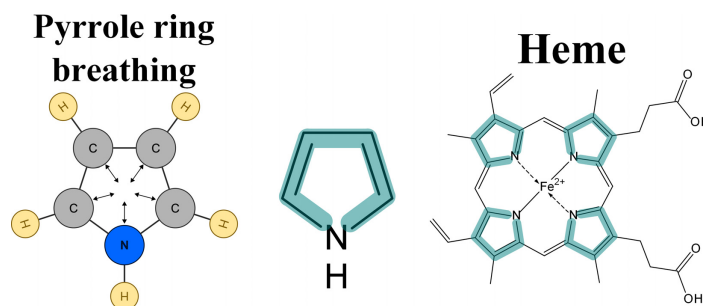

Fig. 15. Heme molecule as an example of a naturally-occurring porphyrin molecule. All porphyrins contain four pyrrole groups, which has a strong ring breathing mode observable by resonance Raman spectroscopy.

Cytochrome c is a hemeprotein found in mitochondria, and its dynamics have been studied in apoptosing cells using resonance Raman of the 750 cm^{-1} pyrrole ring breathing band[113]. The oxygenation state of hemoglobin in single red blood cells can be also be observed with 785 nm-excited resonance Raman, in particular the Fe-O$_2$ stretching mode at 570 cm^{-1} was only seen for oxygenated cells[114].

3.4.3. Carbohydrates

Carbohydrates are defined as any molecule which has a chemical structure of the form $C_m(H_2O)_n$, thus their Raman spectra bands assigned to C-C, C-H, O-H, and C-O/C=O vibrations (often involving three atoms due to their cyclical structure). Spectra of pure carbohydrates typically contain many sharp bands which vary significantly from one molecule to the next, with large changes between monomer/polymer conformations. Whilst useful for isolated studies of carbohydrates, this lack of consistent spectral markers shared by carbohydrates makes it difficult to measure them in biological systems, especially as they are often involved in dynamic metabolic processes.

However some features common to several carbohydrates do exist, such as the C-O-C glycosidic link stretch at 850 cm^{-1}, CH$_3$ rocking 925ish cm^{-1}, and symmetric C-O-C glycosidic link stretch at 1125 cm^{-1}shared by glucose and lactose (see Figure 7(d).). However structures like cellulose (polymerized glucose) lack these bands and instead has a strong peak at 1100 cm^{-1}and 2900 cm^{-1}with many broad and overlapping bands. [70, 115–117].

3.4.4. Water

The strongest bands associated with water are found in the high wavenumber region (see Section 3.5). Far from the rich fingerprint region, these bands have little effect on most Raman spectra. This is one of the major advantages of Raman spectroscopy over infrared absorption spectroscopy. However, some weaker contributions do exist in the fingerprint region, which can present themselves as background. These include librational modes of hydrogen-bonded water (broad envelope from 200-2000 cm^{-1}), and O-H bending (1640 cm^{-1})[118, 119]. Water spectra are rarely studied in the context of life science systems, though the bands >3000 cm^{-1} have been used as an indicator of the water mass in skin samples[120].

3.5. High Wavenumber Region

The high wavenumber Raman spectra of several biological materials is shown in Figure 16 (see Mourant *et al.*.[121]). Bands in this region are much broader, leading to increased spectral overlap. This can increase the difficulty of identifying specific molecular signatures.
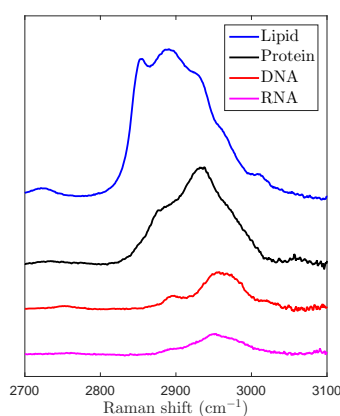

Fig. 16. Raman spectra of biological materials in the high wavenumber region between 2700 and 3100 cm^{-1}. Offset for clarity. Figure adapted from Mourant *et al.*.[121]. Used with permission.

Band location (cm^{-1})	Assignment	Molecule	References
2560-2600	S-H	proteins	[98]
2850-2890	CH$_2$ stretch (symmetric 2850; assymetric 2890)	lipids	[94, 122–126]
2935	chain end CH$_3$ stretch	lipids	[94, 122, 124]
2940	symmetric CH$_3$ stretch	proteins	[123, 124, 126–128]
2960	CH$_3$ stretch	nucleic acids	[129]
2980 (shoulder)	asymmetric CH$_3$ stretch	proteins	[124, 126, 128]
3010	unsaturated = CH stretch	lipids	[94, 122, 125]
3057-3090	Amide B	proteins	[98, 101]
3250	symmetric OH stretch	water	[126]
3280-3308	Amide A	proteins	[98, 101]
3400	asymmetric OH stretch	water	[123, 125–127]

Table 6. Locations and assignments for major Raman bands in the high wavenumber region.

Table 6 contains the locations and assignments of several bands in the high wavenumber region. Because high wavenumber peaks generally contain hydrogen, the strongest bands in biological samples come from lipids, which have hydrogen in greater abundance. In fact, the high wavenumber signal from lipids is usually about an order of magnitude stronger than any band in the fingerprint

region. This strong signal is often exploited for rapid CARS imaging[130]. High wavenumber bands from proteins can sometimes be seen, but nucleic acid signals are too weak to be detected[130, 131]. Water also exhibits broad, overlapping intramolecular O-H stretching contributions in the 3000-3700 cm^{-1} region.

4. TECHNIQUES AND APPLICATIONS

This section will discuss some of the most common Raman spectroscopic techniques used to study biological samples. A brief summary of these techniques can be found in Table 7.

Technique	Main advantages	Challenges	Sample preparation	Full spectrum
Spontaneous Raman microscopy	Spectral detail, classification	Slow	No	Yes
Resonance Raman spectroscopy	More signal, specific target	Only possible with some molecules	No	Yes, some bands enhanced
Coherent anti-Stokes Raman scattering (CARS)	Very fast imaging	Costly instrumentation, signal depends quadraticly on concentration	No	Possible with more complex instrumentation
Stimulated Raman scattering (SRS)	Very fast imaging, signal depends linearly on concentration	Costly instrumentation	No	Possible with more complex instrumentation
Surface enhanced Raman scattering (SERS)	Greatly enhanced signal	High variability in spectra of endogenous molecules	Yes, nanoparticles	Yes, but complex selection rules cause non-standard spectra
Tip enhanced Raman Raman scattering (TERS)	Greatly enhanced signal, sub-diffraction limit resolution	High variability in spectra, tip durability	Yes, nanoparticles	Yes, but complex selection rules cause non-standard spectra
Spatially offset Raman spectroscopy (SORS)	Depth-resolved spectra from turbid media	Poor resolution (lateral and depth)	No	Yes
Transmission Raman spectroscopy	Signal from deep in turbid media	Volume analysis, no depth resolution	No	Yes
Fiber optic probes	Access to remote areas, *in vivo* measurements	Signal from glass fibers	No	Yes
Selective scanning Raman spectroscopy (SSRS)	Faster imaging	Possibly decreased resolution	No	Yes
Stable isotope labels	Non-invasive labeling	Limited targets	Yes, minimally invasive	Yes
Alkyne labels	Non-invasive labeling	Some labels can affect function	Yes, possibly invasive	Yes

Table 7. Summary of various techniques of Raman spectroscopy used to study biological samples.

4.1. Spontaneous Raman Microscopy

4.1.1. Typical System

Spontaneous Raman scattering refers to the standard Raman scattering phenomenon without enhancement through resonance or nonlinear effects. The theory of spontaneous Raman scattering is described in Sections 2.2 and 2.3. The term "Raman spectroscopy" without any other descriptors usually refers to spectroscopy of spontaneous Raman scattering.

Raman spectroscopy became popular in the biological sciences after the invention of the Raman confocal microscope. The first Raman confocal microscope was developed by Delhaye *et al.* in 1975[9]. In 1990, the implementation of improved notch filters by Puppels *et al.*.[10] allowed the development of an improved Raman microscope for biological applications[11] (see Figure 17(b)). The basic system concepts of a Raman system have not changed much since then.

A simplified diagram of a basic Raman spectroscopy system is shown in Figure 17(a). The excitation light source for most Raman systems is a laser. There are two main reasons lasers are used more than other sources. First, Raman scattering is a very weak effect and lasers are capable of delivering a great deal of light to the sample. Higher excitation intensities will lead to stronger detected signals, but at the risk of more damage to the sample.

Secondly, Raman bands are generally very narrow. The fine features of a Raman spectrum contribute to the high information content and accuracy in these measurements. However, each Raman band is made wider through a convolution with the excitation spectrum. Non-laser sources will broaden the Raman band and potentially blur the spectrum. In practice, single-frequency lasers are the most popular Raman sources.

Two competing effects determine the choice of laser wavelength. Equation 12 shows that a shorter wavelength will yield a stronger Raman signal. In addition, the sensitivity of the silicon detectors typically used in Raman spectroscopy are also higher in the visible range. Raman measurements of biomaterials and fixed cells have showed that short acquisition times (100-250 ms) are possible when lasers with wavelength of 488 nm, 514 nm, and 532 nm laser were used[132]. Nevertheless, more careful selection of lasers is required for live cells. Strong absorption of visible wavelengths in biological samples can lead to heating and sample damage (see **Laser damage** below). Excitation with visible wavelengths may also induce auto-fluorescence (see **Fluorescence emission** below). To balance these effects, most Raman spectroscopy studies of biological samples use excitation wavelengths between 780-850 nm.

In addition to the excitation laser, a number of optical filters are very important to a Raman spectrometer. The first is a narrow bandpass filter (BP). This filter cleans up the laser excitation by removing amplified spontaneous emission and other light outside the excitation bandwidth. This ensures monochromatic excitation, improving spectral resolution. The next element is often a dichroic mirror (DM). This mirror will reflect light at the excitation wavelength and allow longer wavelengths to pass through. The laser excitation is reflected by this mirror towards to sample. Raman microscopes will focus the excitation light onto the sample by on objective lens (OL). The same lens collects scattered light. Even systems measuring macroscopic samples will use a lens for focusing and collection of light, albeit with lower optical power.

Collected light is passed back towards the dichroic mirror. The mirror allows red-shifted Raman scattered light to pass through towards the detection arm while rejecting elastic scattering or reflections at the laser wavelength. Light at the laser wavelength is further rejected by one or more notch filters (NF). Focusing collected light onto a pinhole can make the Raman system confocal. This pinhole blocks light collected from regions of the sample outside the focal volume. This can greatly improve the depth resolution of the system, but can also reduce the detected signal.

The detection of Raman spectra is usually achieved by a combination of a spectrometer and charge-coupled device (CCD) detector. The weak signal and fine features of Raman spectra place high demands on the spectrometer. The spectrometer must be efficient to maximize the detected signal and also have good resolution to resolve the narrow bands. Deep-depletion silicon CCDs can be sensitive at the wavelengths corresponding to Raman scattered photons (800-1000 nm) when near infrared excitation is used. Additionally, cooled CCDs have very low dark current, which reduces a source of noise. Efficiently detecting the weak Raman signal while reducing noise factors is the highest priority for the detector.

A Raman system can be easily incorporated into a standard optical microscope. An example of an inverted Raman microscope is shown in Figure 17(c). This microscope is equipped with an environmental chamber allowing live cells to be studied over several days. Raman spectroscopy is well-suited to study biological processes occuring on the order of several minutes to a few days including cell-cell interactions[133], apoptosis[134], mitosis[135], and stem cell differentiation[136].

The resolution of Raman micro-spectroscopy is typically limited by diffraction to 0.5 to 1 μm. More recently structured illumination Raman microscopy has been reported to increase the spatial resolution[137].

4.1.2. Applications

The applications of spontaneous Raman scattering are widespread and diverse. Using data analysis techniques that will be discussed in Section 5, Raman spectroscopy has been used to classify bacteria[14, 15], nano-bio-materials [138–140], cells[141, 142], and animal and human tissues[143, 144]. Because Raman spectroscopy is non-labeling and non-destructive, repeated measurements can be made of the same sample. This allows time-lapsed traces of biological proceses[136, 145].

Hyperspectral imaging   Another common application of Raman spectroscopy is creating hyperspectral images. To accomplish this, the focal volume is scanned across the sample, via either moving the optics or translating the sample itself. Each pixel is associated with a Raman spectrum. Images are created by extracting the concentration of a particular analyte[146] or by classifying the spectrum into a meaningful group[147].

Polarized Raman spectroscopy   Most molecules in biological samples are randomly oriented, so the polarizations of excitation and scattered light play little role in Raman spectroscopy. However, some molecules are highly structured and will scatter differently under illumination from differently polarized light sources. In this case, the intensity of Raman scattering for each vibrational mode will depend on the scattering tensor corresponding to the excitation and detected polarization states (as opposed to the average of the scattering tensor for randomly-oriented molecules)[26].

Polarized Raman spectroscopy is performed by selecting the excitation and detected polarization states. This is usually accomplished using wave plates and analyzers as shown in Figure 18(a). Raman spectra are acquired for each combination of input and output polarization states.
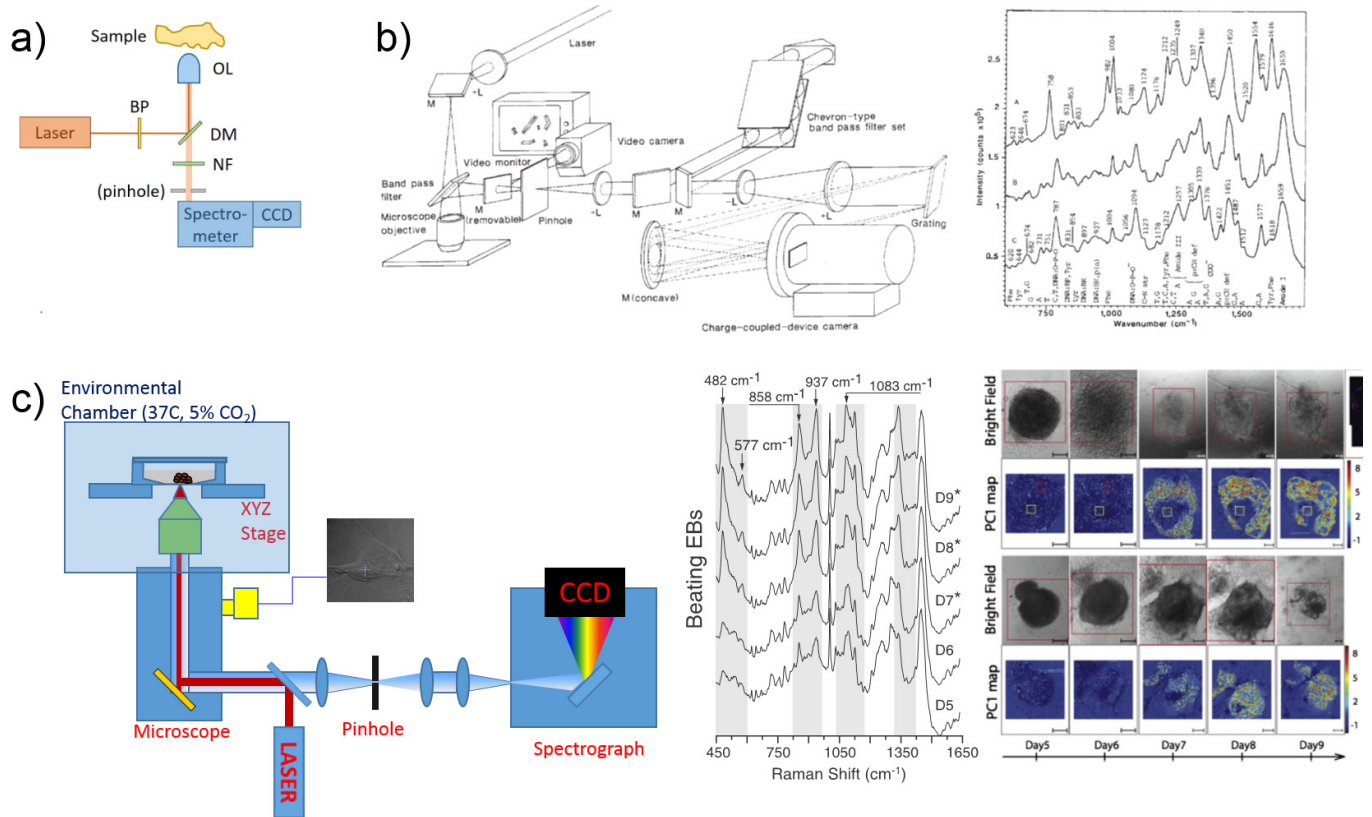
Fig. 17. (a) Simplified diagram of a generic Raman spectrometer. OL = objective lens, BP = bandpass filter, DM = dichroic mirror, NF = notch filter. The system operates confocally with the pinhole in place.

(b) System diagram and example Raman spectra from the first biological confocal Raman microscope by Puppels *et al.*[11] This system was based on an upright microscope with a water dipping objective.

(c) Inverted Raman microscope. The measurement of Raman spectra of cells is performed through a coverslip with a non-contact objective and environmental enclosure, enabling long-term studies of differentiating stem cells (scale bars are 150 μm)[136].
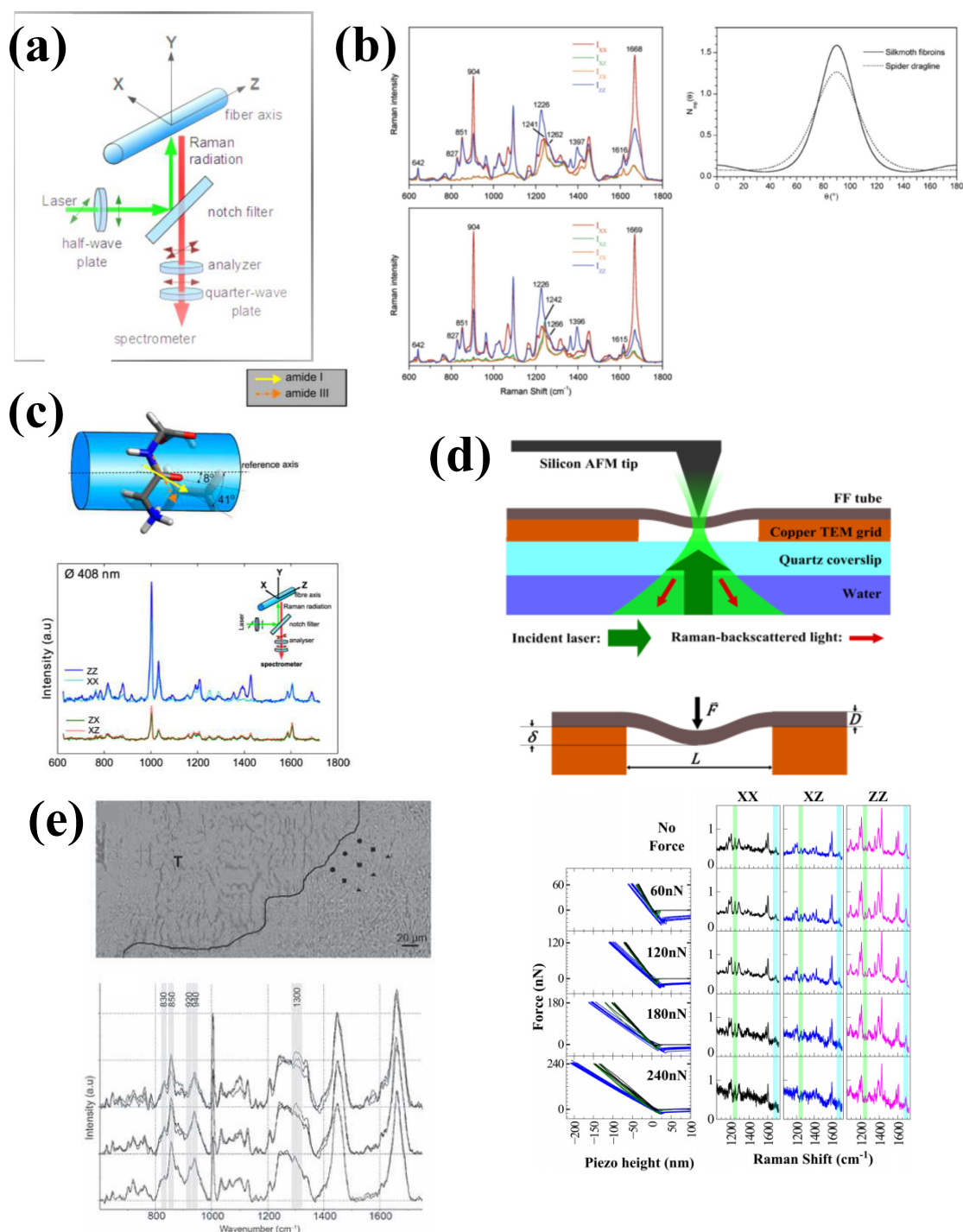
Fig. 18. Polarized Raman micro-spectroscopy.
(a) Schematic of a typical system for polarized Raman micro-spectroscopy.
(b) Polarized Raman spectra of spider and silkworm silk fibers by Rousseau *et al.*[148]. Differences in polarized spectra allowed the authors to determine the orientation distribution functions for the fibers from different species. Reprinted (adapted) with permission. Copyright (2004) American Chemical Society.
(c) Polarized Raman used by Lekprasert *et al.* to study the structure of diphenylalanine (FF) nano- and micro-tubes[139] Reprinted (adapted) with permission. Copyright (2012) American Chemical Society.
(d) Combining polarized Raman with atomic force microscopy for simultaneous measurement of elastic and molecular properties of FF nano- and micro-tubes[140]. The molecules were found to maintain orientation under the application of force.
(e) Polarized Raman spectra from human skin tissue[149]. Order and disorder in collagen molecules allow the detection of changes in stroma structure near tumor regions.

Rousseau *et al.* used polarized Raman spectroscopy to study silk fibers from spiders and silkworms. The highly-ordered molecular structure in these fibers caused polarization-dependent differences in the Amide I vibration bands of polarized Raman spectra. This allowed the authors to determine the orientations of β-sheets within the fibers[148].

Polarized Raman spectroscopy has also been used to characterize highly-ordered peptide structures. Lekprasert *et al.* used polarized Raman spectroscopy in combination with atomic force microscopy to study diphenylalanine nano- and micro-tube[138]. The authors were able to determine the orientation of molecules within the structure[139] and show that the structure remained constant when force was applied using an atomic force microscope[140].

The degree of ordering of certain molecules in tissue can be an indicator of disease. Ly *et al.* measured the ordering of collagen molecules in skin using polarized Raman spectroscopy. Tissue near tumor locations showed increased randomization of collagen orientation and less variation of Raman intensity under different polarization states. This effect was used to classify tumor and healthy skin tissue[149].

Combinations with other techniques   The relative simplicity of a spontaneous Raman spectroscopy system allows flexibility to combine Raman spectroscopy with other optical or non-optical techniques.

Optical tweezers can be a useful tool facilitating the study of microscopic samples such as single cells. This technique employs the optical forces of laser radiation through a microscope objective to confine micro-particles to a small volume. The same lasers used for trapping can also be used to excite Raman scattering, as demonstrated by Thurn *et al.* as early as 1984[150]. Optical tweezers are currently used to extend the possible Raman spectrum acquisition time of floating cells such as bacteria[151] and immune cells[79].

While Raman spectroscopy provides chemical information about the sample, other techniques are added to provide structural information. Atomic force microscopy[152] and quantitative phase microscopy[153] have been used to measure the thicknesses of cells. Angle-resolved elastic scattering has been used to measure the sizes of sub-cellular organelles[154, 155]. Other groups have looked at tissue structure using optical coherence tomography (OCT)[71, 156]. In each of these cases, the Raman spectroscopy part of the instrument required little or no alteration to be combined with the structurally-specific technique.

4.1.3. Challenges

Acquisition time   The most significant issues associated with spontaneous Raman scattering arise from the low level of Raman signal. As a general rule, one photon will be Raman scattered for roughly every 10^8 photons incident on the sample. These Raman scattered photons are distributed across several detector pixels and compete with dark current, detector readout, shot noise, and other sources of noise. As low laser powers are commonly used to avoid damaging biological samples (see below), long acquisition times are usually required to obtain an acceptable signal-to-noise ratio. Acquisition times for a single Raman spectrum vary from around 0.5 seconds to over 3 minutes. Even with a relatively "fast" acquisition time of 0.5 seconds, acquiring a 1024x1024 hyperspectral Raman image would take over six days. This slow speed is often the largest obstacle for Raman spectroscopy.

A number of methods have been developed to increase the speed of Raman hyperspectral image acquisition. One such method that was emerged relatively early is line-scanning[157]. In this modality, a line is probed in a single acquisition instead of a single point. The excitation beam power is distributed across the line.

Line-scanning is possible because a spectrum typically only occupies a single line of pixels on the CCD detector as shown in Figure 19(a). Through the use of cylindrical lenses, a moving mirror, or optical fibers, spectra from different points on a line can be stacked to fill the other pixel rows of the CCD[158]. Line-scanning can be on the order of 20 times faster than point scanning[159]. However, by extending the size of the excitation spot, even in one dimension, the system loses confocality and depth-sensitivity[26].

In multi-focal Raman imaging, the sampling points are arranged two-dimensionally, instead of in a line as in line-scanning. The excitation beam can directed onto the sampling points and directed to the spectrometer slit by a fiber bundle[160], microlens array[161], set of galvo-mirrors[162], spatial light modulator (SLM)[163], or digital micromirror device (DMD)[164]. The spectra from each point can be directed onto rows of the CCD simultaneously (*i.e.* power sharing, see Figure 19(c))[164] or sequentially (*i.e.* time sharing, see Figure 19(d))[162]. Power sharing techniques are generally faster, but require higher laser power to distribute among sampling points. For example, in a power sharing technique, $\approx$ 1.5 W laser power was used to simultaneously measure 10 Raman spectra of polymer samples with only 0.1 second total acquisition time[164].

The pattern of sampling points in multi-focal Raman imaging is adaptable when using the galvo-mirrors[162], SLM, or DMD[164]. This allows multiple regions of interest to be identified in other imaging modalities and rapidly interogated with Raman spectroscopy. Acquiring spectra from multiple points in parallel can dramatically decrease measurement time.

Another technique to improve Raman imaging speed does not involve any spatial scanning. Wide-field hyperspectral Raman images the sample through a tunable spectral filter or a sequence of filters. The detected wavelength is scanned to reconstruct spectra. Wide-field Raman imaging systems typically have better spatial resolution at the expense of some spectral resolution[159]. These systems have been used to image biological systems such as teeth[165] and whole fish[166] at speeds comparable to Raman line-scanning.

Fluorescence Emission   One particularly troublesome source of noise in spontaneous Raman spectroscopy is fluorescence emission. While most materials would not be considered fluorescent at wavelengths relevant to Raman scattering, many can still emit a significant fluorescent signal that can overwhelm a Raman spectrum. Even substrates like glass can produce fluorescence intense enough to disrupt analysis of Raman spectra. To avoid this, many systems use alternative substrates including quartz, calcium fluoride (CF_2), and magnesium fluoride (MgF_2). While these substrates still contribute to the Raman spectrum, their spectral components are less significant and/or contained in a less crucial region of the Raman spectrum.

Even after controlling the spectral contributions of the substrate, the sample itelf can disrupt the Raman signal through auto-fluorescence. The additional photons from fluorescence effects add noise that obscures the Raman spectrum. The true Raman spec-
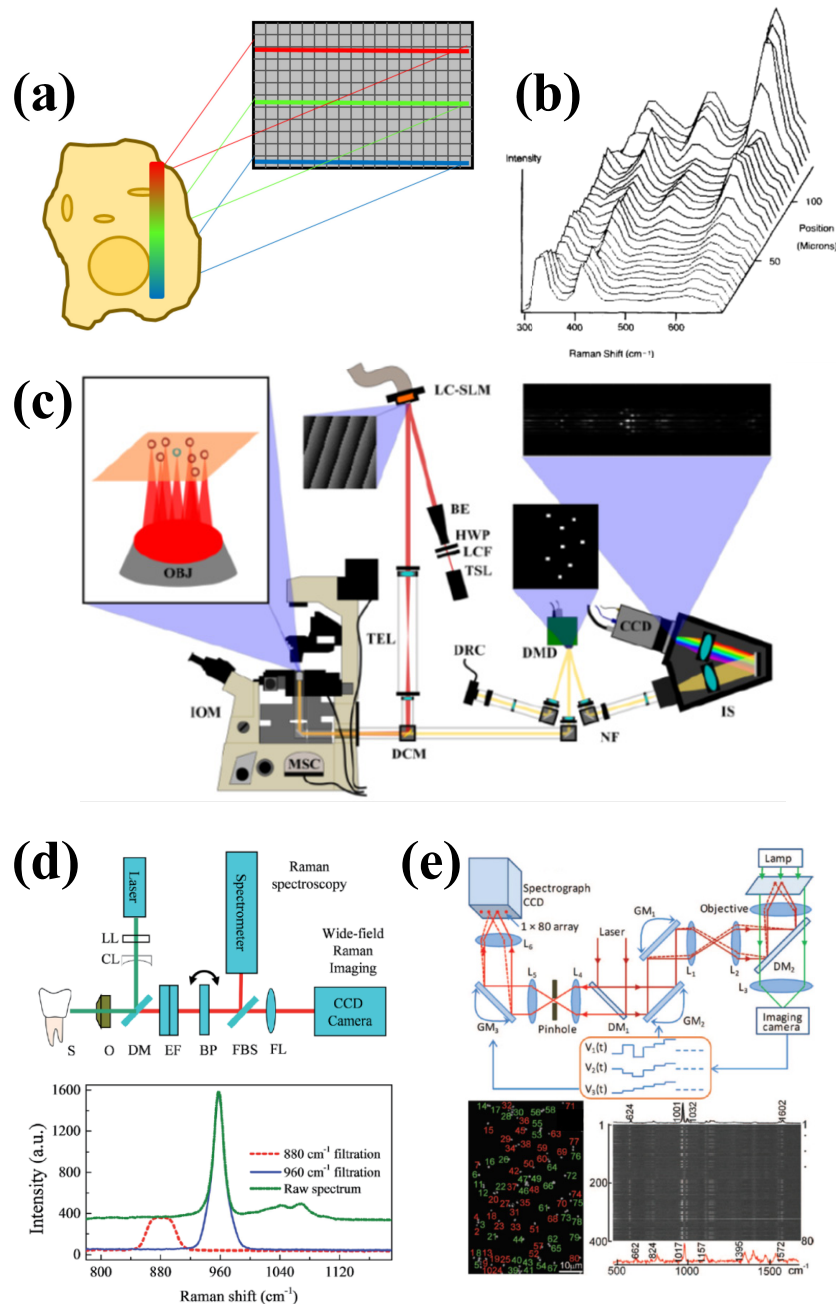
Fig. 19. Techniques for rapid Raman imaging.

(a) In line-scanning Raman imaging, the excitation light is focused into a line. The spectrum from each point along the line is delivered to its own row on the detector.

(b) A line of spectra from the first line-scanning Raman system by Bowden *et al.*[157]. The axes correspond to spectral and spatial dimensions.

(c) Schematic for a power-sharing, multifocal Raman imaging system developed by Sinjab *et al.*[164]. All sampling points are illuminated and detected simultaneously. A spatial light modulator (SLM) creates a pattern of laser sponts on the sample, while a digital micromirror device (DMD) is used to create a matching array of "reflective slits."

(d) Schematic for a time-sharing, multifocal Raman imaging system by Kong *et al.*[162]. Two galvo-mirrors (GM1 and GM2) scan excitation light to programmable points in the sample plane and de-scan collected scattering to the spectrometer pinhole. Another galvo-mirror (GM3) scans the signal from each position to its own row on the CCD.

(e) Schematic for a wide-field Raman imaging system for detecting dental lesions by [165]. This system images the full field of view simultaneously. Spectral sensitivity is gained by scanning a tunable bandpass filter (BP).

trum is also distorted by the broad fluorescent baseline. This strong fluorescence emission background is believed to originate mostly from extracellular matrix molecules, and is not typically observed for fixed cells[132].

A popular method to remove this broad baseline is to subtract a low-order polynomial. Lieber *et al.* developed an iterative polynomial fitting algorithm to isolate and subtract the baseline while leaving Raman spectral features mostly in tact[167]. This algorithm takes advantage of the narrow widths of Raman features relative to the broad baseline (see Figure 20(a)). Beier and Berger later adapted this algorithm to allow simultaneous subtraction of substrate and auto-fluorescence contributions(see Figure 20(b))[168].
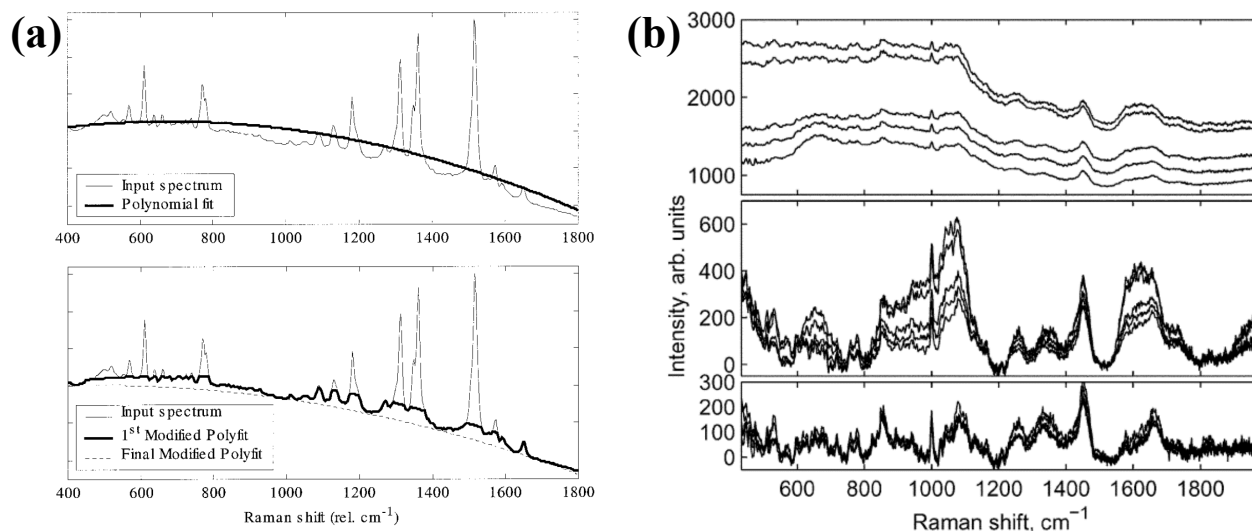

Fig. 20. (a) Raman spectra from skin, cervix, and ovary tissues (A) before and (B) after polynomial subtration. Originally published by Lieber *et al.*[167].
(b)Raman spectra bacteria on glass substrate (A) before, (B) after polynomial subtraction, and (C) after simultaneous background and polynomial subtraction. Originally published by Beier and Berger.[168].
All spectra are normalized and offset for clarity.

Auto-fluorescent background contributions can also be removed by modifications to the Raman instrument. Most common biological samples exhibit more fluorescence with shorter excitation wavelengths. Thus, using a longer wavelength will generally reduce auto-fluorescence. Visible wavelengths are rarely used for Raman spectroscopy of tissues. Patil *et al.* developed a Raman system exciting at 1064 nm to avoid auto-fluorescence[169]. Unfortunately, increasing the wavelength also decreases the Raman signal (see Equation 12) and decreases the effeciency of detectors that far in the infrared. A compromise must be found for each application (usually between 700-900 nm).

Dholakia and his group developed a technique called Modulated Raman Spectroscopy (MRS)[170, 171]. MRS is achieved by modulating the excitation wavelength. This modulation has no effect on the emission spectrum of fluorescence from the tissue or substrate. The Raman spectrum, however, is based on a relative shift in wavenumbers. Therefore, shifting the excitation wavelength will also shift the entire Raman spectrum by roughly the same amount. Thus, modulating the excitation wavelength decouples the Raman spectral features from the stationary fluorescence background. This technique has been used in Raman analysis of blood[172] and urine[173]. Canetta *et al.* have also implemented this technique in a fiber-based probe[173].

As mentioned in Section 2.3, Raman scattering happens on very short (*i.e.* picosecond) timescales. Fluorescence, on the other hand, transitions through relatively stable electronic excited states. Fluorescence lifetimes are typically on the order of nanoseconds. This difference in emission time can be used to detect Raman scattering while rejecting fluorescence. This is achieved using a pulsed laser synchronized with time-gated detection, usually by means of an intensity-activated Kerr gate[174]. Emerging fast detectors also allow time-gated detection[175]. Time-gated Raman spectroscopy has been used to detect Raman spectra from various samples including bone[176] and breast tissues[177].

In cases of high fluorescence emission, Fourier transform Raman systems can also be used[178]. Fourier transform Raman systems use excitation lasers at 1064 nm, but typically have longer acquisition times.

Laser Damage   In addition to maximizing signal and avoiding fluorescence, the choice of excitation laser must also consider damage to the sample. This is less of a concern with non-living biomaterials and fixed cells, so Raman spectroscopy with visible wavelengths is more common. At low laser power, visible lasers can also be used for measuring Raman spectra of viable cells, especially when the laser excites resonance Raman scattering of specific molecules (see Sections 2.4 and 4.2). Resonance Raman spectra of haemoglobin and hemozoin in malaria-infected erythrocytes have been reported using lasers with wavelength of 488 nm, 514 nm, 564 nm, 633 nm, and 780 nm (2 mW power and integration times of 10 s integration times)[179]. A 632.8 nm laser at 1 mW power with 2 min acquisition time (defocused for wide-field imaging) was also reported for studying the oxygenation process of a human erythrocyte[180]. Time-course Raman imaging was also able to measure the rapid release of cytochrome C during apoptosis[113].

Nevertheless, under non-resonant conditions, higher laser powers and longer acquisition are required in order to Raman spectra with acceptable signal to noise ratio. Early work by Puppels *et al.* reported that excitation of cells with lasers in the visible range

(459 nm, 488 nm and 514 nm) induced damage to live human lymphocytes even at laser powers below 5 mW[181]. Lasers with wavelengths of 632 nm and 660 nm allowed for powers as high as 20 mW, but photodamage was apparent above the 20 mW level. Raman spectroscopy experiments of murine lung epithelial cells also indicated rapid damage (as early as 5 minutes) when 488 nm and 514 nm lasers were used at 5 mW power[182]. Nevertheless, no morphological changes indicating damage were observed even after 40 minutes irradiation with a 785 nm laser at 115 mW[182].

Initially, it has been suggested that the damage to cells caused by visible laser was due to two-photon absorption: the potential absorption of 514 nm and 532 nm laser photons matches exactly at the maximum absorption of the DNA band near 260 nm[183]. However, Puppels *et al.*found that the damage depended on the irradiation dose (energy), ruling out a two-photon absorption[181]. Because the absorption coefficients of cells, water and substrate (quartz) do not vary significantly within the 488-700 nm range, heating caused by laser absorption was also considered unlikely. Therefore, the most likely source of cell damage in the visible range may be due to the presence in cells of photosensitiser molecules (*e.g.*, porphyrins). Upon laser excitation, these molecules can react with oxygen to form single-oxygen or superoxide ions, which in turn may interact with DNA bases or amino acids to cause damage to the cells. Alternative mechanisms also included rapid changes in Ca_2^+ concentration in the cells, that can cause damage at high laser powers[184].

Although irradiation of cells with near-infrared lasers induces less damage to live cells, the levels of acceptable powers and irradiation times depend strongly on the laser wavelength. A study on human spermatozoa, showed that exposure to 760 nm laser (108 mW, 100x/1.3 NA) induced an increase in auto-fluorescence emission similar to when cells were exposed to 1.5 mW UVA light from a mercury lamp at 365 nm[185]. The changes in auto-fluorescence emission were accompanied by reduced cell motility, paralysis and finally, loss of viability. However, when cells were exposed to 800 nm laser light under similar experimental conditions (laser power, microscope objective), no change in auto-fluorescence pattern or reduced viability was observed even after 10 min irradiation. The similarities between the cellular response upon irradiation with 365 nm light of the Hg lamp and high-power 760 nm laser light suggested a two-photon absorption mechanism[185].

Deleterious effects of irradiation at 760 nm of cells were also reported on Chinese hamster ovary (CHO) cells[186] and *Escherichia coli*[187]. When the nuclei of CHO cells were exposed to tightly focused laser light with wavelengths in the range 740-900 nm (88-176 mW, 100x/1.3 NA objective, irradiation times 1-20 minutes), the measured clonal growth decreased as the power density and the duration of laser exposure increased[186]. Nevertheless, the maximum cell survivability was found when the laser was tuned in the 800-850 nm or the 950-990 nm regions, while the least clonability was observed at 740-760 nm and 900 nm[186]. Similar spectral dependence of laser-induced damage was found by Neuman *et al.*, who monitored the rotation rates of individual *Escherichia coli* tethered to a glass coverslip by means of a single flagellum (rotation rates are proportional to the bacteria transmembrane proton potential[188]) upon illumination with lasers in the 790-1064 nm range (powers > 100 mW, objective 63x/1.2NA, irradiation times 3-5 minutes)[187]. The laser induced damage was minimal at laser wavelengths of 830 and 970 nm, and exhibited maxima at 870 and 930 nm. Contrary to Konig *et al.*[185], the damage depended linearly with the laser power, supporting a single-photon process. Furthermore, under anaerobic conditions, the laser induced damage was found to reduce to background levels, indicating that oxygen plays a key role in the photodamage pathway. The similarities between the survivability on laser wavelength *E. coli*, hamster and human cells[185–187], may indicate a common mechanism of laser damage, possibly involving a ubiquitous intracellular chromophore, that may be generalised to other organisms.

The results at single cell level *in vitro* have been supported by experiments on a transgenic strain of *Caenorhabditis elegans* that carried an integrated heat-shock-responsive reporter gene[189]. The experimental data showed that expression of the heat-shock gene was most often induced by exposure to 760 nm laser light, and least expressed at 810 nm laser wavelength. It was also found that the stress response increased with laser power and irradiation time (powers 100-480 mW, illumination times 1-4 minutes, objective 100x/1.35 NA). The linear relationship between the damage and the irradiation energy dose in the 700-760 nm range indicated that the stress response is caused by photochemical processes. In contrast, for 810 nm laser wavelength, the stress depended linearly with the laser power, indicating a photothermal effect caused by single photon absorption, although calculations indicated an expected temperature rise only on the order of $1°C$ per 100 mW of laser light (the simulations considered a diffraction limited spot obtained with a microscope objective with 100x/1.35 NA and assumed that all absorbed light is converted to heat)[189].

Considering this body of evidence, it is evident that illumination of live cells by tightly focused near-infrared laser beams induces stress, which increases with the power and irradiation time. Nevertheless, the stress induced by near-infrared lasers does not lead to rapid and irreversible damage, as typically observed when using visible lasers are used (unless specific resonance effects allow the use of low level irradiation in the visible range). Although near-infrared lasers are preferred in Raman spectroscopy of live cells, the choice of wavelength, power and illumination conditions need to be assessed according to the specific biological processes and type of cells investigated. For example, the use of staining tests (Trypan Blue, dead/live kit based on SYTO10 dye and ethidium homodimer-2) has been used to evaluate viability of cells after Raman analysis[190, 191]. Time-course Raman experiments (785 nm laser, <100 mW, 5-10 min illumination, 60x/1.2 NA objective) monitoring the interaction of individual *Toxoplasma gondii* with host human cells indicated no differences in infection potential, whether or not the parasites were analysed by Raman spectroscopy or not[145]. Analysis of beating frequency of individual cardiomyocytes derived from human embryonic stem cells, before and after Raman measurements at similar conditions, indicated no changes in frequency upon laser illumination[192]. *In vitro* time-course Raman mapping of embryoid bodies over a duration of 5 days indicated that cardiac differentiation was successful (as confirmed by staining for the cardiac marker α-actinin), even after laser irradiation during Raman measurements[136]. Gene expression analysis was also used to determine the effect of laser irradiation during Raman spectroscopy on adipose derived stem cells (66 mW, 785 nm laser; 40x/0.8 water immersion objective; acquisition $\approx$ 2 minutes)[193]. While the expression of PPAR and ADIPOQ markers was significantly increased during the adipogenic differentiation of the cells, regardless of whether the cells had undergone Raman spectroscopy analysis or not, significantly lower expression was detected in the cells that had undergone Raman analysis. The biological significance of these differences in gene expression were not clear as a mature adipocyte phenotype was confirmed by the

presence of lipid droplets was observed by Oil Red O staining.

The use of pulsed lasers in techniques such as CARS (see Section 4.3) and SRS (see Section 4.4) introduce other potential concerns for preserving sample viability. Light is temporally more concentrated and two-photon effects are more abundant. This means that cell damage will onset at lower average powers than for continuous-wave (CW) irradiation. Pulsed laser-induced cell damage has largely been investigated in the context of multiphoton microscopy. Konig *et al.* showed that while cell viability was only affected by CW laser powers over 35 mW (wavelength = 780 nm), these effects appeared at 22 mW and 7 mW for 2 ps and 240 fs pulses, respectively, at the same wavelength. Furthermore, damage from pulsed lasers was greater at 780 nm than 920 nm, suggesting that water heating is not responsible for the loss in cell viability. Two-photon absorption by photosensitizer molecules is likely responsible[194]. Further, Yakovlev *et al.* showed that cell damage was more likely with shorter pulses and shorter near-infrared wavelengths (*i.e.* closer to the visible)[195]. These results were confirmed in the specific case of CARS microscopy by Fu *et al.*[196].

4.2. Resonance Raman Spectroscopy

The theory of resonance Raman scattering is described in Section 2.4. This section will discuss the practical considerations of using resonance Raman spectroscopy to study biological samples.

4.2.1. Typical System

The standard resonance Raman spectroscopy system is very similar to a spectrometer used for spontaneous Raman spectroscopy. The most important difference is the excitation wavelength. Resonance Raman is very sensitive to the excitation wavelength, which must be tuned to the electronic transition of the target molecule. This requirement determines the choice of excitation wavelength, regardless of other factors discussed in Section 4.1. For most molecules studied by resonance Raman spectroscopy, the resonant excitation wavelength is relatively short, often in the green, blue, or ultraviolet.

4.2.2. Applications

Resonance Raman is used primarily to measure the concentrations of specific molecules. For example, Salmaso *et al.* used resonance Raman spectroscopy to study the enzyme eosinophil peroxidase in living immune cells[197]. Sijtsema *et al.* were able to distinguish redox states in single immune cells by measuring resonance Raman signals from cytochrome b_{558} and myeloperoxidase[198].

Puppels *et al.* used resonance Raman to quantify the amount of carotenoids in different sub-cellular regions[199]. This led to other studies using resonance Raman to create sub-cellular maps of specific molecules including heme-containing enzymes such as cytochrome b_{558}[146] and globins such as hemoglobin and neuroglobin[200]. Figure 21(a) shows the localization of cytochrome b_{558} within the cell to phagocytosed polystyrene beads.

Cytochrome c is another effective target of resonance Raman spectroscopy. Okada *et al.* observed the release of cytochrome c during apoptosis[113]. Control cells show cytochrome c concentrated in the mitochondria of control cells and dispersed throughout the cytoplasm of apoptotic cells (see Figure 21(b)).

Wood *et al.* used resonance Raman to image trophozoites in malaria-infected cells[201]. Parasite-deposited haemozoin is easily visible in Raman images due to the resonance enhancement (see Figure 21(c)).

The enhancement effect of resonance Raman scattering has also been used to simplify the standard Raman spectrometer[202]. With the strong signal from the target molecule (carotenoids in this case), less excitation power is necessary. The excitation laser can be replaced by less expensive light-emitting diodes (LEDs). However, with this configuration, only the Raman signal from the target molecule will be detectable.

4.2.3. Challenges

Not every molecule with a Raman signature can be studied by resonance Raman spectroscopy. Resonance Raman is only possible if the electronic energy levels correspond to suitable excitation sources. For this reason, we see much of the work in this area focusing on relatively few target molecules.

The constraint on the excitation wavelength creates other experimental concerns. The resonant wavelengths common for electronic transitions are often in the blue or ultraviolet. Many biological molecules exhibit strong absorption at these wavelengths. This increases the danger of overheating or burning the sample. Experimenters must limit the incident irradiance and exposure time to avoid damaging or otherwise altering the sample.

While resonance Raman spectroscopy can be a useful tool when focusing on a single molecule, this specificity can also be a limitation. Exciting near the resonance of a particular molecule changes many features of the Raman spectrum from that molecule. Some bands of this altered signal are also greatly amplified, making it difficult to analyze other molecules in the sample. It can be difficult to compare resonance Raman spectra to spontaneous Raman spectra. Additionally, many analytical tools may not be suitable for resonance Raman studies.

4.3. Coherent Anti-Stokes Raman Scattering (CARS)

Here we will give a brief overview of CARS instruments and applications in the life sciences. More detailed review articles can be found for a general overview[20–23, 42, 203], and in Pezaki *et al.*[204] for biological applications and Le *et al.*[205] for more specific applications relating to lipid research.

4.3.1. Typical CARS System

The development of coherent Raman microscopies came as a solution to the slow imaging inherent to spontaneous Raman scattering-based techniques. CARS microscopy was the first form of coherent Raman microscopy, and was first demonstrated in 1982 by Duncan *et al.* who used a dual-laser setup to measure onion-skin cells soaked in deuterated water. However their instrument suffered from a large background signal due to the choice of laser wavelengths in the visible spectral range[206]. CARS microscopy was
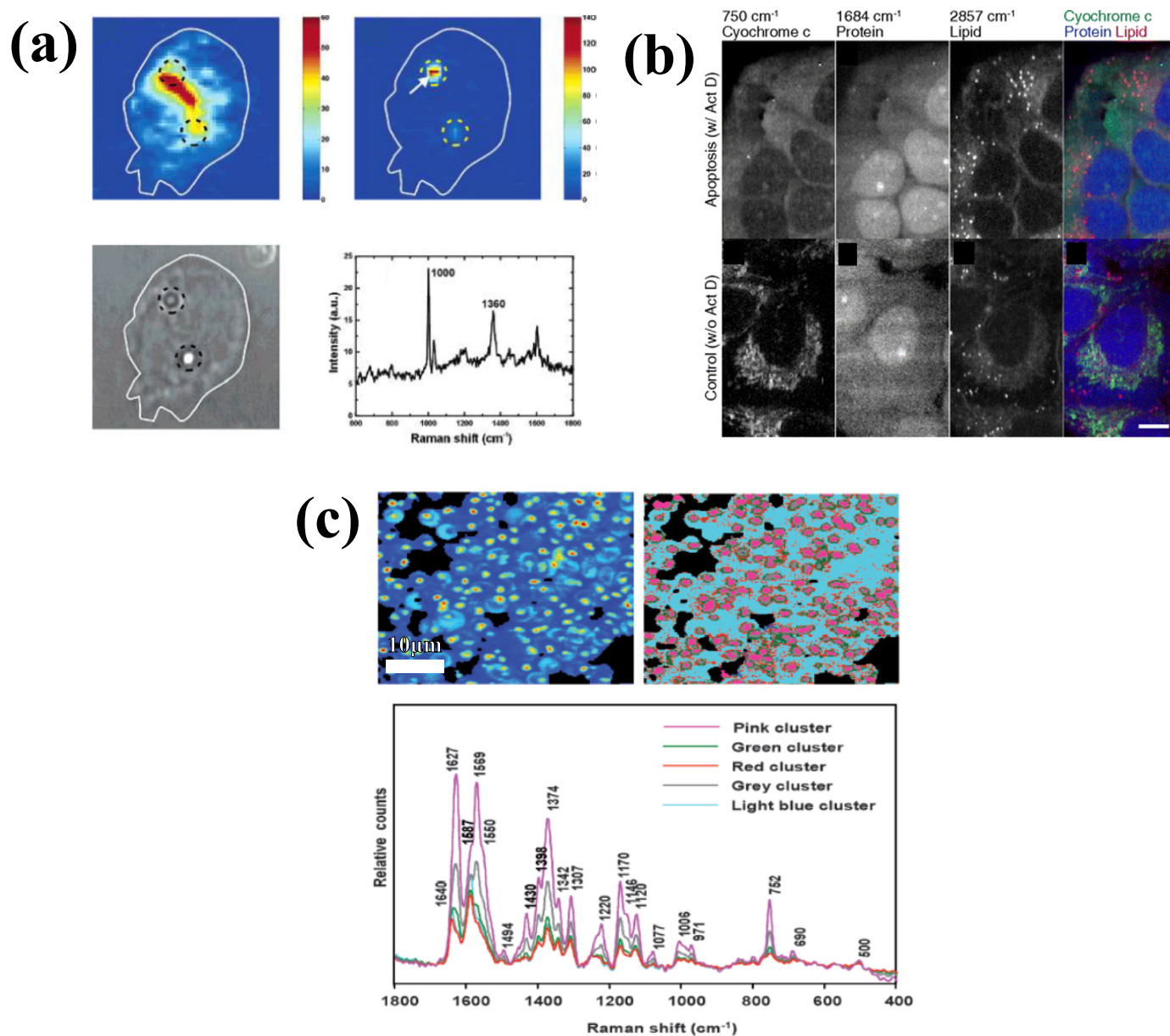
Fig. 21. Examples of resonance Raman images of unlabeled cells.
(a) Resonance Raman images ($15 \times 15\ \mu m^2$) of cytochrome b_{558} shown co-localizing with phagocytosed plastic beads[146]. Reprinted (adapted) with permission. Copyright (2004) American Chemical Society.
(b) Images of resonant cytochrome c and non-resonant protein and lipid Raman bands (scale bar is 10 μm)[113]. Comparison between the images shows the release of cytocrhome c from the mitochondria during apoptosis.
(c) Hyperspectral Raman images of malaria-infected cells[201]. (Left) Raman image of the band from 1620-1680 cm^{-1} assigned to haemozoin, (Right) cluster analysis of Raman spectra. Spectra correspond to the mean spectra of these clusters.

rediscovered later by Zumbusch *et al.* who used longer wavelength lasers in the NIR to minimize effects of the background contributions, allowing higher sensitivity for biological measurements in the high-wavenumber Raman region[207]. Also demonstrated was the improvement of CARS for 3D sectioning by tight focusing of collinear beams using a high NA objective, which relaxes the phase-matching condition (introduced in Section 2.5).

While CARS had been successfully demonstrated for biological samples, there remained several inherent drawbacks for imaging applications. The non-resonant background not only distorts the CARS spectra, but also generates unwanted background signal as seen in Figure 22(c). Furthermore, the point-spread-function for CARS imaging is not as easily defined as for other typical point-scanning microscopies, due to the coherence of the forward and backward CARS signal. This results in a variety of scattering behavior for different sample configurations as seen in Figure 22(b), which can result in imaging artifacts due to interference (shown for polystyrene beads in Figure 22(d)). Furthermore, this interference causes forward scattering to increase while backscattering decreases for samples with more coherent oscillators in the sampling volume. This theoretically makes measurements of thick samples more difficult. However, Evans *et al.* showed that a fraction of the forward-CARS photons can be collected in the epi-direction in turbid materials where photons can exit in the backwards direction via multiple elastic scattering, seen in Figure 22(b), demonstrating the feasibility for CARS imaging of tissues[130]. Another important consideration for medical applications is the miniaturization of instrumentation. To this end, dedicated laser sources have also been developed for CARS which are more compact and deliverable by fiber optic probes[208].
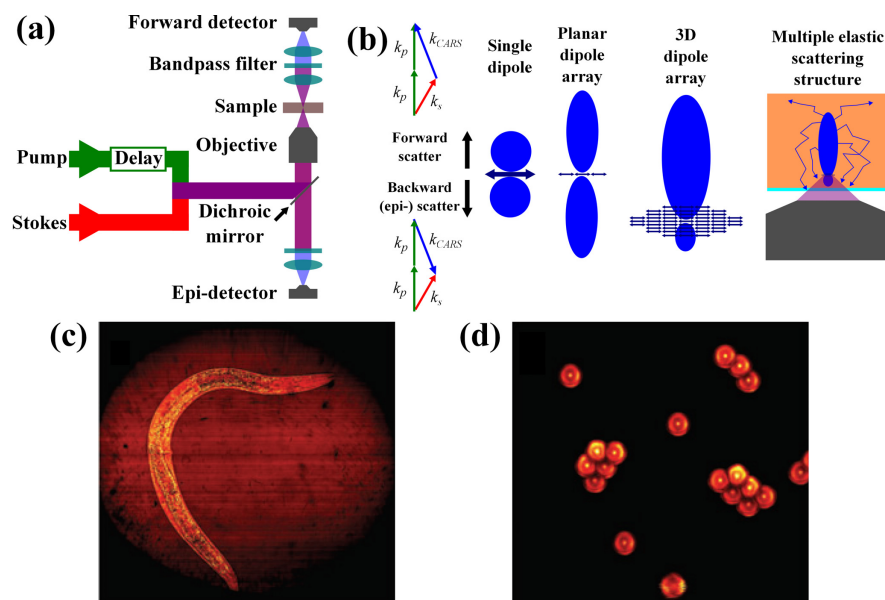

Fig. 22. Concepts of CARS microscopy.
(a) General schematic for forwards and backwards(epi-) detected CARS.
(b) Behaviour of CARS microscopy scattering for different samples. A single dipole will exhibit the well-known symmetric radiation pattern, a plane of dipoles will cause the radiation pattern to become narrower, and a 3D array of dipoles will preferentially scatter in the forwards direction. In a linearly scattering medium (such as tissue), photon diffusion allows a portion of the larger forward-CARS signal to be detected in the backwards direction.
(c) CARS image at the 2845 cm^{-1} lipid band of *C. elegans*, showing the effect of non-resonant contributions in regions without lipids.
(d) CARS micrograph at 2845 cm^{-1} band of 2 μm polystyrene beads showing potential image artifacts due to interference of the coherent signal and its reflections within the sample region (c,d modified with permission from the Annual Review of Physical Chemistry, Volume 62 © 2011 by Annual Reviews, http://www.annualreviews.org [23]).

In addition to allowing CARS imaging of tissue, the epi-detection of multiply-scattered forward-CARS photons actually provides sufficient signal for video rate (20fps) imaging at a single wavenumber. This was demonstrated on mouse skin with sufficient speed to observe the diffusion of mineral oil through the stratum corneum[130]. While narrowband (i.e. single-wavenumber excitation) measurements are useful for fast imaging, the desire for hyperspectral CARS data acquisition led to several groups taking new approaches to CARS micro-spectroscopy. The first demonstrations of multiplex CARS were carried out using a narrowband (ps) pump, and a broadband (i.e. spanning multiple vibrational frequencies) (fs) chirped (i.e. frequency swept) Stokes beam allowing multiple CARS transitions spanning from ≈900-1400 cm^{-1}[209, 210] and ≈2800-3000 cm^{-1}[211]. Cheng *et al.* also demonstrated that polarization-resolved measurements of the CARS spectra was possible using this multiplex approach, and was useful for rejection of the non-resonant background[211]. Several subsequent approaches have also been used for obtaining hyperspectral CARS datasets. Frequency-modulated CARS uses two rapidly switched pump excitation beams at slightly differing frequencies which results in an amplitude-modulated CARS output signal which can be measured using lock-in detection methods to reject the non-resonant background[212]. Another approach known as spectral focussing CARS utilizes excitation beams which are varied linearly in frequency (chirped)[213]. When the chirp of the pump and Stokes beam are matched, CARS spectra of various biological materials

could be obtained over the range 2500-4100 cm^{-1}range with 60 cm^{-1}resolution. A similar spectral focussing approach using a dual-chirped excitation system has also been demonstrated in the fingerprint region (1200-2000 cm^{-1})[214]

An approach from the group of M. Cicerone demonstrated CARS microscopy with a broad spectral range (500-3500 cm^{-1})[215]. This Broadband CARS was achieved by using two excitation approaches for different spectral regions. For the high wavenumber region ($\approx$ 2000-3000 cm^{-1}), a conventional multiplex approach with a narrowband pump and broadband Stokes beam were used. For lower wavenumber CARS spectra, the broadband laser was used for the first (pump) transition in the CARS process in Figure 2(e) as well as the Stokes transition, with the narrowband photons only used for the third transition (often called the 'probe', which is usually from the pump laser field in CARS). This approach allowed broadband spectra to be acquired in times as short as 3.5 ms, with second harmonic generation (SHG) and two-photon excited fluorescence (TPEF) also able to be observed with the same spectrometer CCD. Furthermore, techniques for reconstruction of these CARS spectra into Im($\chi^{(3)}$) using a Kramers-Kronig transform produced spectra that more closely matched those from spontaneous Raman measurements. The measurement speed of broadband CARS was improved further by utilizing high-frequency resonant beam-scanning mirrors[216].

A recent interferometry-based approach to CARS utilizing dual frequency comb excitation was demonstrated for even faster ($\approx$ 16 μs per single-pixel spectrum) hyperspectral imaging, but this has thus far only been demonstrated on non-biological samples[217]. Many other approaches have also been developed, and are discussed in more detail in the recent review by Camp and Cicerone[21].

4.3.2. Applications

CARS initially almost exclusively focused on the signal-rich high-wavenumber region of Raman spectra. Studies predominantly imaged the lipid band at 2840 cm^{-1} using single-narrowband CARS measurements. Potma *et al.* demonstrated CARS imaging of *D. discoideum* amoeba cells using the O-H water stretching vibration to observe cell hydrodynamics[218]. Cheng *et al.* demonstrated simultaneous forward- and backward-CARS of NIH 3T3 cells, with the former giving information on larger structures, and latter on smaller structures (in accordance with the scattering behavior shown in Figure 22(b)), also showing the advantage of polarized CARS on cells for rejecting some of the non-resonant background (as the non-resonant and CARS processes involve different induced polarizations/susceptibilities which have different orientations)[219]. As with polarized spontaneous Raman micro-spectroscopy, polarized CARS microscopy is also useful for understanding the orientation of molecules, particularly for lipid structures[220]. Other orientation-sensitive nonlinear microscopies such as SHG are reliant on the inversion symmetry of the system being studied (as they are a second-order nonlinear process), a requirement that is relaxed for third-order processes such as CARS. Surface-enhanced Raman techniques have also been utilized for some CARS studies of lipids[221, 222].

Many other cell studies have been carried out using CARS, often in combination with other techniques such as fluorescence, DIC, or nonlinear microscopies such as SHG and TPEF. Nan *et al.* measured lipid droplets in live fibroblast cells with CARS[223]. El-Mashtoly *et al.* used CARS imaging in the high-wavenumber region to classify cell components using a model based on hierarchical cluster analysis (HCA), as seen in Figure 23(a)[224]. Downes *et al.* demonstrated combined spontaneous Raman-CARS imaging of adipose-derived stem cells which had differentiated into adipocytes (fat cells, 2845 cm^{-1}) and osteoblasts (bone cells, 960 cm^{-1})[225]. Steuwe *et al.* used CARS to monitor human colorectal cancer cells undergoing drug-induced apoptosis, specifically by monitoring lipid vesicles[226]. Hellerer *et al.* demonstrated 3D CARS imaging of whole organisms, showing lipid distribution inside *C. elegans* (see Figure 23(d))[227]. Nan *et al.* uses CARS lipid imaging combined with TPEF of RNA from Hepatitis C viruses to image Huh-7 human hepatoma cells[228]. Le *et al.* studied adipogenesis (stem cell differentiation into fat cells) at a single-cell level with CARS to investigate phenotypic heterogeneity[229]. Quantitative CARS imaging of fat stem cells fed with different media was demonstrated by Di Napoli *et al.* using differential spectral focussing CARS, as seen in Figure 23(f)[214].

CARS measurements of tissues rely predominantly on the backscattering of forward-generated CARS photons, as introduced in the previous section and seen in Figure 22(b), which is particularly important for endoscope-based CARS. Evans *et al.* used CARS to image mouse brain tissue structures *ex vivo*[230]. Fu *et al.* imaged nerve tissue, revealing calcium-dependent myelin degradation pathways[231]. Garrett *et al.* used lipid-imaging CARS combined with CARS at the 2100 cm^{-1} of a deuterated polymer nanomedicine to investigate the delivery of the drug to different organs in a mouse model[232]. The same group also used CARS to investigate nanoparticle environmental pollutants in water and their localization in fish tissue (see Figure 23(e))[233]. Dietery fat absorbtion was studied by Zhu *et al.* who used CARS imaging of cytoplasmic lipid droplet dynamics and metabolism in mice intestinal tissue models[234]. Wang *et al.* used CARS combined with SHG and TPEF to image various grades of atherosclerotic lipid lesions in porcine arteries, as seen in Figure 23(c)[235]. Atherosclerotic lesions in mice arteries were also imaged using multiplex CARS (2700-3100 cm^{-1}) by Kim *et al.* to investigate the correlation of morphology with lipid chemical content[236]. CARS hyperspectral imaging in the fingerprint region was used to image cortical bone by Pegeraro *et al.* (in combination with SHG for collagen and TPEF for blood imaging)[237]. A comparison of spontaneous Raman and CARS imaging of brain[238] and colon tissue[239] was carried out to interpret CARS images of tissue in the high-wavenumber spectral region. The development of broad-band CARS microspectroscopy with spectral reconstruction demonstrated by Camp *et al.* was applied to ex vivo tissue imaging of liver tissue from mice[215]. This allowed images with contrast generated by features from most of the biological Raman spectral window, as shown in Figure 23(b) (also compatible with SHG/TPEF). CARS-based endoscopy was also demonstrated on various ex vivo thick tissue samples by Balu *et al.*[240].

4.3.3. Challenges

Since the first demonstration of CARS microscopy on biological systems, a concerted effort has been made to minimize many of the drawbacks inherent to the scattering process. Problems such as non-resonant background, broad measurable spectral range and quantification have essentially been solved by various means. However, their implementation is not currently widespread as the increased complexity in instrumentation required restricts the advantages to limited numbers of research groups. The majority of CARS experiments are still carried out in the high wavenumber region for contrast of lipids. However, as particular technologies are
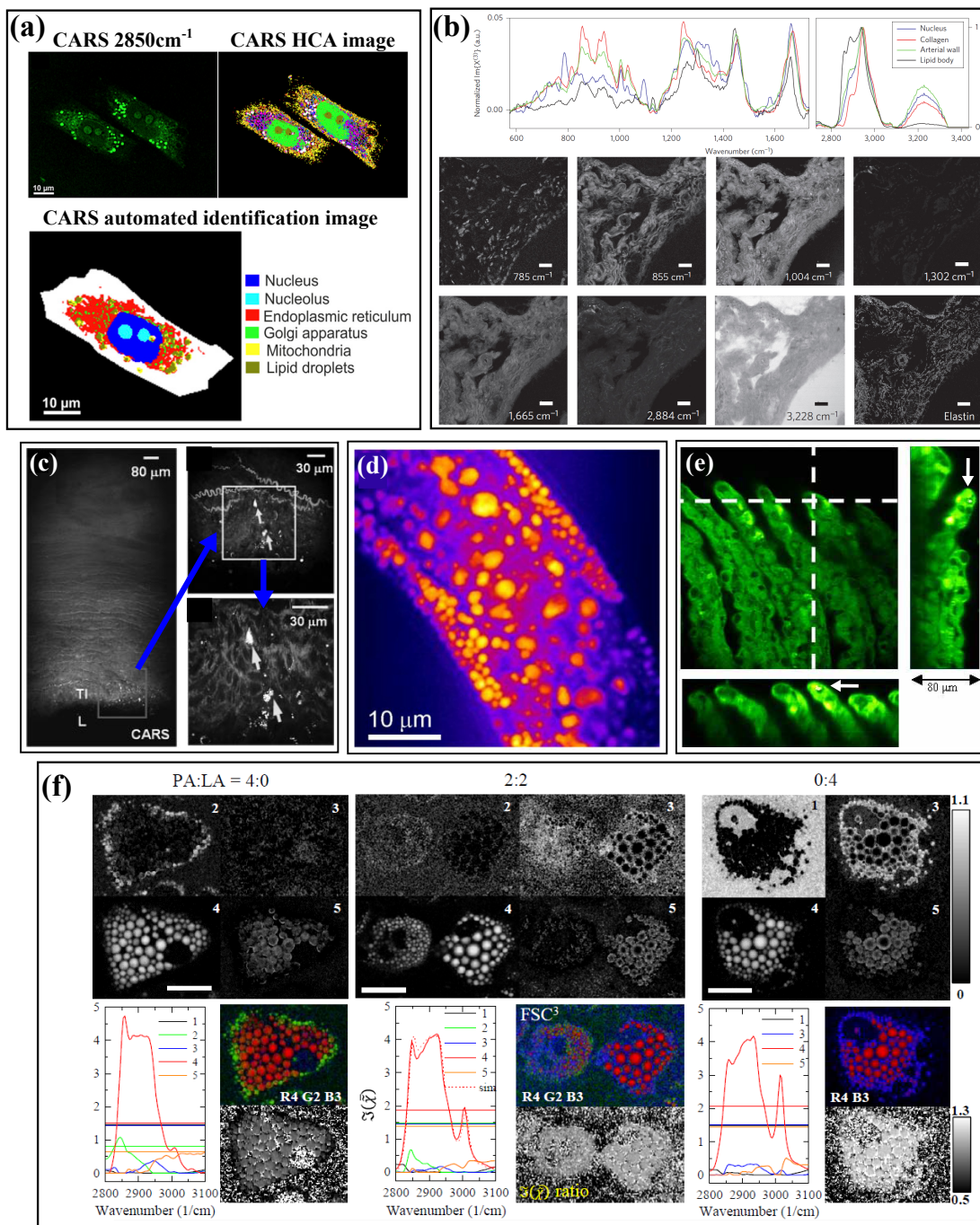
Fig. 23. Applications of CARS microscopy.

(a) Automated cell organelle identification using CARS micro-spectroscopy and hierarchical cluster analysis (HCA) of high-wavenumber spectra of human pancreatic cancer MIA PaCa-2 cells (modified from El-Mashtoly *et al.*[224]).

(b) Broad-band CARS images of mouse liver tissue (20 μm scale bar, elastin image from 1126 and 1030 cm^{-1}) with single-pixel CARS spectra from various tissue components reconstructed using the Kramers-Kronig transform method (modified from Camp *et al.*[215]).

(c) CARS imaging (2840 cm^{-1}) of Type I atherosclerotic lesions from porcine arteries, with cells with large lipid concentrations indicated by arrows (TI: thickened intima, L: lumen)[235].

(d) CARS imaging of lipids (2845 cm^{-1}) inside live *C. elegans*[227]. Copyright (2007) National Academy of Sciences, U.S.A.

(e) Forward-CARS 3D imaging (2854 cm^{-1}) of trout gills exposed to TiO$_2$ nanoparticles for two weeks, with arrows showing nanoparticle localization[233]. Reprinted (adapted) with permission.

(f) Quantitative CARS hyperspectral imaging of human adipose-derived stem cells fed with different ratios of palmitic acid (PA) and α-linolenic acid (LA). Top images show concentration images of different components numbered according to the colored CARS spectra (also correponding to RGB colored component images). $\Im(chi)$ ratio images created from the ratio of 2930:2855 cm^{-1} bands (scale bars 20 μm)[214].

implemented in commercial instruments, this will likely improve.

The field of CARS faces a much larger challenge from the more recently developed technique of SRS microscopy (the subject of Section 4.4). While the recent advance of broadband CARS is currently superior in terms of the spectral range achievable with single-pixel spectroscopy, SRS is inherently shot-noise limited, background-free, has no spectral distortions (*i.e.* directly matches the spontaneous Raman spectrum shape) and has a well defined point-spread function which avoids coherence-induced imaging artifacts. However, CARS and SRS process will typically occur at the same time, only requiring different detection configurations, thus they are well-suited to multi-modal imaging together as well as with other nonlinear microscopies such as TPEF and SHG.

4.4. Stimulated Raman Scattering (SRS)

4.4.1. Typical System

As described in Section 2.5, the CARS process produces photons which are spectrally distinct from the input excitation sources. This is not the case for SRS where the process manifests as an intensity gain/loss in the pump/Stokes fields. This means standard spectroscopically-discriminating apparatus is not suitable for such a process. Instead, one could imagine some sort of absorption–like setup, whereby the absolute intensity of the pump and probe beams are calibrated such that differences could be directly measured. This would work in principle, but as ΔI_p and ΔI_s are very small compared to I_p and I_s and their associated stability and noise, this strategy is not practical for most samples, particularly those in the life sciences.

In order to allow such small intensity changes to be observed from such a noisy environment, alternative detection schemes have been used. In particular lock-in detection is a widespread technique for extracting signals from noisy environments with a known carrier wave reference. Within the context of SRS, this requires a known intensity modulation to be applied to either the pump or probe/Stokes beam, which will be imprinted onto the corresponding partnering beam via a nonlinear Raman interaction, a technique known as "modulation transfer". As mentioned in Section 2.5, this was first demonstrated in using CW lasers and an optical chopper with modulation frequency of 8 kHz for measuring the strong 992 cm^{-1} band in liquid benzene[50]. Ploetz *et al.* later demonstrated SRS micro-spectroscopy of polystyrene beads using femtosecond laser pulses, with a white-light probe/Stokes beam to measure a wider Raman spectral range. However measurement times were comparable to spontaneous Raman spectroscopy and the high laser power meant this approach is generally incompatible with biological measurements[241].

The first demonstration of SRS for biological systems was carried out by Freudiger *et al.*, who used much faster optical modulation
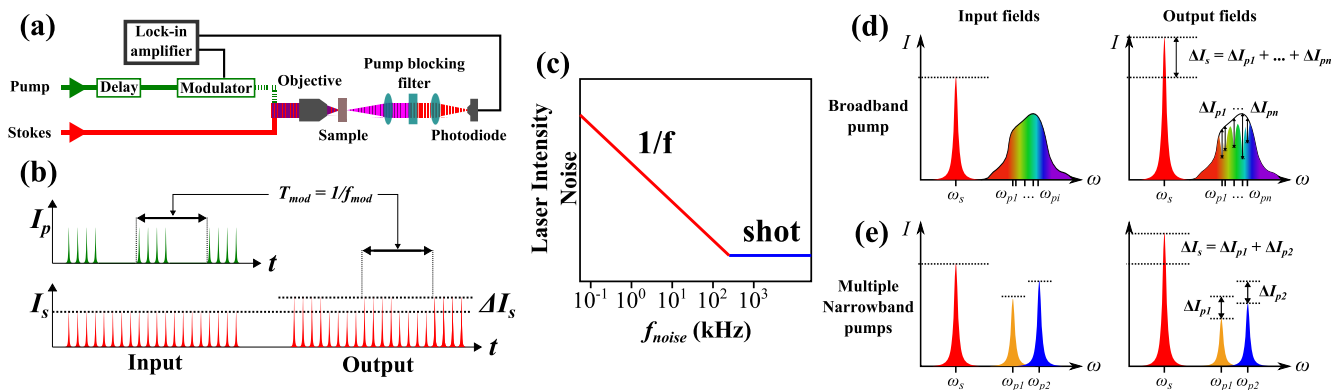

Fig. 24. Concepts of SRS microscopy.
(a) Schematic of an SRS microscope optical train.
(b) Intensity modulation transfer from the pump to the Stokes/probe beam (note: also possible to apply modulation to Stokes beam and detect the pump instead).
(c) Typical laser intensity noise contributions vs frequency.
(d) Multiplex SRS using broadband excitation and (e) multi-narrowband swept or spectrally tailored pump excitation.

transfer (>1 MHz) to obtain increased sensitivity, shot-noise limited measurements, away from the $1/f_{noise}$ regime shown in Figure 24[242]. This also has the added advantage of fast measurement time (<1 ms), allowing rapid, background-free Raman imaging from a single wavenumber at $\omega_p - \omega_s$ (also shown was a dual-wavenumber instrument using a second pump beam). This approach is especially bio-compatible as high laser powers aren't necessary (average power <40 mW[242]).

As the SRS phase-matching condition is automatically satisfied, the point-spread function is definable by more conventional theory compared with CARS. This new form of SRS microscopy was demonstrated on a variety of samples mostly using high-wavenumber Raman bands measured in the forward (transmission) direction. The 3D measurement capability of SRS was also demonstrated by mapping the delivery of different drugs into mouse skin, using Raman bands in the fingerprint region (see Figure 24(a)).

Video-rate SRS imaging (25 fps for 512 × 512 pixels) was later shown using resonant galvanometer scanners and an epi-detection scheme which collected photons scattered backwards from a turbid medium such as living tissue[243]. This development of epi-detected SRS microscopy was an important step towards measurements on non-transparent samples such as biological tissue.

Several routes towards multiple simultaneous wavenumber SRS measurement have been explored. Using a broadband pump source, one can in principle obtain a spectrum as shown in Figure 24(d), though this is usually avoided as there will be contributions to the SRG in the Stokes beam from undesirable but overlapping nearby bands. Other methods utilize various multi-narrowband

excitation. In one example a spectrally tailored pump beam was developed to target particular Raman bands, whilst removing unwanted overlapping contributions[244]. Another example used a rapidly tunable optical parametric oscillator (OPO) which was fast enough to avoid multispectral SRS imaging artifacts due to sample movements[245]. Approaches where the Stokes beam is switchable between narrow- and broad-band have been demonstrated using photonic crystal fibers have also been shown[246].

Another advance in instrumentation was an alternative to the lock-in detection of the modulated light, instead using a tunable amplifier (TAMP). This reduced the Johnson-Nyquist noise, which dominates over shot noise at low laser power, compared with lock-in techniques, showing an order of magnitude improvement in signal-to-noise[247]. This was also extended to a TAMP array to allow multiplexed SRS measurements without using multiple lock-in amplifiers[248].

Specific laser sources are also being developed to cater for the needs of SRS microscopy. Dual-wavelength fiber lasers have been developed to allow for more compact SRS microscopes suitable for clinical use[249]. Recently a simplified solid-state tunable laser system with high-stability was also demonstrated for improved signal-to-noise[250].

The choice of detecting the SRG or SRL should not matter in principle, as they imprint the same change on the Stokes and pump beam respectively. Thus the choice is usually made depending on the sensitivity of the photodetector at ω_p or ω_s[242]. However the choice can change the relative background contributions to the SRS signal, for example the two-photon absorption will generally be more prevalent in the SRL (pump beam) signal[49]. Further detailed discussions of instrumentation and noise considerations can be found in Min *et al.*[23] and Zhang *et al.*[22].

4.4.2. Applications

With suitably chosen excitation beams, the SRS tunability range can cover much of the same spectral range as spontaneous Raman (down to 500 cm^{-1}[242]), though most studies so far have focused on the high-wavenumber region. As shown in Section 3.5 the 2800-3100 cm^{-1} range contains many overlapping bands, with major features corresponding to CH$_2$ and CH$_3$ vibrations, as seen in Figure 24(c). Other features correspond to DNA and part of the higher-wavenumber water tail. Vibrations from Raman labels such as stable-isotope and particularly alkyne tags have bands in the lower 2000 cm^{-1} range, and have been utilised multiple times in SRS studies[251, 252].

Initially lipids and proteins were most commonly measured with SRS in cells and tissues, as they contain the strongest and most intense contributions in the high-wavenumber region. Wei *et al.* used SRS combined with various stable-isotope labeled amino acids, which when metabolically incorporated into cells was able to be used to image newly synthesised proteins[251]. Alkyne labels are also powerful for SRS imaging, and are discussed in Section 4.10 in more detail. DNA was later imaged label-free using the upper part of the CH-stretching region ($\approx$ 2967 cm^{-1}), being able to identify different phases of the cell cycle in both single cells and tissues (see Figure 25(c))[253].

As SRS is background-free and the signal scales linearly with number of molecules sampled, it is suitable for quantitative imaging. Fu *et al.* showed quantitative multiplexed SRS was possible in micro-algal cell cultures where concentrations of protein, lipid and chlorophyll/carotenoid pigments were measured[254]. Lipid storage in *C. elegans* was also imaged with SRS and fluorescence microscopy allowing fat-regulatory genes to be screened with quantitative lipid-distribution information.

Work towards clinical applications of SRS have generally focused on creating images similar to histopathology staining techniques. Freudiger *et al.* used mouse models exhibiting a variety of cancers, and used SRS to create images similar to those from H&E staining at 2845 cm^{-1} (CH$_2$ - mainly lipids) and 2890 cm^{-1} (CH$_3$ - mainly proteins), with addition of two-photon absorption from Hemoglobin showing blood vessels [255]. Ozeki *et al.* used independent component analysis for similar pseudo-H&E images, but was based on high-wavenumber SRS spectra (not single-wavenumber measurements)[256]. Ji *et al.* were also able to obtain multi-color SRS images of human brain tumors which matched well with H&E in detecting various tumor features[257]. Lu *et al.* later extended this idea to whole-tissue imaging of fresh samples removed during neurosurgery with SRS in reasonable measurement times suitable for use during surgery (see Figure 25(a))[258]. SRS is also compatible with other nonlinear optical microscopy techniques such as CARS, second/third harmonic generation and multiphoton fluorescence which share similar instrumentation and usually require simple changes in the detection configuration for measurement. This was demonstrated recently using a programmable supercontinuum laser source for multi-modal nonlinear microscopy, of which SRS was one component, for ex-vivo imaging of cancerous mammary tissue from rats[259].

Drug delivery has been monitored several times with SRS microscopy, where the often unique and strong Raman features of the drugs can easily be separated from the biological Raman bands using multi-color SRS. The pathways through which various anti-inflammatory drugs penetrates the dermal layers of skin was shown by Saar *et al.*[260]. Using 3D-SRS time-course measurements, they were able to rapidly measure penetration pathways and depth of the applied drugs. Fu *et al.* also used SRS imaging to investigate the uptake of therapeutic cancer drugs to single cells, demonstrating localization inside lysozomes and ability to quantify the amount of drugs taken up by the cell[261]. The diffusion of molecules through the keratin network of the human nail was also measured by 3D time-course isotope-labeled SRS to investigate the difficulties in applying drugs to nail diseases[262]. Plant fungicides with cyano-group bands, which have strong bands in the low 2000 cm^{-1} spectral region, have also been imaged with SRS, as seen in Figure 25(b). This allowed the transport of various compounds into leaves to be imaged in 3D, as seen in Figure 25[263].

4.4.3. Challenges

Since the invention of the high-frequency modulation-transfer technique, developments in SRS microscopy have progressed rapidly, leading to improved instrumentation as well as finding a wide variety of applications in the life sciences. While still requiring a more complex optical setup compared with spontaneous Raman imaging, much of the instrumentation from other nonlinear optical microscopy techniques can be utilized to construct an instrument[264]. Furthermore, progress has been made towards the goal of
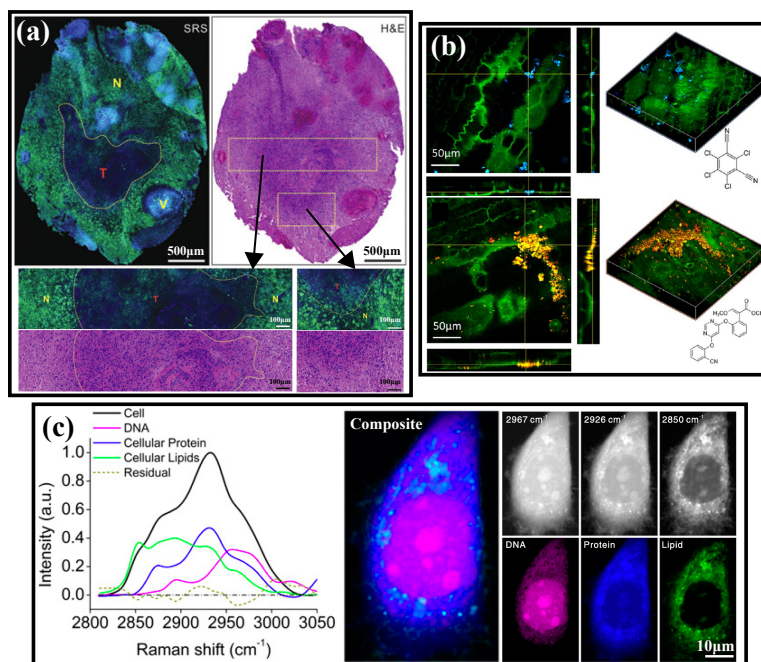
Fig. 25. Example applications of SRS.
(a) Whole-tissue imaging of human brain tissue using two-color SRS based on protein (2940 cm^{-1} signal minus half 2854 cm^{-1} signal, blue) and lipid (2854 cm^{-1} signal, green) with corresponding H& E images (T- tumor, N- necrotic tissue, V- blood vessel)[258].
(b) Uptake of chlorothalonil (2234 cm^{-1}, blue) and azoxystrobin (2225 cm^{-1}, red) fungicides into maize leaves (2930 cm^{-1}, green)[263]. Reprinted (adapted) with permission. Copyright 2013 American Chemical Society.
(c) Three-color imaging of single HeLa cells in the interphase part of the cell cycle using the different high-wavenumber contributions shown in the spectra[253].

simpler, compact bench-top SRS microscopes or endoscopes involving fiber probes and lock-in free detection. Whilst specificity is lower than spontaneous Raman imaging, the speed of SRS imaging will no doubt be appealing for many clinical applications.
Most SRS studies also involve an element of spontaneous Raman spectroscopy (usually not imaging), to identify Raman bands for imaging with SRS. While biological Raman spectra are generally well understood, subtly changing features may be missed when using narrowband-pump SRS. Integrated spontaneous-SRS instruments have been demonstrated[265], and it is foreseeable that this combination will be popular for more exploration-based research where slight spectral changes can be measured before turning to SRS for faster imaging of particular bands from the sample.
An alternative is the improvement of multiplexed SRS techniques to the point where comparable micro-spectroscopy datasets are obtainable to those seen in spontaneous Raman micro-spectroscopy, particularly in the fingerprint region. This has been shown for narrow spectral windows, usually in the high-wavenumber region, but also in the upper (1500-1700 cm^{-1}[256, 266]) part of the fingerprint region.

### 4.5. Surface-enhanced Raman Scattering (SERS)

There exists an enormous variety of approaches to SERS sensing, which has been applied across much of chemistry and materials science as well as the biosciences. For the latter, the approaches are usually carried out using colloidal nanoparticle solutions, and can broadly be split into two general categories: direct SERS measurements of endogeneous biological molecules close to a hot-spot, or SERS measurement of a reporter/tag molecule at the hot-spot, which probes a biological system in some way (often with targeting ligands on the exposed surface).

Even within the biosciences, SERS has been applied to single biomolecules all the way up to tissues. We will mostly restrict discussion here to SERS studies involving cells and tissues. A great selection of reviews exist which go into further detail than is presented here for other related areas within SERS. These reviews include general overviews[267–271], and reviews specific to cell studies[272–275], medical applications[24, 25, 276, 277], and toxicology[278, 279].

In this section the terms reporter/tag/label are used interchangeably, and the following abbreviations are used: nanoparticle (NP), gold (Au), silver (Ag).

4.5.1. Overview of SERS techniques

SERS measurements are often conducted on spontaneous Raman microscopes, as the major difference is simply the Raman enhancement applied to the sample itself. However, there are still important instrument considerations necessary for SERS. It is good practice to measure extinction profiles of the enhancing nanoparticles in order to assess the enhancement performance for a given laser wavelength used for the Raman excitation. Also SERS measurements can be carried out with much lower laser power than is used in spontaneous Raman (typically <10 mW), for integration times of 1 second or less. While NIR lasers are typically preferred for Raman
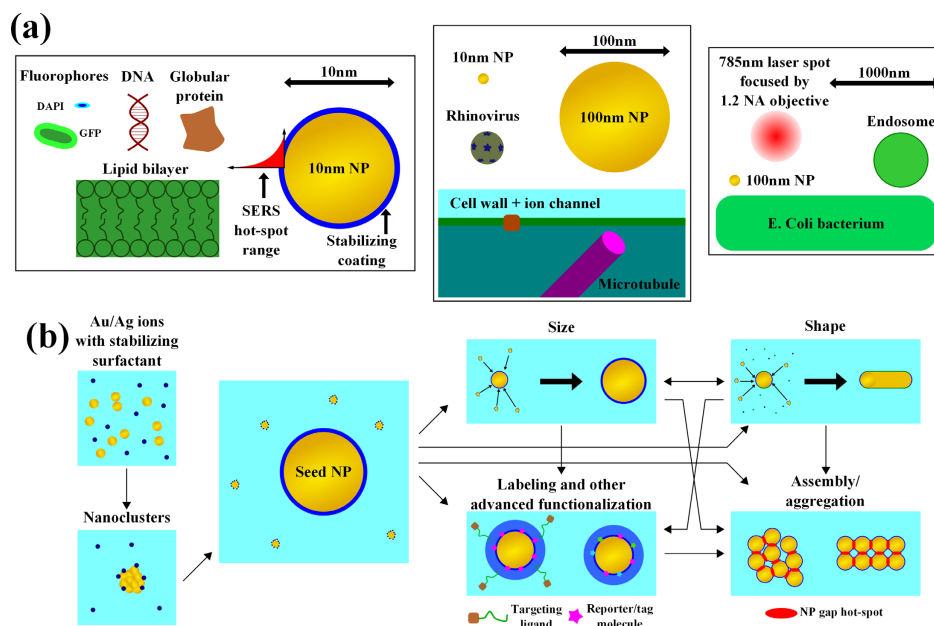
Fig. 26. SERS concepts for life science applications.
(a) Cartoon of various biological objects in comparison with nanoparticles used for SERS which typically range from 10-100 nm in size (Objects in the same box are roughly to scale).
(b) General schematic for creating SERS NPs using solution based methods. Au/Ag salts are typically combined with a stabilizing surfactant, together with input energy (heat/light) to form seed nanoparticles. These seed nanoparticles can be used for further growth into larger NPs, or shape changes can be induced by exploiting the seed crystallinity and a mixture of surfactants which adhere preferentially to certain facets. Assembly/aggregation can be induced to create many hot-spots for increased enhancement at the NP junctions. Reporter molecules can be attached to NPs and a buffer coating created to use SERS as a labeling technique. Specific binding molecules can also be attached for targeted SERS.

spectroscopy in general, lower wavelength lasers are often used at low power for SERS, as Au and Ag NP plasmon resonances tend to be in the 500-700 nm range and fluorescence is quenched, though the excitation can be at a higher wavelength on the shoulder of a resonance, at the cost of enhancement. This choice of NP size is not only important for the enhancement, but also when considering the biological application, as SERS nanoprobes are of considerable size compared with cell-scale biological structures, as illustrated in Figure 26(a).

    The synthesis of SERS probes usually begins with the creation of stabilized colloidal Au/Ag spheres as a starting point. The methods by Turkevich for Au[280], and Lee and Meisel for Ag[281] are almost universally used for this stage of the probe fabrication. These both involve the Au or Ag metal ions/proto-clusters in solution which, when inserting energy (typically via heat or light), causes reduction and aggregation. To prevent uncontrolled runaway aggregation, a protective surfactant must be used to coat the nanoparticles (this often has a dual role as the reducing molecule as well). From this point, the SERS probe can be modified further to achieve a particular purpose, with the flow chart in Figure 26(b) roughly showing popular routes taken. Size control can be obtained by re-growth of the seed particles in a similar manner to the initial growth. Shape control can be achieved by exploiting the crystallinity of different seed particles, with different surfactant stabilizers having affinity for certain crystal facets allowing anisotropic growth[63, 65]. Further complexity can be introduced using a highly-Raman scattering reporter molecule, targeting ligands, and random or controlled aggregation for increased enhancement at NP junctions.

4.5.2. Applications

Initially SERS was used for measuring low-concentration solutions, with single molecule detection sensitivity demonstrated in 1997[66, 67]. However, the first intrinsic SERS experiments of cells were demonstrated later by Kneipp et al. using 60 nm AuNPs with 830 nm excitation, requiring only 3-5 mW to obtain spectra with 1 second integration times, resulting in faster low-power imaging[282, 283]. Since then, some experiments have been performed using the direct SERS approach, but as the SERS spectra often differ significantly from spotaneous Raman, they can be difficult to interpret when in the complex cell environment. For this reason, SERS is increasingly moving towards labeled/targeted NPs[284], where usually only a single strong band from the reporter is required for identification, and can be multiplexed by using different combinations of reporter/targeting molecules.

    A wide variety of cells and organelles have been studied using various modes of SERS such as lymphocytes[285], hemoglobin and other components of red blood cells[286], intracellular lipid compartments[287], mitochondria[288], stem cell differentiation into cardiomyocytes[289], differentiation of neuronal cells[290], and yeast cell wall spectroscopy[291] and imaging[291]. SERS particles functionalized with immunolabels have also been used to measure the external surface of endothelial cell membranes[292]. Specific nucleus-targeting peptides were used to functionalize NPs and also enhanced NP uptake into cells[293]. Modulating the surface charge of the functionalized NP was also shown to give some control over uptake as well[294]. Hybrid multiplexed nanoprobes with

more than a single band used for the reporter were also developed to allow more detailed multivariate analysis for cell imaging[295].

Several organelle-specific targeted SERS reporter NPs for cytoplasm, mitochondria and nucleus targeting were used to decrease excitation power and integration time for imaging, as shown in Figure 27(d)[296]. SERS was also combined with dark-field Rayleigh imaging to monitor the entire cell cycle, with the DNA and protein bands allowing cell-cycle phase to be identified[297].

SERS probes can also be used as sensors for measuring other properties of cells, such as their pH, for example using 4-mercaptobenzoic acid as a reporter[298]. pH-sensitive AuNPs were also designed which could specifically target cancer cells, and aggregate inside to produce a diagnostic SERS reporter signal, while also allowing photothermal therapy from aggregate heating[299]. The intracellular redox potential can also be measured by SERS labelling[300], which was also performed with varying extracellular environment[301], and with some quantification possible[302].

SERS targeted measurement and identification of several types of cancer cell has been shown, including osteosarcoma cells using AuNP SERS[303], cancerous renal cell detection[304], and Ag/Au core-shell nanoparticles conjugated with antibodies were used to image PLCγ protein in HEK293 cells[305]. Targeted SERS detection of circulating tumor cells has been shown in the presence of white blood cells[306]. AgNP functionalized with lectin, which interacts with carbohydrates, was used to measure glycan expression of cancerous and non-cancerous prostate cancer cells, showing better discrimination than fluorescence microscopy[307]. Polarized-SERS using aligned Au nanorods conjugated with antibodies, which were synthesized inside human oral cancer cells, were used to detect diagnostic signatures[308]. SERS dimer NPs with di-thiolated reporters functionalized with peptides were used to control binding and endocytosis, and were used in human glioblastoma cells for cancer targeted Raman imaging[309]. Multiplex SERS particles with several reporters[310, 311] or additional fluorescence probes[312] have also been used to identify different cancer cells.

Several studies involving 3D imaging of SERS particles in cells have been demonstrated, some with particle tracking to follow the nanoparticle as it interacts with the cell[313–315]. Further studies also showed that AuNP SERS particle tracking in cytosol was able to correlate dynamic Raman features to particle motion[316]. Combined label/label-free nanoprobes were also recently used for 3D imaging[317]. Pavillon et al. have also developed automated feature-based SERS spectra recognition in cells[318].

SERS is particularly attractive to studies of bacteria, as they are typically much smaller than most cells, resulting in lower signals which would benefit from enhancement. Bacteria discrimination was first shown with Ag colloid SERS, showing discrimination at the strain level for E. Coli[319]. Differences in SERS spectra of various other bacteria species was also shown shortly after [320], and was shown to be potentially useful for bacteria 'barcoding' using multivariate statistics[321]. Different Ag NPs used for SERS were investigated for their antibacterial activity, and it was found that smaller (18 nm) were more toxic to bacteria than 80nm[322]. Bacteria and bacteriophage discrimination with combined SERS and spontaneous Raman was carried out to investigate species variability[323]. Bacterial biofilms were reproducibly measured in situ using Ag nanoparticle SERS[324], and was later extended to SERS/spontaneous Raman imaging[325, 326]. Porous Au NP functionalized hydrogel substrates were used to culture pseudomonas aeruginos biofilm colonies to investigate a quorum sensing (*i.e.* bacterial communication) metabolite (see Figure 27(b))[327]. At an even smaller scale, DNA sequences from the HIV virus were identified using AgNP SERS particles conjugated with specific DNA-targeting ligands[328].

As intracellular SERS usually requires compromising the cell membrane or forcing uptake of cells via endocytosis, metods have been developed aiming to introduce SERS particles into the cytoplasm with minimal invasiveness. Examples of this include Au NPs grown within cells by incorporating the nanoparticle precursor solution during incubation[329, 330], and delivery of Ag NPs by electroporation[331].

A more invasive but controlled approach involvde using AuNP coated microprobes for direct SERS measurement within the cell[332]. A similar idea was later carried out using a microprobe which had a more specific SERS label 'sandwich' for detecting low copy-number proteins, as illustrated in Figure 27(c)[333].

Medical applications of SERS almost exclusively use NPs functionalized with targeting and reporter molecules, similar to the cancer cell studies mentioned above. Immuno-labeling SERS has was demonstrated for detecting antigens in tissues[334], and was continued using Au nanostar SERS labels for imaging a tumor suppressor in prostate biopsies[335]. Other ex vivo studies of human tissue include breast adenocarcinoma diagnosis using Au/SiO2 nanoclouds[336], colorectal cancer detection by SERS-based blood serum screening[337], measurement of normal and cancerous nasopharyngeal tissue[338], and colon carcinoma vs normal tissue[339].

In vivo studies have so far only been carried out on animal models, first being demonstrated by Qian *et al.* using specific tumor targeting SERS probes injected at the tail, as seen in Figure 27(a)[340]. In comparison with non-targeted NPs, it was shown that the targeted probes were sufficiently distributed at the tumour, but also to the liver and spleen, though mostly avoided accumulation in the brain, kidneys, lungs and muscle. Other in vivo studies include multiplex SERS probes for in vivo imaging[341] and using NIR-specific probes[342]. An instrument specifically designed for handling small animals has also been developed for rapid multiplexed SERS imaging using four different Raman reporter particles, with the ability to scan 1 cm^2 in 6 minutes[343].

Some applications of SERS have also been demonstrated in the food and plant sciences. Ag aggregates were used for SERS on onion layers for structural and pH measurements[344]. Foodborne bacterial pathogens have also been detected with Ag nanorod arrays[345] and with Au NPs in solution giving SERS spectra which were able to identify seven different enterobacteriaceae using multivariate analysis[346].

4.5.3. Challenges

While direct SERS measurements of endogenous cell components are *technically* label-free (in the sense that molecules are not modified chemically), they are invasive. This is because regardless of how the NPs are delivered, in order to exhibit a desirable plasmon resonance for SERS, they will always be at a difficult-to-handle length scale (10-100 nm) for biological systems compared to fluorescent labels (see Figure 26(a)). Furthermore, the complexity of biological systems results in difficulty in assigning many spectra, as molecules can diffuse in and out of the hot-spots causing "blinking": the fluctuation in intensity (even disappearance) of Raman bands.
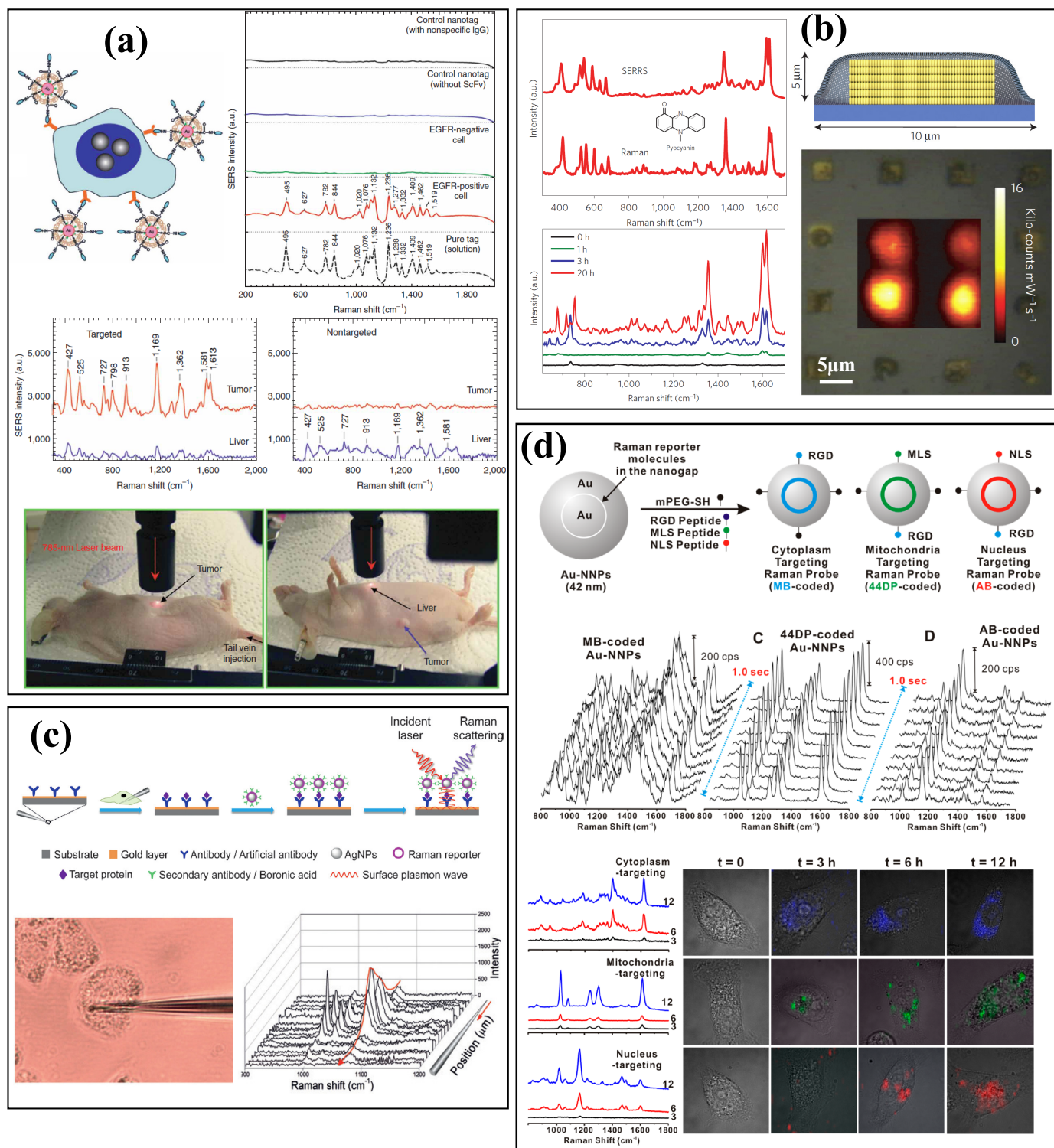
Fig. 27. SERS applications.
(a) Tumor-targeted SERS reporter NPs for in vivo tumor identification[340].
(b) SERS for bacteria colony quorum sensing on Au arrays embedded in polymer hydrogel[327].
(c) A microprobe coated with an antibody-conjugated SERS reporter layer for detection of low-copy number proteins[333].
(d) Multicolor SERS NPs for targeting cytoplasm, nucleus and the cell membrane to allow faster cell imaging at low laser power
(images 38 μm ×38 μm)[296]. Reprinted (adapted) with permission. Copyright 2015 American Chemical Society.

This is in contrast to fluorescence, which can be much more specific as the physical mechanism is less susceptible to confounding factors. For these reasons, label-based SERS is likely to continue to overtake and dominate biological applications.

Regarding clinical applications of SERS, the toxicity of nanoparticles (particularly Au) is often stated to be negligible, often because a biocompatible surfactant is used for stabilization. However it was recently shown that cells exposed to low doses of various gold nanoparticles with 'biocompatible' surfactants induce genetic changes over a long period of time[347]. This particularly resulted in the upregulation of genes associated with oxidative stress and apoptosis (amongst others) for a single (non-chronic) dose, which is the typical approach for SERS measurements. These results are only for the presence of nanoparticles in living systems, before any considerations on photo-induced effects from the SERS measurement process. Whilst the phototoxicity directly from the excitation source will be low, the localized hot-spot intensity is necessarily large, which could induce a variety of unwanted/damaging reactions in a complex cellular environment over time. Despite the recent in vivo studies using mouse models, it will still be difficult to envisage approval for clinical applications of SERS on humans in the near-future without (SERS-specific) long-term studies, in a similar manner to Falagan *et al.*[347]. It is therefore more likely to see *ex vivo* and solution-based SERS techniques achieving success in medical applications.

4.6. Tip-enhanced Raman Scattering (TERS)

4.6.1. Typical System

TERS is inherently a hybrid optical/scanning-probe technique, relying on the ultra-precise positioning of a plasmonically-active nanoscale probe within a focused Raman excitation beam. Variations of this core concept involve different scanning probe microscopy (SPM) modalities, as well as different illumination configurations. Scanning tunneling microscopy (STM) is the superior SPM technique for many aspects of TERS, such as positioning accuracy of the tip, and has been used for the most high-resolution and repeatable TERS studies to date[348]. STM requires the sample to be only a few nm thick as the feedback mechanism relies on electron tunneling to a conductive substrate. For this reason, TERS experiments on biological samples are usually performed with various modes of atomic force microscopy (AFM) instead, where sample thickness does not restrict the feedback mechanism.

Various illumination and detection configurations have been demonstrated for TERS, and are illustrated schematically in Figure 28. An important consideration for any illumination configuration is the polarization of the excitation laser, as this dictates the orientation of the dipolar plasmon, and hence the location of the enhancement hot-spot. A high-NA microscope objective is required for epi-illuminated TERS such that a significant fraction of the excitation beam is incident at a large angle, so that the hot-spot is between the tip and sample (Figure 28 (a)). Alternatively, side-illumination with a lower-NA objectives or a parabolic mirror achieves the same aim (see Figure 28(b-d)). Recent advances in tip fabrication have also suggested that TERS could be achievable with near-field excitation, using a grating which, when illuminated, would launch a plasmon towards the tip apex, removing the far-field background signal completely (see Figure 28(e)).

Once the AFM modality and illumination geometry are chosen, the key aspect of TERS is the probe itself. For some time the most widespread approach utilized the availability of commercial silicon AFM probes, which are modified to have a nanoparticle at the tip apex. Gold is relatively inert and therefore popular for many applications in materials science. However, for biological samples, silver is typically preferred for TERS as it offers much larger enhancement factors at the cost of probe longevity (see Section 2.6). The most widespread method for AFM-based TERS tip fabrication involves chemical vapor deposition of 20-30 nm of silver in vacuum, creating a rough film ideally creating a single particle at the tip apex as in Figure 28 (g). This typically produces relatively low yields of TERS-active probes (estimates vary), and so many tips are usually coated at once and tested by trial and error. This is not ideal as the silver film on the tips also degrade with time, though recent work has shown approaches for increasing the yield by oxidizing the silicon of the AFM probes before silver deposition[349] (see Figure 28(i)), and by storage in inert environments[350]. Etching of Ag wires is very common for STM-TERS tip fabrication[351], although this method has been used for some AFM-TERS setups, particularly those that use shear-force feedback instead of tapping-mode AFM[352]. With the etching approach, as no distinct nanoparticle is present, the radius of curvature of the end of the tip is often used to approximate the size of the plasmon particle.

Other approaches for TERS tip fabrication include photochemical nanoparticle growth localized to the tip using a nanoparticle-seed precursor solution in-situ[353], the fabrication of solid silver cantilevers to avoid loss of enhancement due to wear of the silver films[354], and focused-ion-beam milling of grooves into a metallic wire to engineer specific tip-plasmon resonances[355, 356]. Recently nanoparticle attachment methods using dielectrophoresis have also been explored by several groups [357–359].

For samples with thickness on the order of 10 nm such as lipid bilayers and proteins, a gold or silver substrate can also be used to take advantage of the gap-mode effect, which provides a higher localized field intensity for TERS enhancement (analogous to the improved hot-spots at nanoparticle junctions in SERS). This can be in the form of a metallic film[360, 361], or ultraflat nanoplates grown in solution for bottom-illumination TERS where optically transparent substrates are required[362].

4.6.2. Applications

TERS typically samples volumes of the order of 1000 nm^3 thus most biological applications are targeted at separate macromolecular structures such as proteins, lipids and nucleic acids. For larger structures such as cells, only the first 10-20 nm of the surface (lipids and surface proteins) can be measured due to the evanescent decay of the near-field.

Imaging with TERS has been demonstrated with high reproducibility on semiconductor/carbon nanostructures using gold tips (particularly in vacuum), but is rarely seen in TERS experiments of biological materials in ambient conditions. This is likely to be due to several factors, such as the degradation of silver tips, the complexity and possibility for contamination and fluctuation in biological systems producing spurious signals, and the inherently weaker Raman signal of biomolecules. Despite the daunting appearance of this task, significant progress has been made in the past decade.

For single-point TERS measurements, the difference between spectra acquired with the tip approached and retracted is used as confirmation of nanoscale Raman enhancement. The first biological example of this was by Domke et al., who used STM-TERS to
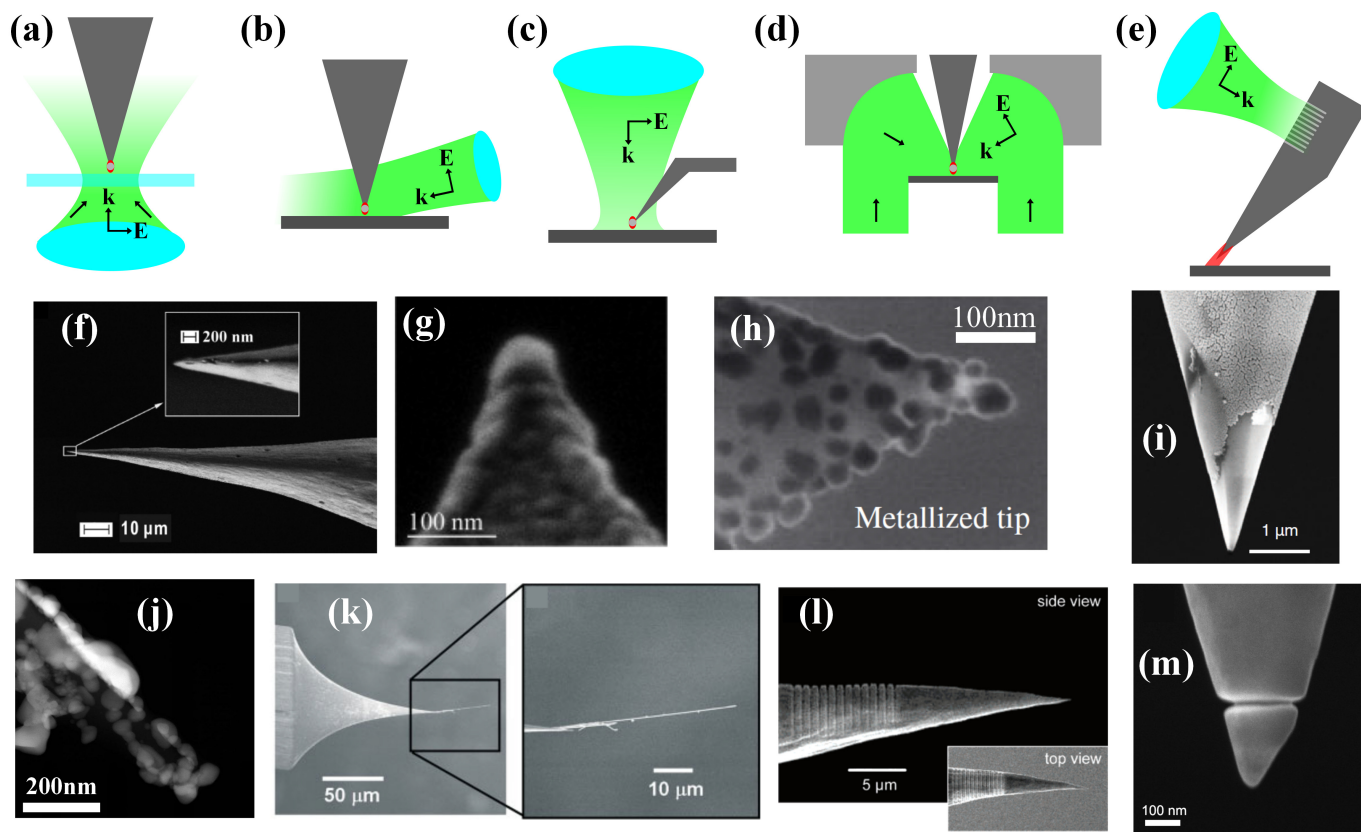
Fig. 28. Examples of TERS optical setup (a-e) and probes (f-m).
(a) Bottom-illumination requiring high-NA objectives and transparent substrate,
(b) side-illumination,
(c) top-illumination with angled AFM tips,
(d) parabolic mirror TERS,
(e) plasmonic grating for near-field-only excitation.
Electron microscope images of (f) electrochemically etched silver wire tips (modified from Zhang *et al.*[351]),
(g) typical TERS probe fabricated by deposition of a thin Ag film[352] (Reprinted (adapted) with permission. Copyright 2009 American Chemical Society.),
(h) oxidized silicon tip with silver deposited as in (g) (modified from Hayazawa *et al.*[349]),
(i) solid Ag TERS cantilever (after TERS experiment, modified from Rodriguez *et al.*[354]),
(j) photochemically grown Ag TERS tips prepared in-situ (modified from Sinjab *et al.*[353]),
(k) Ag nanowire attached via dielectrophoresis[357],
(l) plasmonic grating TERS tip (Ag)[355] (Reprinted (adapted) with permission. Copyright 2007 American Chemical Society.),
(m) tunable Au TERS tip prepared by focused-ion-beam milling[356] (Reprinted (adapted) with permission. Copyright 2008 American Chemical Society.).

study adsorbed DNA nucleobases[363]. Line-profile spectra are also commonly used to indicate the nanoscale spatial variation of chemical constituents. One of the first biological demonstrations of this type of TERS measurement was on a single RNA strand measured using AFM-TERS in ambient conditions[364]. Here it was suggested the spatial evolution of the spectra along the strand could be used as a direct indicator of the base-pair sequence (see Figure 29(a)) and was later also demonstrated for DNA strands[365].

Amyloid protein fibrils were also later measured in a similar manner, with certain amino acids residues with strong unique Raman components being shown to vary across a fibril[366]. These measurements also suggested a change across the fibril of the secondary structure from α-helix to β-sheet regions. Similar measurements were also done on insulin fibrils, with TERS able to distinguish variations in α-helix to β-sheet regions as before, but was also able to distinguish between flat, twisted and proto-filaments[367]. TERS measurements have also been demonstrated on model peptide fibrils which form ordered crystal structures, showing spectral variations across the fibril [353].

TERS imaging in 2D has not been demonstrated very often on biological samples, due to the increased acquisition times involved increasing the likelihood of tip degradation or sample change. Opilik *et al.* demonstrated imaging of two-phase lipid domains with STM-TERS (Figure 29 (b))[368]. Kazemi-Zanjani *et al.* were able to image phosphoprotein osteopontin on calcium oxalate monohydrate crystal facets (relevant to the breakup of kidney stones), with sufficient resolution to observe preferential adherence to the edge facets of the crystal[369].

Early measurements of cells with TERS focused on smaller cells such as bacteria and viruses. Neugebauer *et al.* measured TERS spectra from *Staphylococcus epidermidis*[370, 371], while Cialla *et al.* measured TERS spectra from tobacco mosaic viruses[372]. Other bacteria-derived samples, such as isolated membrane patches from *Halobacterium salinarum* have also been measured with TERS, with different patches able to be distinguished[373]. Wood *et al.* demonstrated measurement of hemozoin crystals in sectioned erythrocytes which had been infected with malaria parasites[374], and were also able to identify nano-oxidation sites with TERS[375].
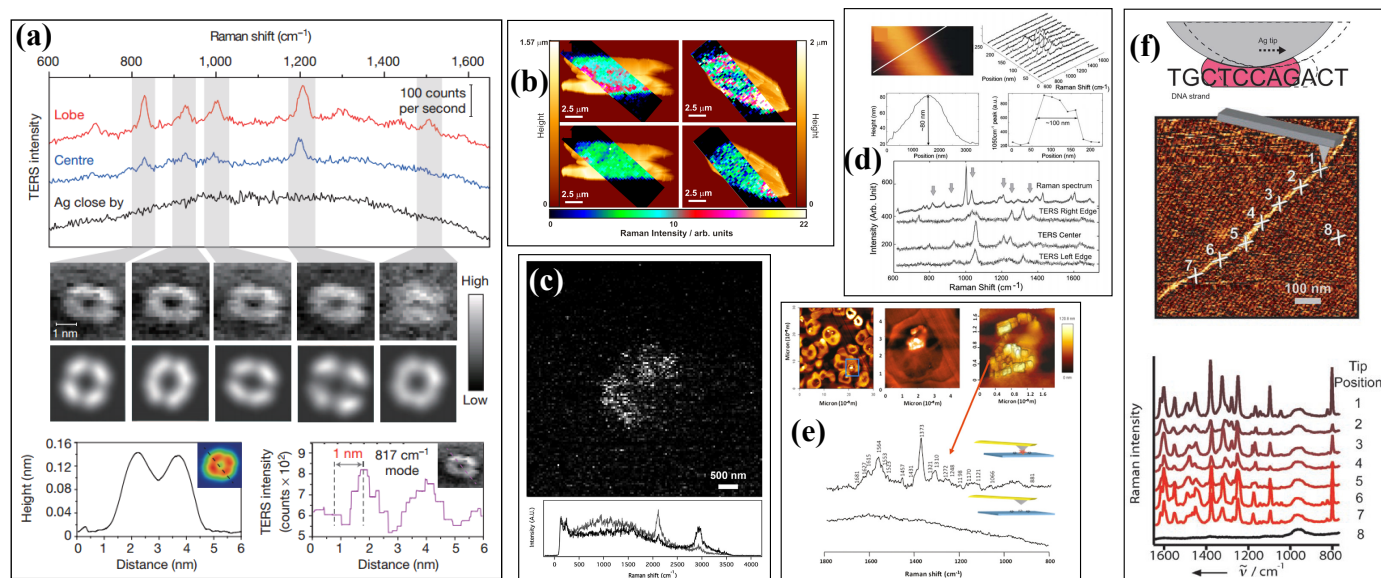
Fig. 29. Examples TERS applications.
(a) Single porphyrin molecule resolution TERS as demonstrated by Zhang *et al.*(modified from Zhang *et al.*[348]).
(b) TERS images of 1464 cm^{-1} band of osteopontin protein showing localization to the edge facets of a calcium oxalate monohydrate crystal[369] (Reprinted (adapted) with permission. Copyright 2012 American Chemical Society.).
(c) TERS image of a two-phase lipid domain, with spectra corresponding to dark and light regions of the image (modified from Opilik *et al.*[368]).
(d) TERS measurement of a model peptide nanofibril showing spectral variations across the diameter (modified from Sinjab *et al.*[353]).
(e) TERS of a hemozoin crystal in a section red blood cell infected with a malaria parasite with AFM topographs indicating the localization of the measurement[374] (Reprinted (adapted) with permission. Copyright 2011 American Chemical Society.).
(f) Illustration of RNA base-pair measurement, with TERS spectra and corresponding locations from an AFM topograph (modified from Balio and Deckert[364]).

Other biologically relevant samples measured by TERS include alginates in biofilms[376] and self-assembled peptide nanotubes[353]. TERS has also been attempted in liquids, which would be very beneficial for measuring biological systems in more realistic environments[377]. TERS in liquid may actually solve some problems such as providing a heat-sink for tip-induced sample heating. However, AFM measurements in liquid are more complex in terms of feedback control, and may only serve to introduce further confounding factors in already difficult to interpret TERS spectra.

4.6.3. Challenges

The major challenge for TERS of biomaterials in ambient conditions has been fabrication of reproducible, stable tips. Significant progress has been made, with a wide variety of probe recipes available and methods for improving their lifetime up to several weeks[349, 350]. With these advances, it is feasible that commercial Ag-coated tips could become available in the same way gold-coated tips recently have.

Sub-nm single-molecule imaging in vacuum has initiated new debates regarding the ultimate spatial resolution achievable with TERS[348]. Zhang *et al.* suggest their resolution originates from a nonlinear process involving luminescence in a plasmonic cavity between tip and sample, but others suggest that the resolution could be due to atomically sharp probes or the steep gradient of the enhanced electric near-field[378]. Further work should continue to unravel the fundamental aspects determining the spatial resolution in order to determine the ultimate achievable limits.

TERS imaging of some biological structures in ambient conditions has been demonstrated, but is still far from being a routine measurement. Whilst further improvements in stable tip fabrication could alleviate many problems involved with imaging, some systems will be fundamentally noisy over the measurement time required for TERS measurements. Approaches based more on statistical analysis of repeated point measurements in a given sampling area could offer nanoscale information in such cases where imaging is not possible.

The spectral variations present in TERS compared with far-field Raman spectra have also been a problem, though this has been addressed to some degree with suggestions that TERS spectra should be accompanied with SERS measurements of the same analyte. This should allow many spectral changes due to localized enhancement to be distinguished, though there may potentially be some changes due to the particular orientation of the single hot-spot on the tip. One of the most well known spectral changes in TERS is the disappearance of the Amide I vibration in several proteins, with no universal explanations as to the reason for these observations[379, 380]. Some suggestions involve steric shielding effects of the protein side-chains on the amide backbone, denaturation of the protein backbone, or dependance on the particular TERS setup geometry.

Whilst TERS continues to advance, other alternative nanoscale spectroscopic imaging techniques are maturing and utilizing emerging technologies. Nanoscale infra-red in particular has been shown to be much more reproducible for imaging, and has recently been made commercially available as a bench top instrument for routine measurements due to advances in high power tunable light sources such as quantum cascade lasers. Several biological applications have been demonstrated recently, with more reproducible spectra which are concordant with FTIR absorption measurements and no spurious features[381]. Whilst commercial TERS systems are available, they typically only demonstrate TERS for simpler nanomaterials using gold TERS tips. With such strong alternative nanoscale chemical imaging modalities emerging, TERS must continue to iron out the reproducibility and spurious signal problems to become a trusted, routine analytic technique. The emergence of these alternative techniques could also be positive for validating findings of TERS measurements, as the field has suffered from a lack of suitably similar techniques to confirm experimental findings.

4.7. Raman Spectroscopy in Turbid Media

4.7.1. Typical System

Various infrared spectroscopic depth profiling techniques exist, but they are usually limited to the range of 1 to 500 microns[382–387]. Initial attempts with Raman spectroscopy relied on exploiting the time-dependent exit of the Raman photons from a turbid sample, which correlated with the likely depth a photon scattered within the medium[388]. This approach could reach ≈ 1 mm into a sample, but required an expensive and complex experimental setup with high–power picosecond excitation and detection, making biomedical applications difficult.

SORS Matousek *et al.* introduced in 2005 a significantly simpler approach using CW excitation which involves laterally offset detection relative to the laser excitation position[389]. This spatially-offset Raman spectroscopy (SORS) is based on the multiple diffuse scattering of light in turbid media. Photons traveling through such materials can be classified in three categories: ballistic, snake, and diffuse, as represented in Figure 30(a). The photons entering the material will initially be composed of ballistic photons, which exponentially decay into snake and then diffuse photons further into the sample. In tissue the ballistic/snake components deplete after several mm, wheras the diffuse component can reach several cm. For conventional imaging systems based on ray optics traceability, diffuse photons are not useable. However for Raman spectroscopy they can be thought of as a non-imaging source for Raman excitation deeper in the sample. The deeper a Raman photon is generated, the broader the distribution of positions from which it exits the sample will be in the backwards direction. This then means that if escaping photons are collected further from the excitation position, the greater the ratio of Raman photons from deeper in the sample to those originating from the surface layer. Measurement of these ratios for Raman photons corresponding to different layers is the fundamental concept behind SORS (see Figure 30(b)).

SORS was shown both experimentally [389] and theoretically (using Monte-Carlo photon scattering simulations[390]) that the ratio of prominent peaks from a surface layer to an embedded layer follow a roughly logarithmic relationship such that $I_{embedded}/I_{surface}$ increases with increased detection offset. However as offset is increased, the diffuse spread of photons means that signal strength also decreases, limiting the possible sample–depths accessible.

Raman scattering signals were able to be detected from subsurface layers embedded at depths an order of magnitude larger than previously demonstrated (several millimeters to centimeters). Initial demonstrations involved separate lenses used to excite a multi-layered sample at one position, and a different lens to measure at one offset position which could be varied[389]. While this approach demonstrates the concept of SORS well, it is inefficient in terms of photon collection. Following this, a popular approach to SORS was to use an annular collection scheme, whereby one fixed offset could be collected from all points in the circle around the excitation point with the radius being the desired offset. This is usually implemented by using ring-fibers with a fixed value of offset chosen for a particular application[391, 392], though other approaches such as line-based SORS[393] or using a digital micro-mirror device

(DMD) placed at a sample-conjugate plane[394] have been developed recently. The DMD allows flexible selection of the offset Δs while providing high efficiency in light collection. Inverse ring-collection SORS is another possibility, whereby the excitation beam has an annular profile at the sample, and the detection is performed at the center of this ring[395]. The offset Δs can then be varied using a conical lens (axicon). The use of a dielectric bandpass filter at the surface can also improve the SORS signal by preventing excitation photons from escaping, whilst allowing the (spectrally shifted) Raman photons to exit.

Microscope-based SORS (μSORS) has also recently emerged as an application of the SORS concept at smaller length scales[396], for measuring thin multi-layered samples such as painted layers and plant seeds[397]. Experimentally, this was carried out in a slightly different manner to standard SORS, by defocusing the objective to collect light exiting the sample from larger offset positions. However this is not exactly concordant with conventional SORS, as it involves collection of a full circular region of the sample, not the annulus from a single offset value. Recent work has presented alternatives to this in line with conventional SORS by using an additional offset objective[398]. More simply, a DMD can be used to select the annulus region as mentioned earlier[394]. The latter approach is especially flexible due to the software-control of offset, and compatibility with microscopes using only a single objective lens, with the maximum offset determined by the field-of-view of the objective being used.

SORS can also be combined with SERS, resulting in surface-enhanced SORS (SESORS) [399]. Whilst this sacrifices non-invasiveness, due to the inclusion of surface-enhancing nanoparticles inside the sample, it can amplify the SORS signal considerably, potentially improving the maximum attainable depths.

Transmission Raman Spectroscopy   Another technique related to SORS that takes advantage of diffuse photon transport is transmission Raman spectroscopy (TRS), whereby the photons exiting the sample in the forward direction are measured instead of those at a laterally offset position[400]. This sacrifices multi-layer sensitivity for complete volumetric measurement of the sample. Raman–based tomography has also been demonstrated using slightly different approaches, which share a common feature of using multiple fibers for excitation/detection surrounding the volume of the sample[401, 402].

4.7.2. Applications

Initial examples of SORS were performed on simple diffusely scattering powders with reasonably large Raman scattering (such as PMMA and trans-Stilbene in Matousek *et al.*[389]), but quickly moved towards a variety of applications in food[403], pharmaceutical[404], security[405] and biomedical areas[406]. The first biomedical application demonstrated was the measurement of bone through several millimeters of tissue[391]. This is possible as hydroxyapatite (HA) is a major mineral component of bone, and contains a strong Raman peak at 962 cm^{-1} due to a phosphate mode which is used as a sub-layer indicator, whilst collagen peaks are typically used to identify the surface layer. These measurements were initially carried out on animals and cadavers[391], but have since progressed to preliminary trials for in-vivo measurements of bone-disease monitoring for fracture risk prediction[407].

Another SORS study of bone involved the detection of heterotopic ossification, which is an abnormal bone formation often seen in burn victims. The Raman measurements were able to detect the presence of heterotopic ossification in mouse models much earlier (5 days post surgery) than microCT (three weeks post surgery). SORS has also been combined with other complementary techniques such as optical coherence tomography for in-vivo bone measurement[408]. One recent development in SORS include non-invasive micro-SORS monitoring of blood donations stored in sterile plastic (PVC) blood-bags[409]. The feasibility of using the DMD-based SORS approach to non-destructively measure mineralization of bone tissue engineering scaffolds has also been reported[410]. The results showed the ability to measure SORS spectra of HA embedded within two different artificial bioengineered scaffold structures and chicken skin. This information is not accessible by other microscopy or spectroscopy techniques, and is promising for *in vivo* measurement of artificial bone.

Another application is the non-invasive detection of breast calcifications, which can be composed of different deposits, typically calcium oxalate dihydrate and calcium hydroxyapatite. Using TRS it was possible to measure the phosphate peak of 0.125% calcium HA embedded in a phantom composed of 20mm thick porcine tissue. Furthermore, tissue, calcium HA and calcium oxalate dihydrate contributions to spectra were able to be separated with PCA[400].

Increasing interest in SESORS is developing as it offers improved SNR and larger attainable depths through multiple tissue/bone layers. So far applications for brain measurements through the skull have been proposed (see Figure 31)[411], as well as blood glucose monitoring[412] and Stokes/anti-Stokes temperature sensing of tissue[413, 414].

4.7.3. Challenges

SORS has progressed remarkably quickly over the past decade, with measurements being taken from increasingly greater depths (up to several cm) and with improved signal-to-noise. For biomedical purposes, the safe maximum laser power for tissue is already easily achievable, imposing a limit on the maximum achievable depth of diffuse photons for SORS to the order of several cm. Whilst SESORS has demonstrated enhancement in the SORS signal, in principle making measurements through the skull possible[411], the requirement for plasmonic nanoparticles raises the barrier towards clinical applications in the near future. The only conceivable way to attain larger measurement depths would be with an invasive needle fiber probe. For these reasons, it is likely that effort will be focused on optimizing photon collection and post-processing of the weaker signals at larger offsets. Such advances should also benefit biomedical applications of TRS and micro-SORS. Separation of the layers by library-based modeling could also be promising for extracting more specific information such as mineral to matrix ratios in bone/tissue layers[415].

4.8. Fiber Optic Probes

One of the key advantages of Raman spectroscopy is the ability to measure molecular vibrational spectra using visible or near-infrared light. Fibers at these wavelengths are much more accessible and easier to work with compared to fibers for infrared wavelengths.

Optical fiber probes can be hand-held or delivered through an endoscope. These systems allow more accessibility to *in vivo* tissues. They move the Raman measurements from the laboratory into the clinic.
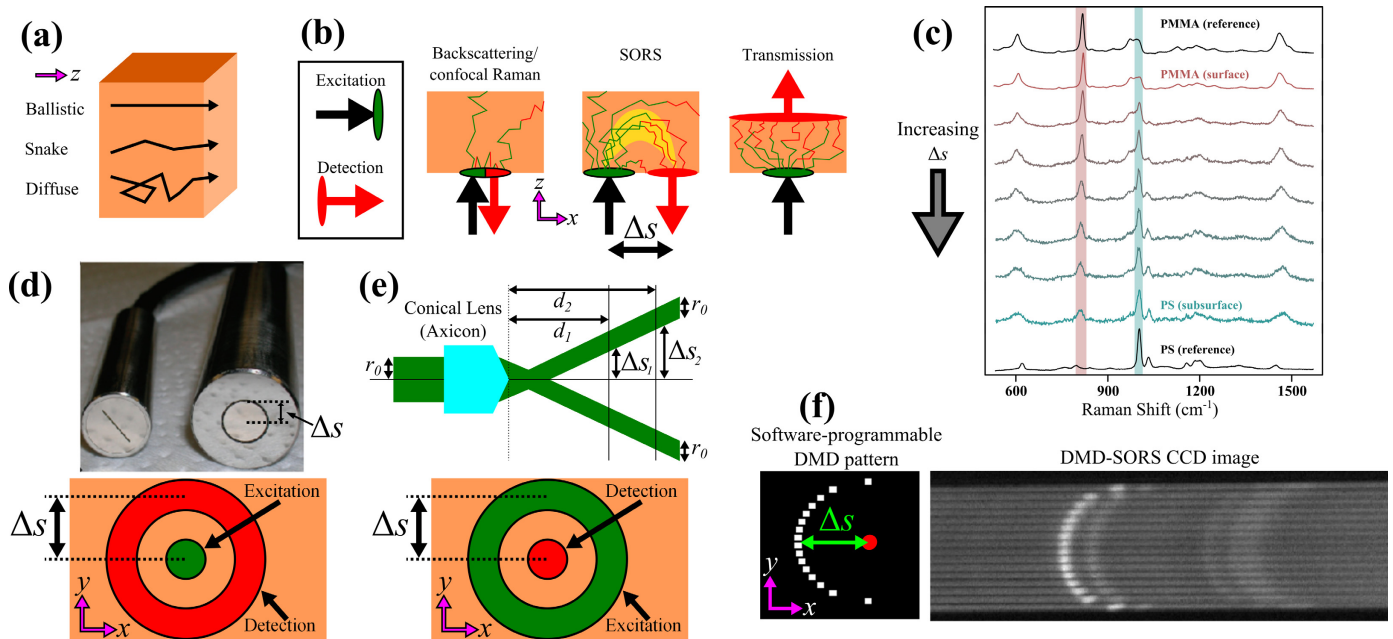
Fig. 30. Principles of SORS.
(a) Diagram showing the concept of ballistic, snake–like, and diffuse photon transport in a turbid medium such as tissue.
(b) Comparison of excitation/detection configurations in Raman spectroscopy, including conventional backscattering, SORS, and transmission Raman.
(c) An example of SORS spectra for a simple two-layer system composed of PMMA and polystyrene. The strongest peak from each material is highlighted to show how their ratio changes.
(d) Photograph of a SORS fiber probe (adapted with permission from Yuen *et al.*[412]. Copyright 2010 American Chemical Society), showing the point excitation and ring collection geometry at one end, converted to a linear fiber exit pattern for spectrometer slit compatibility at the other end.
(e) Inverse-SORS concept utilizing ring-illumination with an axicon (conical lens), the radius (and thus offset) of which can be varied by changing lens-sample distance.
(f) Example of SORS using a DMD device in a sample-conjugate imaging plane, which can be programmed with a binary offset pattern to produce SORS, with an example of a spectrometer CCD image for this setup[394].
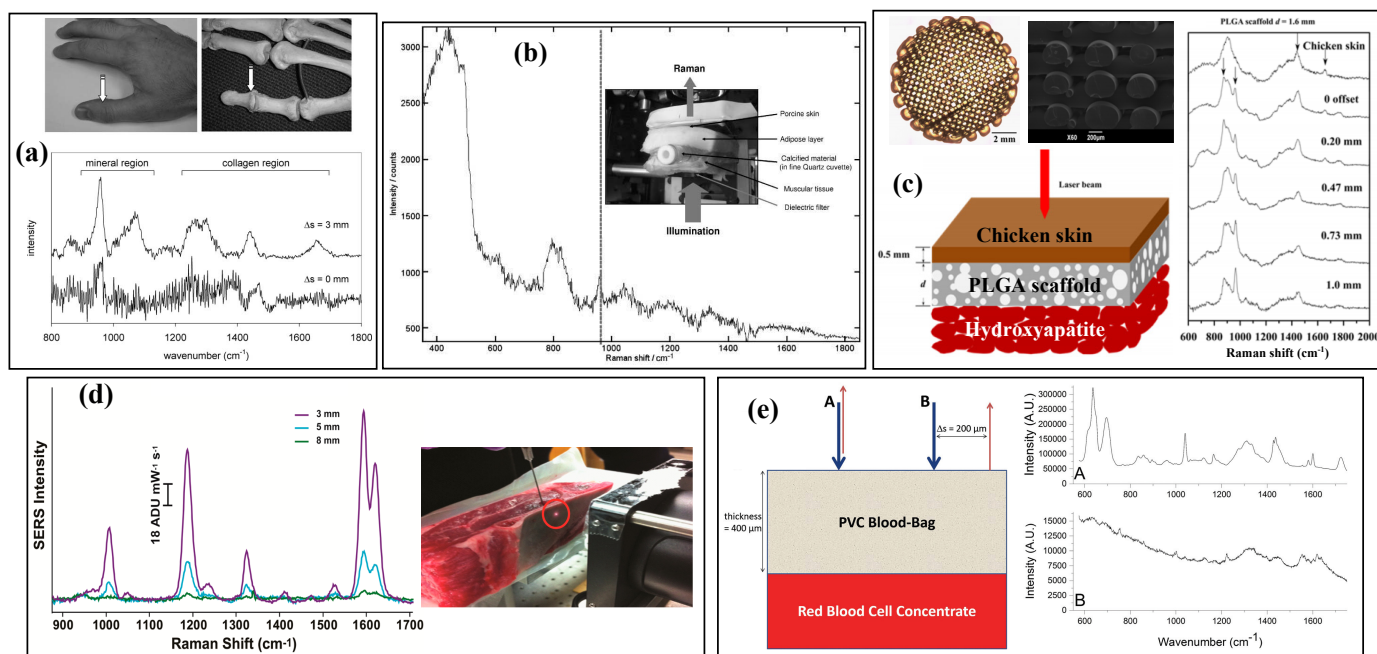
Fig. 31. Examples of SORS and TRS applications in the life sciences.

(a) First SORS bone measurements showing spectral features due to collagen and bone for different offsets (modified from Matousek *et al.*[391]).

(b) TRS spectra of 0.125% of HA (highlighted peak) embedded in a 20 mm thick breast phantom (inset shows photograph of phantom). A dielectric filter was used to prevent excitation photons escaping in the backwards direction (modified from Stone *et al.*[400]).

(c) DMD-implemented micro-SORS of a tissue engineering model implant consisting of HA underneath a PLGA scaffold and chicken skin, with light and electron microscopy images of the scaffold structure[410] (Reprinted (adapted) with permission. Copyright 2008 American Chemical Society.).

(d) SESORS measurement through a skull phantom consisting of an ovine shoulder bone with attached tissue using SERS nanoparticles tagged with a trans-1,2-bis(4-pyridyl)-ethylene (BPE) reporter molecule[411] (Reprinted (adapted) with permission. Copyright 2013 American Chemical Society.).

(e) non-invasive micro-SORS of blood donations stored in PVC bags (modified from Buckley *et al.*[409]).

4.8.1. Typical System

The basic design of a Raman fiber probe is similar to a standard Raman spectroscopy system. The sample is illuminated by a laser and Raman scattered light is delivered to a spectrometer. The major differences are found in the way the laser excitation is delivered to the sample and how the Raman scattered light is collected. Excitation and collection light travels through optical fibers (see Figure 32(a)) typically with larger cores ($\approx 100 - 200$ μm) to maximize optical throughput.

The delivery and collection fibers are usually, but not always, made of glass. The high intensity laser light propagating through glass generates Raman and fluorescent signals not associated with the sample. These signals must be removed before light reaches the sample to avoid compromising the signal from the sample. Additionally, any light scattered at the laser wavelength must be removed before entering the collection fiber to avoid similar contaminating signalS. These strict requirements on filters for the excitation and collection fibers necessitates using separate fibers for each. This issue will be discussed further below.

4.8.2. Applications

Several versions of the basic Raman probe have been created to improve performance. Mo *et al.* used computer simulations to create an optimized probe based on a ball lens (see Figure 32(b)). This lens allowed their probe to be depth selective[416] and thus improve tissue diagnosis. Agenant *et al.* developed a probe that rejected light from deep tissue. Measurements from this superficial probe benefited from improved signal-to-noise ratio[417]. Wang *et al.* improved their signal-to-noise ratio by creating a confocal system[418]. The fibers were beveled prior to focusing by a ball lens to improve focusing efficiency.

Several groups have used arrays of optical fibers to increase the speed of Raman hyperspectral imaging[158, 419, 420]. In this technique, the scattered light is imaged onto a fiber bundle. The fibers are reoriented into a line at the entrance slit of the spectrometer. At this point, each fiber in the line contains light at all wavelengths from a "pixel" in the image of the sample. The spectrometer disperses this line of fibers into a stack of spectra. Each spectrum in the stack corresponds to a point in the sample plane. This can be remapped in software. This technique acquires several Raman spectra in parallel, greatly reducing the time required relative to point-scanning.

Other Raman probes have diverged from the usual shape to specialize for specific tasks. Day *et al.* developed a probe small enough to fit inside a hypodermic needle (see Figure 32(c))[421]. This probe is able to deliver and collect light beneath the surface of skin. Pudney *et al.* developed a much larger probe designed for easier handling while measuring more accessible tissues (such as scalp, mouth, and skin) *in vivo*[422].

Fiber probes have also been used with spatially-offset Raman spectroscopy (SORS, see Section 4.7). Wang *et al.* built a SORS fiber probe using a mechanical iris to vary to measurement depth[423]. Maher *et al.* used Monte Carlo simulations to determine the optimal fiber separation to balance measurement depth with signal-to-noise ratio in transcutaneous Raman measurements of bone[392]. A similarly optimized SORS probe was developed by Keller *et al.* to evaluate breast tumour margins[424]. Stone *et al.* used a SORS probe to identify calcifications inside breast tissue[425].

Fiber probes have been used to bring Raman spectroscopy to many parts of the body. Bergholt *et al.* used a Raman fiber probe to study various locations within the oral cavity[426]. Short *et al.* studied the gastrointestinal tract with Raman spectra in the high wavenumber region[427]. Richards-Kortum and her group developed a Raman probe to investigate cervical cancer[428, 429]. Horsnell *et al.* measured lymph node metastases using a hand-held Raman probe[430]. Huang *et al.* used their Raman probe to study the entire body of a mouse[431]. Recently, Desroches *et al.* applied their Raman probe during surgery to identify tumor in the brain[432].

4.8.3. Challenges

Eliminating the strong background signal produced by Raman and fluorescence emission by the optical fibers is one of the main challenges for Raman fiber probes. While this problem can be lessened with filters on the ends of the delivery and collection fibers, this is not a complete solution. Imperfect filters still allow some light through. Due to the weak signals in Raman spectroscopy, even this small amount can negatively affect measurements. Additionally, these filters may often come in contact with patient tissue and become biologically contaminated.

Several researchers have explored methods to improve the delivery and collection methods for Raman fiber probes. The group led by Jürgen Popp has made these filters more effective and more convenient by inscribing Bragg gratings directly into the delivery and collection fibers (see Figure 32(d))[433]. As Bragg gratings are more effective in single mode fibers, this probe collected Raman scattered light by a bundle of multicore single-mode fibers. The multiple cores improved collection efficiency.

The Rottwitt group transmitted 1064 nm light and generated 532 nm light within the delivery fiber by second harmonic generation. The 532 nm Raman excitation light has traveled through only a portion of the fiber and thereby generated less contaminating signal[434]. The Morris group avoided the glass problem by using a fluorocarbon probe. This avoids any of the silica-associated artifacts[435].

The Puppels group was able to avoid glass fluorescence in their fiber probes by concentrating on the high wavenumber region at 2400-3200 cm^{-1}. This avoids the glass signal existing primarily in the fingerprint region (600-1800 cm^{-1})[124]. They found that the Raman signal from the high wavenumber region contained similar information and could create similar hyperspectral images to those from specta in the fingerprint region[436]. They used this high wavenumber Raman probe to classify different types of brain tissue[129] and distinguish between basal cell carcinoma and other skin conditions[131].

Wang *et al.* addressed several issues associated with bringing Raman probes into the clinic. They create a disposable sheath to cover their probe. This overcomes issues of contamination and probe degradation through contact with patient tissues[437].

Another difficulty when using Raman probes is identifying the measurement location. Bergholt *et al.* have shown that the measurement location can have a large effect on the acquired Raman signal[426]. Because Raman spectroscopy is fundamentally a point-based measurement technique, additional information is required to ensure that data is acquired from the correct location. This leads to

(a)

(b)

(c)

(d)
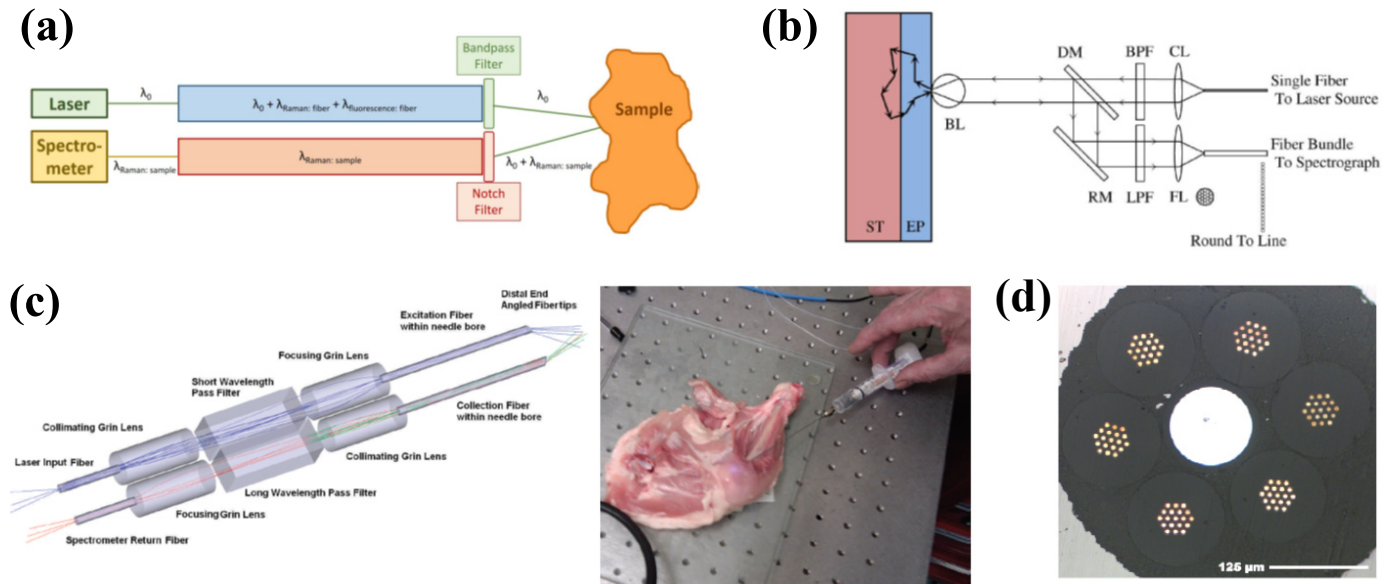
Fig. 32. (a) Simplified diagram of a Raman fiber probe.
(b) Schematic of a depth-selective Raman probe by Mo *et al.* using a ball lens[416].
(c) Raman probe inside a hypodermic needle by Day *et al.*[421].
(d) Fiber bundle for Raman spectroscopy created by the group led by Jürgen Popp[433]. Excitation light is delivered by the multi-mode fiber in the center. Raman scattered light is collected by the surrounding bundle of multicore single-mode fibers. Excitation and collection fibers are inscribed with Bragg grating filters during the drawing process.

combinations of Raman spectroscopy with other endoscopic imaging techniques such as narrow-band imaging[438] and white-light reflectance[439].

Finally, the variable nature of *in vivo* measurements can negatively affect Raman probes. Schleusener *et al.* studied the effects of many experimental factors including ambient light and probe pressure[440]. These can be difficult to control and have the potential to confound sensitive Raman measurements.

4.9. Selective Scanning Raman Spectroscopy

Hyperspectral Raman imaging based on raster scanning is a powerful tool for classification and provides the ultimate spatial resolution if appropriate sampling frequency is used. Yet, the low signal level makes raster scanning slow in practice (see Section 4.1). In many applications, samples have a high level of spatial correlation, in which case raster scanned images may include a redundant information. However, the spatial features of the sample are unknown prior to analysis. One strategy for reducing the acquisition times of Raman hyperspectral imaging is to use information related to the spatial properties of the sample to guide where Raman spectra should be acquired. This selective sampling reduces the number of spectra required and can greatly reduce the overall acquisition time from hours to minutes.

4.9.1. Typical System

Selective sampling Raman spectroscopy (SSRS) can be performed either with computational models (spatial properties are estimated in real time during Raman measurements) or from an alternative imaging modality (prior to Raman measurements). In both cases, a standard Raman spectroscopy system is used (see Section 4.1). Other instrumental details will vary if another imaging modality is used. SSRS instruments can be microscope- or probe-based.

Real-time computational methods   The goal of SSRS is to reduce the number of Raman measurements required to accurately create a hyperspectral image. This could be achieved by reducing the resolution of a raster scan, but this risks missing small spatial features. Rowlands *et al.* developed a computational technique to minimally sample a field of view while still sufficiently resolving small features[441]. This selective scanning technique is based on an iterative process of measurement and image analysis (interpolation). After sparse sampling, subsequent Raman spectra are acquired from locations with large differences between the predictions of two interpolative models (spline and Kriging). For interpolation, each spectrum is characterized by a single value (*e.g.*, principal component score (see Section 5)). An example of this process is shown in Figure 33. The results show that in regions with fewer spatial features, the difference between the two interpolants were small, leading to fewer sampling points. On the other hand, in regions with higher spatial variation, more sampling points were required to reconcile the two interpolants. Thus, the algorithm increases the sampling point density only in regions where it is needed while drastically reducing the overall acquisition time.

Multimodal imaging methods   SSRS can also use a fast, wide-area technique to image the sample prior to Raman measurements. In the example shown below, this is the confocal auto-fluorescence images in Figure 34. Such images can be acquired quickly (< 1 minute), but do not offer the same diagnostic accuracy as Raman spectroscopy.
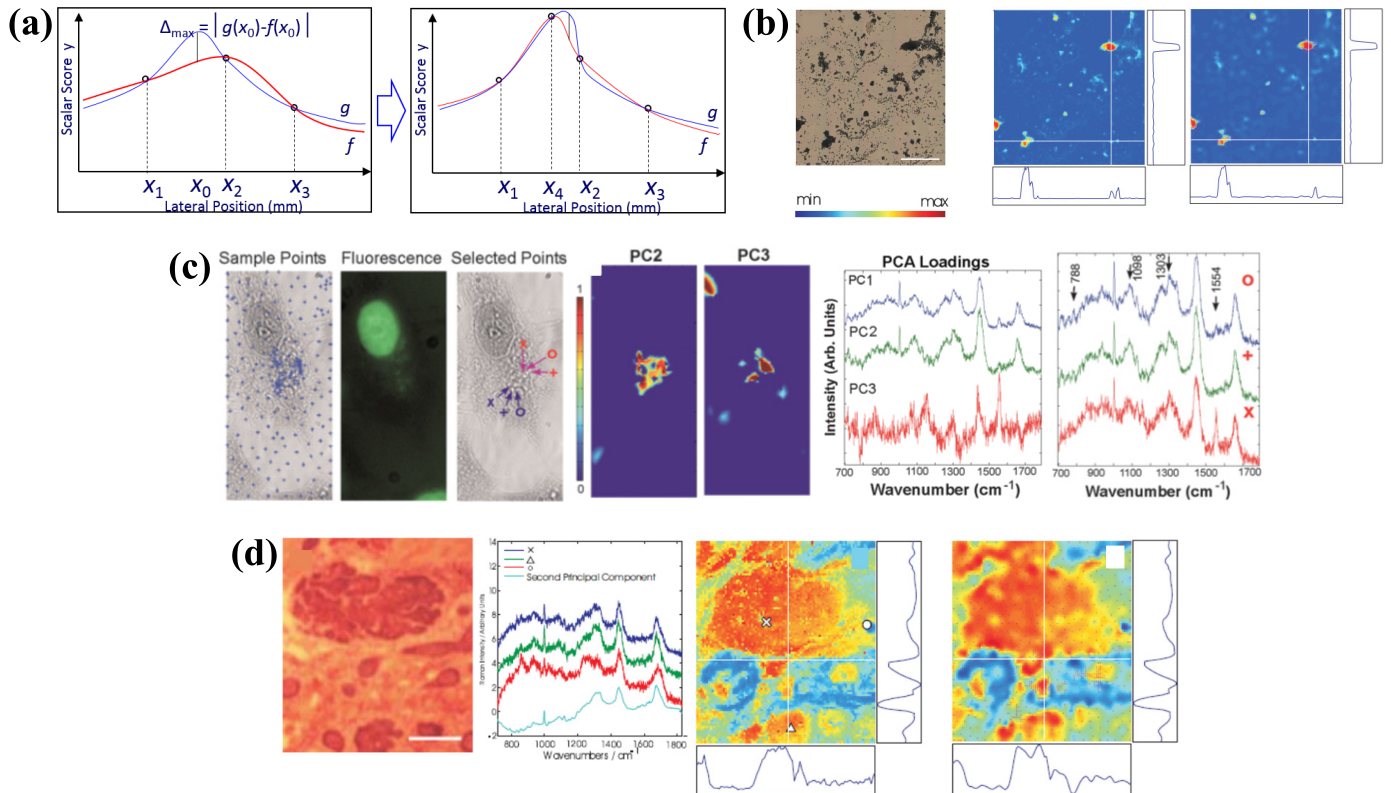
Fig. 33. Example of computation-based selective Raman scanning.

(a) Method of selecting sample points by interpolation comparison. Line f is a spline interpolation (maximizes smoothness) and line g is a Kriging interpolation (minimizes predictive error). The next sampling point chosen is the location of the largest difference between this interpolative models (x_0). This process is repeated until a threshold is reached (*e.g.*, time limit, sufficient resolution).

(b) Images of polystyrene microspheres[441]. A: Bright field microscope image (scale bar is 100 μm), B: Raman raster scan, C: SSRS image requiring approximately 20$\times$ fewer measurements than the full raster scan.

(c) Measurements of parasites infecting human endothelial cells[442]. Interpolative models for sampling locations were based on the ratio of lipid to protein Raman bands correlating with the presence of a parasite. This image was acquired in about 4 minutes, whereas a full raster scan would have required 50 minutes.

(d) Measurements of human skin tissue[441]. A: Hematoxylin and eosin (H&E) image (scale bar is 200 μm). The darker region corresponds to basal cell carcinoma. B: Raman spectra from marked loactions as well as the second principal component score (used to guide sampling and create images C and D). C: Raster scan image (9216 total spectra). D: SSRS image (750 total spectra).

Second, the fast image is analyzed to select areas to be investigated by Raman spectroscopy. For the example shown, regions with tumor tend to have less fluorescence at the detected wavelength and appear darker in the auto-fluorescence image. These dark areas will be preferentially sampled. In the segmented images in Figure 34, the black dots show sampling points that were chosen based on analysis of the auto-fluorescence image.

The overall technique saves time by only acquiring Raman spectra at selected locations instead of scanning the full image area. A comparison of the selective scanning image and the full raster scanning image in Figure 34(a) shows that little information has been lost by scanning only the selected points.

4.9.2. Applications

Computation-based SSRS has been used to rapidly image parasites infecting human cells[442]. SSRS scans were acquired in approximately 4 minutes per cell with spatial resolution similar to a raster scan with 1 μm steps ($\approx$ 50 minutes on the same system). The same technique was also used to rapidly measure skin tissue[441]. Areas of tissue measuring 1 mm^2 were measured in less than 30 minutes with 10 μm equivalent resolution.

Multimodal SSRS systems have been developed using a diverse range of technologies. Typically, the accompanying technique identifies suspicious regions that are then manual probed by Raman spectroscopy. Huang and his group have used this method with their *in vivo* Raman probes. They use a combination of white light and narrowband imaging to guide the probe to suspicious regions for acquisition of Raman spectra[438, 439]. A confocal system detecting reflectance was used by Patil *et al.* to select Raman sampling points on skin surfaces[443]. Optical coherence tomography (OCT) has been another popular companion of Raman spectroscopy. OCT images are used to identify suspicious areas, sometimes deep within tissue. Ko *et al.* used this strategy to investigate dental caries[444]. Patil *et al.* used the same spectrograph and CCD to detect both OCT and Raman signals[71]. Their instrument was used to detect skin cancer[445].

More recently, the multiple modes in SSRS have been integrated to allow automated operation of the complete system. The image obtained by the initial (fast) modality is analyzed using a range of image processing algorithms to automatically assign coordinates for Raman spectroscopy measurements. The key advantage of this technique is that no user input is required to manually select sampling points, which is a key step towards clinical implementation. Although fewer Raman measurems are acquired, which reduces the acquisition time by two orders of magnitude, the spatial resolution of the SSRS images are determined by the first imaging modality. Kong *et al.* showed that it is possible to use integrated confocal auto-fluorescence imaging and Raman spectroscopy for fast detection of tumors in surgical resessions of skin[144] and breast tissue[446]. The auto-fluorescence image provided high resolution, while Raman spectroscopy provided chemical specificity for accuracy diagnosis. These measurements were acquired in less than 30 minutes, which could allow clinical intra-operative implementation of this technique.
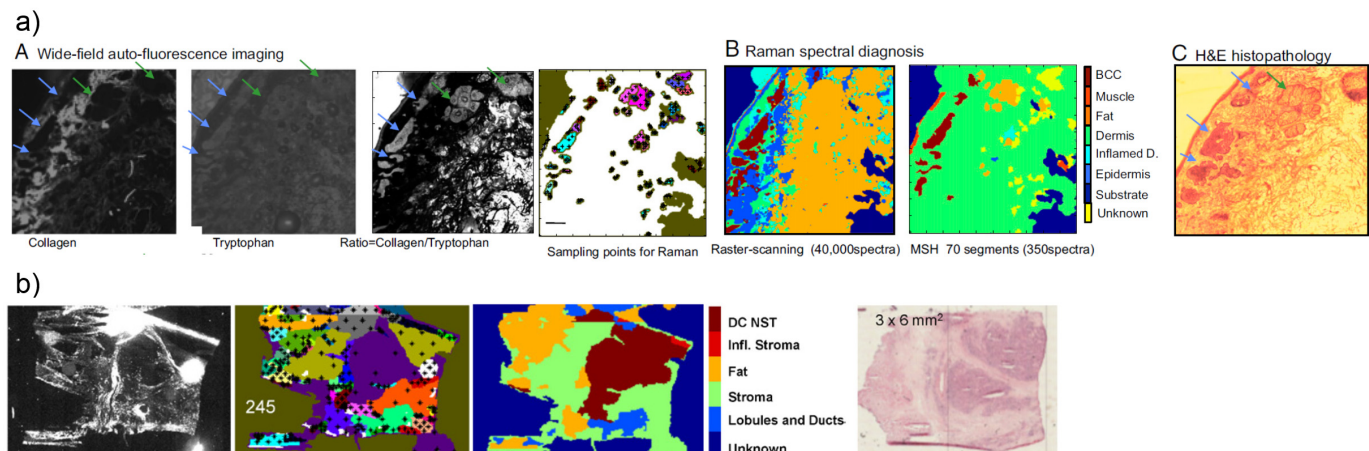
Fig. 34. Example of selective Raman scanning of (a) skin (scale bar is 0.5 mm)[144] and (b) breast tissue[446] using integrated auto-fluorescence and Raman microscopy. The series of images for each tissue type includes: auto-fluorescence image(s), segmented image with automated Raman sampling points, Raman diagnosis image(s), and an H&E image. Darker regions on H&E images correspond to tumor.

4.9.3. Challenges

While the computation-based SSRS methods provide faster acquisition time with no additional optical components, the real-time computation of interpolation surfaces from Raman spectra can be time consuming.

The challenges of multimodal SSRS depend greatly on the techniques used to pre-select the sampling locations for Raman spectroscopy. Multimodal measurements must be fast, compatible with the Raman system, and sensitive to the particular problem. Algorithms to select sampling points must be efficient and consistent across a broad range of samples (*e.g.*, different patients, disease stage, etc.)[447]. If the selection technique lacks sensitivity, then important locations will never be sampled by Raman spectroscopy. On the other hand, techniques with low specificity will require too many Raman spectra and become slow. These requirements are added to the usual need for high accuracy from Raman spectroscopy.

4.10. Raman Label-based Techniques

4.10.1. Stable isotopes

Although Raman spectroscopy is usually a non-labeling technique, there are ways to tag specific molecules for detection by their Raman signal. One of these techniques is called stable isotope labeling.

Stable isotope labeling is used in biology to track atoms through a molecular process. It has been used to study how organisms assimilate compounds they eat[448]. It has also been combined with other methods to study changes to proteins in glycoloysis[449].

In stable isotope labeling, an atom within a molecule is replaced by another stable isotope of the same element. This is done by replacing a molecule in the sample's cell growth medium or other food source. The new isotope may be either lighter or heavier than the original, but any effect on the chemcial or biological properties of the molecule will be minimal. The added or removed neutrons are inert and much smaller than other labels (*e.g.*, fluorophores, nanoparticles, etc.). This makes isotope labeling method particularly non-invasive.

In relation to Raman spectroscopy, the change in atomic mass will change the reduced mass used to calculate the vibration energy (see Equation 3). This shifts the location of the Raman band, making it possible to differentiate labeled and unlabeled molecules by their Raman spectra (see Figure 35(a)).

Through experimental design, the shifted band can often be in an otherwise empty spectral region. This isolates the signal from the labeled molecule from signals from other molecules or other forms of noise. Thus, the appearance of the shifted band uniquely marks the presence of the labeled molecule.

Applications   Huang *et al.* replaced one of the carbons (usually ^{12}C) in phenylalanine with ^{13}C, shifting the band from 1003 to 967 cm^{-1}. They detected no biological effects on the labeled microbes[450]. The same group later used ^{13}C labels on RNA to track molecules through transcription and translation[451].

Van Manen *et al.* labeled phenylalanine molecules by replacing hydrogen with deuterium. This moved the C-H vibration band from the crowded high wavenumber region at 2800-3100 cm^{-1} to the an unoccupied gap between the fingerprint and high wavenumber regions at 2100-2300 cm^{-1}[452]. This allowed the authors to quantify the uptake of amino acids into cells (see Figure 35(b)).

Matthäus *et al.* studied metabolism of lipids by macrophages. Cells were labeled with either deuterated oleic acid or deuterated palmitic acid, fixed, and imaged to study the formation of lipid droplets within the cell[453]. The isotope labels allowed the authors to image specific fatty acids in a cellular environment. Example images can be seen in Figure 35(c). Both fatty acids studied showed similar uptake patterns.
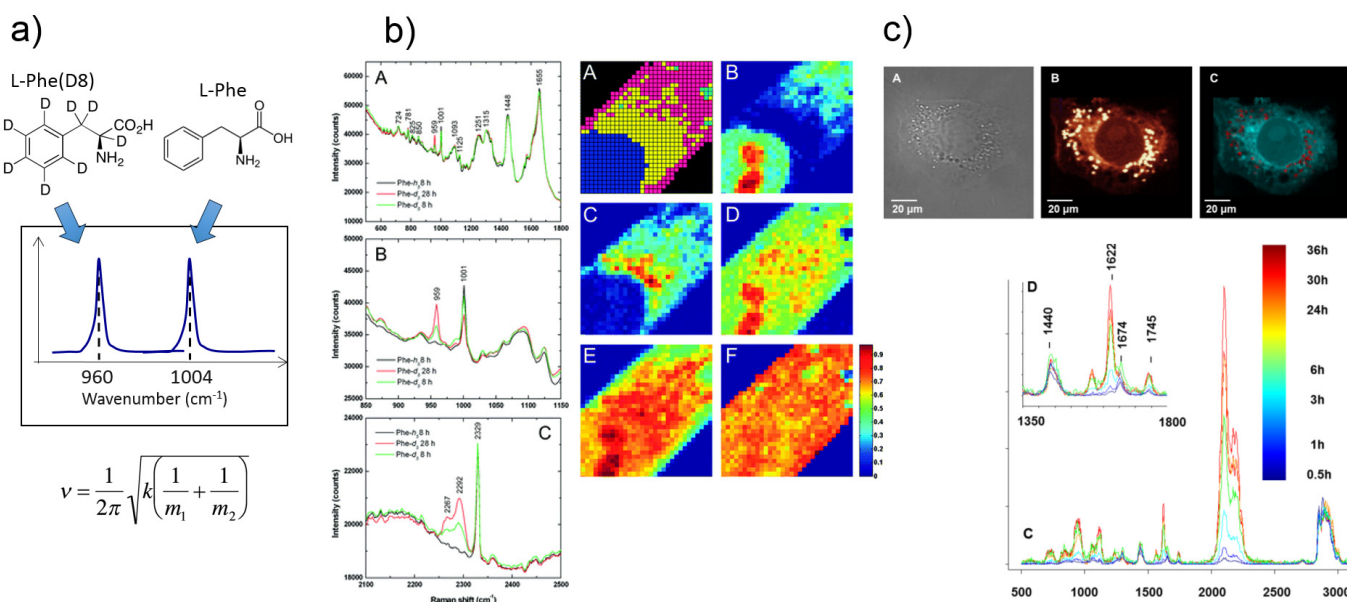
Fig. 35. (a) An example illustrating the principle of stable isotope labels. Replacing the hydrogen atoms in phenylalanine with deuterium shifts the ring breathing band from 1004 to 960 cm^{-1}. This is a result of the slightly heavier atomic mass.
(b) Spectra and band-intensity images (15 $\times$ 15 μm^2) of cells incubated with deuterium-labeled phenylalanine prior to fixation[452]. Images - A: hierarchical cluster analysis image (see Section 5), B: nucleotides (770-790 cm^{-1}), C: phospholipids (700-730 cm^{-1}), D: Phe-d_5 (950-965 cm^{-1}), E: Phe-h_5 (995-1005 cm^{-1}), F: Ratio of Phe-d_5 to Phe-h_5. Reprinted (adapted) with permission. Copyright 2008 American Chemical Society.
(c) Images of a fixed macrophage cell[453]. A: Bright field image, B: total area of CH Raman spectral bands, C: Raman image of protein (blue) and stable isotope-labeled d_{31}-palmitic acid. The accompanying Raman spectra of lipid droplets show the band locations shifting as the isotope label is allowed more time to incubate. Reprinted (adapted) with permission. Copyright 2012 American Chemical Society.

A significant advantage of stable isotope labels is the ability to label and measure live cells with negligible adverse effects.

Venkata *et al.* labeled glucose with ^{13}C and observed its uptake by live yeast cells[454]. The authors showed that the ^{13}C was incorporated into proteins (marked by the phenylalanine peak shifted from 1003 to 967 cm^{-1}) localized in lipid droplets (see Figure 36(a)).
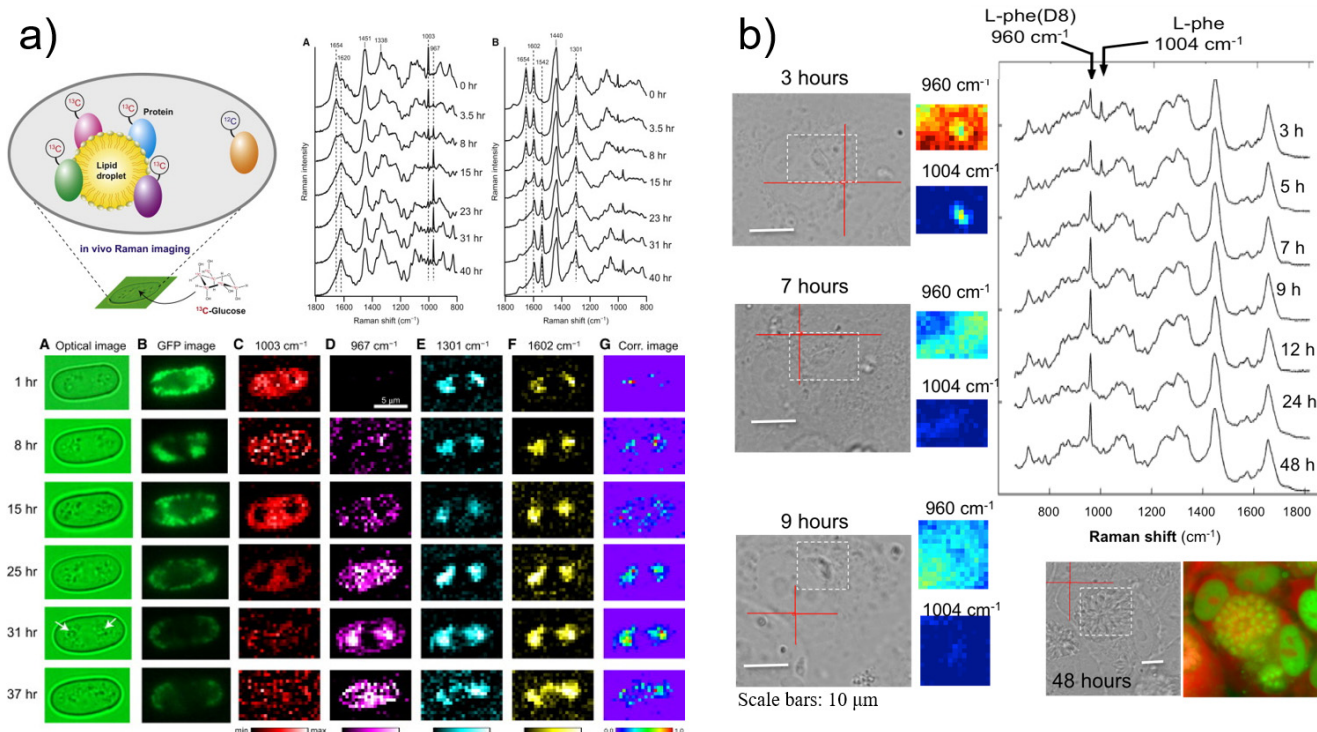
Fig. 36. Raman imaging studies of stable-isotope labeled live cells.
(a) Uptake and metabolism of ^{13}C-labeled glucose by live yeast cells by [454]. ^{13}C is incorporated into proteins in lipid droplets over 30+ hours.
(b) Interaction of *Toxoplasma gondii* parasites and host cells studied by Naemat *et al.*[145]. Host cells were incubated in media containing deuterated phenylalanine (Raman band at 960 cm^{-1}). Parasites were incubated in normal media (Phe band at 1004 cm^{-1}). This allowed the authors to quantify the uptake of protein into the parasite over time.

Stable isotope labeling has also been used with Raman spectroscopy to track molecules during interactions between live cells. For example, Naemat *et al.* studied the uptake of nutrients by parasites infecting individual human cells. In this experiment, the host cells were cultured with isotope while the parasites received normal media. In Figure 36(b), the parasite is clearly identifiable by its un-deuterated phenylalanine signal at 1004 cm^{-1}at early time points, but less so as it uptakes more deuterated protein from the host cell. This allowed Raman spectroscopy to track and quantify the movement of labeled phenylalanine from the host cells into the parasites[145].

4.10.2. Alkynes

The region in biological Raman spectra from 1800 cm^{-1} to 2800 cm^{-1} is often termed "Raman silent", due to the lack of features observed here. There are exceptions to this rule, one example being vibrations in alkyne molecules, *i.e.* those containing a carbon-carbon triple bond. This bond is not present in biological molecules and has a larger force constant with a corresponding a sharp, higher-wavenumber Raman band being associated with it in the silent region, typically from 2080-2260 cm^{-1} depending on the local environment of the triple bond[455]. Alkyne tags are minimally invasive due to their small size, as shown schematically in Figure 37(a).

Applications   Inspired by click-chemistry methods used for small-molecule fluorescence microscopy, alkynes can be conjugated with specific biomolecules which can be metabolically incorporated into live cells allowing alkyne-tag Raman imaging (ATaRI), first demonstrated by Yakamoshi *et al.* [456]. The first Raman alkyne tag was a thymidine analogue, which can be incorporated into DNA, called EdU (5-ethynyl-2'-deoxyuridine) with a Raman band at 2122–2125 cm^{-1}(see Figure 37(b)). The EdU label was incorporated into HeLa cells, allowing clear distinction of the nucleus from the rest of the cell in the Raman band images, with other images were generated from conventional cell Raman features such as lipids and proteins.
Since the demonstration of EdU, many other alkyne tags have been put forward as candidates for ATaRI. A follow up study by Yamakoshi *et al.* investigated several alkyne tag molecules, including their relative Raman intensity, as well as with other silent-region tags such as azides, nitriles and certain stable isotopes[455]. It was found that alkynes gave higher Raman scattering intensity than these alternatives, particularly when conjugated with an aromatic rings (*e.g.*, phenylalanine) or with a second carbon triple bond (known as a diyne). Using these general design strategies, several candidate molecules were trialled for ATaRI of lipids, simultaneously with EdU, allowing multi-colour ATaRI for targeting several specific biomolecules at once. The same design strategies were
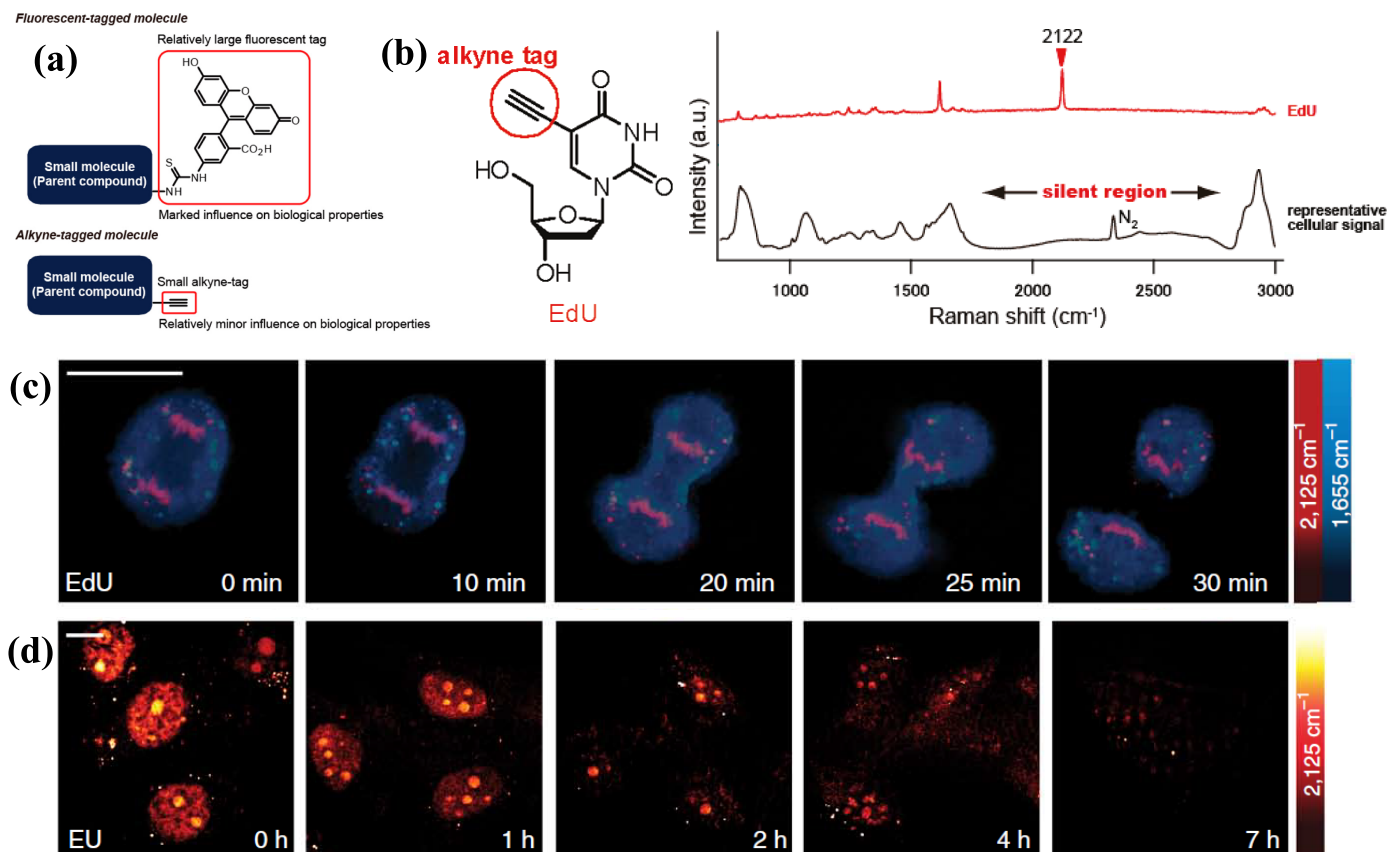
Fig. 37. Alkyne-tag Raman spectroscopy.

(a) Comparison of alkyne tag size with a typical fluorescent label[455] (Reprinted (adapted) with permission. Copyright 2012 American Chemical Society.).

(b) Molecular schematic and Raman spectrum of the EdU alkyne tag, with a typical cell Raman spectrum for comparison[456] (Reprinted (adapted) with permission. Copyright 2011 American Chemical Society.).

(c) SRS time-course imaging of DNA (EdU tag, 2125 cm^{-1}) and protein (1655 cm^{-1}) in a dividing HeLa cell.

(d) SRS microscopy of RNA (EU tag, 2125 cm^{-1}) depletion in cell nucleoli ((scale bars for (d) and (d) 10 μm), (c), (d) modified from Wei *et al.*[252]).

also used to identify an alkyne tag called bisarylbutadiyne, and was used for specific ATaRI imaging of mitochondria in live cells [457]. Other novel alkyne tags have recently been demonstrated as SERS reporters[458], for tumor hypoxia Raman labelling[459] and as a minimally invasive sphingomyelin Raman label for lipid raft measurements[460].

As alkyne tags typically exhibit single sharp band in the higher wavenumber region of the Raman silent region, they are particularly suited to nonlinear Raman microscopy which images rapidly at a single Raman shift value. This was demonstrated on live cells simultaneously by two groups in 2014[252, 461], who used SRS microscopy and an array of alkyne tags targeted at DNA, RNA, proteins, phospholipids and triglycerides in living systems. Various applications were demonstrated, such as time-course imaging of DNA in a dividing cell using EdU (Figure 37(c)), RNA depletion in nucleoli using an EU (5-ethynyl uridine) alkyne tag (Figure 37(d)), and triglyceride imaging in *C. elegans* using a 17-ODYA (17-octadecynoic acid) alkyne tag. Further work has also demonstrated SRS-based ATaRI for visualizing glucose uptake in live cells using a glucose analogue alkyne tag called 3-OPG (3-O-propargy-D-glucose)[462].

In summary, ATaRI is an emerging but very promising labeling strategy for bridging the gap between the minimal invasiveness of Raman measurements, and the labeling specificity of fluorescence microscopy. It is particularly attractive for SRS microscopy, where images of faster biological processes could be observed. With the design rules suggested by Yamakoshi *et al.*,[455] the creation of novel alkyne tags for specific ATaRI applications will be attractive for many problems across the life sciences.

4.10.3. Challenges

One of the key challenges in Raman labeling techniques is ensuring specific labeling of the molecule of interest. In the case of stable isotopes, this is routinely achieved through incorporation of labeled molecules in the culture medium with no adverse effects on cells. On the other hand, the alkyne molecules must be conjugated to small biological molecules in order to be uptaken. Both of these require substantial sample preparation and would be difficult to implement *in vivo*.

5. DATA ANALYSIS TECHNIQUES

Although Raman spectroscopy can have very high accuracy, spectral differences between various samples can be very slight. Researchers use a variety of analysis methods to extract different parameters including chemical concentration, bacterial species, or tissue type. This section will discuss the most common analysis methods, focusing on when and why each of them is most successfully applied.

5.1. General Procedure

When creating a model to analyze Raman spectra, it is important to avoid bias. Models will almost always perform better when analyzing spectra that were used when creating the model than with new spectra. The true accuracy of the model can only be tested on spectra that were unused during model creation.

This leads to a set of standard steps that are followed when creating any classification mode. The data are separated into three groups. The first group is called the "training set." The training set is used to create the model. The features in these spectra are compared while knowing the "truth" about the desired classification parameter (*e.g.*, diagnosis, species, chemical concentration, etc.). Some methods by which these features are identified to create the model will be discussed below.

Once the model has been created, it is then applied to the "validation set." The validation set consists of spectra not included in the training set. This evaluates the performance of the model when applied to new spectra that were not used when creating the model. The validation and training sets should consist of spectra that are independent of each other, *i.e.* they come from different patients, different samples, etc. If the model performs very well on the training set but fails on the validation set, it is said to be "over-trained." Causes for over-training include small training set size, low diversity in the training set, large number of available parameters, or small differences between classes.

Often, the training-validation process is repeated a number of times by redistributing the spectra into new training and validation sets, creating a new model, and evaluating the performance. This gives a more reliable estimate of the model's performance independent of the particular spectra used to create it.

The smallest possible validation set is a single spectrum. When several training and validation sets are created in this way, it is called leave one out cross-validation (LOOCV). Another popular method is n-fold cross-validation. In this method, the data are separated into n groups. One group is used for validation after the others train the model. A model is considered more robust if it performs well with a larger validation set.

During this process, it is expected that researchers will be adjusting various parameters to increase the model's performance on validation sets. This introduces the possibility that the optimized model is biased to perform better on these spectra. For this reason, a "test set" is used after the model has been finalized. The test set is made of spectra that were never in any training or validation sets. The test set evaluates the model's performance on spectra that are completely new to the model and estimates the potential performance in practical applications.

The following sections will discuss specific methods used choose Raman spectral features to create a model for classification or quantification. These methods are summarized in Table 8.

5.2. Direct Peak Analysis

The most fundamental way to evaluate a Raman spectrum is to directly analyze the individual spectral features. This usually requires *a priori* information about which features will be important to the particular situation. These direct analytical methods inherently retain more chemical information and a closer connection to physiology.

Method	Summary	Supervised	Target	Sensitivity
Direct peak analysis	Peak areas indicate concentration of analyte	either	any	low
Principal component analysis (PCA)	Finds variables responsible for variance between spectra	no	none	high
Cluster analysis	Indentifies groups of similar spectra	no	none	medium
Linear discriminant analysis (LDA)	Separates classes using linear boundary	yes	binary classes	low
Logistic regression	Separates classes using logarithmic boundary	yes	classes	medium
Support vector machines (SVM)	Maximizes separation between classes using higher-order boundary	yes	classes	high
Decision tree (incl. random forest)	Classifies spectra based on series of binary decisions	yes	classes	high
Partial least squares (PLS)	Identifies spectral features correlated to training values	yes	numerical value (*e.g.*, concentration)	medium
Artificial neural network (ANN)	Calculations through a series of "neurons"	yes	classes or numerical value	high
Ant colony optimization	Paths to successful models attract subsequent paths	yes	fitness parameter	high
Genetic algorithm	Model parameters "evolve" to succeeding generations	yes	fitness parameter	high

Table 8. Summary of various methods for analysis of Raman spectra. High sensitivity indicates that the method is capable of distinguishing smaller differences between spectra, but also has a higher tendency for over-training.

The number of molecules generating a band can be estimated by calculating the area of that band above the baseline. The maximum value of a band is sometimes used as a simple substitute. Using the intensity of a single Raman band, Deng *et al.* measured the effect of alcohol exposure on red blood cells[463] and Huang *et al.* measured concentrations of citric acid in plasma[464]. Using multiple bands, Jung *et al.* measured changes in DNA after cell adhesion[465] and Lee *et al.* measured changes in DNA during apoptosis[466].

Sometimes background contributions or other effects corrupt analysis of the absolute analysis of Raman bands. In some of these situations, ratios of Raman bands can be useful indicators. Buchwal *et al.* used Raman band ratios as indicators of bone structure and composition[467] while Li *et al.* used band ratios to measure the effects of maleic acid on human sperm[468].

Another direct analysis method has been to normalize all spectra for equal total intensity and identify changes by subtraction. Subtracting spectra of one group from spectra of another can reveal which features show differences. This method was used by Saxena *et al.* to identify changes associated with spinal cord injury[469] and by Bai *et al.* to measure senescence in stem cells[470].

If sufficient molecular components contributing to a Raman spectrum are known, then it can be modeled as a linear combination of these components. This allows direct analysis of the chemical constituents of the sample instead of values from the spectrum. This reduces the spectrum to a smaller, more manageable data set while also conveying a more physical interpretation. This has been used to analyze a particular component of interest, such as calcifications by Barman *et al.*[471]

More commonly, each spectrum is modeled by a method called spectral deconvolution. This reconstructs the spectrum as a linear combination of Gaussian or Lorentzian features. These features often overlap and are positioned to best fit the spectrum. While this simplifies the full spectrum into a collection of contributing components, it can sacrifice some of the physical meaning behind these features. Spectral deconvolution has been used to analyze Raman spectra in a variety of applications, including gastric cancer[426], effects of pesticides[472], red blood cell disease[473], breast cancer[474], and stem cell differentiation[475].

5.3. Prinicpal Component Analysis

Principal component analysis (PCA) has its origins in linear algebra. PCA is a robust method used to find spectral features that vary between samples in the dataset. PCA finds a linearly independent set of normal variables (called principal components (PCs) or loading vectors) that account for the most variance in the dataset. Each PC is essentially a weighting for each wavenumber value in a spectrum. Each spectrum can then be described as a linear combination of PCs.

The first PC describes the most variance within the data set. This means that the spectral features heavily weighted by the first PC vary more from spectrum to spectrum than any other linear combination of features. The second PC describes the most variance of features not included in the first PC, and so on. In practice, the first few PCs can provide useful information regarding spectral differences within the dataset. After several PCs, the remainder describe mostly noise. Thus, a spectrum can often be adequately reconstructed from its first several PCs. This is sometimes used to reduce noise in Raman spectra[72].

PCA is a common method used to simplify a dataset from large spectra to a few PCs. It is often used as an initial step to simplify data before further analysis with other methods. It can also provide a way to easily visualize spectral similarities or differences.

The loading vectors from PCA also provide a useful tool to examine what spectral features best differentiate between spectra. This has helped researchers learn the chemical differences associated with immune cell activation[476], lung cancer[477], and different types of cell death[478]. PCA has also been used to study the chemical changes associated with processes such as the cell division cycle[479] and differentiation into cancer[480].

PCA finds the set of variables responsible for the largest variance regardless of whether that variance corresponds to the variable or classification of interest. In this sense, PCA is not a classifier, but it can still be used as such if the variable or classification of interest is a significant cause of variance in the dataset[481]. More commonly, PCA is used to simplify the dataset before more specialized methods perform the classificaiton.

5.4. Cluster Analysis

Similar to PCA, cluster analysis is another untrained technique, meaning that it does not use any information about the "true" classes associated with the sample. It finds similaries between spectra to put them into a user-defined number of groups. Algorithms can also find hierarchical clusters, meaning that each group of similar spectra is further divided into other groups, and so on.

Cluster analysis is primarily used to quickly identify groups of similar spectra. The clusters gain significance when they match sample classes or other parameters. This technique can highlight similarities and differences between groups of samples such as bacteria[482] and proteins affected by disease[483].

5.5. Linear Discriminant Analysis

Unlike PCA and cluster analysis, Linear Discriminant Analysis (LDA) uses the information of the classes associated with each spectrum in the training set. LDA then identifies linear combinations of spectral features that distinguish the classes. The underlying assumptions of LDA require the classes to be similar in number of samples and covariance between spectra.

LDA is often performed on selected spectral features or the PC scores of data analyzed with PDA instead of the raw dataset. This increases speed and accuracy as the algorithm is not burdened by inconsequential spectral features.

LDA has been used with Raman spectroscopy to create binary classification models to identify leukemia[484] and gastric dysplasia[438]. LDA can also be performed multiple times to create a multi-level classification model (*i.e.* a model classifying spectra into more than two groups). This has been used by several groups to identify stages of the cell cycle[135], species of bacteria[485], skin cancer[147], and tumor metastasis to other tissues[486].

5.6. Logistic Regression

As the name implies, logistic regression (LR) uses logarithms when combining spectral features. This allows more flexibility than the linear models of LDA, resulting in models that are generally more accurate, but can also be over-trained more easily. LR also relies upon fewer assumptions than LDA with respect to sample size and covariance.

A LR model calculates the probability that a given measurement is in each classification group. It has been used to discriminate between Raman spectra from different bacterial species[14], tissue types (including skin cancer)[144], and brain tissue from patients with Alzheimer's[487].

5.7. Support Vector Machines

Support Vector Machines (SVMs) are nonlinear classification models. An SVM considers all spectra in the dataset to occupy a multi-dimensional phase space (one dimension for each acquired wavelength) where each spectrum is a single point. An SVM finds a hyperplane (which can be curved) within this phase space to separate points of different classes, especially focusing on the points that are close to those in other classes. The classification model is based on the hyperplane with maximum thickness between classes. In this way, the model is not finished training even when the training set is perfectly classified; the algorithm still tries to maximize thickness of the hyperplane. This is intended to minimize possibility of future error. Unfortunately, however, this increases the danger of over-training the model. Additionally, the flexibility of the model increases the computational demands for classification.

SVM has been used as a classifier for a variety of Raman spectroscopy applications. Some of these include the evaluation of antibiotic treatments[488], identification of circulating tumor cells[489], and classification of inflammatory bowel disease[490]. Stöckel *et al.* used a hierarchy of SVM and LDA classifiers to identify bacterial species[491]. SVM can also be trained to quantify the concentration of specific chemicals, such as glucose[492].

5.8. Decision Trees

It is also possible to classify spectra based on series of binary decisions. These decisions are usually based on whether a feature in the spectrum is greater than or less than a certain value determined during training. This series of decisions creates a decision tree. Decision trees can be useful in some cases as they perform classification sequentially. The criteria for identifying one class of spectra may be very different from the criteria to identify another. These classifications are made separately in a decision tree. Decision trees have been used to diagnose gastric cancer[493] and classify organic and inorganic particulates [494].

Many decision trees can be randomly created and combined to build a random forest. Algorithms can generate and evaluate several random forests to create a classification model. For each spectrum, the classification of the entire model (or forest) is taken to be the plurality of the classifications by the individual decision trees. Random forest classification models have been used by Teh *et al.* to diagnose laryngeal carcinoma[495] and by Draga *et al.* to diagnose bladder cancer[496].

5.9. Partial Least Squares Regression

Haaland and Thomas demonstrated the application of partial least squares (PLS) regression to spectra in 1988[497]. PLS consists of a series of linear algebra operations including classical and inverse least-squares. PLS is trained to a particular score associated with each spectrum. In Raman spectroscopy, this score is often the concentration of a particular chemical. PLS is a very popular technique when extracting continuous parameters from spectra, rather than assigning spectra to different classes.

The most common application of PLS to Raman spectroscopy is quantification of chemicals within the sample. PLS has been used by Bechtel *et al.* to quantify various components in tissue phantoms[498], by Mekisiarun *et al.* to measure the level of saturation of fat in milk[499], by Saatkamp *et al.* to quantify levels of creatinine and urea in urine[500], and by Shih *et al.* to extract blood glucose concentration[501]. PLS can also be trained to predict non-chemical properties of the sample. For example, Maher *et al.* used PLS and Raman spectroscopy to measure bone strength[502] and Duraipandian *et al.* estimated the probability of future development of cancer[503].

5.10. Other Techniques

Other statistical and computational techniques continue to be developed and applied to the classification of Raman spectra. One of these emerging techniques is the artificial neural network (ANN). ANN is designed to mimic the activity of neurons in the brain. The spectrum is input to feed a number of nodes (called neurons). Each neuron calculates a new parameter. Each parameter is passed to another set of neurons. This continues for a set number of layers until the final layer makes a classification decision. Jürgen Popp and his group have used ANN to classify Raman spectra from various bacterial species[15]. One criticism of this model is its "black box" nature; it can be difficult to extract which features were responsible for the classification.

Ant colony optimization (ACO) executes a random search for classification parameters until a "successful" iteration is found. The successful set of classification parameters (called an "ant") then releases "pheromones" to attract other "ants." ACO can be faster than other searching algorithms because the discovery of a successful model actively leads to more success. ACO has been applied to Raman spectroscopy to create models to diagnose colorectal cancer[504] and gastric cancer[505].

Another emerging search algorithm is based on genetic evolution. The genetic algorithm begins with a starting model used as a guess. The model is applied to determine a "fitness" parameter based on the model's performance. "Children" are then created from the starting model. Each child is similar to the starting model with a few changes ("mutations") to the model. Each child is then evaluated to find the fitness parameter. Successful changes are kept and passed on to the next "generation" of children. This process continues for a set number of generations or until a certain fitness is met. A genetic algorithm has been used the create a Raman modeld to detect cervical precancer[506].

A complete list of methods and algorithms used to generate classification models of Raman spectra cannot be presented here. There is also no "best choice" of classifier that will outperform others in all situations. The choice of classifier will depend on many aspects of the particular application. Some of these include the consistency of spectral differences between groups, the number of spectra in the dataset, the level of noise present in the data, and the physical meaning of the target classes.

6. FUTURE PERSPECTIVE

Technological advances during the last two decades, related in particular to lasers, detectors and optical components, have enabled the development of a broad range of Raman spectroscopy techniques for applications in life sciences. Raman spectroscopy offers a combination of some unique features well-suited for non-destructive physical and chemical analysis of biological samples as well as novel diagnostic tools for medical applications.

Raman spectroscopy provides high-chemical specificity without requiring labelling, which is an important feature when studying live cells. As the technique is based on light scattering, measurements can be carried out with little or no sample preparation.

To obtain information regarding molecular vibrations in the sample, Raman spectroscopy uses light in the visible or near-infrared spectral regions, and thus benefits from the advanced optical microscopy and fiber optics technology. The microscopes provide high spatial resolution (0.5-1 μm) required to analyse individual cells and cellular components, while the fibre optics have enabled the development of a broad range of Raman hand-held probes and endoscopes suitable for *in vivo* medical diagnostics. In addition, Raman spectroscopy can also be integrated with other analytical techniques (scanning probe microscopy, electron microscopy, optical coherence tomography, etc.), and the lasers used for the excitation of Raman spectra can be used to measure the elastic scattering properties of the samples or as a tool for accurate positioning and manipulation of cells (optical tweezers). Raman spectra can be easily measured of live cells in aqueous solutions (*i.e.* culture media), allowing quantification of endogenous biomolecules. The use of multivariate spectral analysis techniques have enabled the development of classification models for quantitative analysis/identification of cells, as well as objective diagnosis and imaging of tissues.

Nevertheless, one of the most important challenges to Raman spectroscopy in life-sciences is related to the low Raman scattering cross-section of most biomolecules, leading to relatively long acquisition times (0.1-1 second per spectrum). This limitation is particularly important when Raman spectral imaging is required at high-speed.

Another challenge is the detection of specific biomolecules within a biological sample. As all molecules excited by the laser will contribute to the Raman scattered light detected by the spectrometer, the Raman spectra of complex biological samples will consist of overlapped and convoluted bands. These overlapped bands create a background against which it is difficult to detect the signal from only specific molecules if those molecules do not possess vibrational modes that interact resonantly with the excitation wavelength. For similar reasons, many materials widely used in life sciences, such as glass microscopy slides or coverslips or plastic cell-culture containers, are difficult to use. Instead, slides made out of quartz or more specialized materials such as calcium fluorite or magnesium fluorite are used.

Another challenge in Raman spectroscopy is the difficulty in measuring non-invasively biological samples deeper below the surface. Such measurements are of high interest, for example when investigating live cells growing in 3D cultures in-vitro or for in-vivo medical diagnosis of subsurface lesions. Although the near-infrared light used for excitation can penetrate deep into tissue, the high level of scattering reduces the signal-to-noise ratio of the measured Raman spectra.

Despite these challenges, new strategies are being developed. Although none of these technologies solve every problem, specific applications can be approached using one or more of these techniques. For example, new imaging modalities based on non-linear Raman scattering (CARS and SRS) have been developed that have demonstrated video-rate imaging of cells and tissue. Additionally, selective sampling strategies based on multimodal integration and adaptive-sampling spontaneous Raman microscopy have been designed to allow fast objective diagnosis of excised tissue specimens in cancer surgery, based on multivariate classification models. Other approaches relied on novel nanomaterials and photonic structures to enhance the Raman signals (SERS), allowing short measurements and high detection sensitivity (up to single molecule detection). These techniques also allow increased chemical specificity, as only the vibrational modes of the molecules in the vicinity (near-field) of these nanostructures are enhanced. Similar techniques can also be used for enhancing the spatial resolution down to only few nanometers (TERS). Techniques based on structured illumination Raman microscopy have also been reported to increase the spatial resolution beyond the diffraction limit. Chemical specificity can also be increased by using stable-isotope labelling, which is a non-invasive technique that has allowed monitoring of molecular transfer and cell-cell communication at single live cells level. Raman labels based on small functional groups exhibiting high Raman scattering cross-sections (*e.g.*, alkynes) have also been used for monitoring cellular processes.

Significant progress has been made for *in vivo* measurements of Raman spectra at different parts of the body for medical diagnostic purposes. A broad range of fibre-optics probes have been designed to build Raman hand-held diagnostic devices and endoscopes. Improved filtering methods for the background signals have been reported; multimodal probes integrating Raman spectroscopy, tissue auto-fluorescence and diffuse reflectance are currently being tested in clinical environments. Techniques based on spatially-offset and transmission Raman spectroscopy, as well as needle-probes have been developed for deep and subsurface diagnostics, as well as applications in tissue engineering and regenerative medicine. These developments have made important steps toward maximising the diagnostic accuracy and speed, and often rely on cost-effective solutions that are likely to be adopted into the healthcare services. These developments demonstrate that clearly Raman spectroscopy is a powerful emerging technique in the life sciences, and has the potential to underpin fundamental advances in our understanding of molecular and cellular processes, as well as development of tools for *in vivo* disease detection and diagnosis.

REFERENCES

1. C. V. Raman and K. S. Krishnan, "A new type of secondary radiation," Nature **121**, 501–502 (1928).
2. J. H. E. t. Hibben, *The Raman Effect and Its Chemical Applications* (Reinhold Publishing, 1939).
3. G. Herzberg, *Molecular spectra and molecular structure*, vol. vol II: Infrared and Raman spectra (D. Van Nostrand Company.; New York, 1945).
4. T. Burke, D. Smith, and A. Nielsen, "The molecular structure of mof6, wf6, and uf6 from infrared and raman spectra," The Journal of Chemical Physics **20**, 447–454 (1952).
5. S. Porto and D. Wood, "Ruby optical maser as a raman source," JOSA **52**, 251–252 (1962).
6. H. Kogelnik and S. Porto, "Continuous helium-neon red laser as a raman source," JOSA **53**, 1446–1447 (1963).
7. H. Susi and J. S. Ard, "Laser-raman spectra of lactose," Carbohydrate Research **37**, 351–354 (1974).
8. D. Rousseau, "Raman difference spectroscopy as a probe of biological molecules," Journal of Raman Spectroscopy **10**, 94–99 (1981).
9. M. Delhaye and P. Dhamelincourt, "Raman microprobe and microscope with laser excitation," Journal of Raman Spectroscopy **3**, 33–43 (1975).
10. G. Puppels, A. Huizinga, H. Krabbe, H. De Boer, G. Gijsbers, and F. De Mul, "A high-throughput raman notch filter set," Review of scientific instruments **61**, 3709–3712 (1990).
11. G. Puppels, F. De Mul, C. Otto, J. Greve, M. Robert-Nicoud, D. Arndt-Jovin, and T. Jovin, "Studying single living cells and chromosomes by confocal raman microspectroscopy," Nature (1990).
12. G. Puppels, H. Garritsen, G. Segers-Nolten, F. De Mul, and J. Greve, "Raman microspectroscopic approach to the study of human granulocytes." Biophysical journal **60**, 1046 (1991).
13. G. Puppels, T. B. Schut, N. Sijtsema, M. Grond, F. Maraboeuf, C. De Grauw, C. Figdor, and J. Greve, "Development and application of raman microspectroscopic and raman imaging techniques for cell biological studies," Journal of Molecular Structure **347**, 477–483 (1995).

14. B. D. Beier, R. G. Quivey, and A. J. Berger, "Identification of different bacterial species in biofilms using confocal raman microscopy," Journal of biomedical optics **15**, 066001–066001 (2010).

15. A. Walter, W. Schumacher, T. Bocklitz, M. Reinicke, P. Rösch, E. Kothe, and J. Popp, "From bulk to single-cell classification of the filamentous growing streptomyces bacteria by means of raman spectroscopy," Applied spectroscopy **65**, 1116–1125 (2011).

16. O. Samek, S. Bernatová, J. Ježek, M. Šiler, M. Šerý, V. Krzyžánek, K. Hrubanová, P. Zemánek, V. Holá, and F. Růžička, "Identification of individual biofilm-forming bacterial cells using raman tweezers," Journal of biomedical optics **20**, 051038–051038 (2015).

17. K. Kong, C. Kendall, N. Stone, and I. Notingher, "Raman spectroscopy for medical diagnostics - from in-vitro biofluid assays to in-vivo cancer detection," Advanced drug delivery reviews **89**, 121–134 (2015).

18. M. Diem, A. Mazur, K. Lenau, J. Schubert, B. Bird, M. Miljković, C. Krafft, and J. Popp, "Molecular pathology via ir and raman spectral imaging," Journal of biophotonics **6**, 855–886 (2013).

19. C. Krafft, B. Dietzek, M. Schmitt, and J. Popp, "Raman and coherent anti-stokes raman scattering microspectroscopy for biomedical applications," Journal of biomedical optics **17**, 0408011–04080115 (2012).

20. C. L. Evans and X. S. Xie, "Coherent anti-stokes raman scattering microscopy: chemical imaging for biology and medicine," Annu. Rev. Anal. Chem. **1**, 883–909 (2008).

21. C. H. Camp Jr and M. T. Cicerone, "Chemically sensitive bioimaging with coherent raman scattering," Nature Photonics **9**, 295–305 (2015).

22. C. Zhang, D. Zhang, and J.-X. Cheng, "Coherent raman scattering microscopy in biology and medicine," Annual review of biomedical engineering **17**, 415 (2015).

23. W. Min, C. W. Freudiger, S. Lu, and X. S. Xie, "Coherent nonlinear optical imaging: beyond fluorescence microscopy," Annual review of physical chemistry **62**, 507 (2011).

24. W. Xie and S. Schlücker, "Medical applications of surface-enhanced raman scattering," Physical Chemistry Chemical Physics **15**, 5329–5344 (2013).

25. S. McAughtrie, K. Faulds, and D. Graham, "Surface enhanced raman spectroscopy (sers): potential applications for disease detection and treatment," Journal of Photochemistry and Photobiology C: Photochemistry Reviews **21**, 40–53 (2014).

26. G. Turrell and J. Corset, *Raman microscopy: developments and applications* (Academic Press, 1996).

27. R. Mulliken, "Report on notation for the spectra of polyatomic molecules," J. chem. Phys **23**, 1997 (1955).

28. D. A. Long, *The Raman Effect* (John Wiley and Sons, Ltd., West Sussex, England, 2002).

29. M. Diem, *Introduction to modern vibrational spectroscopy*, vol. 543 (Wiley New York, 1993).

30. G. Placzek, *Rayleigh-streuung und Raman-effekt*, vol. 2 (Akad. Verlag-Ges., 1934).

31. D. J. Griffiths, "Introduction to electrodynamics," (1999).

32. R. C. Prince, R. R. Frontiera, and E. O. Potma, "Stimulated raman scattering: From bulk to nano," Chemical Reviews (2016).

33. B. R. Masters and P. So, *Handbook of biomedical nonlinear optical microscopy* (Oxford University Press, 2008).

34. D. J. Griffiths, *Introduction to quantum mechanics* (Pearson Education India, 2005).

35. T. Hart, R. Aggarwal, and B. Lax, "Temperature dependence of raman scattering in silicon," Physical Review B **1**, 638 (1970).

36. R. P. Lucht, S. Roy, T. R. Meyer, and J. R. Gord, "Femtosecond coherent anti-stokes raman scattering measurement of gas temperatures from frequency-spread dephasing of the raman coherence," Applied Physics Letters **89**, 251112 (2006).

37. B. Welz, M. Sperling, G. Schlemmer, N. Wenzel, and G. Marowsky, "Spatially and temporally resolved gas phase temperature measurements in a massmann-type graphite tube furnace using coherent anti-stokes raman scattering," Spectrochimica Acta Part B: Atomic Spectroscopy **43**, 1187–1207 (1988).

38. R. W. Boyd, *Nonlinear Optics* (Academic Press, 2008).

39. M. Levenson and S. Kano, "Introduction to nonlinear optical spectroscopy," Academic, New York (1988).

40. S. Mukamel, *Principles of nonlinear optical spectroscopy*, 6 (Oxford University Press on Demand, 1999).

41. P. Maker and R. Terhune, "Study of optical effects due to an induced polarization third order in the electric field strength," Physical Review **137**, A801 (1965).

42. J.-X. Cheng and X. S. Xie, "Coherent anti-stokes raman scattering microscopy: instrumentation, theory, and applications," The Journal of Physical Chemistry B **108**, 827–840 (2004).

43. E. Woodbury and W. Ng, "Ruby laser operation in near ir," Proceedings of the Institute of Radio Engineers **50**, 2367 (1962).

44. N. Bloembergen, "The stimulated raman effect," American Journal of Physics **35**, 989–1023 (1967).

45. G. Eckhardt, R. Hellwarth, F. McClung, S. Schwarz, D. Weiner, and E. Woodbury, "Stimulated raman scattering from organic liquids," Physical Review Letters **9**, 455 (1962).

46. R. W. Hellwarth, "Theory of stimulated raman scattering," Physical Review **130**, 1850 (1963).

47. D. Zhang, P. Wang, M. N. Slipchenko, and J.-X. Cheng, "Fast vibrational imaging of single cells and tissues by stimulated raman scattering microscopy," Accounts of chemical research **47**, 2282–2290 (2014).

48. D. Zhang, M. N. Slipchenko, D. E. Leaird, A. M. Weiner, and J.-X. Cheng, "Spectrally modulated stimulated raman scattering imaging with an angle-to-wavelength pulse shaper," Optics express **21**, 13864–13874 (2013).

49. M. Andreana, M.-A. Houle, D. J. Moffatt, A. Ridsdale, E. Buettner, F. Légaré, and A. Stolow, "Amplitude and polarization modulated hyperspectral stimulated raman scattering microscopy," Optics express **23**, 28119–28131 (2015).

50. A. Owyoung and E. D. Jones, "Stimulated raman spectroscopy using low-power cw lasers," Optics letters **1**, 152–154 (1977).

51. M. Fleischmann, P. J. Hendra, and A. McQuillan, "Raman spectra of pyridine adsorbed at a silver electrode," Chemical Physics Letters **26**, 163–166 (1974).

52. D. L. Jeanmaire and R. P. Van Duyne, "Surface raman spectroelectrochemistry: Part i. heterocyclic, aromatic, and aliphatic amines adsorbed on the anodized silver electrode," Journal of Electroanalytical Chemistry and Interfacial Electrochemistry **84**, 1–20 (1977).

53. P. B. Johnson and R.-W. Christy, "Optical constants of the noble metals," Physical review B **6**, 4370 (1972).

54. E. D. Palik, *Handbook of optical constants of solids*, vol. 3 (Academic press, 1998).

55. S. Babar and J. Weaver, "Optical constants of cu, ag, and au revisited," Applied Optics **54**, 477–481 (2015).

56. K. M. McPeak, S. V. Jayanti, S. J. Kress, S. Meyer, S. Iotti, A. Rossinelli, and D. J. Norris, "Plasmonic films can easily be better: rules and recipes," ACS photonics **2**, 326–333 (2015).

57. L. Novotny and B. Hecht, *Principles of nano-optics* (Cambridge university press, 2012).

58. C. F. Bohren and D. R. Huffman, *Absorption and scattering of light by small particles* (John Wiley & Sons, 2008).

59. E. Le Ru and P. Etchegoin, *Principles of Surface-Enhanced Raman Spectroscopy: and related plasmonic effects* (Elsevier, 2008).

60. M. Faraday, "The bakerian lecture: experimental relations of gold (and other metals) to light," Philosophical Transactions of the Royal Society of London **147**, 145–181 (1857).

61. S. Link and M. A. El-Sayed, "Size and temperature dependence of the plasmon absorption of colloidal gold nanoparticles," The Journal of Physical Chemistry B **103**, 4212–4217 (1999).

62. K. L. Kelly, E. Coronado, L. L. Zhao, and G. C. Schatz, "The optical properties of metal nanoparticles: the influence of size, shape, and dielectric environment," The Journal of Physical Chemistry B **107**, 668–677 (2003).

63. Y. Xia, Y. Xiong, B. Lim, and S. E. Skrabalak, "Shape-controlled synthesis of metal nanocrystals: Simple chemistry meets complex physics?" Angewandte Chemie International Edition **48**, 60–103 (2009).

64. R. A. Sperling and W. Parak, "Surface modification, functionalization and bioconjugation of colloidal inorganic nanoparticles," Philosophical Transactions of the Royal Society of London A: Mathematical, Physical and Engineering Sciences **368**, 1333–1383 (2010).

65. M. Rycenga, C. M. Cobley, J. Zeng, W. Li, C. H. Moran, Q. Zhang, D. Qin, and Y. Xia, "Controlling the synthesis and assembly of silver nanostructures for plasmonic applications," Chemical reviews **111**, 3669–3712 (2011).

66. S. Nie and S. R. Emory, "Probing single molecules and single nanoparticles by surface-enhanced raman scattering," science **275**, 1102–1106 (1997).

67. K. Kneipp, Y. Wang, H. Kneipp, L. T. Perelman, I. Itzkan, R. R. Dasari, and M. S. Feld, "Single molecule detection using surface-enhanced raman scattering (sers)," Physical review letters **78**, 1667 (1997).

68. H. Xu, E. J. Bjerneld, M. Käll, and L. Börjesson, "Spectroscopy of single hemoglobin molecules by surface enhanced raman scattering," Physical review letters **83**, 4357 (1999).

69. I. Notingher, S. Verrier, S. Haque, J. Polak, and L. Hench, "Spectroscopic study of human lung epithelial cells (a549) in culture: living cells versus dead cells," Biopolymers **72**, 230–240 (2003).

70. J. De Gelder, K. De Gussem, P. Vandenabeele, and L. Moens, "Reference database of raman spectra of biological molecules," Journal of Raman Spectroscopy **38**, 1133–1147 (2007).

71. C. A. Patil, J. Kalkman, D. J. Faber, J. S. Nyman, T. G. van Leeuwen, and A. Mahadevan-Jansen, "Integrated system for combined raman spectroscopy–spectral domain optical coherence tomography," Journal of biomedical optics **16**, 011007–011007 (2011).

72. N. Uzunbajakava, A. Lenferink, Y. Kraan, B. Willekens, G. Vrensen, J. Greve, and C. Otto, "Nonresonant raman imaging of protein distribution in single human cells," Biopolymers **72**, 1–9 (2003).

73. A. Nijssen, T. C. B. Schut, F. Heule, P. J. Caspers, D. P. Hayes, M. H. Neumann, and G. J. Puppels, "Discriminating basal cell carcinoma from its surrounding tissue by raman spectroscopy," Journal of Investigative Dermatology **119**, 64–69 (2002).

74. I. Notingher, C. Green, C. Dyer, E. Perkins, N. Hopkins, C. Lindsay, and L. L. Hench, "Discrimination between ricin and sulphur mustard toxicity in vitro using raman spectroscopy," Journal of the Royal Society Interface **1**, 79–90 (2004).

75. G. Shetty, C. Kendall, N. Shepherd, N. Stone, and H. Barr, "Raman spectroscopy: elucidation of biochemical changes in carcinogenesis of oesophagus," British journal of cancer **94**, 1460–1464 (2006).

76. S. Farquharson, C. Shende, F. E. Inscore, P. Maksymiuk, and A. Gift, "Analysis of 5-fluorouracil in saliva using surface-enhanced raman spectroscopy," Journal of Raman Spectroscopy **36**, 208–212 (2005).

77. R. A. Bitar, H. da Silva Martinho, C. J. Tierra-Criollo, L. N. Z. Ramalho, M. M. Netto, and A. A. Martin, "Biochemical analysis of human breast tissues using fourier-transform raman spectroscopy," Journal of biomedical optics **11**, 054001–054001 (2006).

78. N. Stone, C. Kendall, N. Shepherd, P. Crow, and H. Barr, "Near-infrared raman spectroscopy for the classification of epithelial pre-cancers and cancers," Journal of Raman spectroscopy **33**, 564–573 (2002).

79. J. W. Chan, D. S. Taylor, T. Zwerdling, S. M. Lane, K. Ihara, and T. Huser, "Micro-raman spectroscopy detects individual neoplastic and normal hematopoietic cells," Biophysical journal **90**, 648–656 (2006).

80. S. C. Erfurth, E. J. Kiser, and W. L. Peticolas, "Determination of the backbone structure of nucleic acids and nucleic acid oligomers by laser raman scattering," Proceedings of the National Academy of Sciences **69**, 938–941 (1972).

81. J. M. Benevides, S. A. Overman, and G. J. Thomas, "Raman, polarized raman and ultraviolet resonance raman spectroscopy of nucleic acids and their complexes," Journal of Raman Spectroscopy **36**, 279–299 (2005).

82. X. Zhang, M. B. Roeffaers, S. Basu, J. R. Daniele, D. Fu, C. W. Freudiger, G. R. Holtom, and X. S. Xie, "Label-free live-cell imaging of nucleic acids using stimulated raman scattering microscopy," ChemPhysChem **13**, 1054–1059 (2012).

83. R. Malini, K. Venkatakrishna, J. Kurien, K. M Pai, L. Rao, V. Kartha, and C. M. Krishna, "Discrimination of normal, inflammatory, premalignant, and malignant oral tissue: a raman spectroscopy study," Biopolymers **81**, 179–193 (2006).

84. A. Ruiz-Chica, M. Medina, F. Sanchez-Jimenez, and F. Ramirez, "Characterization by raman spectroscopy of conformational changes on guanine–cytosine and adenine–thymine oligonucleotides induced by aminooxy analogues of spermidine," Journal of Raman spectroscopy **35**, 93–100 (2004).

85. N. Stone, C. Kendall, J. Smith, P. Crow, and H. Barr, "Raman spectroscopy for identification of epithelial cancers," Faraday discussions **126**, 141–157 (2004).

86. H. Schulz and M. Baranska, "Identification and quantification of valuable plant substances by ir and raman spectroscopy," Vibrational Spectroscopy **43**, 13–25 (2007).

87. A. Robichaux Viehoever, D. Anderson, D. Jansen, and A. Mahadevan-Jansen, "Organotypic raft cultures as an effective in vitro tool for understanding raman spectral analysis of tissue," Photochemistry and photobiology **78**, 517–524 (2003).

88. D. P. Lau, Z. Huang, H. Lui, D. W. Anderson, K. Berean, M. D. Morrison, L. Shen, and H. Zeng, "Raman spectroscopy for optical diagnosis in the larynx: preliminary findings," Lasers in Surgery and Medicine **37**, 192–200 (2005).

89. Z. Huang, A. McWILLIAMS, S. Lam, J. English, D. I. McLEAN, H. Lui, and H. Zeng, "Effect of formalin fixation on the near-infrared raman spectroscopy of normal and cancerous human bronchial tissues," International journal of oncology **23**, 649–655 (2003).

90. H. G. Edwards, D. W. Farwell, A. C. Williams, B. W. Barry, and F. Rull, "Novel spectroscopic deconvolution procedure for complex biological systems: vibrational components in the ft-raman spectra of ice-man and contemporary skin," Journal of the Chemical Society, Faraday Transactions **91**, 3883–3887 (1995).

91. R. J. Lakshmi, V. Kartha, C. Murali Krishna, J. R. Solomon, G. Ullas, and P. Uma Devi, "Tissue raman spectroscopy for the study of radiation damage: brain irradiation of mice," Radiation research **157**, 175–182 (2002).

92. E. Hanlon, R. Manoharan, T. Koo, K. Shafer, J. Motz, M. Fitzmaurice, J. Kramer, I. Itzkan, R. Dasari, and M. Feld, "Prospects for in vivo raman spectroscopy," Physics in medicine and biology **45**, R1 (2000).

93. R. K. Dukor, "Vibrational spectroscopy in the detection of cancer," Handbook of vibrational spectroscopy (2002).

94. C. Krafft, L. Neudert, T. Simat, and R. Salzer, "Near infrared raman spectra of human brain lipids," Spectrochimica Acta Part A: Molecular and Biomolec-

ular Spectroscopy **61**, 1529–1535 (2005).

95. L. Silveira, S. Sathaiah, R. A. Zângaro, M. T. Pacheco, M. C. Chavantes, and C. A. Pasqualucci, "Correlation between near-infrared raman spectroscopy and the histopathological analysis of atherosclerosis in human coronary arteries," Lasers in surgery and medicine **30**, 290–297 (2002).

96. D. Naumann, "Infrared and nir raman spectroscopy in medical microbiology," in "BiOS'98 International Biomedical Optics Symposium," (International Society for Optics and Photonics, 1998), pp. 245–257.

97. C. J. Frank, R. L. McCreery, and D. C. Redd, "Raman spectroscopy of normal and diseased human breast tissues," Analytical chemistry **67**, 777–783 (1995).

98. A. T. Tu and A. Tu, *Raman spectroscopy in biology: principles and applications* (Wiley New York, 1982).

99. I. Ashikawa and K. Itoh, "Raman spectra of polypeptides containing l-histidine residues and tautomerism of imidazole side chain," Biopolymers **18**, 1859–1876 (1979).

100. S. Krimm and J. Bandekar, "Vibrational spectroscopy and conformation of peptides, polypeptides, and proteins," Advances in protein chemistry **38**, 181–364 (1986).

101. E. Carter, H. Edwards, H. Gremlich, and B. Yan, "Infrared and raman spectroscopy of biological materials," (2000).

102. G. Zhu, X. Zhu, Q. Fan, and X. Wan, "Raman spectra of amino acids and their aqueous solutions," Spectrochimica Acta Part A: Molecular and Biomolecular Spectroscopy **78**, 1187–1195 (2011).

103. S. A. Overman, K. L. Aubrey, K. E. Reilly, O. Osman, S. J. Hayes, P. Serwer, and G. J. Thomas, "Conformation and interactions of the packaged double-stranded dna genome of bacteriophage t7," Biospectroscopy **4**, S47–S56 (1998).

104. B. G. Frushour and J. L. Koenig, "Raman scattering of collagen, gelatin, and elastin," Biopolymers **14**, 379–391 (1975).

105. I. Notingher and L. L. Hench, "Raman microspectroscopy: a noninvasive tool for studies of individual living cells in vitro," Expert review of medical devices **3**, 215–234 (2006).

106. W.-T. Cheng, M.-T. Liu, H.-N. Liu, and S.-Y. Lin, "Micro-raman spectroscopy used to identify and grade human skin pilomatrixoma," Microscopy research and technique **68**, 75–79 (2005).

107. D. P. Lau, Z. Huang, H. Lui, C. S. Man, K. Berean, M. D. Morrison, and H. Zeng, "Raman spectroscopy for optical diagnosis in normal and cancerous tissue of the nasopharynx: preliminary findings," Lasers in surgery and medicine **32**, 210–214 (2003).

108. E. Katainen, M. Elomaa, U.-M. Laakkonen, E. Sippola, P. Niemelä, J. Suhonen, and K. Järvinen, "Quantification of the amphetamine content in seized street samples by raman spectroscopy," Journal of forensic sciences **52**, 88–92 (2007).

109. R. A. Shaw and H. H. Mantsch, "Vibrational biospectroscopy: from plants to animals to humans. a historical perspective," Journal of molecular structure **480**, 1–13 (1999).

110. S. Koljenovic, T. B. Schut, A. Vincent, J. M. Kros, and G. J. Puppels, "Detection of meningioma in dura mater by raman spectroscopy," Analytical chemistry **77**, 7958–7965 (2005).

111. A. Carden and M. D. Morris, "Application of vibrational spectroscopy to the study of mineralized tissues (review)," Journal of biomedical optics **5**, 259–268 (2000).

112. H. W. Siesler, *Infrared and Raman spectroscopic imaging* (John Wiley & Sons, 2009).

113. M. Okada, N. I. Smith, A. F. Palonpon, H. Endo, S. Kawata, M. Sodeoka, and K. Fujita, "Label-free raman observation of cytochrome c dynamics during apoptosis," Proceedings of the National Academy of Sciences **109**, 28–32 (2012).

114. B. R. Wood, P. Caspers, G. J. Puppels, S. Pandiancherri, and D. McNaughton, "Resonance raman spectroscopy of red blood cells using near-infrared laser excitation," Analytical and bioanalytical chemistry **387**, 1691–1703 (2007).

115. U. P. Agarwal, "Raman imaging to investigate ultrastructure and composition of plant cell walls: distribution of lignin and cellulose in black spruce wood (picea mariana)," Planta **224**, 1141–1153 (2006).

116. M. Harz, P. Rösch, K.-D. Peschke, O. Ronneberger, H. Burkhardt, and J. Popp, "Micro-raman spectroscopic identification of bacterial cells of the genus staphylococcus and dependence on their cultivation conditions," Analyst **130**, 1543–1550 (2005).

117. A. Williams and H. Edwards, "Fourier transform raman spectroscopy of bacterial cell walls," Journal of Raman spectroscopy **25**, 673–677 (1994).

118. P. C. Cross, J. Burnham, and P. A. Leighton, "The raman spectrum and the structure of water," Journal of the American Chemical Society **59**, 1134–1147 (1937).

119. M. Moskovits and K. Michaelian, "A reinvestigation of the raman spectrum of water," The Journal of Chemical Physics **69**, 2306–2311 (1978).

120. P. Caspers, G. Lucassen, and G. Puppels, "Combined in vivo confocal raman spectroscopy and confocal microscopy of human skin," Biophysical journal **85**, 572–580 (2003).

121. J. R. Mourant, K. W. Short, S. Carpenter, N. Kunapareddy, L. Coburn, T. M. Powers, and J. P. Freyer, "Biochemical differences in tumorigenic and nontumorigenic cells measured by raman and infrared spectroscopy," Journal of biomedical optics **10**, 031106–03110615 (2005).

122. D. Borchman, D. Tang, and M. C. Yappert, "Lipid composition, membrane structure relationships in lens and muscle sarcoplasmic reticulum membranes," Biospectroscopy **5**, 151–167 (1999).

123. J. Mo, W. Zheng, J. J. Low, J. Ng, A. Ilancheran, and Z. Huang, "High wavenumber raman spectroscopy for in vivo detection of cervical dysplasia," Analytical chemistry **81**, 8908–8915 (2009).

124. L. F. Santos, R. Wolthuis, S. Koljenovic, R. M. Almeida, and G. J. Puppels, "Fiber-optic probes for in vivo raman spectroscopy in the high-wavenumber region," Analytical chemistry **77**, 6747–6752 (2005).

125. A. García-Flores, L. Raniero, R. Canevari, K. J. Jalkanen, R. Bitar, H. Martinho, and A. Martin, "High-wavenumber ft-raman spectroscopy for in vivo and ex vivo measurements of breast cancer," Theoretical Chemistry Accounts **130**, 1231–1238 (2011).

126. M. Gniadecka, O. F. Nielsen, S. Wessel, M. Heidenheim, D. H. Christensen, and H. C. Wulf, "Water and protein structure in photoaged and chronically aged skin," Journal of investigative dermatology **111**, 1129–1132 (1998).

127. S. Duraipandian, W. Zheng, J. Ng, J. J. Low, A. Ilancheran, and Z. Huang, "Simultaneous fingerprint and high-wavenumber confocal raman spectroscopy enhances early detection of cervical precancer in vivo," Analytical chemistry **84**, 5913–5919 (2012).

128. N. S. Eikje, Y. Ozaki, K. Aizawa, and S. Arase, "Fiber optic near-infrared raman spectroscopy for clinical noninvasive determination of water content in diseased skin and assessment of cutaneous edema," Journal of biomedical optics **10**, 014013–01401313 (2005).

129. S. Koljenovic, T. Bakker Schut, R. Wolthuis, A. Vincent, G. Hendriks-Hagevi, L. Santos, J. Kros, and G. Puppels, "Raman spectroscopic characterization of porcine brain tissue using a single fiber-optic probe," Analytical chemistry **79**, 557–564 (2007).

130. C. L. Evans, E. O. Potma, M. Puoris' haag, D. Côté, C. P. Lin, and X. S. Xie, "Chemical imaging of tissue in vivo with video-rate coherent anti-stokes raman scattering microscopy," Proceedings of the National Academy of Sciences of the United States of America **102**, 16807–16812 (2005).

131. A. Nijssen, K. Maquelin, L. F. Santos, P. J. Caspers, T. C. B. Schut, J. C. den Hollander, M. H. Neumann, and G. J. Puppels, "Discriminating basal cell

carcinoma from perilesional skin using high wave-number raman spectroscopy," Journal of biomedical optics **12**, 034004–034004 (2007).

132. C. Matthäus, T. Chernenko, J. A. Newmark, C. M. Warner, and M. Diem, "Label-free detection of mitochondrial distribution in cells by nonresonant raman microspectroscopy," Biophysical journal **93**, 668–673 (2007).

133. A. B. Zoladek, R. K. Johal, S. Garcia-Nieto, F. Pascut, K. M. Shakesheff, A. M. Ghaemmaghami, and I. Notingher, "Label-free molecular imaging of immunological synapses between dendritic and t cells by raman micro-spectroscopy," Analyst **135**, 3205–3212 (2010).

134. A. Zoladek, F. C. Pascut, P. Patel, and I. Notingher, "Non-invasive time-course imaging of apoptotic cells by confocal raman micro-spectroscopy," Journal of Raman Spectroscopy **42**, 251–258 (2011).

135. R. J. Swain, G. Jell, and M. M. Stevens, "Non-invasive analysis of cell cycle dynamics in single living cells with raman micro-spectroscopy," Journal of cellular biochemistry **104**, 1427–1438 (2008).

136. F. C. Pascut, S. Kalra, V. George, N. Welch, C. Denning, and I. Notingher, "Non-invasive label-free monitoring the cardiac differentiation of human embryonic stem cells in-vitro by raman spectroscopy," Biochimica et Biophysica Acta (BBA)-General Subjects **1830**, 3517–3524 (2013).

137. K. Watanabe, A. F. Palonpon, N. I. Smith, A. Kasai, H. Hashimoto, S. Kawata, K. Fujita *et al.*, "Structured line illumination raman microscopy," Nature communications **6** (2015).

138. B. Lekprasert, V. Sedman, C. J. Roberts, S. J. Tedler, and I. Notingher, "Nondestructive raman and atomic force microscopy measurement of molecular structure for individual diphenylalanine nanotubes," Optics letters **35**, 4193–4195 (2010).

139. B. Lekprasert, V. Korolkov, A. Falamas, V. Chis, C. J. Roberts, S. J. Tendler, and I. Notingher, "Investigations of the supramolecular structure of individual diphenylalanine nano-and microtubes by polarized raman microspectroscopy," Biomacromolecules **13**, 2181–2187 (2012).

140. F. Sinjab, G. Bondakov, and I. Notingher, "Co-localised raman and force spectroscopy reveal the roles of hydrogen bonds and π-π interactions in defining the mechanical properties of diphenylalanine nano-and micro-tubes," Applied Physics Letters **104**, 251905 (2014).

141. I. Notingher, I. Bisson, A. E. Bishop, W. L. Randle, J. M. Polak, and L. L. Hench, "In situ spectral monitoring of mrna translation in embryonic stem cells during differentiation in vitro," Analytical chemistry **76**, 3185–3193 (2004).

142. H. G. Schulze, S. O. Konorov, N. J. Caron, J. M. Piret, M. W. Blades, and R. F. Turner, "Assessing differentiation status of human embryonic stem cells noninvasively using raman microspectroscopy," Analytical chemistry **82**, 5020–5027 (2010).

143. A. S. Haka, Z. Volynskaya, J. A. Gardecki, J. Nazemi, R. Shenk, N. Wang, R. R. Dasari, M. Fitzmaurice, and M. S. Feld, "Diagnosing breast cancer using raman spectroscopy: prospective analysis," Journal of biomedical optics **14**, 054023–054023 (2009).

144. K. Kong, C. J. Rowlands, S. Varma, W. Perkins, I. H. Leach, A. A. Koloydenko, H. C. Williams, and I. Notingher, "Diagnosis of tumors during tissue-conserving surgery with integrated autofluorescence and raman scattering microscopy," Proceedings of the National Academy of Sciences **110**, 15189–15194 (2013).

145. A. Naemat, H. M. Elsheikha, R. A. Boitor, and I. Notingher, "Tracing amino acid exchange during host-pathogen interaction by combined stable-isotope time-resolved raman spectral imaging," Scientific reports **6** (2016).

146. H.-J. van Manen, Y. M. Kraan, D. Roos, and C. Otto, "Intracellular chemical imaging of heme-containing enzymes involved in innate immunity using resonance raman microscopy," The Journal of Physical Chemistry B **108**, 18762–18771 (2004).

147. M. Larraona-Puy, A. Ghita, A. Zoladek, W. Perkins, S. Varma, I. H. Leach, A. A. Koloydenko, H. Williams, and I. Notingher, "Development of raman microspectroscopy for automated detection and imaging of basal cell carcinoma," Journal of biomedical optics **14**, 054031–054031 (2009).

148. M.-E. Rousseau, T. Lefevre, L. Beaulieu, T. Asakura, and M. Pézolet, "Study of protein conformation and orientation in silkworm and spider silk fibers using raman microspectroscopy," Biomacromolecules **5**, 2247–2257 (2004).

149. E. Ly, A. Durlach, F. Antonicelli, P. Bernard, M. Manfait, and O. Piot, "Probing tumor and peritumoral tissues in superficial and nodular basal cell carcinoma using polarized raman microspectroscopy," Experimental dermatology **19**, 68–73 (2010).

150. R. Thurn and W. Kiefer, "Raman-microsampling technique applying optical levitation by radiation pressure," Applied spectroscopy **38**, 78–83 (1984).

151. J. W. Chan, A. Esposito, C. Talley, C. Hollars, S. Lane, and T. Huser, "Reagentless identification of single bacterial spores in aqueous solution by confocal laser tweezers raman spectroscopy," Analytical chemistry **76**, 599–603 (2004).

152. R. Boitor, F. Sinjab, S. Strohbuecker, V. Sottile, and I. Notingher, "Towards quantitative molecular mapping of cells by raman microscopy: using afm for decoupling molecular concentration and cell topography," Faraday discussions (2015).

153. J. W. Kang, N. Lue, C.-R. Kong, I. Barman, N. C. Dingari, S. J. Goldfless, J. C. Niles, R. R. Dasari, and M. S. Feld, "Combined confocal raman and quantitative phase microscopy system for biomedical diagnosis," Biomedical optics express **2**, 2484–2492 (2011).

154. Z. J. Smith and A. J. Berger, "Integrated raman-and angular-scattering microscopy," Optics letters **33**, 714–716 (2008).

155. Z. J. Smith, J.-C. E. Wang, S. A. Quataert, and A. J. Berger, "Integrated raman and angular scattering microscopy reveals chemical and morphological differences between activated and nonactivated cd8+ t lymphocytes," Journal of biomedical optics **15**, 036021–036021 (2010).

156. P. C. Ashok, B. B. Praveen, N. Bellini, A. Riches, K. Dholakia, and C. S. Herrington, "Multi-modal approach using raman spectroscopy and optical coherence tomography for the discrimination of colonic adenocarcinoma from normal colon," Biomedical optics express **4**, 2179–2186 (2013).

157. M. Bowden, D. J. Gardiner, G. Rice, and D. L. Gerrard, "Line-scanned micro raman spectroscopy using a cooled ccd imaging detector," Journal of Raman spectroscopy **21**, 37–41 (1990).

158. S. Stewart, R. J. Priore, M. P. Nelson, and P. J. Treado, "Raman imaging," Annual Review of Analytical Chemistry **5**, 337–360 (2012).

159. S. Schlücker, M. D. Schaeberle, S. W. Huffman, and I. W. Levin, "Raman microspectroscopy: a comparison of point, line, and wide-field imaging methodologies," Analytical Chemistry **75**, 4312–4318 (2003).

160. A. Z. Samuel, S. Yabumoto, K. Kawamura, and K. Iwata, "Rapid microstructure characterization of polymer thin films with 2d-array multifocus raman microspectroscopy," Analyst **140**, 1847–1851 (2015).

161. M. Okuno and H.-o. Hamaguchi, "Multifocus confocal raman microspectroscopy for fast multimode vibrational imaging of living cells," Optics letters **35**, 4096–4098 (2010).

162. L. Kong, P. Zhang, P. Setlow, and Y.-q. Li, "Multifocus confocal raman microspectroscopy for rapid single-particle analysis," Journal of biomedical optics **16**, 120503–1205033 (2011).

163. L. Kong and J. Chan, "A rapidly modulated multifocal detection scheme for parallel acquisition of raman spectra from a 2-d focal array," Analytical chemistry **86**, 6604–6609 (2014).

164. F. Sinjab, K. Kong, G. Gibson, S. Varma, H. Williams, M. Padgett, and I. Notingher, "Tissue diagnosis using power-sharing multifocal raman micro-spectroscopy and auto-fluorescence imaging," Biomedical Optics Express **7**, 2993–3006 (2016).

165. S. Yang, B. Li, A. Akkus, O. Akkus, and L. Lang, "Wide-field raman imaging of dental lesions," Analyst **139**, 3107–3114 (2014).

166. Y. Oshima, H. Sato, H. Kajiura-Kobayashi, T. Kimura, K. Naruse, and S. Nonaka, "Light sheet-excited spontaneous raman imaging of a living fish by optical sectioning in a wide field raman microscope," Optics Express **20**, 16195–16204 (2012).

167. C. A. Lieber and A. Mahadevan-Jansen, "Automated method for subtraction of fluorescence from biological raman spectra," Applied spectroscopy **57**, 1363–1367 (2003).

168. B. D. Beier and A. J. Berger, "Method for automated background subtraction from raman spectra containing known contaminants," Analyst **134**, 1198–1202 (2009).

169. C. A. Patil, I. J. Pence, C. A. Lieber, and A. Mahadevan-Jansen, "1064 nm dispersive raman spectroscopy of tissues with strong near-infrared autofluorescence," Optics letters **39**, 303–306 (2014).

170. A. C. De Luca, M. Mazilu, A. Riches, C. S. Herrington, and K. Dholakia, "Online fluorescence suppression in modulated raman spectroscopy," Analytical Chemistry **82**, 738–745 (2009).

171. M. Mazilu, A. C. De Luca, A. Riches, C. S. Herrington, and K. Dholakia, "Optimal algorithm for fluorescence suppression of modulated raman spectroscopy," Optics express **18**, 11382–11395 (2010).

172. S. Dochow, N. Bergner, C. Krafft, J. Clement, M. Mazilu, B. B. Praveen, P. C. Ashok, R. Marchington, K. Dholakia, and J. Popp, "Classification of raman spectra of single cells with autofluorescence suppression by wavelength modulated excitation," Analytical Methods **5**, 4608–4614 (2013).

173. E. Canetta, M. Mazilu, A. C. De Luca, A. E. Carruthers, K. Dholakia, S. Neilson, H. Sargeant, T. Briscoe, C. S. Herrington, and A. C. Riches, "Modulated raman spectroscopy for enhanced identification of bladder tumor cells in urine samples," Journal of biomedical optics **16**, 037002–037002 (2011).

174. P. Matousek, M. Towrie, A. Stanley, and A. Parker, "Efficient rejection of fluorescence from raman spectra using picosecond kerr gating," Applied Spectroscopy **53**, 1485–1489 (1999).

175. J. Kostamovaara, J. Tenhunen, M. Kögler, I. Nissinen, J. Nissinen, and P. Keränen, "Fluorescence suppression in raman spectroscopy using a time-gated cmos spad," Optics express **21**, 31632–31645 (2013).

176. M. D. Morris, P. Matousek, M. Towrie, A. W. Parker, A. E. Goodship, and E. R. Draper, "Kerr-gated time-resolved raman spectroscopy of equine cortical bone tissue," Journal of biomedical optics **10**, 014014–0140147 (2005).

177. R. Baker, P. Matousek, K. L. Ronayne, A. W. Parker, K. Rogers, and N. Stone, "Depth profiling of calcifications in breast tissue using picosecond kerr-gated raman spectroscopy," Analyst **132**, 48–53 (2007).

178. T. Hirschfeld and B. Chase, "Ft-raman spectroscopy: development and justification," Applied spectroscopy **40**, 133–137 (1986).

179. B. R. Wood, S. J. Langford, B. M. Cooke, F. K. Glenister, J. Lim, and D. McNaughton, "Raman imaging of hemozoin within the food vacuole of plasmodium falciparum trophozoites," FEBS letters **554**, 247–252 (2003).

180. B. R. Wood, L. Hammer, L. Davis, and D. McNaughton, "Raman microspectroscopy and imaging provides insights into heme aggregation and denaturation within human erythrocytes," Journal of biomedical optics **10**, 014005–01400513 (2005).

181. G. Puppels, J. Olminkhof, G. Segers-Nolten, C. Otto, F. De Mul, and J. Greve, "Laser irradiation and raman spectroscopy of single living cells and chromosomes: sample degradation occurs with 514.5 nm but not with 660 nm laser light," Experimental cell research **195**, 361–367 (1991).

182. I. Notingher, S. Verrier, H. Romanska, A. Bishop, J. Polak, and L. Hench, "In situ characterisation of living cells by raman spectroscopy," Journal of Spectroscopy **16**, 43–51 (2002).

183. P. P. Calmettes and M. W. Berns, "Laser-induced multiphoton processes in living cells," Proceedings of the National Academy of Sciences **80**, 7197–7199 (1983).

184. H. Friedmann and R. Lubart, "Towards an explanation of visible and infrared laser induced stimulation and damage of cell cultures," Laser Therapy **4**, 39–42 (1992).

185. K. König, Y. Tadir, P. Patrizio, M. W. Berns, and B. J. Tromberg, "Andrology: Effects of ultraviolet exposure and near infrared laser tweezers on human spermatozoa," Human Reproduction **11**, 2162–2164 (1996).

186. H. Liang, K. T. Vu, P. Krishnan, T. C. Trang, D. Shin, S. Kimel, and M. W. Berns, "Wavelength dependence of cell cloning efficiency after optical trapping." Biophysical journal **70**, 1529 (1996).

187. K. C. Neuman, E. H. Chadd, G. F. Liou, K. Bergman, and S. M. Block, "Characterization of photodamage to escherichia coli in optical traps," Biophysical journal **77**, 2856–2863 (1999).

188. M. D. Manson, P. Tedesco, and H. C. Berg, "Energetics of flagellar rotation in bacteria," Journal of molecular biology **138**, 541–561 (1980).

189. G. Leitz, E. Fällman, S. Tuck, and O. Axner, "Stress response in caenorhabditis elegans caused by optical tweezers: wavelength, power, and time dependence," Biophysical journal **82**, 2224–2231 (2002).

190. F. Draux, P. Jeannesson, A. Beljebbar, A. Tfayli, N. Fourre, M. Manfait, J. Sulé-Suso, and G. D. Sockalingum, "Raman spectral imaging of single living cancer cells: a preliminary study," Analyst **134**, 542–548 (2009).

191. A. Ghita, F. C. Pascut, M. Mather, V. Sottile, and I. Notingher, "Cytoplasmic rna in undifferentiated neural stem cells: a potential label-free raman spectral marker for assessing the undifferentiated status," Analytical chemistry **84**, 3155–3162 (2012).

192. F. C. Pascut, H. T. Goh, N. Welch, L. D. Buttery, C. Denning, and I. Notingher, "Noninvasive detection and imaging of molecular markers in live cardiomyocytes derived from human embryonic stem cells," Biophysical journal **100**, 251–259 (2011).

193. A. Mitchell, L. Ashton, X. B. Yang, R. Goodacre, A. Smith, and J. Kirkham, "Detection of early stage changes associated with adipogenesis using raman spectroscopy under aseptic conditions," Cytometry Part A **87**, 1012–1019 (2015).

194. K. König, "Multiphoton microscopy in life sciences," Journal of microscopy **200**, 83–104 (2000).

195. V. Yakovlev, "Advanced instrumentation for non-linear raman microscopy," Journal of Raman Spectroscopy **34**, 957–964 (2003).

196. Y. Fu, H. Wang, R. Shi, and J.-X. Cheng, "Characterization of photodamage in coherent anti-stokes raman scattering microscopy," Optics Express **14**, 3942–3951 (2006).

197. B. Salmaso, G. Puppels, P. Caspers, R. Floris, R. Wever, and J. Greve, "Resonance raman microspectroscopic characterization of eosinophil peroxidase in human eosinophilic granulocytes." Biophysical journal **67**, 436 (1994).

198. N. Sijtsema, C. Otto, G. Segers-Nolten, A. Verhoeven, and J. Greve, "Resonance raman microspectroscopy of myeloperoxidase and cytochrome b 558 in human neutrophilic granulocytes," Biophysical journal **74**, 3250–3255 (1998).

199. G. Puppels, H. Garritsen, J. Kummer, and J. Greve, "Carotenoids located in human lymphocyte subpopulations and natural killer cells by raman microspectroscopy," Cytometry **14**, 251–256 (1993).

200. K. Ramser, E. Malinina, and S. Candefjord, "Resonance micro-raman investigations of the rat medial preoptic nucleus: Effects of a low-iron diet on the neuroglobin content," Applied spectroscopy **66**, 1454–1460 (2012).

201. B. R. Wood, A. Hermelink, P. Lasch, K. R. Bambery, G. T. Webster, M. A. Khiavi, B. M. Cooke, S. Deed, D. Naumann, and D. McNaughton, "Resonance raman microscopy in combination with partial dark-field microscopy lights up a new path in malaria diagnostics," Analyst **134**, 1119–1125 (2009).

202. S. D. Bergeson, J. B. Peatross, N. J. Eyring, J. F. Fralick, D. N. Stevenson, and S. B. Ferguson, "Resonance raman measurements of carotenoids using light-emitting diodes," Journal of biomedical optics **13**, 044026–044026 (2008).

203. A. Alfonso-García, R. Mittal, E. S. Lee, and E. O. Potma, "Biological imaging with coherent raman scattering microscopy: a tutorial," Journal of biomedical optics **19**, 071407–071407 (2014).

204. J. P. Pezacki, J. A. Blake, D. C. Danielson, D. C. Kennedy, R. K. Lyn, and R. Singaravelu, "Chemical contrast for imaging living systems: molecular vibrations drive cars microscopy," Nature chemical biology **7**, 137–145 (2011).

205. T. T. Le, S. Yue, and J.-X. Cheng, "Shedding new light on lipid biology with coherent anti-stokes raman scattering microscopy," Journal of lipid research **51**, 3091–3102 (2010).

206. M. D. Duncan, J. Reintjes, and T. Manuccia, "Scanning coherent anti-stokes raman microscope," Optics letters **7**, 350–352 (1982).

207. A. Zumbusch, G. R. Holtom, and X. S. Xie, "Three-dimensional vibrational imaging by coherent anti-stokes raman scattering," Physical review letters **82**, 4142 (1999).

208. M. Baumgartl, M. Chemnitz, C. Jauregui, T. Meyer, B. Dietzek, J. Popp, J. Limpert, and A. Tünnermann, "All-fiber laser source for cars microscopy based on fiber optical parametric frequency conversion," Optics express **20**, 4484–4493 (2012).

209. M. Müller and J. M. Schins, "Imaging the thermodynamic state of lipid membranes with multiplex cars microscopy," The Journal of Physical Chemistry B **106**, 3715–3723 (2002).

210. G. W. Wurpel, J. M. Schins, and M. Müller, "Chemical specificity in three-dimensional imaging with multiplex coherent anti-stokes raman scattering microscopy," Optics letters **27**, 1093–1095 (2002).

211. J.-x. Cheng, A. Volkmer, L. D. Book, and X. S. Xie, "Multiplex coherent anti-stokes raman scattering microspectroscopy and study of lipid vesicles," The Journal of Physical Chemistry B **106**, 8493–8498 (2002).

212. F. Ganikhanov, C. L. Evans, B. G. Saar, and X. S. Xie, "High-sensitivity vibrational imaging with frequency modulation coherent anti-stokes raman scattering (fm cars) microscopy," Optics letters **31**, 1872–1874 (2006).

213. A. F. Pegoraro, A. Ridsdale, D. J. Moffatt, Y. Jia, J. P. Pezacki, and A. Stolow, "Optimally chirped multimodal cars microscopy based on a single ti: sapphire oscillator," Optics express **17**, 2984–2996 (2009).

214. C. Di Napoli, I. Pope, F. Masia, P. Watson, W. Langbein, and P. Borri, "Hyperspectral and differential cars microscopy for quantitative chemical imaging in human adipocytes," Biomedical optics express **5**, 1378–1390 (2014).

215. C. H. Camp Jr, Y. J. Lee, J. M. Heddleston, C. M. Hartshorn, A. R. H. Walker, J. N. Rich, J. D. Lathia, and M. T. Cicerone, "High-speed coherent raman fingerprint imaging of biological tissues," Nature photonics **8**, 627–634 (2014).

216. I. S. Ryu, C. H. Camp, Y. Jin, M. T. Cicerone, and Y. J. Lee, "Beam scanning for rapid coherent raman hyperspectral imaging," Optics letters **40**, 5826–5829 (2015).

217. T. Ideguchi, S. Holzner, B. Bernhardt, G. Guelachvili, N. Picqué, and T. W. Hänsch, "Coherent raman spectro-imaging with laser frequency combs," Nature **502**, 355–358 (2013).

218. E. O. Potma, W. P. de Boeij, P. J. van Haastert, and D. A. Wiersma, "Real-time visualization of intracellular hydrodynamics in single living cells," Proceedings of the National Academy of Sciences **98**, 1577–1582 (2001).

219. J.-X. Cheng, Y. K. Jia, G. Zheng, and X. S. Xie, "Laser-scanning coherent anti-stokes raman scattering microscopy and applications to cell biology," Biophysical journal **83**, 502–509 (2002).

220. E. O. Potma and X. S. Xie, "Detection of single lipid bilayers with coherent anti-stokes raman scattering (cars) microscopy," Journal of Raman spectroscopy **34**, 642–650 (2003).

221. C. Steuwe, C. F. Kaminski, J. J. Baumberg, and S. Mahajan, "Surface enhanced coherent anti-stokes raman scattering on nanostructured gold surfaces," Nano letters **11**, 5339–5343 (2011).

222. A. Fast, J. P. Kenison, C. D. Syme, and E. O. Potma, "Surface-enhanced coherent anti-stokes raman imaging of lipids," Applied optics **55**, 5994–6000 (2016).

223. X. Nan, J.-X. Cheng, and X. S. Xie, "Vibrational imaging of lipid droplets in live fibroblast cells with coherent anti-stokes raman scattering microscopy," Journal of lipid research **44**, 2202–2208 (2003).

224. S. F. El-Mashtoly, D. Niedieker, D. Petersen, S. D. Krauss, E. Freier, A. Maghnouj, A. Mosig, S. Hahn, C. Kötting, and K. Gerwert, "Automated identification of subcellular organelles by coherent anti-stokes raman scattering," Biophysical journal **106**, 1910–1920 (2014).

225. A. Downes, R. Mouras, P. Bagnaninchi, and A. Elfick, "Raman spectroscopy and cars microscopy of stem cells and their derivatives," Journal of Raman Spectroscopy **42**, 1864–1870 (2011).

226. C. Steuwe, I. I. Patel, M. Ul-Hasan, A. Schreiner, J. Boren, K. M. Brindle, S. Reichelt, and S. Mahajan, "Cars based label-free assay for assessment of drugs by monitoring lipid droplets in tumour cells," Journal of biophotonics **7**, 906–913 (2014).

227. T. Hellerer, C. Axäng, C. Brackmann, P. Hillertz, M. Pilon, and A. Enejder, "Monitoring of lipid storage in caenorhabditis elegans using coherent anti-stokes raman scattering (cars) microscopy," Proceedings of the National Academy of Sciences **104**, 14658–14663 (2007).

228. X. Nan, A. M. Tonary, A. Stolow, X. S. Xie, and J. P. Pezacki, "Intracellular imaging of hcv rna and cellular lipids by using simultaneous two-photon fluorescence and coherent anti-stokes raman scattering microscopies," ChemBioChem **7**, 1895–1897 (2006).

229. T. T. Le and J.-X. Cheng, "Single-cell profiling reveals the origin of phenotypic variability in adipogenesis," PLoS One **4**, e5189 (2009).

230. C. L. Evans, X. Xu, S. Kesari, X. S. Xie, S. T. Wong, and G. S. Young, "Chemically-selective imaging of brain structures with cars microscopy," Optics express **15**, 12076–12087 (2007).

231. Y. Fu, H. Wang, T. B. Huff, R. Shi, and J.-X. Cheng, "Coherent anti-stokes raman scattering imaging of myelin degradation reveals a calcium-dependent pathway in lyso-ptdcho-induced demyelination," Journal of neuroscience research **85**, 2870–2881 (2007).

232. N. Garrett, A. Lalatsa, D. Begley, L. Mihoreanu, I. Uchegbu, A. Schätzlein, and J. Moger, "Label-free imaging of polymeric nanomedicines using coherent anti-stokes raman scattering microscopy," Journal of Raman Spectroscopy **43**, 681–688 (2012).

233. J. Moger, B. D. Johnston, and C. R. Tyler, "Imaging metal oxide nanoparticles in biological structures with cars microscopy," Optics express **16**, 3408–3419 (2008).

234. J. Zhu, B. Lee, K. K. Buhman, and J.-X. Cheng, "A dynamic, cytoplasmic triacylglycerol pool in enterocytes revealed by ex vivo and in vivo coherent anti-stokes raman scattering imaging," Journal of lipid research **50**, 1080–1089 (2009).

235. H.-W. Wang, I. M. Langohr, M. Sturek, and J.-X. Cheng, "Imaging and quantitative analysis of atherosclerotic lesions by cars-based multimodal nonlinear optical microscopy," Arteriosclerosis, thrombosis, and vascular biology **29**, 1342–1348 (2009).

236. S.-H. Kim, E.-S. Lee, J. Y. Lee, E. S. Lee, B.-S. Lee, J. E. Park, and D. W. Moon, "Multiplex coherent anti-stokes raman spectroscopy images intact atheromatous lesions and concomitantly identifies distinct chemical profiles of atherosclerotic lipids," Circulation research **106**, 1332–1341 (2010).

237. A. F. Pegoraro, A. D. Slepkov, A. Ridsdale, D. J. Moffatt, and A. Stolow, "Hyperspectral multimodal cars microscopy in the fingerprint region," J. Biophotonics **7**, 49–58 (2014).

238. T. Meyer, N. Bergner, A. Medyukhina, B. Dietzek, C. Krafft, B. F. Romeike, R. Reichart, R. Kalff, and J. Popp, "Interpreting cars images of tissue within the c–h-stretching region," Journal of biophotonics **5**, 729–733 (2012).

239. C. Krafft, A. A. Ramoji, C. Bielecki, N. Vogler, T. Meyer, D. Akimov, P. Rösch, M. Schmitt, B. Dietzek, I. Petersen *et al.*, "A comparative raman and cars imaging study of colon tissue," Journal of biophotonics **2**, 303–312 (2009).

240. M. Balu, G. Liu, Z. Chen, B. J. Tromberg, and E. O. Potma, "Fiber delivered probe for efficient cars imaging of tissues," Optics express **18**, 2380–2388 (2010).

241. E. Ploetz, S. Laimgruber, S. Berner, W. Zinth, and P. Gilch, "Femtosecond stimulated raman microscopy," Applied Physics B **87**, 389–393 (2007).

242. C. W. Freudiger, W. Min, B. G. Saar, S. Lu, G. R. Holtom, C. He, J. C. Tsai, J. X. Kang, and X. S. Xie, "Label-free biomedical imaging with high sensitivity by stimulated raman scattering microscopy," Science **322**, 1857–1861 (2008).

243. B. G. Saar, C. W. Freudiger, J. Reichman, C. M. Stanley, G. R. Holtom, and X. S. Xie, "Video-rate molecular imaging in vivo with stimulated raman scattering," Science **330**, 1368–1370 (2010).

244. C. W. Freudiger, W. Min, G. R. Holtom, B. Xu, M. Dantus, and X. S. Xie, "Highly specific label-free molecular imaging with spectrally tailored excitation-stimulated raman scattering (ste-srs) microscopy," Nature photonics **5**, 103–109 (2011).

245. L. Kong, M. Ji, G. R. Holtom, D. Fu, C. W. Freudiger, and X. S. Xie, "Multicolor stimulated raman scattering microscopy with a rapidly tunable optical parametric oscillator," Optics letters **38**, 145–147 (2013).

246. H. T. Beier, G. D. Noojin, and B. A. Rockwell, "Stimulated raman scattering using a single femtosecond oscillator with flexibility for imaging and spectral applications," Optics express **19**, 18885–18892 (2011).

247. M. N. Slipchenko, R. A. Oglesbee, D. Zhang, W. Wu, and J.-X. Cheng, "Heterodyne detected nonlinear optical imaging in a lock-in free manner," Journal of biophotonics **5**, 801–807 (2012).

248. C.-S. Liao, M. N. Slipchenko, P. Wang, J. Li, S.-Y. Lee, R. A. Oglesbee, and J.-X. Cheng, "Microsecond scale vibrational spectroscopic imaging by multiplex stimulated raman scattering microscopy," Light: Science & Applications **4**, e265 (2015).

249. C. W. Freudiger, W. Yang, G. R. Holtom, N. Peyghambarian, X. S. Xie, and K. Q. Kieu, "Stimulated raman scattering microscopy with a robust fibre laser source," Nature photonics **8**, 153–159 (2014).

250. T. Steinle, V. Kumar, M. Floess, A. Steinmann, M. Marangoni, C. Koch, C. Wege, G. Cerullo, and H. Giessen, "Synchronization-free all-solid-state laser system for stimulated raman scattering microscopy," Light: Science and Applications (2016).

251. L. Wei, Y. Yu, Y. Shen, M. C. Wang, and W. Min, "Vibrational imaging of newly synthesized proteins in live cells by stimulated raman scattering microscopy," Proceedings of the National Academy of Sciences **110**, 11226–11231 (2013).

252. L. Wei, F. Hu, Y. Shen, Z. Chen, Y. Yu, C.-C. Lin, M. C. Wang, and W. Min, "Live-cell imaging of alkyne-tagged small biomolecules by stimulated raman scattering," Nature methods **11**, 410–412 (2014).

253. F.-K. Lu, S. Basu, V. Igras, M. P. Hoang, M. Ji, D. Fu, G. R. Holtom, V. A. Neel, C. W. Freudiger, D. E. Fisher *et al.*, "Label-free dna imaging in vivo with stimulated raman scattering microscopy," Proceedings of the National Academy of Sciences **112**, 11624–11629 (2015).

254. D. Fu, F.-K. Lu, X. Zhang, C. Freudiger, D. R. Pernik, G. Holtom, and X. S. Xie, "Quantitative chemical imaging with multiplex stimulated raman scattering microscopy," Journal of the American Chemical Society **134**, 3623–3626 (2012).

255. C. W. Freudiger, R. Pfannl, D. A. Orringer, B. G. Saar, M. Ji, Q. Zeng, L. Ottoboni, W. Ying, C. Waeber, J. R. Sims *et al.*, "Multicolored stain-free histopathology with coherent raman imaging," Laboratory investigation **92**, 1492–1502 (2012).

256. Y. Ozeki, W. Umemura, Y. Otsuka, S. Satoh, H. Hashimoto, K. Sumimura, N. Nishizawa, K. Fukui, and K. Itoh, "High-speed molecular spectral imaging of tissue with stimulated raman scattering," Nature photonics **6**, 845–851 (2012).

257. M. Ji, S. Lewis, S. Camelo-Piragua, S. H. Ramkissoon, M. Snuderl, S. Venneti, A. Fisher-Hubbard, M. Garrard, D. Fu, A. C. Wang *et al.*, "Detection of human brain tumor infiltration with quantitative stimulated raman scattering microscopy," Science translational medicine **7**, 309ra163–309ra163 (2015).

258. F.-K. Lu, D. Calligaris, O. I. Olubiyi, I. Norton, W. Yang, S. Santagata, X. S. Xie, A. J. Golby, and N. Y. Agar, "Label-free neurosurgical pathology with stimulated raman imaging," Cancer research pp. canres–0270 (2016).

259. H. Tu, Y. Liu, D. Turchinovich, M. Marjanovic, J. K. Lyngsø, J. Lægsgaard, E. J. Chaney, Y. Zhao, S. You, W. L. Wilson *et al.*, "Stain-free histopathology by programmable supercontinuum pulses," Nature Photonics (2016).

260. B. G. Saar, L. R. Contreras-Rojas, X. S. Xie, and R. H. Guy, "Imaging drug delivery to skin with stimulated raman scattering microscopy," Molecular pharmaceutics **8**, 969–975 (2011).

261. D. Fu, J. Zhou, W. S. Zhu, P. W. Manley, Y. K. Wang, T. Hood, A. Wylie, and X. S. Xie, "Imaging the intracellular distribution of tyrosine kinase inhibitors in living cells with quantitative hyperspectral stimulated raman scattering," Nature chemistry **6**, 614–622 (2014).

262. W. S. Chiu, N. A. Belsey, N. L. Garrett, J. Moger, M. B. Delgado-Charro, and R. H. Guy, "Molecular diffusion in the human nail measured by stimulated raman scattering microscopy," Proceedings of the National Academy of Sciences **112**, 7725–7730 (2015).

263. J. C. Mansfield, G. R. Littlejohn, M. P. Seymour, R. J. Lind, S. Perfect, and J. Moger, "Label-free chemically specific imaging in planta with stimulated raman scattering microscopy," Analytical chemistry **85**, 5055–5063 (2013).

264. M. C. Fischer, J. W. Wilson, F. E. Robles, and W. S. Warren, "Invited review article: Pump-probe microscopy," Review of Scientific Instruments **87**, 031101 (2016).

265. M. N. Slipchenko, T. T. Le, H. Chen, and J.-X. Cheng, "High-speed vibrational imaging and spectral analysis of lipid bodies by compound raman microscopy," The Journal of Physical Chemistry B **113**, 7681–7686 (2009).

266. P. Wang, B. Liu, D. Zhang, M. Y. Belew, H. A. Tissenbaum, and J.-X. Cheng, "Imaging lipid metabolism in live caenorhabditis elegans using fingerprint vibrations," Angewandte Chemie International Edition **53**, 11787–11792 (2014).

267. W. Smith, "Practical understanding and use of surface enhanced raman scattering/surface enhanced resonance raman scattering in chemical and biological analysis," Chemical Society Reviews **37**, 955–964 (2008).

268. S. Schlücker, "Sers microscopy: nanoparticle probes and biomedical applications," ChemPhysChem **10**, 1344–1354 (2009).

269. G. McNay, D. Eustace, W. E. Smith, K. Faulds, and D. Graham, "Surface-enhanced raman scattering (sers) and surface-enhanced resonance raman scattering (serrs): a review of applications," Applied spectroscopy **65**, 825–837 (2011).

270. K. Saha, S. S. Agasti, C. Kim, X. Li, and V. M. Rotello, "Gold nanoparticles in chemical and biological sensing," Chemical reviews **112**, 2739–2779 (2012).

271. M. M. Harper, K. S. McKeating, and K. Faulds, "Recent developments and future directions in sers for bioanalysis," Physical Chemistry Chemical Physics **15**, 5312–5328 (2013).

272. J. Kneipp, H. Kneipp, B. Wittig, and K. Kneipp, "Novel optical nanosensors for probing and imaging live cells," Nanomedicine: Nanotechnology, Biology and Medicine **6**, 214–226 (2010).

273. E. A. Vitol, Z. Orynbayeva, G. Friedman, and Y. Gogotsi, "Nanoprobes for intracellular and single cell surface-enhanced raman spectroscopy (sers)," Journal of Raman Spectroscopy **43**, 817–827 (2012).

274. B. Kann, H. L. Offerhaus, M. Windbergs, and C. Otto, "Raman microscopy for cellular investigations-from single cell imaging to drug carrier uptake visualization," Advanced drug delivery reviews **89**, 71–90 (2015).

275. D. Radziuk and H. Moehwald, "Prospects for plasmonic hot spots in single molecule sers towards the chemical imaging of live cells," Physical Chemistry Chemical Physics **17**, 21072–21093 (2015).

276. X.-M. Qian and S. Nie, "Single-molecule and single-nanoparticle sers: from fundamental mechanisms to biomedical applications," Chemical Society Reviews **37**, 912–920 (2008).

277. L. A. Austin, M. A. Mackey, E. C. Dreaden, and M. A. El-Sayed, "The optical, photothermal, and facile surface chemical properties of gold and silver nanoparticles in biodiagnostics, therapy, and drug delivery," Archives of toxicology **88**, 1391–1417 (2014).

278. D. Drescher and J. Kneipp, "Nanomaterials in complex biological systems: insights from raman spectroscopy," Chemical Society Reviews **41**, 5780–5799 (2012).

279. B. Pelaz, G. Charron, C. Pfeiffer, Y. Zhao, J. M. De La Fuente, X.-J. Liang, W. J. Parak, and P. Del Pino, "Interfacing engineered nanoparticles with biological systems: anticipating adverse nano–bio interactions," Small **9**, 1573–1584 (2013).

280. J. Turkevich, P. C. Stevenson, and J. Hillier, "A study of the nucleation and growth processes in the synthesis of colloidal gold," Discussions of the Faraday Society **11**, 55–75 (1951).

281. P. Lee and D. Meisel, "Adsorption and surface-enhanced raman of dyes on silver and gold sols," The Journal of Physical Chemistry **86**, 3391–3395 (1982).

282. K. Kneipp, A. S. Haka, H. Kneipp, K. Badizadegan, N. Yoshizawa, C. Boone, K. E. Shafer-Peltier, J. T. Motz, R. R. Dasari, and M. S. Feld, "Surface-enhanced raman spectroscopy in single living cells using gold nanoparticles," Applied Spectroscopy **56**, 150–154 (2002).

283. J. Kneipp, H. Kneipp, A. Rajadurai, R. W. Redmond, and K. Kneipp, "Optical probing and imaging of live cells using sers labels," Journal of Raman Spectroscopy **40**, 1–5 (2009).

284. J. Kneipp, H. Kneipp, W. L. Rice, and K. Kneipp, "Optical probes for biological applications based on surface-enhanced raman scattering from indocyanine green on gold nanoparticles," Analytical chemistry **77**, 2381–2385 (2005).

285. C. Eliasson, A. Lorén, J. Engelbrektsson, M. Josefson, J. Abrahamsson, and K. Abrahamsson, "Surface-enhanced raman scattering imaging of single living lymphocytes with multivariate evaluation," Spectrochimica Acta Part A: Molecular and Biomolecular Spectroscopy **61**, 755–760 (2005).

286. D. Drescher, T. Büchner, D. McNaughton, and J. Kneipp, "Sers reveals the specific interaction of silver and gold nanoparticles with hemoglobin and red blood cell components," Physical Chemistry Chemical Physics **15**, 5364–5373 (2013).

287. J. Kneipp, H. Kneipp, M. McLaughlin, D. Brown, and K. Kneipp, "In vivo molecular probing of cellular compartments with gold nanoparticles and nanoaggregates," Nano Letters **6**, 2225–2231 (2006).

288. Ö. F. Karataş, E. Sezgin, Ö. Aydın, and M. Çulha, "Interaction of gold nanoparticles with mitochondria," Colloids and Surfaces B: Biointerfaces **71**, 315–318 (2009).

289. R. R. Sathuluri, H. Yoshikawa, E. Shimizu, M. Saito, and E. Tamiya, "Gold nanoparticle-based surface-enhanced raman scattering for noninvasive molecular probing of embryonic stem cell differentiation," PloS one **6**, e22802 (2011).

290. A. Huefner, W.-L. Kuan, R. A. Barker, and S. Mahajan, "Intracellular sers nanoprobes for distinction of different neuronal cell types," Nano letters **13**, 2463–2470 (2013).

291. A. Sujith, T. Itoh, H. Abe, A. A. Anas, K. Yoshida, V. Biju, and M. Ishikawa, "Surface enhanced raman scattering analyses of individual silver nanoaggregates on living single yeast cell wall," Applied Physics Letters **92**, 103901 (2008).

292. M. D. Hodges, J. G. Kelly, A. J. Bentley, S. Fogarty, I. I. Patel, F. L. Martin, and N. J. Fullwood, "Combining immunolabeling and surface-enhanced raman spectroscopy on cell membranes," ACS nano **5**, 9535–9541 (2011).

293. M. K. Gregas, J. P. Scaffidi, B. Lauly, and T. Vo-Dinh, "Surface-enhanced raman scattering detection and tracking of nanoprobes: enhanced uptake and nuclear targeting in single cells," Applied spectroscopy **64**, 858–866 (2010).

294. M. K. Gregas, F. Yan, J. Scaffidi, H.-N. Wang, and T. Vo-Dinh, "Characterization of nanoprobe uptake in single cells: spatial and temporal tracking via sers labeling and modulation of surface charge," Nanomedicine: Nanotechnology, Biology and Medicine **7**, 115–122 (2011).

295. A. Matschulat, D. Drescher, and J. Kneipp, "Surface-enhanced raman scattering hybrid nanoprobe multiplexing and imaging in biological systems," ACS nano **4**, 3259–3269 (2010).

296. J. W. Kang, P. T. So, R. R. Dasari, and D.-K. Lim, "High resolution live cell raman imaging using subcellular organelle-targeting sers-sensitive gold nanoparticles with highly narrow intra-nanogap," Nano letters **15**, 1766–1772 (2015).

297. B. Kang, L. A. Austin, and M. A. El-Sayed, "Real-time molecular imaging throughout the entire cell cycle by targeted plasmonic-enhanced rayleigh/raman spectroscopy," Nano letters **12**, 5369–5375 (2012).

298. C. E. Talley, L. Jusinski, C. W. Hollars, S. M. Lane, and T. Huser, "Intracellular ph sensors based on surface-enhanced raman scattering," Analytical chemistry **76**, 7064–7068 (2004).

299. S. Jung, J. Nam, S. Hwang, J. Park, J. Hur, K. Im, N. Park, and S. Kim, "Theragnostic ph-sensitive gold nanoparticles for the selective surface enhanced raman scattering and photothermal cancer therapy," Analytical chemistry **85**, 7674–7681 (2013).

300. C. A. Auchinvole, P. Richardson, C. McGuinnes, V. Mallikarjun, K. Donaldson, H. McNab, and C. J. Campbell, "Monitoring intracellular redox potential changes using sers nanosensors," ACS nano **6**, 888–896 (2011).

301. A. Jaworska, L. E. Jamieson, K. Malek, C. J. Campbell, J. Choo, S. Chlopicki, and M. Baranska, "Sers-based monitoring of the intracellular ph in endothelial cells: the influence of the extracellular environment and tumour necrosis factor-α," Analyst **140**, 2321–2329 (2015).

302. J. Jiang, C. Auchinvole, K. Fisher, and C. J. Campbell, "Quantitative measurement of redox potential in hypoxic cells using sers nanosensors," Nanoscale **6**, 12104–12110 (2014).

303. H.-W. Tang, X. B. Yang, J. Kirkham, and D. A. Smith, "Probing intrinsic and extrinsic components in single osteosarcoma cells by near-infrared surface-enhanced raman scattering," Analytical chemistry **79**, 3646–3653 (2007).

304. S. Mert and M. Çulha, "Surface-enhanced raman scattering-based detection of cancerous renal cells," Applied spectroscopy **68**, 617–624 (2014).

305. S. Lee, S. Kim, J. Choo, S. Y. Shin, Y. H. Lee, H. Y. Choi, S. Ha, K. Kang, and C. H. Oh, "Biological imaging of hek293 cells expressing plcγ1 using surface-enhanced raman microscopy," Analytical chemistry **79**, 916–922 (2007).

306. X. Wang, X. Qian, J. J. Beitler, Z. G. Chen, F. R. Khuri, M. M. Lewis, H. J. C. Shin, S. Nie, and D. M. Shin, "Detection of circulating tumor cells in human peripheral blood using surface-enhanced raman scattering nanoparticles," Cancer research **71**, 1526–1532 (2011).

307. D. Craig, S. McAughtrie, J. Simpson, C. McCraw, K. Faulds, and D. Graham, "Confocal sers mapping of glycan expression for the identification of

cancerous cells," Analytical chemistry **86**, 4775–4782 (2014).

308. X. Huang, I. H. El-Sayed, W. Qian, and M. A. El-Sayed, "Cancer cells assemble and align gold nanorods conjugated to antibodies to produce highly enhanced, sharp, and polarized surface raman spectra: a potential cancer diagnostic marker," Nano letters **7**, 1591–1597 (2007).

309. A. Indrasekara, B. J. Paladini, D. J. Naczynski, V. Starovoytov, P. V. Moghe, and L. Fabris, "Dimeric gold nanoparticle assemblies as tags for sers-based cancer detection," Advanced healthcare materials **2**, 1370–1376 (2013).

310. K. K. Maiti, A. Samanta, M. Vendrell, K.-S. Soh, M. Olivo, and Y.-T. Chang, "Multiplex cancer cell detection by sers nanotags with cyanine and triphenylmethine raman reporters," Chemical communications **47**, 3514–3516 (2011).

311. S. Lee, H. Chon, J. Lee, J. Ko, B. H. Chung, D. W. Lim, and J. Choo, "Rapid and sensitive phenotypic marker detection on breast cancer cells using surface-enhanced raman scattering (sers) imaging," Biosensors and Bioelectronics **51**, 238–243 (2014).

312. S. Lee, H. Chon, S.-Y. Yoon, E. K. Lee, S.-I. Chang, D. W. Lim, and J. Choo, "Fabrication of sers-fluorescence dual modal nanoprobes and application to multiplex cancer cell imaging," Nanoscale **4**, 124–129 (2012).

313. S. McAughtrie, K. Lau, K. Faulds, and D. Graham, "3d optical imaging of multiple sers nanotags in cells," Chemical Science **4**, 3566–3572 (2013).

314. A. Huefner, D. Septiadi, B. D. Wilts, I. I. Patel, W.-L. Kuan, A. Fragniere, R. A. Barker, and S. Mahajan, "Gold nanoparticles explore cells: Cellular uptake and their use as intracellular probes," Methods **68**, 354–363 (2014).

315. K.-C. Huang, K. Bando, J. Ando, N. I. Smith, K. Fujita, and S. Kawata, "3d sers (surface enhanced raman scattering) imaging of intracellular pathways," Methods **68**, 348–353 (2014).

316. K. Bando, N. I. Smith, J. Ando, K. Fujita, and S. Kawata, "Analysis of dynamic sers spectra measured with a nanoparticle during intracellular transportation in 3d," Journal of Optics **17**, 114023 (2015).

317. Y. Chen, X. Bai, L. Su, Z. Du, A. Shen, A. Materny, and J. Hu, "Combined labelled and label-free sers probes for triplex three-dimensional cellular imaging," Scientific reports **6** (2016).

318. N. Pavillon, K. Bando, K. Fujita, and N. I. Smith, "Feature-based recognition of surface-enhanced raman spectra for biological targets," Journal of biophotonics **6**, 587–597 (2013).

319. R. M. Jarvis and R. Goodacre, "Discrimination of bacteria using surface-enhanced raman spectroscopy," Analytical Chemistry **76**, 40–47 (2004).

320. W. Premasiri, D. Moir, M. Klempner, N. Krieger, G. Jones, and L. Ziegler, "Characterization of the surface enhanced raman scattering (sers) of bacteria," The journal of physical chemistry B **109**, 312–320 (2005).

321. I. Patel, W. Premasiri, D. Moir, and L. Ziegler, "Barcoding bacterial cells: a sers-based methodology for pathogen identification," Journal of Raman Spectroscopy **39**, 1660–1672 (2008).

322. L. Cui, P. Chen, S. Chen, Z. Yuan, C. Yu, B. Ren, and K. Zhang, "In situ study of the antibacterial activity and mechanism of action of silver nanoparticles by surface-enhanced raman spectroscopy," Analytical chemistry **85**, 5436–5443 (2013).

323. L. J. Goeller and M. R. Riley, "Discrimination of bacteria and bacteriophages by raman spectroscopy and surface-enhanced raman spectroscopy," Applied spectroscopy **61**, 679–685 (2007).

324. N. P. Ivleva, M. Wagner, H. Horn, R. Niessner, and C. Haisch, "In situ surface-enhanced raman scattering analysis of biofilm," Analytical chemistry **80**, 8538–8544 (2008).

325. N. P. Ivleva, M. Wagner, A. Szkola, H. Horn, R. Niessner, and C. Haisch, "Label-free in situ sers imaging of biofilms," The Journal of Physical Chemistry B **114**, 10184–10194 (2010).

326. N. P. Ivleva, M. Wagner, H. Horn, R. Niessner, and C. Haisch, "Raman microscopy and surface-enhanced raman scattering (sers) for in situ analysis of biofilms," Journal of biophotonics **3**, 548–556 (2010).

327. G. Bodelón, V. Montes-García, V. López-Puente, E. H. Hill, C. Hamon, M. N. Sanz-Ortiz, S. Rodal-Cedeira, C. Costas, S. Celiksoy, I. Pérez-Juste *et al.*, "Detection and imaging of quorum sensing in pseudomonas aeruginosa biofilm communities by surface-enhanced resonance raman scattering," Nature Materials (2016).

328. M. B. Wabuyele and T. Vo-Dinh, "Detection of human immunodeficiency virus type 1 dna sequence using plasmonics nanoprobes," Analytical chemistry **77**, 7810–7815 (2005).

329. Anshup, J. S. Venkataraman, C. Subramaniam, R. R. Kumar, S. Priya, T. S. Kumar, R. Omkumar, A. John, and T. Pradeep, "Growth of gold nanoparticles in human cells," Langmuir **21**, 11562–11567 (2005).

330. A. Shamsaie, M. Jonczyk, J. Sturgis, J. P. Robinson, and J. Irudayaraj, "Intracellularly grown gold nanoparticles as potential surface-enhanced raman scattering probes," Journal of biomedical optics **12**, 020502–020502 (2007).

331. J. Lin, R. Chen, S. Feng, Y. Li, Z. Huang, Y. Xie, Y. Yu, M. Cheng, and H. Zeng, "Rapid delivery of silver nanoparticles into living cells by electroporation for surface-enhanced raman spectroscopy," Biosensors and Bioelectronics **25**, 388–394 (2009).

332. E. A. Vitol, Z. Orynbayeva, M. J. Bouchard, J. Azizkhan-Clifford, G. Friedman, and Y. Gogotsi, "In situ intracellular spectroscopy with surface enhanced raman spectroscopy (sers)-enabled nanopipettes," ACS nano **3**, 3529–3536 (2009).

333. J. Liu, D. Yin, S. Wang, H.-Y. Chen, and Z. Liu, "Probing low-copy-number proteins in a single living cell," Angewandte Chemie International Edition **55**, 13215–13218 (2016).

334. S. Schlücker, B. Küstner, A. Punge, R. Bonfig, A. Marx, and P. Ströbel, "Immuno-raman microspectroscopy: in situ detection of antigens in tissue specimens by surface-enhanced raman scattering," Journal of Raman Spectroscopy **37**, 719–721 (2006).

335. M. Schütz, D. Steinigeweg, M. Salehi, K. Kömpe, and S. Schlücker, "Hydrophilically stabilized gold nanostars as sers labels for tissue imaging of the tumor suppressor p63 by immuno-sers microscopy," Chemical Communications **47**, 4216–4218 (2011).

336. E. Cepeda-Pérez, T. López-Luke, P. Salas, G. Plascencia-Villa, A. Ponce, J. Vivero-Escoto, M. José-Yacamán, and E. de la Rosa, "Sers-active au/sio 2 clouds in powder for rapid ex vivo breast adenocarcinoma diagnosis," Biomedical Optics Express **7**, 2407–2418 (2016).

337. D. Lin, S. Feng, J. Pan, Y. Chen, J. Lin, G. Chen, S. Xie, H. Zeng, and R. Chen, "Colorectal cancer detection by gold nanoparticle based surface-enhanced raman spectroscopy of blood serum and statistical analysis," Optics express **19**, 13565–13577 (2011).

338. S. Feng, J. Lin, M. Cheng, Y.-Z. Li, G. Chen, Z. Huang, Y. Yu, R. Chen, and H. Zeng, "Gold nanoparticle based surface-enhanced raman scattering spectroscopy of cancerous and normal nasopharyngeal tissues under near-infrared laser excitation," Applied spectroscopy **63**, 1089–1094 (2009).

339. S. C. Pînzaru, L. Andronie, I. Domsa, O. Cozar, and S. Astilean, "Bridging biomolecules with nanoparticles: surface-enhanced raman scattering from colon carcinoma and normal tissue," Journal of Raman Spectroscopy **39**, 331–334 (2008).

340. X. Qian, X.-H. Peng, D. O. Ansari, Q. Yin-Goen, G. Z. Chen, D. M. Shin, L. Yang, A. N. Young, M. D. Wang, and S. Nie, "In vivo tumor targeting and spectroscopic detection with surface-enhanced raman nanoparticle tags," Nature biotechnology **26**, 83–90 (2008).

341. K. K. Maiti, U. Dinish, A. Samanta, M. Vendrell, K.-S. Soh, S.-J. Park, M. Olivo, and Y.-T. Chang, "Multiplex targeted in vivo cancer detection using sensitive near-infrared sers nanotags," Nano Today **7**, 85–93 (2012).

342. A. Samanta, K. K. Maiti, K.-S. Soh, X. Liao, M. Vendrell, U. Dinish, S.-W. Yun, R. Bhuvaneswari, H. Kim, S. Rautela *et al.*, "Ultrasensitive near-infrared raman reporters for sers-based in vivo cancer detection," Angewandte Chemie International Edition **50**, 6089–6092 (2011).

343. S. E. Bohndiek, A. Wagadarikar, C. L. Zavaleta, D. Van de Sompel, E. Garai, J. V. Jokerst, S. Yazdanfar, and S. S. Gambhir, "A small animal raman instrument for rapid, wide-area, spectroscopic imaging," Proceedings of the National Academy of Sciences **110**, 12408–12413 (2013).

344. M. Espina Palanco, K. B. Mogensen, and K. Kneipp, "Raman spectroscopic probing of plant material using sers," Journal of Raman Spectroscopy **47**, 156–161 (2016).

345. H. Chu, Y. Huang, and Y. Zhao, "Silver nanorod arrays as a surface-enhanced raman scattering substrate for foodborne pathogenic bacteria detection," Applied spectroscopy **62**, 922–931 (2008).

346. Y. Xie, L. Xu, Y. Wang, J. Shao, L. Wang, H. Wang, H. Qian, and W. Yao, "Label-free detection of the foodborne pathogens of enterobacteriaceae by surface-enhanced raman spectroscopy," Analytical Methods **5**, 946–952 (2013).

347. P. Falagan-Lotsch, E. M. Grzincic, and C. J. Murphy, "One low-dose exposure of gold nanoparticles induces long-term changes in human cells," Proceedings of the National Academy of Sciences **113**, 13318–13323 (2016).

348. R. Zhang, Y. Zhang, Z. Dong, S. Jiang, C. Zhang, L. Chen, L. Zhang, Y. Liao, J. Aizpurua, Y. e. Luo *et al.*, "Chemical mapping of a single molecule by plasmon-enhanced raman scattering," Nature **498**, 82–86 (2013).

349. N. Hayazawa, T.-a. Yano, and S. Kawata, "Highly reproducible tip-enhanced raman scattering using an oxidized and metallized silicon cantilever tip as a tool for everyone," Journal of Raman Spectroscopy **43**, 1177–1182 (2012).

350. N. Kumar, S. J. Spencer, D. Imbraguglio, A. M. Rossi, A. J. Wain, B. M. Weckhuysen, and D. Roy, "Extending the plasmonic lifetime of tip-enhanced raman spectroscopy probes," Physical Chemistry Chemical Physics **18**, 13710–13716 (2016).

351. W. Zhang, B. S. Yeo, T. Schmid, and R. Zenobi, "Single molecule tip-enhanced raman spectroscopy with silver tips," The Journal of Physical Chemistry C **111**, 1733–1738 (2007).

352. B.-S. Yeo, J. Stadler, T. Schmid, R. Zenobi, and W. Zhang, "Tip-enhanced raman spectroscopy–its status, challenges and future directions," Chemical Physics Letters **472**, 1–13 (2009).

353. F. Sinjab, B. Lekprasert, R. A. Woolley, C. J. Roberts, S. J. Tendler, and I. Notingher, "Near-field raman spectroscopy of biological nanomaterials by in situ laser-induced synthesis of tip-enhanced raman spectroscopy tips," Optics letters **37**, 2256–2258 (2012).

354. R. Rodriguez, E. Sheremet, S. Müller, O. Gordan, A. Villabona, S. Schulze, M. Hietschold, and D. Zahn, "Compact metal probes: A solution for atomic force microscopy based tip-enhanced raman spectroscopy," Review of scientific instruments **83**, 123708 (2012).

355. C. Ropers, C. Neacsu, T. Elsaesser, M. Albrecht, M. Raschke, and C. Lienau, "Grating-coupling of surface plasmons onto metallic tips: a nanoconfined light source," Nano letters **7**, 2784–2788 (2007).

356. T. L. Vasconcelos, B. S. Archanjo, B. Fragneaud, B. S. Oliveira, J. Riikonen, C. Li, D. S. Ribeiro, C. Rabelo, W. N. Rodrigues, A. Jorio *et al.*, "Tuning localized surface plasmon resonance in scanning near-field optical microscopy probes," ACS nano **9**, 6297–6304 (2015).

357. Y. You, N. Purnawirman, H. Hu, J. Kasim, H. Yang, C. Du, T. Yu, and Z. Shen, "Tip-enhanced raman spectroscopy using single-crystalline ag nanowire as tip," Journal of Raman Spectroscopy **41**, 1156–1162 (2010).

358. C. Leiterer, T. Deckert-Gaudig, P. Singh, J. Wirth, V. Deckert, and W. Fritzsche, "Dielectrophoretic positioning of single nanoparticles on atomic force microscope tips for tip-enhanced raman spectroscopy," Electrophoresis **36**, 1142–1148 (2015).

359. C. S. Sweetenham, R. A. Woolley, and I. Notingher, "In-situ fabrication of gold nanoparticle functionalized probes for tip-enhanced raman spectroscopy by dielectrophoresis," Journal of Nanophotonics **10**, 030502–030502 (2016).

360. I. Notingher and A. Elfick, "Effect of sample and substrate electric properties on the electric field enhancement at the apex of spm nanotips," The Journal of Physical Chemistry B **109**, 15699–15706 (2005).

361. W. Zhang, T. Schmid, B.-S. Yeo, and R. Zenobi, "Near-field heating, annealing, and signal loss in tip-enhanced raman spectroscopy," The Journal of Physical Chemistry C **112**, 2104–2108 (2008).

362. T. Deckert-Gaudig and V. Deckert, "Ultraflat transparent gold nanoplates-ideal substrates for tip-enhanced raman scattering experiments," Small **5**, 432–436 (2009).

363. K. F. Domke, D. Zhang, and B. Pettinger, "Tip-enhanced raman spectra of picomole quantities of dna nucleobases at au (111)," Journal of the American Chemical Society **129**, 6708–6709 (2007).

364. E. Bailo and V. Deckert, "Tip-enhanced raman spectroscopy of single rna strands: Towards a novel direct-sequencing method," Angewandte Chemie International Edition **47**, 1658–1661 (2008).

365. R. Treffer, X. Lin, E. Bailo, T. Deckert-Gaudig, and V. Deckert, "Distinction of nucleobases–a tip-enhanced raman approach," Beilstein journal of nanotechnology **2**, 628–637 (2011).

366. D. Kurouski, T. Deckert-Gaudig, V. Deckert, and I. K. Lednev, "Structure and composition of insulin fibril surfaces probed by ters," Journal of the American Chemical Society **134**, 13323–13329 (2012).

367. D. Kurouski, T. Deckert-Gaudig, V. Deckert, and I. K. Lednev, "Surface characterization of insulin protofilaments and fibril polymorphs using tip-enhanced raman spectroscopy (ters)," Biophysical journal **106**, 263–271 (2014).

368. L. Opilik, T. Bauer, T. Schmid, J. Stadler, and R. Zenobi, "Nanoscale chemical imaging of segregated lipid domains using tip-enhanced raman spectroscopy," Physical Chemistry Chemical Physics **13**, 9978–9981 (2011).

369. N. Kazemi-Zanjani, H. Chen, H. A. Goldberg, G. K. Hunter, B. Grohe, and F. Lagugne-Labarthet, "Label-free mapping of osteopontin adsorption to calcium oxalate monohydrate crystals by tip-enhanced raman spectroscopy," Journal of the American Chemical Society **134**, 17076–17082 (2012).

370. U. Neugebauer, P. Rösch, M. Schmitt, J. Popp, C. Julien, A. Rasmussen, C. Budich, and V. Deckert, "On the way to nanometer-sized information of the bacterial surface by tip-enhanced raman spectroscopy," ChemPhysChem **7**, 1428–1430 (2006).

371. U. Neugebauer, U. Schmid, K. Baumann, W. Ziebuhr, S. Kozitskaya, V. Deckert, M. Schmitt, and J. Popp, "Towards a detailed understanding of bacterial metabolism-spectroscopic characterization of staphylococcus epidermidis," ChemPhysChem **8**, 124–137 (2007).

372. D. Cialla, T. Deckert-Gaudig, C. Budich, M. Laue, R. Möller, D. Naumann, V. Deckert, and J. Popp, "Raman to the limit: tip-enhanced raman spectroscopic investigations of a single tobacco mosaic virus," Journal of Raman Spectroscopy **40**, 240–243 (2009).

373. T. Deckert-Gaudig, R. Böhme, E. Freier, A. Sebesta, T. Merkendorf, J. Popp, K. Gerwert, and V. Deckert, "Nanoscale distinction of membrane patches–a ters study of halobacterium salinarum," Journal of biophotonics **5**, 582–591 (2012).

374. B. R. Wood, E. Bailo, M. A. Khiavi, L. Tilley, S. Deed, T. Deckert-Gaudig, D. McNaughton, and V. Deckert, "Tip-enhanced raman scattering (ters) from hemozoin crystals within a sectioned erythrocyte," Nano letters **11**, 1868–1873 (2011).

375. B. R. Wood, M. Asghari-Khiavi, E. Bailo, D. McNaughton, and V. Deckert, "Detection of nano-oxidation sites on the surface of hemoglobin crystals using tip-enhanced raman scattering," Nano letters **12**, 1555–1560 (2012).

376. T. Schmid, A. Messmer, B.-S. Yeo, W. Zhang, and R. Zenobi, "Towards chemical analysis of nanostructures in biofilms ii: tip-enhanced raman spectroscopy of alginates," Analytical and bioanalytical chemistry **391**, 1907–1916 (2008).

377. T. Schmid, B.-S. Yeo, G. Leong, J. Stadler, and R. Zenobi, "Performing tip-enhanced raman spectroscopy in liquids," Journal of Raman Spectroscopy **40**, 1392–1399 (2009).

378. F. Latorre, S. Kupfer, T. Bocklitz, D. Kinzel, S. Trautmann, S. Gräfe, and V. Deckert, "Spatial resolution of tip-enhanced raman spectroscopy–dft assessment of the chemical effect," Nanoscale **8**, 10229–10239 (2016).

379. C. Blum, T. Schmid, L. Opilik, N. Metanis, S. Weidmann, and R. Zenobi, "Missing amide i mode in gap-mode tip-enhanced raman spectra of proteins," The Journal of Physical Chemistry C **116**, 23061–23066 (2012).

380. D. Kurouski, T. Postiglione, T. Deckert-Gaudig, V. Deckert, and I. K. Lednev, "Amide i vibrational mode suppression in surface (sers) and tip (ters) enhanced raman spectra of protein specimens," Analyst **138**, 1665–1673 (2013).

381. R. Wiens, C. R. Findlay, S. G. Baldwin, L. Kreplak, J. M. Lee, S. P. Veres, and K. M. Gough, "High spatial resolution (1.1 μm and 20 nm) ftir polarization contrast imaging reveals pre-rupture disorder in damaged tendon," Faraday discussions (2016).

382. S. Ekgasit and H. Ishida, "New optical depth-profiling technique by use of the multiple-frequency approach with single atr ft-ir spectrum: Theoretical development," Applied spectroscopy **51**, 1488–1495 (1997).

383. M. W. Urban, C. L. Allison, G. L. Johnson, and F. Di Stefano, "Stratification of butyl acrylate/polyurethane (ba/pur) latexes: Atr and step-scan photoacoustic studies," Applied Spectroscopy **53**, 1520–1527 (1999).

384. R. W. Jones and J. F. McClelland, "Quantitative depth profiling using saturation-equalized photoacoustic spectra," Applied spectroscopy **56**, 409–418 (2002).

385. W. Faubel, S. Heissler, and R. A. Palmer, "Quantitative analysis of corroded copper patina by step scan and rapid scan photoacoustic fourier transform infrared spectroscopy," Review of scientific instruments **74**, 331–333 (2003).

386. I. Notingher, R. E. Imhof, P. Xiao, and F. C. Pascut, "Spectral depth profiling of arbitrary surfaces by thermal emission decay-fourier transform infrared spectroscopy," Applied spectroscopy **57**, 1494–1501 (2003).

387. I. Notingher and R. E. Imhof, "Mid-infrared in vivo depth-profiling of topical chemicals on skin," Skin Research and Technology **10**, 113–121 (2004).

388. P. Matousek, N. Everall, M. Towrie, and A. Parker, "Depth profiling in diffusely scattering media using raman spectroscopy and picosecond kerr gating," Applied spectroscopy **59**, 200–205 (2005).

389. P. Matousek, I. Clark, E. Draper, M. Morris, A. Goodship, N. Everall, M. Towrie, W. Finney, and A. Parker, "Subsurface probing in diffusely scattering media using spatially offset raman spectroscopy," Applied spectroscopy **59**, 393–400 (2005).

390. P. Matousek, M. Morris, N. Everall, I. Clark, M. Towrie, E. Draper, A. Goodship, and A. Parker, "Numerical simulations of subsurface probing in diffusely scattering media using spatially offset raman spectroscopy," Applied spectroscopy **59**, 1485–1492 (2005).

391. P. Matousek, E. R. Draper, A. E. Goodship, I. P. Clark, K. L. Ronayne, and A. W. Parker, "Noninvasive raman spectroscopy of human tissue in vivo," Applied spectroscopy **60**, 758–763 (2006).

392. J. R. Maher and A. J. Berger, "Determination of ideal offset for spatially offset raman spectroscopy," Applied spectroscopy **64**, 61–65 (2010).

393. J. Qin, M. S. Kim, W. F. Schmidt, B.-K. Cho, Y. Peng, and K. Chao, "A line-scan hyperspectral raman system for spatially offset raman spectroscopy," Journal of Raman Spectroscopy (2015).

394. Z. Liao, F. Sinjab, G. Gibson, M. Padgett, and I. Notingher, "Dmd-based software-configurable spatially-offset raman spectroscopy for spectral depth-profiling of optically turbid samples," Optics Express **24**, 12701–12712 (2016).

395. P. Matousek, "Inverse spatially offset raman spectroscopy for deep noninvasive probing of turbid media," Applied spectroscopy **60**, 1341–1347 (2006).

396. C. Conti, C. Colombo, M. Realini, G. Zerbi, and P. Matousek, "Subsurface raman analysis of thin painted layers," Applied spectroscopy **68**, 686–691 (2014).

397. C. Conti, M. Realini, C. Colombo, K. Sowoidnich, N. K. Afseth, M. Bertasa, A. Botteon, and P. Matousek, "Noninvasive analysis of thin turbid layers using microscale spatially offset raman spectroscopy," Analytical chemistry **87**, 5810–5815 (2015).

398. C. Conti, M. Realini, C. Colombo, and P. Matousek, "Comparison of key modalities of micro-scale spatially offset raman spectroscopy," Analyst **140**, 8127–8133 (2015).

399. N. Stone, K. Faulds, D. Graham, and P. Matousek, "Prospects of deep raman spectroscopy for noninvasive detection of conjugated surface enhanced resonance raman scattering nanoparticles buried within 25 mm of mammalian tissue," Analytical chemistry **82**, 3969–3973 (2010).

400. N. Stone and P. Matousek, "Advanced transmission raman spectroscopy: a promising tool for breast disease diagnosis," Cancer Research **68**, 4424–4430 (2008).

401. J.-L. H. Demers, S. C. Davis, B. W. Pogue, and M. D. Morris, "Multichannel diffuse optical raman tomography for bone characterization in vivo: a phantom study," Biomedical optics express **3**, 2299–2305 (2012).

402. S. Sil and S. Umapathy, "Raman spectroscopy explores molecular structural signatures of hidden materials in depth: Universal multiple angle raman spectroscopy," Scientific reports **4** (2014).

403. D. Yang and Y. Ying, "Applications of raman spectroscopy in agricultural products and food analysis: A review," Applied Spectroscopy Reviews **46**, 539–560 (2011).

404. C. Eliasson and P. Matousek, "Noninvasive authentication of pharmaceutical products through packaging using spatially offset raman spectroscopy," Analytical Chemistry **79**, 1696–1701 (2007).

405. C. Eliasson, N. Macleod, and P. Matousek, "Noninvasive detection of concealed liquid explosives using raman spectroscopy," Analytical chemistry **79**, 8185–8189 (2007).

406. P. Matousek and N. Stone, "Development of deep subsurface raman spectroscopy for medical diagnosis and disease monitoring," Chemical Society Reviews **45**, 1794–1802 (2016).

407. K. Buckley, J. G. Kerns, J. Vinton, P. D. Gikas, C. Smith, A. W. Parker, P. Matousek, and A. E. Goodship, "Towards the in vivo prediction of fragility fractures with raman spectroscopy," Journal of Raman Spectroscopy **46**, 610–618 (2015).

408. J.-L. H. Demers, F. W. Esmonde-White, K. A. Esmonde-White, M. D. Morris, and B. W. Pogue, "Next-generation raman tomography instrument for non-invasive in vivo bone imaging," Biomedical optics express **6**, 793–806 (2015).

409. K. Buckley, C. Atkins, D. Chen, H. Schulze, D. Devine, M. Blades, and R. Turner, "Non-invasive spectroscopy of transfusable red blood cells stored inside sealed plastic blood-bags," Analyst **141**, 1678–1685 (2016).

410. Z. Liao, F. Sinjab, A. Nommeots-Nomm, J. R. Jones, L. Ruiz Cantu, J. Yang, F. Rose, and I. Notingher, "Feasibility of spatially-offset raman spectroscopy for in-vitro and in-vivo monitoring mineralisation of bone tissue-engineering scaffolds," Analytical Chemistry **89**, 847–853 (2017).

411. B. Sharma, K. Ma, M. R. Glucksberg, and R. P. Van Duyne, "Seeing through bone with surface-enhanced spatially offset raman spectroscopy," Journal

of the American Chemical Society **135**, 17290–17293 (2013).

412. J. M. Yuen, N. C. Shah, J. T. Walsh Jr, M. R. Glucksberg, and R. P. Van Duyne, "Transcutaneous glucose sensing by surface-enhanced spatially offset raman spectroscopy in a rat model," Analytical chemistry **82**, 8382–8385 (2010).

413. B. Gardner, P. Matousek, and N. Stone, "Temperature spatially offset raman spectroscopy (t-sors): Subsurface chemically specific measurement of temperature in turbid media using anti-stokes spatially offset raman spectroscopy," Analytical chemistry **88**, 832–837 (2015).

414. B. Gardner, N. Stone, and P. Matousek, "Non-invasive chemically specific measurement of subsurface temperature in biological tissues using surface-enhanced spatially offset raman spectroscopy," Faraday discussions (2016).

415. J. R. Maher, J. A. Inzana, H. A. Awad, and A. J. Berger, "Overconstrained library-based fitting method reveals age-and disease-related differences in transcutaneous raman spectra of murine bones," Journal of biomedical optics **18**, 077001–077001 (2013).

416. J. Mo, W. Zheng, and Z. Huang, "Fiber-optic raman probe couples ball lens for depth-selected raman measurements of epithelial tissue," Biomedical optics express **1**, 17–30 (2010).

417. M. Agenant, M. Grimbergen, R. Draga, E. Marple, R. Bosch, and C. van Swol, "Clinical superficial raman probe aimed for epithelial tumor detection: Phantom model results," Biomedical optics express **5**, 1203–1216 (2014).

418. J. Wang, M. S. Bergholt, W. Zheng, and Z. Huang, "Development of a beveled fiber-optic confocal raman probe for enhancing in vivo epithelial tissue raman measurements at endoscopy," Optics letters **38**, 2321–2323 (2013).

419. J. Ma and D. Ben-Amotz, "Rapid micro-raman imaging using fiber-bundle image compression," Applied spectroscopy **51**, 1845–1848 (1997).

420. M. P. Nelson and M. Myrick, "Single-frame chemical imaging: Dimension reduction fiber-optic array improvements and application to laser-induced breakdown spectroscopy," Applied spectroscopy **53**, 751–759 (1999).

421. J. C. Day and N. Stone, "A subcutaneous raman needle probe," Applied spectroscopy **67**, 349–354 (2013).

422. P. D. Pudney, E. Y. Bonnist, P. J. Caspers, J.-P. Gorce, C. Marriot, G. J. Puppels, S. Singleton, and M. J. van der Wolf, "A new in vivo raman probe for enhanced applicability to the body," Applied spectroscopy **66**, 882–891 (2012).

423. Z. Wang, H. Ding, G. Lu, and X. Bi, "Use of a mechanical iris-based fiber optic probe for spatially offset raman spectroscopy," Optics letters **39**, 3790–3793 (2014).

424. M. D. Keller, E. Vargis, N. de Matos Granja, R. H. Wilson, M.-A. Mycek, M. C. Kelley, and A. Mahadevan-Jansen, "Development of a spatially offset raman spectroscopy probe for breast tumor surgical margin evaluation," Journal of biomedical optics **16**, 077006–077006 (2011).

425. N. Stone, R. Baker, K. Rogers, A. W. Parker, and P. Matousek, "Subsurface probing of calcifications with spatially offset raman spectroscopy (sors): future possibilities for the diagnosis of breast cancer," Analyst **132**, 899–905 (2007).

426. M. S. Bergholt, W. Zheng, and Z. Huang, "Characterizing variability in in vivo raman spectroscopic properties of different anatomical sites of normal tissue in the oral cavity," Journal of Raman Spectroscopy **43**, 255–262 (2012).

427. M. A. Short, I. T. Tai, D. Owen, and H. Zeng, "Using high frequency raman spectra for colonic neoplasia detection," Optics express **21**, 5025–5034 (2013).

428. A. Mahadevan-Jansen, M. F. Mitchell, N. Ramanujam, U. Utzinger, and R. Richards-Kortum, "Development of a fiber optic probe to measure nir raman spectra of cervical tissue in vivo," Photochemistry and photobiology **68**, 427–431 (1998).

429. U. Utzinger, D. L. Heintzelman, A. Mahadevan-Jansen, A. Malpica, M. Follen, and R. Richards-Kortum, "Near-infrared raman spectroscopy for in vivo detection of cervical precancers," Applied spectroscopy **55**, 955–959 (2001).

430. J. Horsnell, P. Stonelake, J. Christie-Brown, G. Shetty, J. Hutchings, C. Kendall, and N. Stone, "Raman spectroscopy: a new method for the intra-operative assessment of axillary lymph nodes," Analyst **135**, 3042–3047 (2010).

431. N. Huang, M. Short, J. Zhao, H. Wang, H. Lui, M. Korbelik, and H. Zeng, "Full range characterization of the raman spectra of organs in a murine model," Optics express **19**, 22892–22909 (2011).

432. J. Desroches, M. Jermyn, K. Mok, C. Lemieux-Leduc, J. Mercier, K. St-Arnaud, K. Urmey, M.-C. Guiot, E. Marple, K. Petrecca *et al.*, "Characterization of a raman spectroscopy probe system for intraoperative brain tissue classification," Biomedical optics express **6**, 2380–2397 (2015).

433. S. Dochow, I. Latka, M. Becker, R. Spittel, J. Kobelke, K. Schuster, A. Graf, S. Brückner, S. Unger, M. Rothhardt *et al.*, "Multicore fiber with integrated fiber bragg gratings for background-free raman sensing," Optics express **20**, 20156–20169 (2012).

434. A. C. Brunetti, W. Margulis, and K. Rottwitt, "Raman probes based on optically-poled double-clad fiber and coupler," Optics express **20**, 28563–28572 (2012).

435. P. I. Okagbare and M. D. Morris, "Fluorocarbon fiber-optic raman probe for non-invasive raman spectroscopy," Applied spectroscopy **66**, 728–730 (2012).

436. S. Koljenovic, T. B. Schut, R. d. Wolthuis, B. De Jong, L. Santos, P. J. Caspers, J. M. Kros, and G. J. Puppels, "Tissue characterization using high wave number raman spectroscopy," Journal of biomedical optics **10**, 031116–03111611 (2005).

437. W. Wang, M. Short, I. T. Tai, and H. Zeng, "Disposable sheath that facilitates endoscopic raman spectroscopy," Journal of biomedical optics **21**, 025001–025001 (2016).

438. Z. Huang, M. S. Bergholt, W. Zheng, K. Lin, K. Y. Ho, M. Teh, and K. G. Yeoh, "In vivo early diagnosis of gastric dysplasia using narrow-band image-guided raman endoscopy," Journal of biomedical optics **15**, 037017–037017 (2010).

439. M. S. Bergholt, K. Lin, W. Zheng, D. P. C. Lau, and Z. Huang, "In vivo, real-time, transnasal, image-guided raman endoscopy: defining spectral properties in the nasopharynx and larynx," Journal of biomedical optics **17**, 0770021–0770027 (2012).

440. J. Schleusener, P. Gluszczynska, C. Reble, I. Gersonde, J. Helfmann, H.-J. Cappius, J. W. Fluhr, and M. C. Meinke, "Perturbation factors in the clinical handling of a fiber-coupled raman probe for cutaneous in vivo diagnostic raman spectroscopy," Applied spectroscopy **69**, 243–256 (2015).

441. C. J. Rowlands, S. Varma, W. Perkins, I. Leach, H. Williams, and I. Notingher, "Rapid acquisition of raman spectral maps through minimal sampling: applications in tissue imaging," Journal of biophotonics **5**, 220–229 (2012).

442. K. Kong, C. J. Rowlands, H. Elsheikha, and I. Notingher, "Label-free molecular analysis of live neospora caninum tachyzoites in host cells by selective scanning raman micro-spectroscopy," Analyst **137**, 4119–4122 (2012).

443. C. A. Patil, C. L. Arrasmith, M. A. Mackanos, D. L. Dickensheets, and A. Mahadevan-Jansen, "A handheld laser scanning confocal reflectance imaging–confocal raman microspectroscopy system," Biomedical optics express **3**, 488–502 (2012).

444. A. C.-T. Ko, M. Hewko, L. Leonardi, M. G. Sowa, C. C. Dong, P. Williams, B. Cleghorn *et al.*, "Ex vivo detection and characterization of early dental caries by optical coherence tomography and raman spectroscopy," Journal of biomedical optics **10**, 031118–03111816 (2005).

445. C. A. Patil, H. Kirshnamoorthi, D. L. Ellis, T. G. van Leeuwen, and A. Mahadevan-Jansen, "A clinical instrument for combined raman spectroscopy-optical coherence tomography of skin cancers," Lasers in surgery and medicine **43**, 143–151 (2011).

446. K. Kong, F. Zaabar, E. Rakha, I. Ellis, A. Koloydenko, and I. Notingher, "Towards intra-operative diagnosis of tumours during breast conserving surgery

by selective-sampling raman micro-spectroscopy," Physics in medicine and biology **59**, 6141 (2014).

447. S. Takamori, K. Kong, S. Varma, I. Leach, H. C. Williams, and I. Notingher, "Optimization of multimodal spectral imaging for assessment of resection margins during mohs micrographic surgery for basal cell carcinoma," Biomedical optics express **6**, 98–111 (2015).

448. J. D. Neufeld, M. Wagner, and J. C. Murrell, "Who eats what, where and when? isotope-labelling experiments are coming of age," The ISME Journal **1**, 103–110 (2007).

449. H. Zhang, X.-j. Li, D. B. Martin, and R. Aebersold, "Identification and quantification of n-linked glycoproteins using hydrazide chemistry, stable isotope labeling and mass spectrometry," Nature biotechnology **21**, 660–666 (2003).

450. W. E. Huang, K. Stoecker, R. Griffiths, L. Newbold, H. Daims, A. S. Whiteley, and M. Wagner, "Raman-fish: combining stable-isotope raman spectroscopy and fluorescence in situ hybridization for the single cell analysis of identity and function," Environmental Microbiology **9**, 1878–1889 (2007).

451. W. E. Huang, A. Ferguson, A. C. Singer, K. Lawson, I. P. Thompson, R. M. Kalin, M. J. Larkin, M. J. Bailey, and A. S. Whiteley, "Resolving genetic functions within microbial populations: in situ analyses using rrna and mrna stable isotope probing coupled with single-cell raman-fluorescence in situ hybridization," Applied and environmental microbiology **75**, 234–241 (2009).

452. H.-J. van Manen, A. Lenferink, and C. Otto, "Noninvasive imaging of protein metabolic labeling in single human cells using stable isotopes and raman microscopy," Analytical chemistry **80**, 9576–9582 (2008).

453. C. Matthäus, C. Krafft, B. Dietzek, B. R. Brehm, S. Lorkowski, and J. Popp, "Noninvasive imaging of intracellular lipid metabolism in macrophages by raman microscopy in combination with stable isotopic labeling," Analytical chemistry **84**, 8549–8556 (2012).

454. H. N. N. Venkata and S. Shigeto, "Stable isotope-labeled raman imaging reveals dynamic proteome localization to lipid droplets in single fission yeast cells," Chemistry & biology **19**, 1373–1380 (2012).

455. H. Yamakoshi, K. Dodo, A. Palonpon, J. Ando, K. Fujita, S. Kawata, and M. Sodeoka, "Alkyne-tag raman imaging for visualization of mobile small molecules in live cells," Journal of the American Chemical Society **134**, 20681–20689 (2012).

456. H. Yamakoshi, K. Dodo, M. Okada, J. Ando, A. Palonpon, K. Fujita, S. Kawata, and M. Sodeoka, "Imaging of edu, an alkyne-tagged cell proliferation probe, by raman microscopy," Journal of the American Chemical Society **133**, 6102–6105 (2011).

457. H. Yamakoshi, A. Palonpon, K. Dodo, J. Ando, S. Kawata, K. Fujita, and M. Sodeoka, "A sensitive and specific raman probe based on bisarylbutadiyne for live cell imaging of mitochondria," Bioorganic & medicinal chemistry letters **25**, 664–667 (2015).

458. Y. Chen, J.-Q. Ren, X.-G. Zhang, D.-Y. Wu, A.-G. Shen, and J.-M. Hu, "Alkyne-modulated surface-enhanced raman scattering-palette for optical interference-free and multiplex cellular imaging," Analytical Chemistry (2016).

459. R. Kurihara, Y. Ikemura, and K. Tanabe, "Preparation of alkyne-labeled 2-nitroimidazoles for identification of tumor hypoxia by raman spectroscopy," Bioorganic & Medicinal Chemistry Letters **26**, 4892–4894 (2016).

460. J. Cui, S. Matsuoka, M. Kinoshita, N. Matsumori, F. Sato, M. Murata, J. Ando, H. Yamakoshi, K. Dodo, and M. Sodeoka, "Novel raman-tagged sphingomyelin that closely mimics original raft-forming behavior," Bioorganic & medicinal chemistry **23**, 2989–2994 (2015).

461. S. Hong, T. Chen, Y. Zhu, A. Li, Y. Huang, and X. Chen, "Live-cell stimulated raman scattering imaging of alkyne-tagged biomolecules," Angewandte Chemie International Edition **53**, 5827–5831 (2014).

462. F. Hu, Z. Chen, L. Zhang, Y. Shen, L. Wei, and W. Min, "Vibrational imaging of glucose uptake activity in live cells and tissues by stimulated raman scattering," Angewandte Chemie **127**, 9959–9963 (2015).

463. J. Deng, Q. Wei, M. Zhang, Y. Wang, and Y.-Q. Li, "Study of the effect of alcohol on single human red blood cells using near-infrared laser tweezers raman spectroscopy," Journal of Raman Spectroscopy **36**, 257–261 (2005).

464. Z. Huang, X. Chen, Y. Li, J. Chen, J. Lin, J. Wang, J. Lei, and R. Chen, "Quantitative determination of citric acid in seminal plasma by using raman spectroscopy," Applied spectroscopy **67**, 757–760 (2013).

465. G. B. Jung, Y. J. Lee, G. Lee, and H.-K. Park, "A simple and rapid detection of tissue adhesive-induced biochemical changes in cells and dna using raman spectroscopy," Biomedical optics express **4**, 2673–2682 (2013).

466. Y. J. Lee, H. J. Ahn, G.-J. Lee, G. B. Jung, G. Lee, D. Kim, J.-H. Shin, K.-H. Jin, and H.-K. Park, "Investigation of biochemical property changes in activation-induced cd8+ t cell apoptosis using raman spectroscopy," Journal of biomedical optics **20**, 075001–075001 (2015).

467. T. Buchwald, K. Niciejewski, M. Kozielski, M. Siatkowski, H. Krauss et al., "Identifying compositional and structural changes in spongy and subchondral bone from the hip joints of patients with osteoarthritis using raman spectroscopy," Journal of biomedical optics **17**, 0170071–0170077 (2012).

468. N. Li, D. Chen, Y. Xu, S. Liu, and H. Zhang, "Confocal raman micro-spectroscopy for rapid and label-free detection of maleic acid-induced variations in human sperm," Biomedical optics express **5**, 1690–1699 (2014).

469. T. Saxena, B. Deng, D. Stelzner, J. Hasenwinkel, and J. Chaiken, "Raman spectroscopic investigation of spinal cord injury in a rat model," Journal of biomedical optics **16**, 027003–027003 (2011).

470. H. Bai, H. Li, Z. Han, C. Zhang, J. Zhao, C. Miao, S. Yan, A. Mao, H. Zhao, and Z. Han, "Label-free assessment of replicative senescence in mesenchymal stem cells by raman microspectroscopy," Biomedical optics express **6**, 4493–4500 (2015).

471. I. Barman, N. C. Dingari, A. Saha, S. McGee, L. H. Galindo, W. Liu, D. Plecha, N. Klein, R. R. Dasari, and M. Fitzmaurice, "Application of raman spectroscopy to identify microcalcifications and underlying breast lesions at stereotactic core needle biopsy," Cancer research **73**, 3206–3215 (2013).

472. G. Perna, M. Lasalvia, A. Castro, E. Mezzenga, N. L'Abbate, P. Biagi, and V. Capozzi, "Detection of pesticide effects in human keratinocytes by means of raman microspectroscopy," Applied Physics Letters **95**, 083701 (2009).

473. A. C. De Luca, G. Rusciano, R. Ciancia, V. Martinelli, G. Pesce, B. Rotoli, L. Selvaggi, and A. Sasso, "Spectroscopical and mechanical characterization of normal and thalassemic red blood cells by raman tweezers," Optics express **16**, 7943–7957 (2008).

474. A. S. Haka, K. E. Shafer-Peltier, M. Fitzmaurice, J. Crowe, R. R. Dasari, and M. S. Feld, "Diagnosing breast cancer by using raman spectroscopy," Proceedings of the National Academy of Sciences of the United States of America **102**, 12371–12376 (2005).

475. A. Ghita, F. C. Pascut, V. Sottile, and I. Notingher, "Monitoring the mineralisation of bone nodules in vitro by space-and time-resolved raman micro-spectroscopy," Analyst **139**, 55–58 (2014).

476. G. Das, R. La Rocca, T. Lakshmikanth, F. Gentile, R. Tallerico, L. P. Zambetti, J. Devitt, P. Candeloro, F. De Angelis, E. Carbone et al., "Monitoring human leukocyte antigen class i molecules by micro-raman spectroscopy at single-cell level," Journal of biomedical optics **15**, 027007–027007 (2010).

477. N. D. Magee, J. R. Beattie, C. Carland, R. Davis, K. McManus, I. Bradbury, D. A. Fennell, P. W. Hamilton, M. Ennis, J. J. McGarvey et al., "Raman microscopy in the diagnosis and prognosis of surgically resected nonsmall cell lung cancer," Journal of biomedical optics **15**, 026015–026015 (2010).

478. Y. H. Ong, M. Lim, and Q. Liu, "Comparison of principal component analysis and biochemical component analysis in raman spectroscopy for the discrimination of apoptosis and necrosis in k562 leukemia cells," Optics express **20**, 22158–22171 (2012).

479. Q. Matthews, A. Jirasek, J. Lum, X. Duan, and A. G. Brolo, "Variability in raman spectra of single human tumor cells cultured in vitro: correlation with cell cycle and culture confluency," Applied spectroscopy **64**, 871–887 (2010).

480. S. Barkur, A. Bankapur, M. Pradhan, S. Chidangil, D. Mathur, and U. Ladiwala, "Probing differentiation in cancer cell lines by single-cell micro-raman spectroscopy," Journal of Biomedical Optics **20**, 085001–085001 (2015).

481. E. E. Rossi, L. Silveira, A. L. B. Pinheiro, S. R. Zamuner, F. Aimbire, M. Maia, and M. T. T. Pacheco, "Raman spectroscopy for differential diagnosis of endophthalmitis and uveitis in rabbit iris in vitro," Experimental eye research **91**, 362–368 (2010).

482. M. L. Paret, S. K. Sharma, L. M. Green, and A. M. Alvarez, "Biochemical characterization of gram-positive and gram-negative plant-associated bacteria with micro-raman spectroscopy," Applied spectroscopy **64**, 433–441 (2010).

483. E. Azrad, E. Cagnano, S. Halevy, S. Rosenwaks, and I. Bar, "Bullous pemphigoid detection by micro-raman spectroscopy and cluster analysis: structure alterations of proteins," Journal of Raman Spectroscopy **36**, 1034–1039 (2005).

484. J. W. Chan, D. S. Taylor, S. M. Lane, T. Zwerdling, J. Tuscano, and T. Huser, "Nondestructive identification of individual leukemia cells by laser trapping raman spectroscopy," Analytical Chemistry **80**, 2180–2187 (2008).

485. P. Rösch, S. Stöckel, S. Meisel, A. Bossecker, U. Münchberg, S. Kloss, W. Schumacher, and J. Popp, "Bacterial identification in real samples by means of micro-raman spectroscopy," in "European Conferences on Biomedical Optics," (International Society for Optics and Photonics, 2011), pp. 808708–808708.

486. T. Bhattacharjee, S. Tawde, R. Hudlikar, M. Mahimkar, G. Maru, A. Ingle, and C. M. Krishna, "Ex vivo raman spectroscopic study of breast metastatic lesions in lungs in animal models," Journal of biomedical optics **20**, 085006–085006 (2015).

487. P. Chen, A. Shen, W. Zhao, S.-J. Baek, H. Yuan, and J. Hu, "Raman signature from brain hippocampus could aid alzheimer's disease diagnosis," Applied optics **48**, 4743–4748 (2009).

488. G. B. Jung, S. W. Nam, S. Choi, G.-J. Lee, and H.-K. Park, "Evaluation of antibiotic effects on pseudomonas aeruginosa biofilm using raman spectroscopy and multivariate analysis," Biomedical optics express **5**, 3238–3251 (2014).

489. U. Neugebauer, T. Bocklitz, J. Clement, C. Krafft, and J. Popp, "Towards detection and identification of circulating tumour cells using raman spectroscopy," Analyst **135**, 3178–3182 (2010).

490. C. Bielecki, T. W. Bocklitz, M. Schmitt, C. Krafft, C. Marquardt, A. Gharbi, T. Knösel, A. Stallmach, and J. Popp, "Classification of inflammatory bowel diseases by means of raman spectroscopic imaging of epithelium cells," Journal of biomedical optics **17**, 0760301–0760308 (2012).

491. S. Stöckel, S. Meisel, M. Elschner, P. Rosch, and J. Popp, "Identification of bacillus anthracis via raman spectroscopy and chemometric approaches," Analytical chemistry **84**, 9873–9880 (2012).

492. N. C. Dingari, I. Barman, J. W. Kang, C.-R. Kong, R. R. Dasari, and M. S. Feld, "Wavelength selection-based nonlinear calibration for transcutaneous blood glucose sensing using raman spectroscopy," Journal of biomedical optics **16**, 087009–087009 (2011).

493. S. K. Teh, W. Zheng, K. Y. Ho, M. Teh, K. G. Yeoh, and Z. Huang, "Diagnosis of gastric cancer using near-infrared raman spectroscopy and classification and regression tree techniques," Journal of biomedical optics **13**, 034013–034013 (2008).

494. W. Schumacher, M. Kühnert, P. Rösch, and J. Popp, "Identification and classification of organic and inorganic components of particulate matter via raman spectroscopy and chemometric approaches," Journal of Raman Spectroscopy **42**, 383–392 (2011).

495. S. K. Teh, W. Zheng, D. P. Lau, and Z. Huang, "Spectroscopic diagnosis of laryngeal carcinoma using near-infrared raman spectroscopy and random recursive partitioning ensemble techniques," Analyst **134**, 1232–1239 (2009).

496. R. O. Draga, M. C. Grimbergen, P. L. Vijverberg, C. F. v. Swol, T. G. Jonges, J. A. Kummer, and J. Ruud Bosch, "In vivo bladder cancer diagnosis by high-volume raman spectroscopy," Analytical chemistry **82**, 5993–5999 (2010).

497. D. M. Haaland and E. V. Thomas, "Partial least-squares methods for spectral analyses. 1. relation to other quantitative calibration methods and the extraction of qualitative information," Analytical Chemistry **60**, 1193–1202 (1988).

498. K. L. Bechtel, W.-C. Shih, and M. S. Feld, "Intrinsic raman spectroscopy for quantitative biological spectroscopy part ii: experimental applications," Optics express **16**, 12737–12745 (2008).

499. P. Meksiarun, N. Spegazzini, H. Matsui, K. Nakajima, Y. Matsuda, and H. Sato, "In vivo study of lipid accumulation in the microalgae marine diatom thalassiosira pseudonana using raman spectroscopy," Applied spectroscopy **69**, 45–51 (2015).

500. C. J. Saatkamp, M. L. de Almeida, J. A. M. Bispo, A. L. B. Pinheiro, A. B. Fernandes, and L. Silveira, "Quantifying creatinine and urea in human urine through raman spectroscopy aiming at diagnosis of kidney disease," Journal of biomedical optics **21**, 037001–037001 (2016).

501. W.-C. Shih, K. L. Bechtel, and M. V. Rebec, "Noninvasive glucose sensing by transcutaneous raman spectroscopy," Journal of biomedical optics **20**, 051036–051036 (2015).

502. J. R. Maher, M. Takahata, H. A. Awad, and A. J. Berger, "Raman spectroscopy detects deterioration in biomechanical properties of bone in a glucocorticoid-treated mouse model of rheumatoid arthritis," Journal of biomedical optics **16**, 087012–087012 (2011).

503. S. Duraipandian, M. S. Bergholt, W. Zheng, K. Y. Ho, M. Teh, K. G. Yeoh, J. B. Y. So, A. Shabbir, and Z. Huang, "Real-time raman spectroscopy for in vivo, online gastric cancer diagnosis during clinical endoscopic examination," Journal of biomedical optics **17**, 081418–081418 (2012).

504. S. Li, G. Chen, Y. Zhang, Z. Guo, Z. Liu, J. Xu, X. Li, and L. Lin, "Identification and characterization of colorectal cancer using raman spectroscopy and feature selection techniques," Optics express **22**, 25895–25908 (2014).

505. M. S. Bergholt, W. Zheng, K. Lin, K. Y. Ho, M. Teh, K. G. Yeoh, J. B. Yan So, and Z. Huang, "In vivo diagnosis of gastric cancer using raman endoscopy and ant colony optimization techniques," International journal of cancer **128**, 2673–2680 (2011).

506. S. Duraipandian, W. Zheng, J. Ng, J. J. Low, A. Ilancheran, and Z. Huang, "In vivo diagnosis of cervical precancer using raman spectroscopy and genetic algorithm techniques," Analyst **136**, 4328–4336 (2011).

AUTHOR BIOGRAPHIES

Dustin Shipp received his BSc (Physics and Mathematics) in 2008 from Brigham Young University. In 2014, he graduated with his PhD (Optics) from the University of Rochester. His pursued his dissertation research in angular light scattering and Raman micro-spectroscopy under the supervision of Andrew Berger. Before joining Prof. Notingher's group, Dustin taught physics for a year as a Lecturer at Rochester Institute of Technology. His current research interests include Raman hyperspectral imaging and other non-labeling methods in biomedical optics.

Faris Sinjab received a 1st class MPhys (Physics with Theoretical Physics) from the University of Manchester in 2010. He received his PhD (Physics) in 2015 at the University of Nottingham in the group of Ioan Notingher, where he carried out experiments using enhanced Raman spectroscopy for nanoscale investigations of novel biomaterials. He was awarded an EPSRC Doctoral Prize fellowship (2015-2017) during which his research involved exploring new technologies and complementary techniques to partner with Raman microscopy for improved biological applications.

Ioan Notingher is Professor of Physics in the School of Physics and Astronomy at the University of Nottingham. He graduated from Babes-Bolyai University Cluj-Napoca (Romania) in 1998, with a BSc (1st class) in Physics, and received his PhD in 2001 (London South Bank University, Professor Bob Imhof's group). During his PhD, he developed a new technique for non-contact non-invasive spectral measurements of materials, with the main focus in-vivo skin characterisation. In 2001 he took a postdoctoral position at Imperial College London and started working with Professor Larry Hench on developing Raman spectroscopy techniques for label-free characterisation of live cells and tissue engineering constructs. In 2004 he moved to Edinburgh University (Dr Alistair Elfick's group) where he worked on near-field Raman spectroscopy. In 2006, Ioan joined as an assistant professor the School of Physics and Astronomy at the University of Nottingham, where he established the Biophotonics Group.